The Thesis Committee for Canalp Ozkul
Certifies that this is the approved version of the following thesis:

Fracture Abundance and Strain in Folded Cardium Formation, Alberta Fold-and-Thrust Belt, Canada

APPROVED BY
SUPERVISING COMMITTEE:

Supervisor:

Peter Eichhubl

Co-Supervisor:

Estibalitz Ukar

Randall Marrett

William Fisher

Fracture Abundance and Strain in Folded Cardium Formation, Alberta Fold-and-Thrust Belt, Canada

by

Canalp Ozkul, B.S

Thesis

Presented to the Faculty of the Graduate School of

The University of Texas at Austin

in Partial Fulfillment

of the Requirements

for the Degree of

Master of Science in Geological Sciences

The University of Texas at Austin

December 2014

Dedication

This thesis is dedicated to my mother, Saniye Ozkul, my father, Aziz Ozkul and my brother, Yigitalp Ozkul for their love, support, and encouragement.

Acknowledgements

I would like to express my utmost gratitude to my supervisor, Dr. Peter Eichhubl for his continuous academic and research support and guidance over the course of my master studies. Dr. Eichhubl comments and discussion has improved this thesis significantly. I am also grateful to my co-supervisor, Dr. Estiblitz Ukar for her supervision support during my master studies. Dr. Ukar has significantly contributed to improving my SEM work, kinematic modeling, and scaling analysis. Both advisors have also assisted me tremendously during my field work in Alberta, Canada. It was my pleasure to study under their supervision. I foresee this experience to be very valuable for my future career. I thank my thesis committee members Dr. Randall Marrett and Dr. William Fisher for taking time to review this work and providing insightful feedback. I would also like to thank Dr. Stephen Laubach, Dr. Julia Gale, and Dr. András Fall for helpful discussions. This work was supported by the Industrial Associates of the Fracture Research and Application Consortium at the Bureau of Economic Geology. I am very grateful for Turkish Petroleum Corporation-TPAO for providing scholarship support to pursue a master's degree.

I would like to acknowledge the Bureau of Economic Geology staff for their support and assistance throughout my work. I thank Patrick Smith for providing training on carbon coating and for supporting my work at the SEM lab. I am also thankful for Sarah Elliot help and assistance carbon coating samples and troubleshooting SEM issues. I would like to acknowledge my fellow graduate students and friends in Austin who provided me with moral and academic support. I thank Yaser Alzayer, Nike Tokan-Lawal, Jon Major, and Owen Callahan for providing feedback and support whenever I needed it and engaging in discussions.

Abstract

Fracture Abundance and Strain in Folded Cardium Formation, Alberta Fold-and-Thrust Belt, Canada

Canalp Ozkul, M.S Geo. Sci.

The University of Texas at Austin, 2014

Supervisor: Peter Eichhubl

Co- Supervisor: Estibalitz Ukar

The folded and thrusted Mesozoic clastic sequence of the Canadian Rocky Mountain foothills forms important hydrocarbon reservoirs. Understanding the distribution of natural fractures, their evolution, and timing of formation relative to the evolution of the fold-and-thrust system could potentially improve exploration and development outcomes in these otherwise tight unconventional reservoirs. However, the formation of fractures and their timing relative to folding and thrusting have remained unclear.

I investigated the relation between folding and fracture formation in the Upper Cretaceous Cardium Sandstone by combining field structural observations and kinematic modeling of the fold-and-thrust belt evolution. I explored the relationship between fracture intensity and fracture strain with structural position by analyzing fracture spacing or frequency and aperture data collected along outcrop and micro-scanlines in the backlimb, in the forelimb close to the crest, and in the steeper dipping forelimb away

from the crest of the Red Deer River anticline. Fracture frequency and aperture data collected both at the outcrop and micro scales indicate that variation in fracture strain is small across these three structural domains of the fold, with somewhat lower fracture intensity in the forelimb close to the crest.

These fracture strain measurements are qualitatively consistent with calculated horizontal strain in the tectonic transport direction obtained through kinematic numerical models that simulate fold development associated with slip along the underlying Burnt Timber thrust. The models predict roughly similar amount of horizontal extension in both the back and forelimbs, and somewhat lower extension in the upper forelimb during early development of the Red Deer River anticline. Fracture formation early during fold development is consistent with the field structural observations of shear reactivation during later stages of folding.

This combined kinematic modeling and field structural study demonstrates that deforming fold and thrust belts can undergo a complex evolution of bed-parallel extension in both space and time, resulting in spatially variable fracture formation in such structurally complex subsurface reservoirs.

Table of Contents

List of Tables

List of Figures

Chapter 1: Introduction

The Canadian Rocky Mountains are one of the most extensively studied foreland fold-and-thrust belts, with specific focus on the Foothills and Front Ranges because of their hydrocarbon potential (Leckie and Smith, 1992; Price, 1994; Boettcher et al., 2010). The Foothills of the Canadian Rocky Mountains have been investigated for oil and gas exploration since the early part of the 20th century. Exploration focused primarily on conventional hydrocarbon reservoirs during the early part of the 20th century, and the unconventional hydrocarbon reservoirs of the region have been the focus in recent years. Because natural fractures affect permeability and thus production from these unconventional reservoirs, an understanding of the spatial distribution of natural fractures, their structural and diagenetic attributes, and the spatial and temporal relationships of fracture formation relative to the fold-and-thrust belt evolution are important (Narr and Currie, 1982; Newson, 2001; Salvini and Storti, 2001; Jager, 2008). However, the spatial and temporal relationships between fracture formation and the development of folds and thrusts as determined based on field structural criteria are often ambiguous, making it difficult to reconstruct the conditions under which fractures formed. Well tests and flow rates that are incompatible with production from the rock matrix alone have convinced some operators in western Canada that natural fractures can contribute to producibility (e.g., Cooper, 1992; Jamison, 1997; Newson, 2001; Solano et al., 2011). This study explores natural fractures in outcrops of western Canada producing units and identifies fracture attributes and evidence for fracture network evolution that

may be useful for designing drilling strategies for some western Canada reservoirs.

Current knowledge of fracture formation in fold-and-thrust belts frequently assumes that the formation of fractures a consequence of folding (Price 1966; Stearns, 1968; Hancock, 1985; Twiss and Moores, 1992). However, fractures may also predate folding with the possibility to become reactivated in opening-mode or by shearing during folding (Dunne 1986; Marrett and Laubach, 2001; Pollard and Bergbauer, 2004). Furthermore, fractures may form during uplift and exhumation concurrently with, or after, folding and thrusting (Laubach et al., 2010; Casini et al., 2011; Lorenz and Cooper, 2011; Reif et al., 2012).

Previous studies that addressed the spatial and temporal relationships between fracture formation and fold and thrust development focused mainly on the analysis of fracture orientation and the temporal relationships between fracture formation and fault-related folding using cross-cutting relationships in the field (Muecke and Charlesworth, 1966**;** Barton, 1983; a detailed literature summary is provided in Chapter 2). Comprehensive understanding of the fold-fracture relationships in thrust belts, however, requires analysis of fracture characteristics and distribution within their structural and stratigraphic setting. Hence, for this thesis, I conducted a study that addresses timing and spatial distribution of fractures relative to thrust-related folds. The study combines (i) field investigation to analyze fracture characteristics such as aperture, height, and average spacing in a structural context; (ii) macro- and microscanline analyses to measure fracture intensity and strain within structural position; and (iii) kinematic models to constrain the timing of fracturing in the Foothills relative to the overall structural evolution of the fold

-and-thrust belt, and to compare strain distributions from the models to those measured using scanlines in the field. The principal hypotheses tested are: 1. Fractures formed concurrently with folding; in this case, fracture abundance (frequency) or strain accommodated by the fractures is expected to correlate with the strain associated with folding. 2. Fractures formed prior to folding in which case no correlation between fracture strain and folding strain is expected. However, fractures may become reactivated during folding, with the kinematics of fracture reactivation compatible with the kinematics of the fold. 3. Fractures formed after folding, possibly in response to uplift and exhumation. No correlation between fracture and folding strain is expected.

I tested these hypotheses using outcrop structural observations and kinematic models of the Cretaceous Cardium Formation exposed in the Alberta Foothills. The Cardium Formation is a tight gas and oil sandstone reservoir with low porosity and permeability and considered to be the youngest important hydrocarbon-bearing formation in the region (Newson, 2003). Fractures observed in outcrop generally show the same diagenetic attributes as fractures observed in core allowing use of outcrop information to constrain properties of the fractured reservoir at depth. The Red Deer River anticline, located in the Alberta Foothills northwest of Calgary provides a suitable location for studying natural fractures in the Cardium Formation with accessible outcrops across a broad range of structural positions.

In this study, I characterized fractures in their structural context by analyzing the number of fracture sets and their orientation within outcrops of the Red Deer River anticline. I quantified fracture intensity and strain across the fold using macro- and

microscanline surveys to demonstrate correspondence between fracture formation and structural position. Fracture strain data were then compared to strain calculated through numerical fault and fold kinematic models predicting significant strain accumulation in the Cardium Formation in the forelimb of the anticline. This comparison of measured fracture strain data and strain predicted by these kinematic models shows a significant discrepancy. Based on these results and field structural observations, I conclude that the fractures formed prior to folding as regional sets of fractures.

Outline of this thesis

Chapter 2 provides a review of published literature on the spatial and temporal relationships between folds and fractures including proposed geometric and mechanical models relating fracture formation to folding are generally based on geometric considerations, and observations on fractures that display uniquely developed fracture patterns and distributions that are not compatible with simple fold-related fracture models.

Chapter 3 provides a regional geological summary and a description of the tectonic and stratigraphic setting of the region and of the lithologies and structures in the field area of the Red Deer River.

Chapter 4 reports structural observations, including field and lab-based fracture scanline results. It combines analyses of the orientation and distribution of opening-mode fractures and strain distribution within structural position. I also establish the relationship between relative timing of fracture development and the formation of meso-scale

structures.

Chapter 5 describes and interprets the numerical kinematic models and strain calculations. It includes maps and structural cross-sections of the study area. Chapter 5 presents kinematic models that are used to test the validity of proposed models of deformation and explore possible deformation styles that could have produced present-day structures. The models demonstrate the effects of structural architecture on the strain distribution during deformation.

Structural observations and numerical results are discussed in Chapter 6. An overall summary of this study is presented in Chapter 7.

Chapter 2: Geometric and Kinematic Relationships between Folds and Fractures

The spatial and temporal relationships between folds and fractures are generally seen as a first step toward predicting the permeability of fractured reservoirs (Narr and Currie, 1982; Nelson, 1985; Laubach, 1997). The spatial and mechanistic relationships between folds and fractures have thus received significant attention in the structural geologic literature (Price 1966, 1967; Stearns, 1968; Hancock, 1985; Twiss and Moores, 1992; Cooper, 1992; Lisle, 1994; Bergbauer and Pollard, 2004). Models that relate fracture formation to folding are generally based on geometric considerations, or on simple mechanical models such as the bending of an elastic beam. Fractures that exhibit symmetrical relations with respect to a fold have traditionally been interpreted to be fold-related fractures whereas fractures that display uniquely developed fracture patterns and distribution not compatible with simple fold-related fracture models are considered to be unrelated to fold development (Stearns, 1968; Hancock, 1985; Cooper, 1992). Based on their relative orientation to the fold axis, fold-related fractures have been described as fold-axis- or strike-parallel, strike-perpendicular, and oblique to the fold axis (Stearns, 1968; Hancock, 1985; Cooper, 1992; Tavani et al., 2006). These fracture patterns have been utilized to predict the orientation, distribution, and intensity of fractures where fracture data are scarce.

Stearns's (1968) classification of fold-related fractures distinguishes 11 main fracture orientations that fall into five fracture types (Figure 2.1) Stearn's use of the term type includes fractures of multiple orientations that are kinematically compatible and thus inferred to have formed concurrently. This use differs from the more common use (employed in the remainder of this thesis) of type describing fractures of common

orientation. Stearn's types 1 and 2 are the most commonly described fold-related fracture sets. Type 1 includes opening-mode fractures perpendicular to the fold axis and two sets of strike-slip faults whose acute bisector coincides with the opening-mode fractures. Type 2 includes opening-mode fractures parallel to the fold trend and two sets of strike-slip faults whose acute bisector coincides with the opening-mode fractures. Type 1 fractures occur where the maximum compressive principal stress is parallel to the dip direction of bedding whereas Type 2 fracture form when the maximum compressive principal stress is oriented parallel to the fold axis (Figure 3). Stearns (1968) suggested that Type 1 fractures form early during folding, and Type 2 fractures form when extension is normal to the fold. Types 3 and 4 are interpreted to be formed during bending or buckling. Type 4 fractures form two orientations of thrust faults. Type 5 fractures are developed in response to flexural slip during folding (Bergbauer and Pollard, 2004).

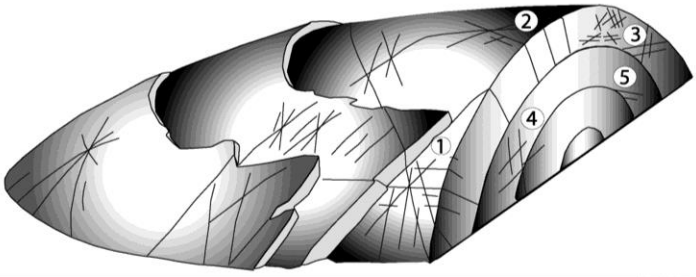

Figure 2.1 Spatial relationship of fracture with respect to fold geometry (From Bergbauer and Pollard (2004) after Stearns 1968).

Figure 2.2 shows the Stearns model as depicted by Twiss and Moores (1992) with the 5 main fracture sets. Spatial distribution of Set 1 and Set 4 fractures, which are both perpendicular to bedding, show that they are commonly observed on the limbs whereas Set 2, 3 and 5 are commonly found in fold hinges.

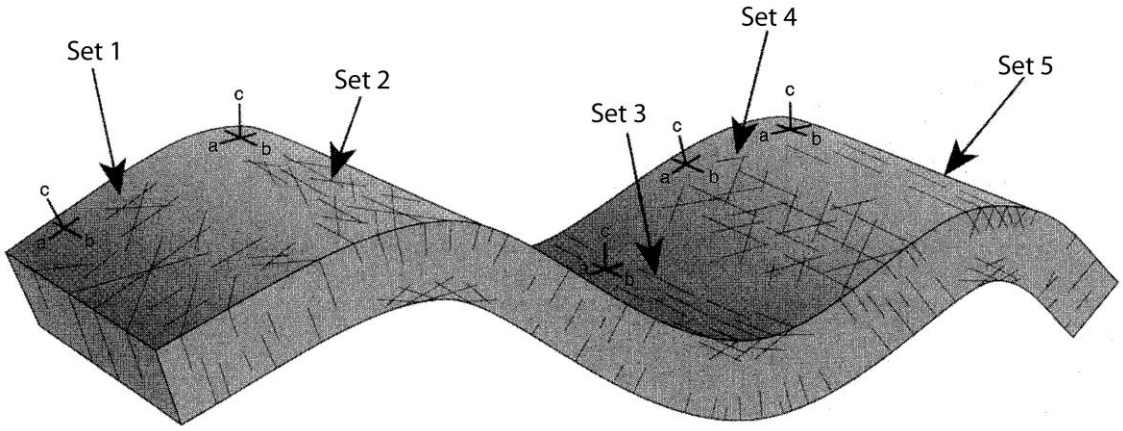

Figure 2.2 Orientation of main fracture sets with respect to fold (From Twiss and Moores, 1992).

The Stearns (1968) model has found wide acceptance because it is based on simple geometric relationships. However, it only relates formation of fractures to folding, not accounting for fractures that pre-date or post-date folding and are thus unrelated to folding; such fractures may not obey simple symmetrical relationships as proposed by Stearns (Hancock, 1985; Dunn, 1986; Price and Cosgrove 1990; Twiss and Moores, 1992).

Hancock (1985) studied the fracture-fold relation in thrust-belt systems and suggested that fractures formed prior or after folding show no symmetrical relationships with respect to folds. He also suggested that the orientation of fractures that obey symmetrical relationships varies depending on the dip of deformed strata, the fold plunge, and the attitude of the axial plane.

In thrust belts, deformational features, such as stylolites, extensional fractures (joints and veins), and small-scale faults, form due to changes in the local stress field

during the evolution of folds associated with thrust displacement (Hancock, 1985; Salvini and Storti, 2004). Factors that control the spatial distribution and intensity of fractures in thrust-belt systems include fold mechanics, mechanical stratigraphy, variations in the stress field, and variations of the preexisting deformational history (Salvini and Storti, 2004; Tavani, 2006).

FOLDING MECHANISMS

The formation of fractures associated with folding may be influenced by the mechanism of folding (Cooper, 1992; Dahlstrom, 1990, Fischer et al., 1992; Srivastava and Engelder, 1990; Storti and Salvini, 1996; Salvini and Storti, 2001). Two end-member mechanisms of thrust-related folding can be defined: folds with a fixed hinge and folds with an active or rolling hinge (Salvini and Storti, 2004). In the fixed-hinge folding model, the hinge remains stationary relative to the folded strata while limbs rotate about a fixed axial surface (De Sitter, 1956; Gosh and Saha, 2005; Mercier et al., 2007). In this case, folding strain monotonically increases with increasing deformation. In active-hinge folds, the hinge migrates relative to the folded strata as the strata move laterally along active fault surfaces (Suppe et al., 1983). In this case, as a rock volume passes through the fold hinge, the rock volume may experience an initial increase in folding strain as it moves into the hinge, followed by a decrease in folding strain or a flattening of the layers as the volume moves out of the hinge. For folds that form with a fixed hinge, highest fracture intensity is expected to occur in the fold hinge (De Sitter, 1956; McConnell, 1994; Salvini and Storti, 2004). In this case, layer-parallel shortening causes outer-arc extension above a

neutral fiber in the developing fold that favors the formation of opening-mode fractures (Murray, 1968). In fixed-hinge folds, the spatial distribution and intensity of fractures appear to be controlled by the fold interlimb angle (Murray, 1968; Salvini and Storti, 2004). Fisher et al. (2009) provided examples of fracture formation in fixed-hinge folds composed of multiple layers separated by detachment horizons (flexural slip folds) (Fig. 2.3). On the other hand, for folds with an active or rolling hinge, thrust-related fold kinematics may result in a complex evolutionary path of a fold and thus in complex fracture geometry and intensity patterns (Hancock, 1985). These patterns differ from fracture patterns developed as a function a of simple layer curvature (Murray, 1968). In this case, high fracture intensity would be expected to be found along the hinge migration path (Fischer et al., 1992; Salvini and Storti, 2004). Thus, fracture intensities and patterns will depend on the folding mechanism, and they will vary with structural position. Whereas deformation in fixed hinged folds is expected to concentrate at the hinges and decrease towards the limbs, deformation in active-hinge folds will be highest in the fold limbs in the wake of the fold hinge migrating over the ramp (e.g. Salvini and Storti, 2001; Suppe, 1983).

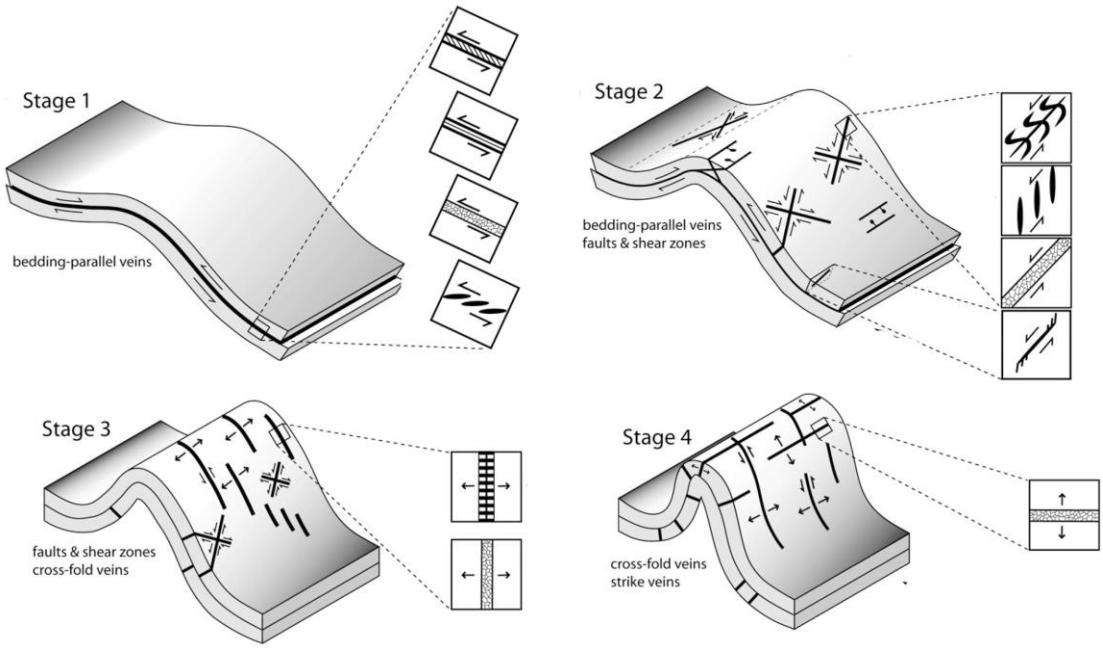

Figure 2.3 Evolution of the Nuncios Detachment fold. The sequential stage of the fold evolution illustrate fracture formation (From Fisher et al., 2009)

Fault propagation folds are usually characterized by fixed hinges and rotating limb folding. (Larsen, 2009). In fault- propagation folds, limbs become deformed and folded as the fault propagates whereas the crest region of the fold remains undeformed (Suppe, 1985). The forelimb is anticipated to be more deformed than the backlimb and is commonly rotated and overturned (Salvini and Storti, 2001) (Figure 2.4).

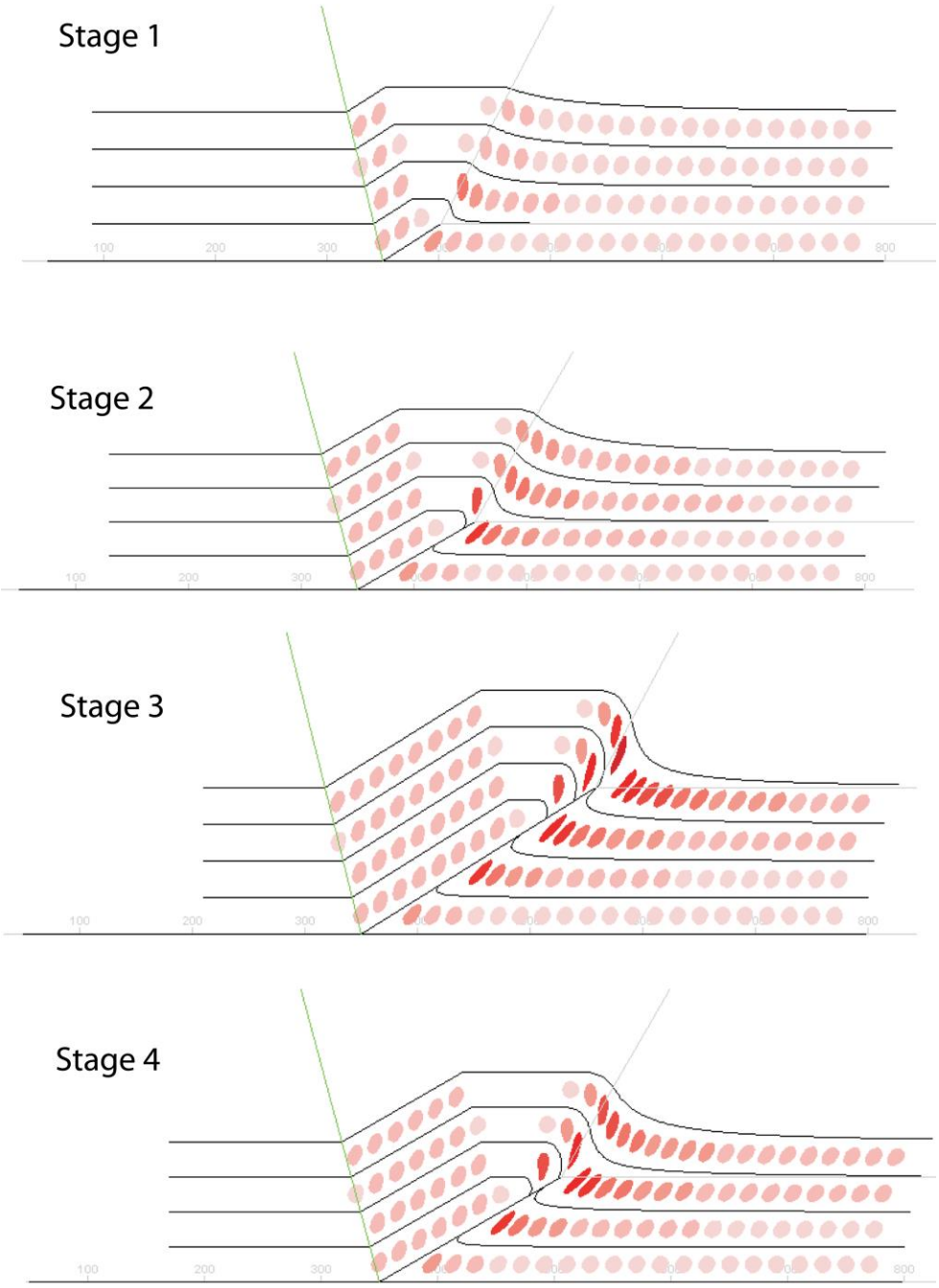

Figure 2.4 An example of a fault-propagation fold. Strain ellipses indicate magnitude and orientation of strain. Darker colors indicate areas of higher strain that may be associated with higher fracture intensity (From Shackleton, 2003).

Figure 2.5 shows the evolution of a fault-bend-fold where folding strain is accommodated by bending and faulting in the limbs above the ramp in the early stage of deformation (Figures 2.5 and 2.6a). As displacement along the fault increases, faults also develop in the crest of the fold (Panel 3 in Figure 2.6b) (Salvini and Storti, 2004). The highest fault or fracture intensity is located in the limbs and will vary over time. With increasing slip along the ramp, the highest deformation is predicted for panel 3 (in the crest of the fold, Figure 2.6b), and for the forelimb (panel 2) (Salvini and Storti, 2001; Larsen, 2009).

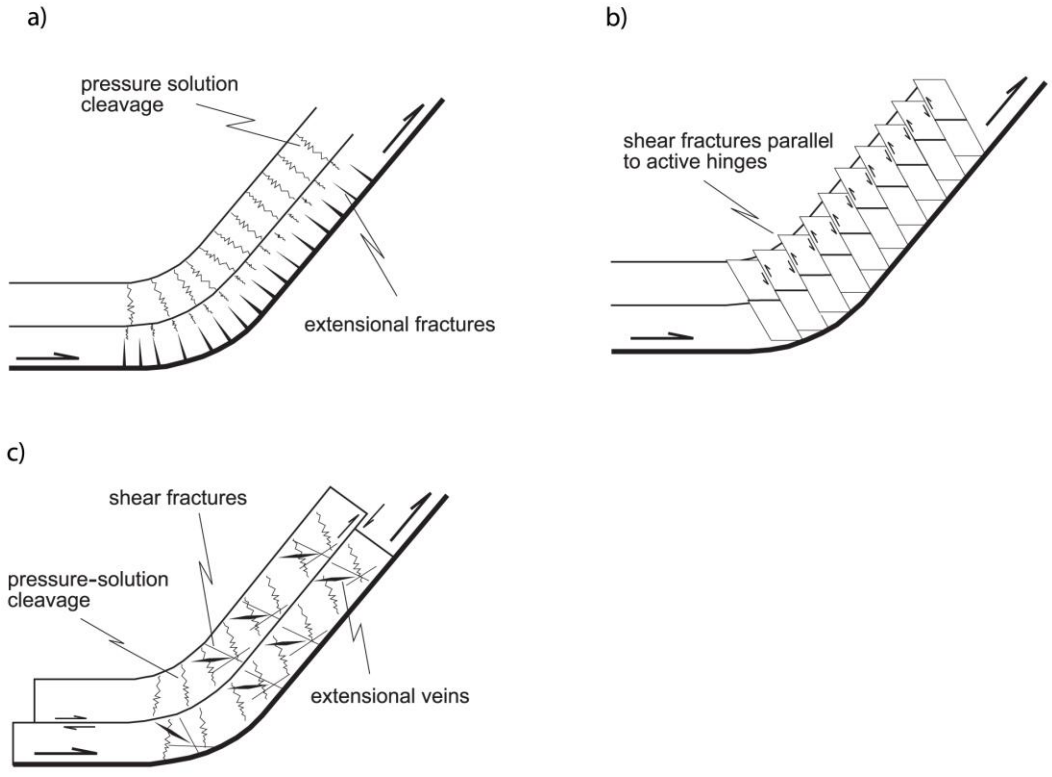

Figure 2.5 Deformation patterns formed during bending and faulting of layers about an active axial surface (modified from Salvini and Storti, 2004).

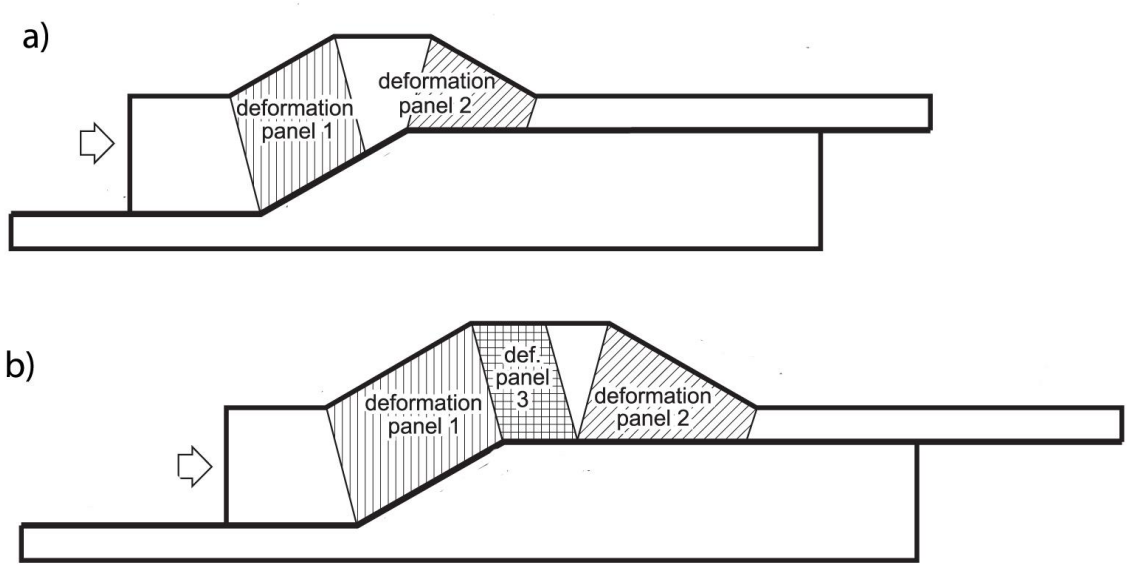

Figure 2.6 Evolution of deformation in a fault-bend-fold. a) Early stage of deformation. b) Later stage of deformation. (Modified from Salvini and Storti, 2004)

MECHANICAL LAYER THICKNESS

Mechanical stratigraphy, considered to be a primary factor in determining the brittle deformation processes of layered units, is controlled by bed thickness, the contrast in competence and rock strength, and the mechanical properties of bedding planes. Mechanical stratigraphy is (e.g. De Sitter, 1956; Ramsay, 1974; Ladeira and Price, 1981; Sanderson, 1982; Dahlstrom, 1990; Srivastava and Engelder, 1990; Helgeson and Aydin, 1991; Narr and Suppe, 1991; Fischer et al., 1992; Storti and Salvini, 1996; Salvini and Storti, 2001; Laubach et al., 2009). Fractures are typically confined by layer boundaries where fracture height equals layer thickness (Helgson and Aydin, 1991). Mechanical layer thickness can thus influence fracture length and spacing (e.g. Wu and Pollard, 1995; Bai and Pollard 2000; Bai et al.,

2000). Mechanical layer thickness show usually inverse relationship with fracture intensity. Thus, fracture intensity going to be higher, when mechanical layering is thinner (Wennberg et al., 2006; Cook et al., 2006). Similarly, propagation and linkage of fractures in interlayered brittle and ductile rocks depends on the mechanical layer thickness and the ductility of the rocks (Rijken and Cooke, 2001; Friedman et al., 1994). In addition, the rock strength appears to be an important control in determining the fracture intensity. The stronger the rock, the more fracture it contains. Thus, stronger rocks show higher fracture intensity (Nelson, 1985). Laubach et al. (2009) emphasized that present day mechanical stratigraphy may not coincide with the observed fracture stratigraphy because of diagenetic changes in rock properties since fracture formation.

EVOLUTION OF STRESS CONDITION INSIDE FOLDED LAYERS

The formation of fractures associated with folding may be influenced by the stress distribution and orientation inside the folded layer (Jamison 1992; Lemiszki et al., 1994). Figure 2.7 shows the effect of stress distribution associated with layer-parallel compression and buckling, illustrating the heterogeneous stress distribution with different parts of a fold. This heterogeneity of the stress field in deformed layers causes different characteristics of observed fracture patterns, including extension fractures and conjugate shear fractures, across folds (Twiss and Moores, 1992).

In recent years, numerical simulations of stress distribution in folded strata have been used to determine the mechanism of fracture formation and the sequence of fracturing and folding (Twiss and Moores, 1992; Salvini and Storti, 2001). As folds

develop, orientations and magnitudes of stresses in folded strata can change in magnitude and orientation (Figure 2.7). For example, before buckling, the maximum principal stress is parallel to the length of the layer whereas the least principal stress is perpendicular to the length of the layer. Within the developing fold, the least principal stress becomes parallel to the convex side of the layer (outer arch) whereas the maximum principal stress is approximately perpendicular to the bar (Twiss and Moores, 1992). Stress trajectories for a buckle fold are shown in Figure 2.7.

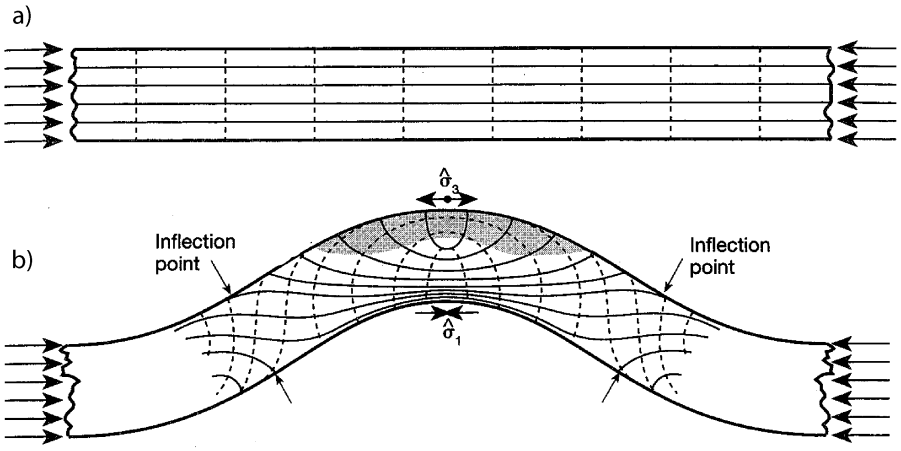

Figure 2 7 a: Orientation stress trajectories before deformation. b: Orientation of stress trajectories after deformation showing complex stress condition. Solid lines indicate the maximum principle stresses whereas the dashed lines indicate the minimum principle stresses (Modified from Twiss and Moores, 1992).

PRE-EXISTING FRACTURES

Bergbauer and Pollard (2004) emphasized the importance of pre-folding fractures that can cause mechanical (strength) anisotropy of the strata thus affecting subsequent

fracturing during folding. Figure 2.8 shows the orientation of preexisting fractures and synfolding fractures in the Emigrant Gap anticline, Wyoming. Fractures that formed before folding are generally not expected to be oriented in a preferred symmetric orientation with respect to the fold axis, especially if they formed under stress conditions that were different from those during folding (Dunn, 1986). These pre-fold fractures may result in strength anisotropy of the folded rocks that will influence subsequent fracturing during folding (Twiss and Moores, 1992; Pollard and Bergbauer, 2004).

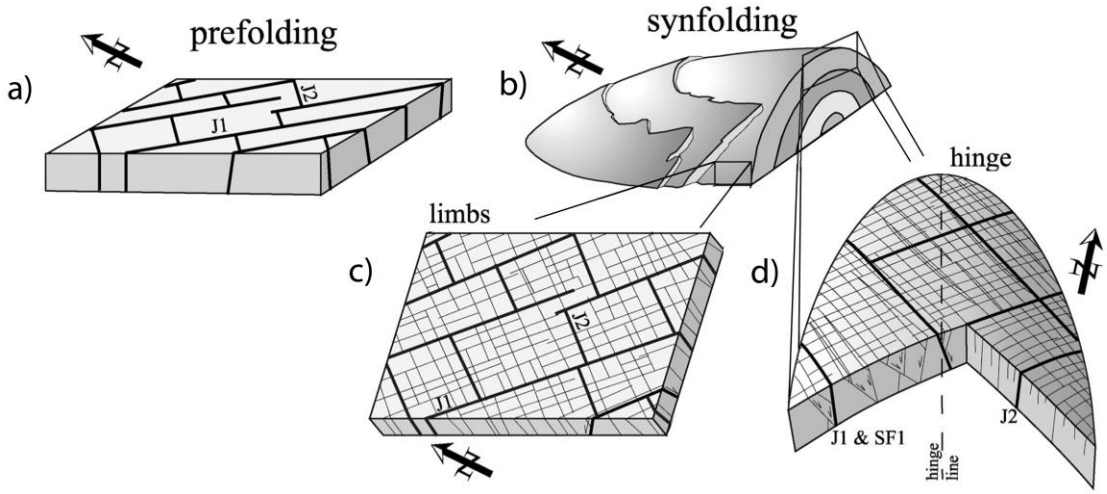

Figure 2.8 The relationship between fractures and folding in the Emigrant Gap anticline. a: Preexisting fractures before folding. b; Folded strata. c: Orientation of fractures on the limb. d: Orientation of fractures in the hinge of the anticline (From Bergbauer & Pollard, 2004).

Most of the existing fold-related-fracturing models underestimate, or ignore, the existence of prefolding fractures and their contribution to mechanical anisotropy. These pre-existing fractures can be reactivated during folding due to changes in stress

conditions associated with folding and tilting of the layers. Reactivation usually results in shearing of fractures that originally formed as opening-mode fractures.

Heterogeneity in the spatial distribution of fractures can be indicative of fractures that formed before folding, but it could also indicate that fractures formed after folding, during exhumation of folded strata (Dunne, 1986; Bellahsen, 2006; Allwardt et al., 2007). The orientation of such exhumation-related fractures may be influenced by the layering of the folded strata and thus show systematic variations in dip across the fold (Jager et al., 2008; English, 2012). Similar to fractures that form before folding, fractures that form after folding and during exhumation are expected to display orientations that do not correspond with the stress field that was present during folding. In contrast to fractures that formed during folding, fracture abundance of exhumation-related fractures would not be expected to relate to structural position. Similar to the reactivation of pre-folding fractures during folding, exhumation may reactivate earlier formed fractures in shear (Doré et al., 2002). Therefore, the correct application of a fold-related fracture study requires not only the analysis of purely geometric models (e.g. Stearns's model) but also an approach that combines mechanical (kinematic and dynamic, i.e. stress-based) models and field observations to predict fracture density and orientations of fractures across a fold (Murray, 1986; Lisle 1994).

CURVATURE ANALYSIS VS. KINEMATIC MODELS

The concept of the curvature analyses provides a quantitative estimation of the degree of deformation or strain of deformed strata that can be then used to predict fracture

orientations and intensities (Murray 1968; Lisle 1994). The relationship of curvature and stress-strain is thus used as a proxy for fracture prediction (Bergbauer, 2007) where areas of high Gaussian curvature are assumed to coincide with areas of high fracture intensity (Lisle 1994; Hennings et al., 2000). One of the shortcomings of the curvature analyses, however, is that it only takes into account the present-day geometry of a fold, but does not take into account the deformation associated with the evolution of folds through time (e.g., rolling hinges). Similarly, pre-folding fractures that may become reactivated during folding are ignored.

This study presents an approach that uses kinematic models to 1) model the evolution of folds and thrusts through time, and 2) predict the distribution of fracture strain and associated fractures across a fold. Results from these kinematic models were compared to fracture intensities and fracture strain measured in the field. This was achieved by complete analysis of mechanical models, fracture characteristics based primarily on field and thin section investigations including spatial distribution of fractures, and the chronological relationship of fracture sets.

Chapter 3 Geological Setting

General Geology

The Foothills of the Canadian Rocky Mountains form one of the best-studied foreland fold-and-thrust-belts (FFTB) in the world. The Foothills of west central Alberta are located in the eastern part of the Rocky Mountains belt (Monger, 1989) and comprise a thin-skinned, Late Jurassic to Eocene foreland fold-and-thrust belt. The Foothills are located between the Front Range to the west and Triangle Zone to the east (Figure 3.1).

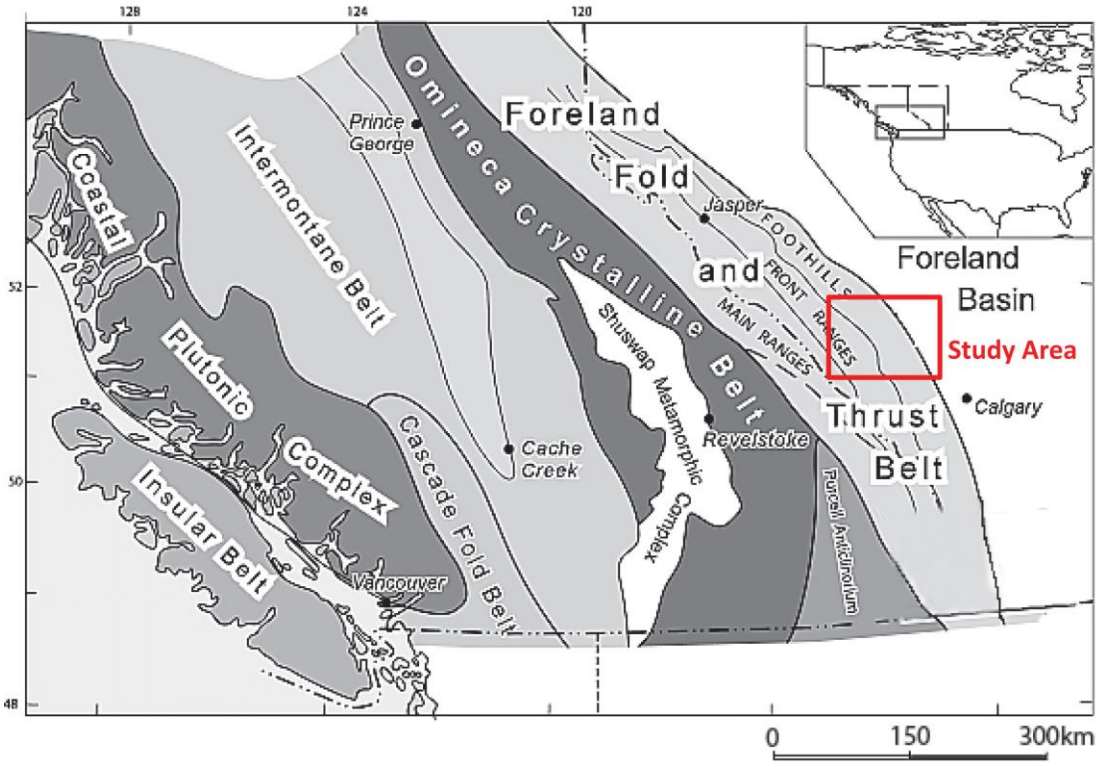

Figure 3.1 Tectonic subdivisions in the southern Canadian Cordillera. Modified from Hardebol et al. (2009). The location of the study area is marked by the box.

The western boundary of the Foothills with the Front Ranges is marked by major thrust faults, imbricate thrust slices, and duplexes commonly developed along the leading edge of each major thrust fault (McMechan, 2012), whereas the eastern boundary of the Alberta Foothills is marked by the triangle zone at the transition between the Great Plains and the Foothills that becomes less distinctive towards the north (Thompson, 1977, MacKay et al., 1996; Osborn et al. 2006, p. 458). The eastern boundary between the Plains and the Foothills can be traced by relief and ruggedness differences, and by the different ages and lithologies that are exposed at the surface between the Foothills and the adjacent Great Plains (Fox, 1959; Price and Mountjoy, 1970; Taerum, 2011).

In the Alberta Foothills, the structural framework of the region contains numerous steeply-dipping, northeasterly-verging imbricate thrust sheets of the Mesozoic foreland basin and eastward-tapering sedimentary wedge rocks that were deposited on the North American crystalline basement (Price, 1994; Fermor, 1999). These rocks include a main Upper Jurassic to Cretaceous sedimentary sequence that is well-exposed in the region. The allochthonous sedimentary rocks, delaminated from the crystalline basement, can be divided into two groups according to their age, composition, depositional style, and provenance (Monger, 1989; Ross and Stephenson, 1989). The first group comprises the marine carbonates, shales, and sandstones, which were deposited along the western margin of North America during the Paleozoic. The second group is composed of lower Jurassic to Paleogene age rocks comprising sandstone, siltstone, conglomerate, and shales that were deposited in the foreland basin. The first group is composed of rocks that are

mechanically stronger than the rocks of the second group. This mechanical anisotropy had a strong control on the deformation throughout the fold-and-thrust-belt in west central Alberta during the Laramide orogeny (Price, 1981; Taerum, 2011).

STRUCTURAL SETTING

The deformation history in the Canadian Rocky Mountains is marked by northeastward displacement during the Laramide orogeny from Campanian to Eocene times (Price, 1984, Eisbacher et al., 1974). Regional shortening caused the formation of folds cut by numerous east-verging thrust faults that have thickened and contracted the sedimentary wedge but not the underlying Precambrian crystalline basement formed during the Paleoproterozoic (Bally et al., 1966; Price, 1981; Langenberg, 1983; Ross and Stephenson, 1989). Therefore, the structural style of the region is thin-skinned deformation (Dahlstrom, 1970). Lithospheric gravitational loading due to thrusting caused the Precambrian crystalline basement to dip gently toward the SW (Price, 1981, Beaumont, 1981). The western part of the wedge was internally thickened and shortened by thrusting and folding (Fermor, 1999).

The structural style of the Foothills is controlled by foreland-verging thrusts and a triangle zone that is typically characterized by a foreland-directed lower detachment fault, a hinterland-directed upper detachment fault, and a foreland-directed thrust adjacent to the upper detachment (Stockmal, 2001). Triangle zones develop episodically throughout the progressive development of an orogenic belt where very weak detachments tend to promote foreland-directed thrusting whereas moderately weak detachments promote

hinterland-directed thrusting (Couzens–Schultz et al., 2003). The triangle zone in the Alberta Foothills typically contains significant internal shortening in which the hanging wall rocks were displaced towards the foreland (Couzens-Schultz et al., 2003).

The structural style of the Foothills displays three different manifestations of faulting and associated folding: fault-bend-folds, fault propagation folds, and detachment folds. Thrust faults propagate eastward with large displacement; however, the large thrusts are replaced by large-amplitude folds and the amount of displacement on minor thrust faults are less than the displacement in the southern structures (Cooper, 1992). In the Alberta Foothills, west-dipping thrust faults carried the Paleozoic carbonates northeastward onto less resistant Mesozoic siliciclastic rocks (Bally et al, 1996; Fermor, 1999). These west-dipping thrust faults merge at depth into a basal detachment within Cambrian sedimentary rocks, whereas listric thrusts bounding thrust slices merge at depth into a detachment within Jurassic marine shales of the Fernie Formation and a detachment near the base of the Upper Cretaceous Blackstone Formation (Fermor, 1999). The regionally significant detachment in the Fernie Formation separates the folded and thrusted sequence of Cretaceous and Jurassic rocks from Triassic and Upper Paleozoic rocks that include most of the carbonate reservoirs (Cooper, 1992). The mechanical anisotropy in the rock strength between the Paleozoic carbonate unit and Mesozoic clastic units, and the detachment within the Blackstone Formation, have a major impact on the deformational style of the region (Taerum, 2011).

STRATIGRAPHY AND LITHOLOGY

In the Alberta Foothills, Paleozoic to Jurassic rocks consist of predominantly massive thick-bedded dolomite and limestone with minor shale successions that were deposited along the western margin of the North American craton (Price, 1981). Mid-Jurassic to Paleocene rocks were deposited during the formation of the Canadian Cordillera (Price, 1986). Large quantities of Cretaceous and Tertiary clastic sediments sourced from the mountains were deposited as marine shale, siltstone, deltaic and fluvial sandstone and conglomerate successions onto the foreland basin (Stott, 1984, Bally et al., 1966; Beaumont, 1981). These Mesozoic siliciclastic successions show variable thicknesses varying from 4,500 meters thick at the eastern edge of the Foothills to more than 7,500 meters in the west (Barton, 1983; Stott, 1984; Shank and Plint, 2013).

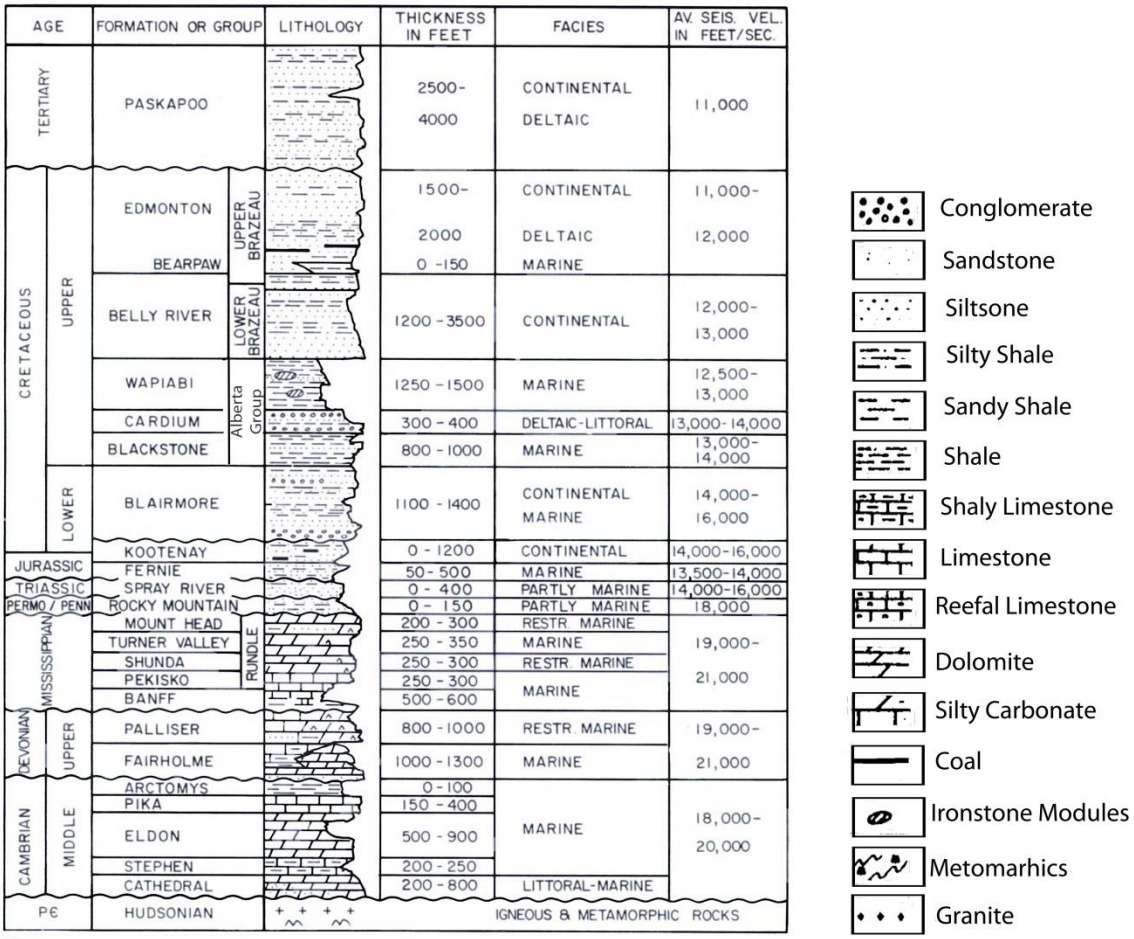

Figure 3. 2. Stratigraphic column of the Alberta Foothills and Front Ranges (Gordy et al., 1975) with seismic velocities of Sukaramongkol (1993).

The clastic succession of Mesozoic age rocks includes the prominent Upper Cretaceous Alberta Group. This group consists of predominantly marine to coastal marine foreland basin fill deposited in a thick northeasterly prism of Paleozoic to Cenozoic sediments and is characterized by shale, siltsone, and sandstone lithological units (Stott, 1963). The prominent sandstone unit of this group is the Cardium Formation, which subdivides a thick section of shale into the Wapiabi and Blackstone Formations above and below the

Cardium Formation. This package of sandstone encapsulated within thick shales is thus mechanically decoupled from over- and underlying competent units (Wall, 1967). The Blackstone Formation is overlain by the Cardium Formation and comprises mostly shale, locally silty or calcareous dark gray to black sideritic concretions, siltstone, and sandstone (Stott, 1963). The upper contact with the Cardium Formation is transitional, coarsening upward from marine shale to shoreface sandstone (Stott 1963). The Cardium Formation is in turn conformably overlain by the marine shales of the Wapiabi Formation, containing minor amounts of siltstone, sandstone, and limestone.

The Cardium Formation

The name of the Cardium Formation was first assigned to the prominent sandy unit that crops out along the Rocky Mountain Foothills and is present in the subsurface of the Alberta Plains. The formation extends over an approximately 100 km long arcuate strip that curves from Waterton Lakes and the Canada-US border, past Grande Prairie, Alberta, to Dawson Creek, British Columbia (Krause et al., 1994). The formation comprises a terrigenous muddy, sandy, and conglomeratic clastic wedge that was deposited on the western margin of the Western Interior Seaway during the Turonian and Coniacian ages of the Late Cretaceous epoch (Stott 1984, Krause et al., 1994, Shank, 2013) The sandstones of the formation display brownish-gray to gray, rusty-red to brown weathering colors, are well sorted, fine-grained, and without appreciable horizontal or vertical variation in grain size (Krause et al., 1994). The formation thickness is approximately 150 m thickness in surface exposures where the formation is brought to

the surface by thrust faults, and around 50 m in the subsurface under the Plains (Krause et al., 1994). The formation has locally well-developed fracture sets (Muecke and Charlesworth, 1966; Barton, 1983; Hartel, 2009).

The Cardium Formation contains large hydrocarbon reserves in the deformed Plains east of the Foothills, forming the youngest oil-bearing formation and a major producer in the Pembina field southwest of Edmonton (Newson, 2003) The initial oil in place is present in at least 42 fields and makes up almost one quarter of the total oil volume of the Western Canada Sedimentary Basin (Krause al., 1994). The amount of reserves discovered show more than $1.6x10^6$ m^3 of oil (Krause et al., 1994).

The Cardium Formation in outcrops in the foothills of Alberta is divided into seven Members that are, from bottom to top, the Ram, Kiska, Cardinal, Leyland, Sturrock, Moosehound and Baytree Members (Stott, 1963 and 1967)(Figure 3.4a). Stott (1963) suggested that the Members vary by location as the Kiska, Cardinal, Leyland and Sturrock Members become the Moosehound Member in the south to north (Figure 3.3a). A different subdivision of the Cardium Formation is used in the subsurface (Figure 3.3b).

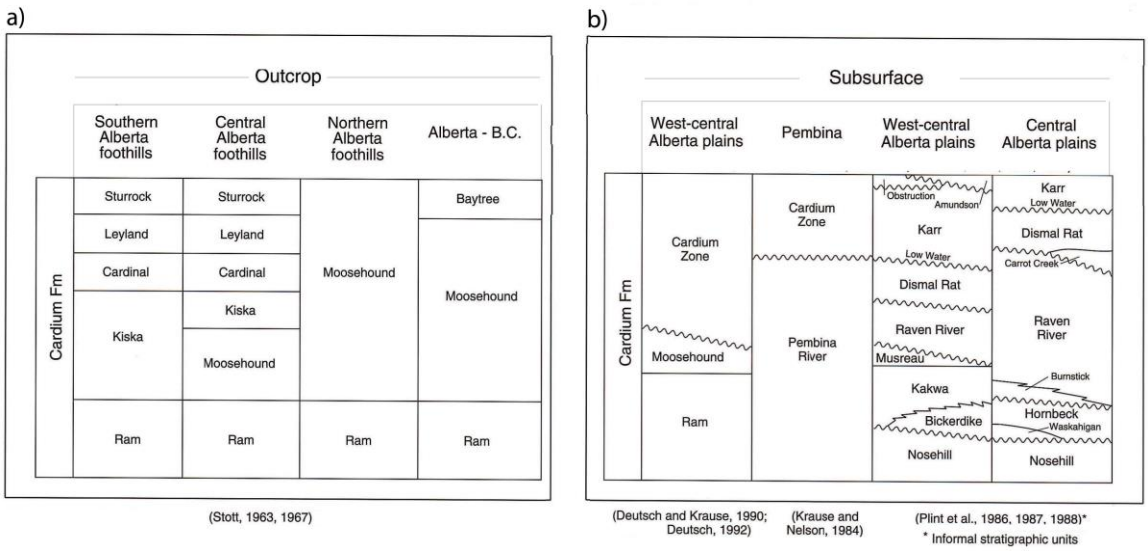

Figure 3.3 The Members of the Cardium Formation. a: s in outcrop; b: in the subsurface (From Krause al., 1994).

Over the past decade, naturally fractured reservoirs of the Kakwa Member of the Cardium Formation have played an important role as hydrocarbon reservoirs because of their abundant in-place reserves (Dechesne and Veilleux, 2000). The Cardium Formation is generally characterized as a tight-gas sandstone (TGS) reservoir. Typical reservoir properties for the Kakwa sandstone vary from low to moderate porosity (<6% and 13%), and permeability values between 0.01-4.0 mD (Table 3.1). The reservoirs of the Kakwa Member comprised of coarser-grained clastics of low-stand shorefaces show higher porosity and permeability than the medium- to fine-grained sandstones of the Kakwa Member (Plint, et al. 1988).

Table 3.1. Typical reservoir parameters for the Kakwa Member of the Cardium Formation (Dechesne and Veilleux, 2000).

	Porosity Range	**Permeability**
Minimum	< 6%	< 0.01- 0.01mD
Mean	6-9%	0.01- 1.0 mD
Maximum	9-13%	0.1- 4.0 mD
Red Deer River (Outcrop Samples)	4.5-5.5%	0.03- 0.04 mD

Red Deer River Area

The Cardium Formation is exposed for about 1 km along the NW-plunging Red Deer River anticline (Olleranshaw, 1996). This structure is located at N 51°65' latitude/W - 115° 27' longitude, immediately north of the Reed Deer River across the Mountain Aire Lodge along the Ya Ha Tinda Ranch road (Figure 3.4). This anticline provides well-exposed accessible outcrops of the Cardium Formation bodies across a broad range of structural positions. On the Red Deer River anticline, beds dip from approximately 25-30° in the western limb to 35 -40° in the eastern limb and average approximately 50° in the easternmost part of the east limb.

Figure 3. 4 The location of the Red Deer River outcrops are shown by the red box. (Canada Geological Survey).

The Cardium Formation in the study area is generally composed of very fine- to medium-grained, gray to dark gray-brown colored sandstone bodies. The sandstones show different types of internal lamination, including hummocky cross-stratification, and mild to pronounced bioturbation. In the Red Deer River anticline, the Cardium Formation can be subdivided into three Members, from base to top: the Kakwa, Low Water, and Karr Members, separated by finer-grained slope-forming mudstone units (Figure 3.5). This Member classification is based upon similarity in stratigraphic position relative to the Musreau/Kakwa delta succession to the northwest (Plint et al. 1988).

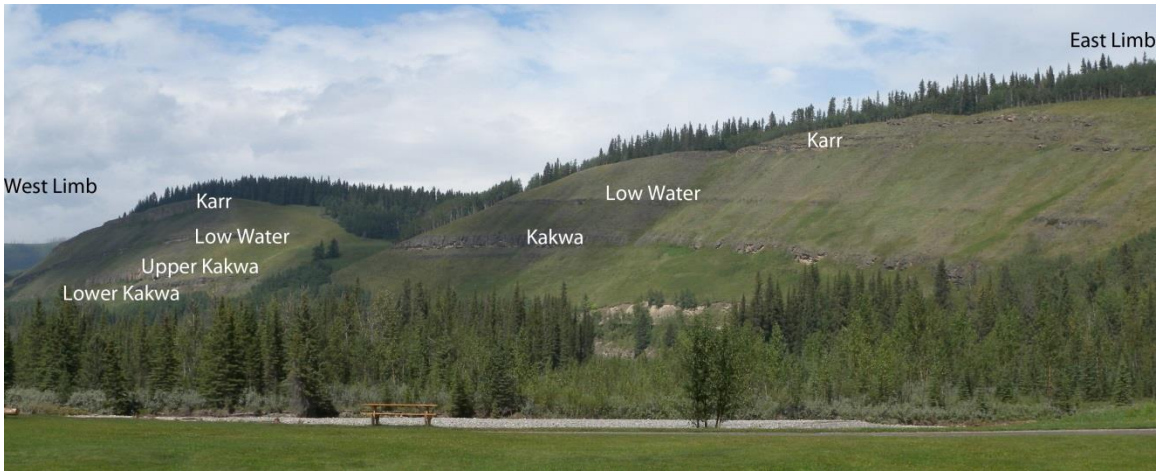

Figure 3.5 Sandstone Members of the Cardium Formation exposed on both limbs of the Red Deer River anticline based on Plint et al., 1988.

The three Members of the Cardium Formation are well-exposed on the west and east limbs of the Red Deer River anticline on the hillside, and in two smaller outcrops in the north and south banks of the Red Deer River adjacent to the Mountain Aire Lodge.

The hinge of the anticline has been removed by erosion now forming a valley. The Kakwa Member is thickest on the western limb of the fold and it consists of well-developed Upper Kakwa and Lower Kakwa Members. Both Members are thinner in the east limb of the fold, to the point that the Lower Kakwa Member is not visible from a distance. The overlying Low Water Member displays approximately constant thickness along the 1 km-wide exposure. The Low Water Member is finer-grained than the Kakwa Member and more highly bioturbated. The overlying Karr Member displays the greatest variability; it is composed of thinner, amalgamated, hummocky cross-stratified, upper flow regime sandstone and thicker bioturbated, fine-grained muddy silty turbidities on the western limb where it is composed of very fine- to fine-grained sandstone with planar to hummocky cross-stratified bed forms.

Domains

Based on structural observations, I divided the exposure of the Red Deer River anticline into three structural domains. The west limb of the anticline is herein referred to as Domain I and the east limb of the anticline is divided into two domains; Domain II spans the shallow part of the east limb and Domain III spans the steep part (easternmost part) of the east limb (Figure 3.6). Note that the hinge of the anticline is eroded and it is not characterized as a domain.

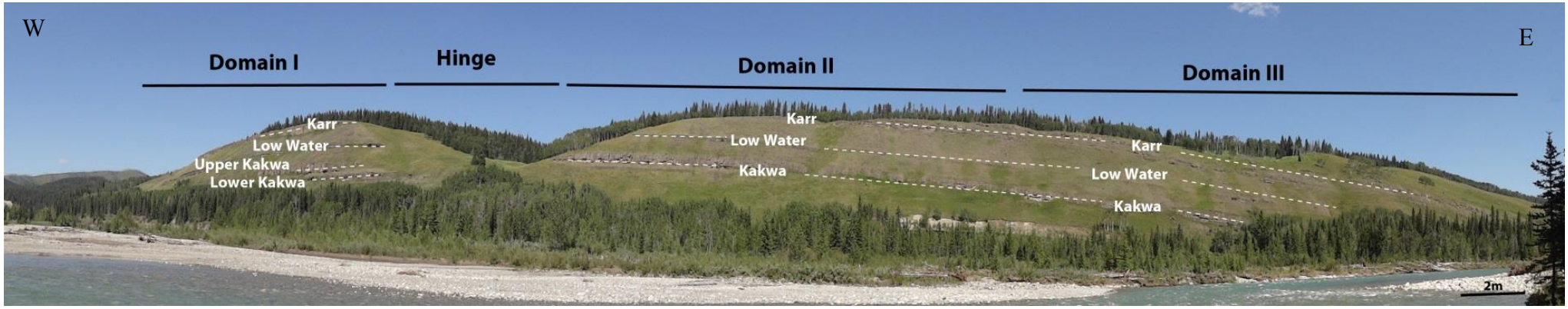

Figure 3.6. Domains I, II, and III across the NW-plunging Red Deer River anticline. Dashed lines indicate the exposed sandstone bodies of the Cardium Formation.

Domain I

Domain I comprises the western end of the Red Deer River anticline where the Karr, Low Water, and the Upper and Lower Kakwa Members are exposed (Figure 3.7). The Upper Kakwa Member is the thickest Member in Domain I.

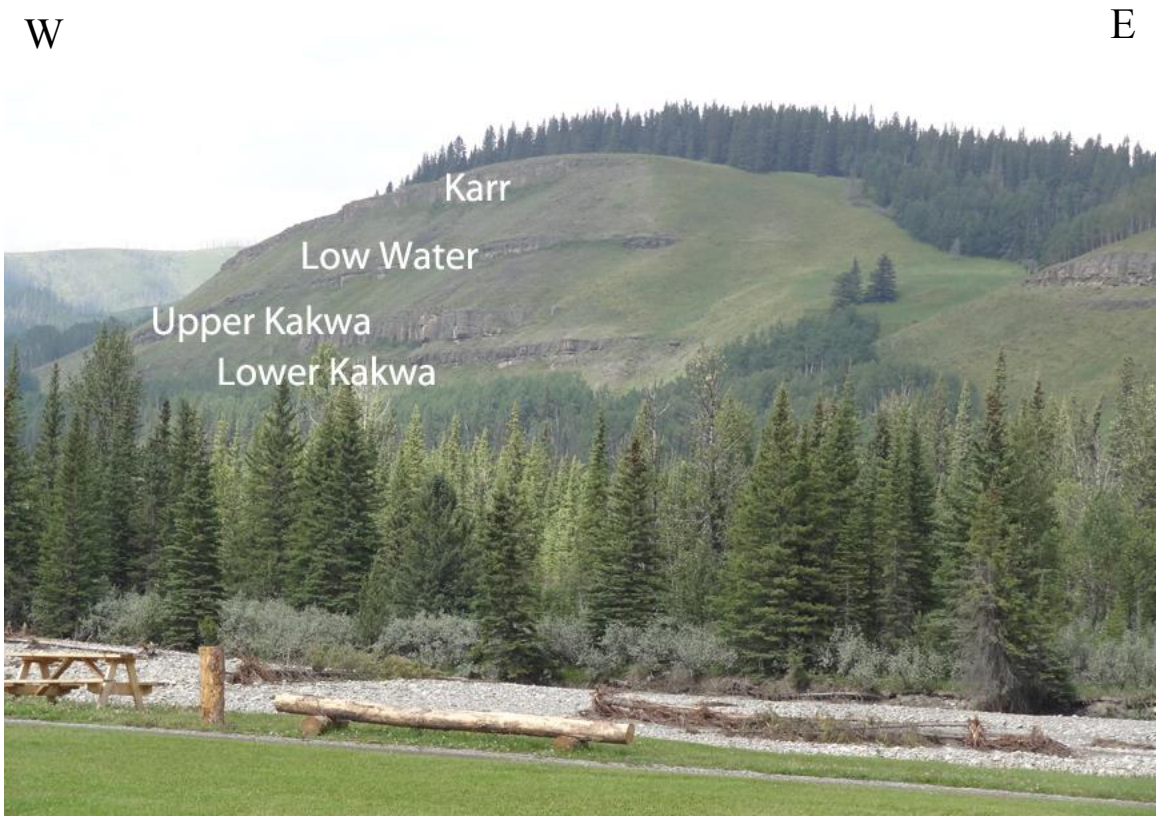

Figure 3.7 The exposed sandstone bodies of the Cardium Formation in Domain I of the Red Deer River anticline.

Domain II

Domain II is located in the east limb of the Red Deer River anticline and consists of the Karr, Low Water, and Kakwa Members of Cardium Formation (Figure 3.8). Both Kakwa Members are thinner in Domain II than in Domain I, to the point that only the Upper Kakwa is visible from a distance.

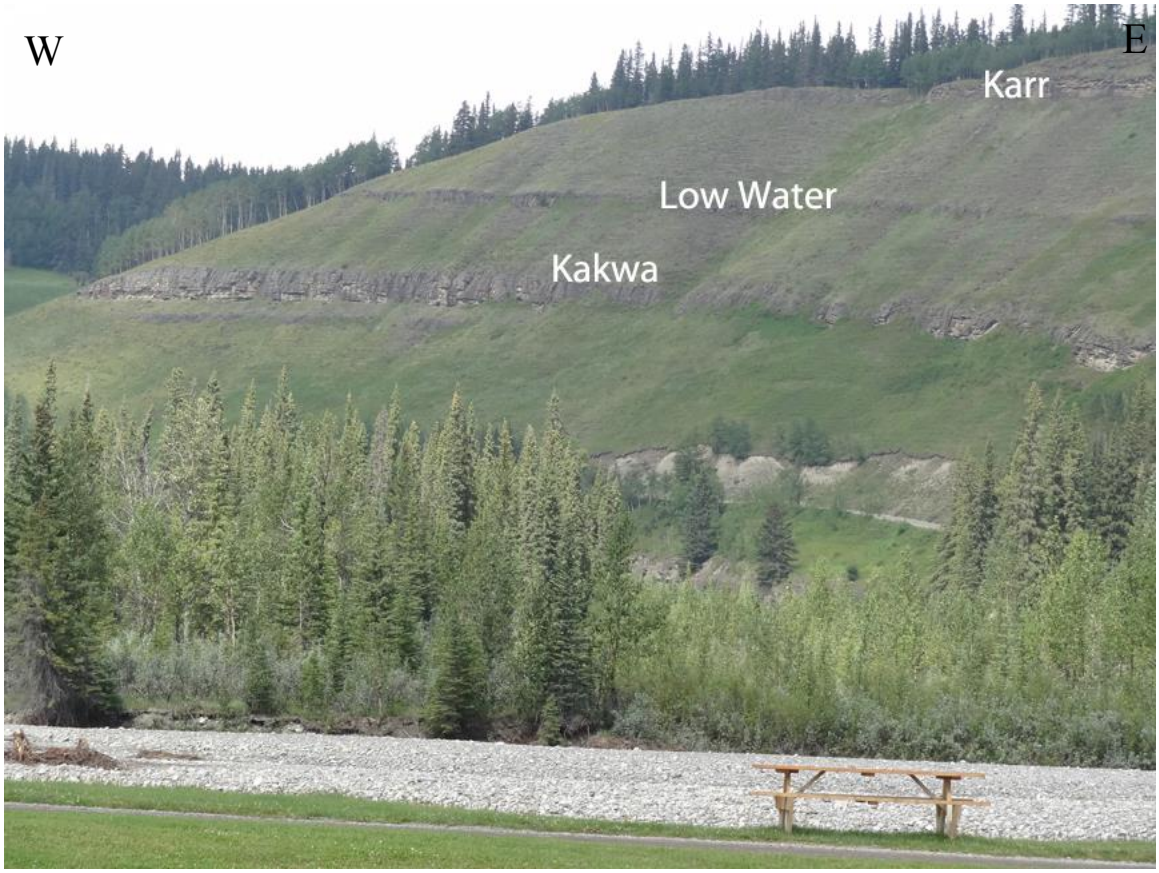

Figure 3.8 The Members of the Cardium Formation exposed in Domain II.

Domain III

Domain III is comprised of the most steeply-dipping part of the east limb, which outcrops on the hillside as well as along a small exposure located on the south side of the Red Deer River. This small exposure is inferred to be part of the Kakwa Member based on lithological properties and stratigraphic/structural location. The Kakwa Member contains three distinct lithological units in this river exposure,from top to bottom: a bioturbated unit (A), a. planar-laminated lithological unit (B), and a cross-laminated unit (C) (Figure 3.9).

Figure 3.9. Exposure of the Cardium Formation in Domain III on the orographic right side of the Red Deer River. The exposure includes three different lithological units; A: bioturbated layers, B: planar-laminated, and C: hummocky cross-stratified units. Hand samples were collected from each different lithological unit at this location.

Chapter 4: Fracture Characterization

The aim of this chapter is an assessment of 1) the orientation of opening-mode fractures in the Cardium Formation across the Red Deer River anticline 2) variation in fracture aperture scaling and fracture abundance across the fold, and 3) fracture strain distribution relative to structural position. I aim to analyze fracture characteristics such as aperture and average spacing, intensity and fracture strain in the forelimb and compare these characteristics to the backlimb of the anticline. These data are used to evaluate the relative timing of fracture development with respect to the formation of meso-scale structures. This chapter builds on field data collected by Ukar and field assistants Nick Perez, Jon Major, and Eichhubl during the summer of 2012 (summarized in Ukar et al., 2013), and on field data and fracture scaling samples collected by myself, Ukar, and Eichhubl during the summer of 2013.

FRACTURE ORIENTATIONS

Fracture Sets and Fracture Orientation

I examined fracture orientations in the Kakwa and Karr members in Domains I and III, and the Kakwa Member in Domain II. Based on the orientation of the fractures in the Kakwa and Karr members in different parts of the fold, three prominent sets of opening mode fractures are recognized (Figure 4. 1). All three fracture sets are perpendicular to bedding, and most are bed-bounded, i.e. they terminate against bedding surfaces. Fracture orientations are shown as poles-to-fracture planes in Figure 4. 2. Bedding is indicated with great circles. In domain I, set 2 fractures strike roughly N-S, set 3 fractures E-W, and set 1 fractures NW-SE. In domain II and III, the relative orientations are preserved but all fracture sets rotate progressively clockwise by 40-60° consistent with the change in bedding across the fold.

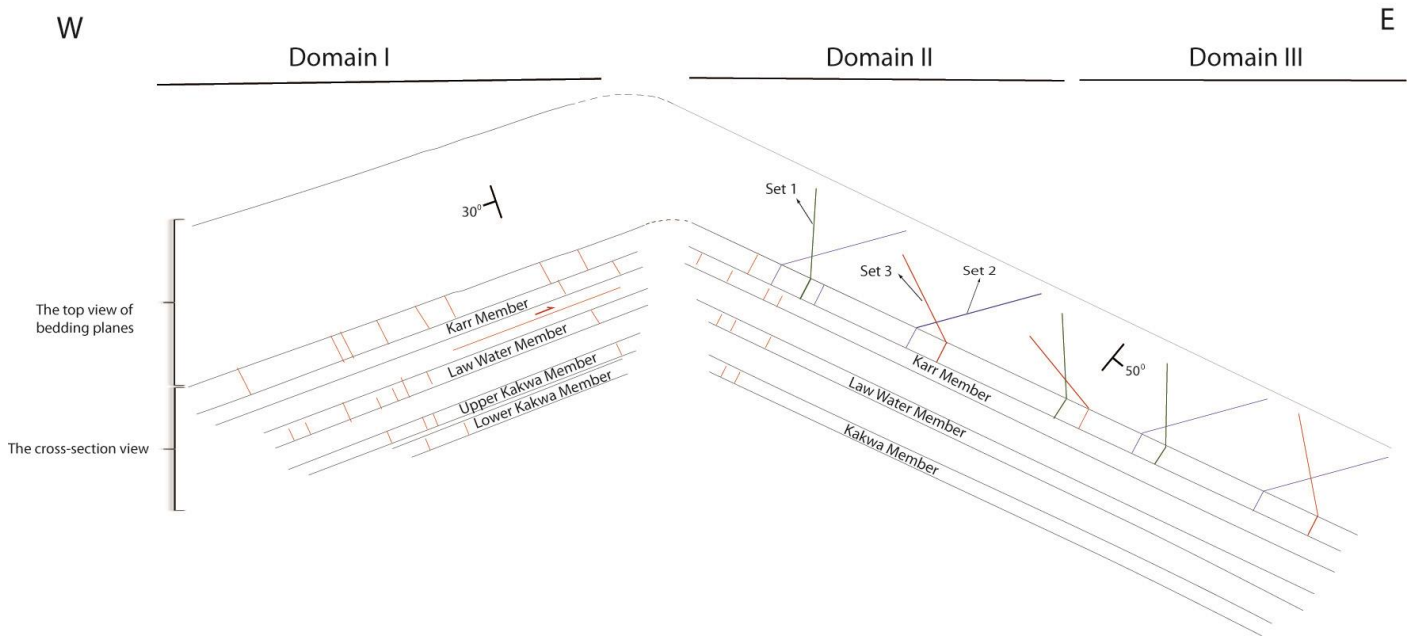

Figure 4. 1 Perspective view of three main fracture sets observed in the Red Deer River anticline

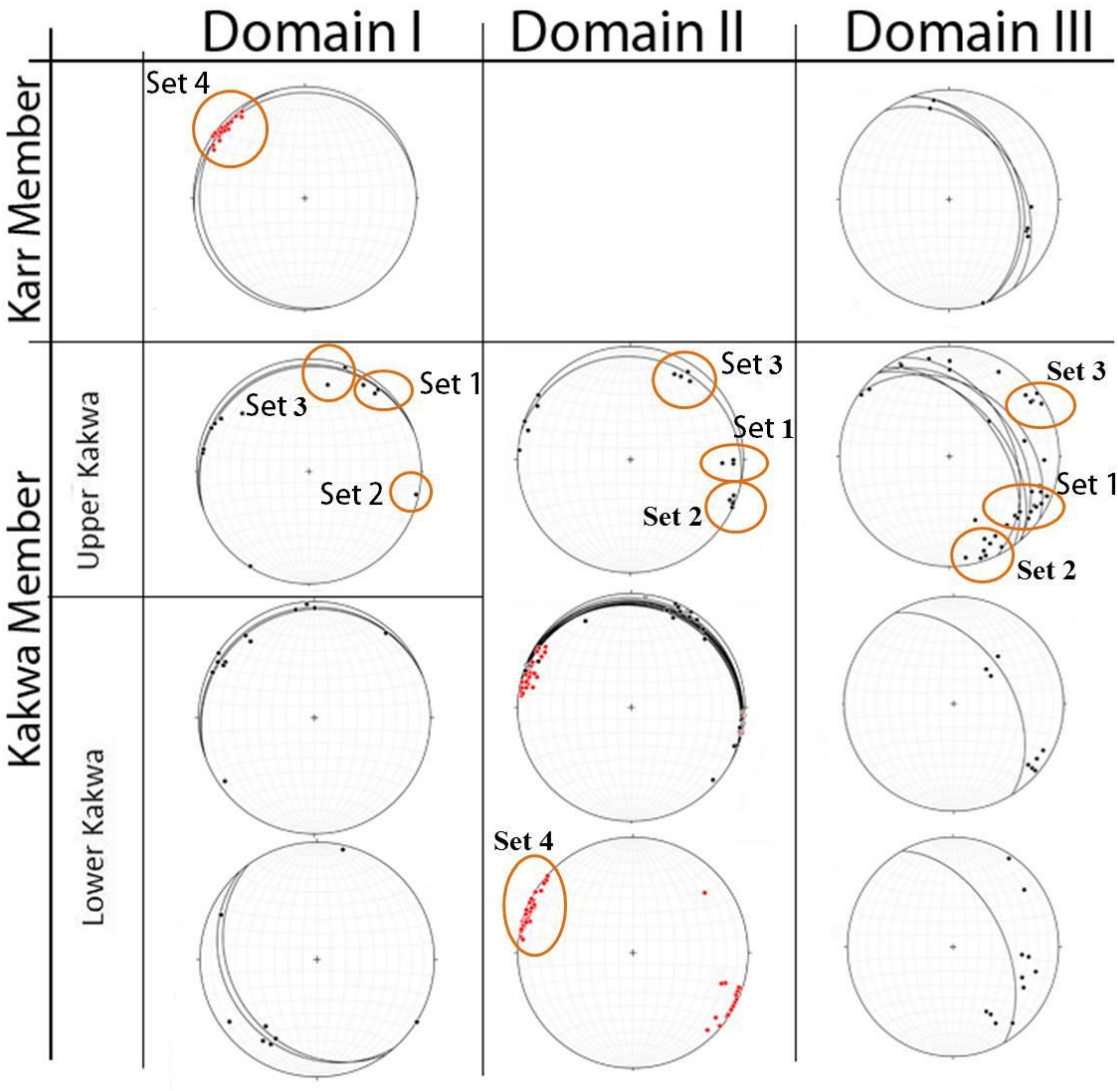

Figure 4. 2: Fracture orientation data by domain. Red colors indicate macrofracture orientation measured along scanlines in the field whereas black indicates macrofracture orientations obtained outside of the scanline measurements.

Although most opening-mode fractures tip out against bedding contacts, a lesser number of through-going, several meters-tall fractures cut the sandstone layers of the Kakwa member from top to bottom (Figure 4. 4). Although of same orientation as set 2 fracture, these through-going fractures are interpreted as a separate fracture set (Set 4) because of their different structural style. It is possible that these fractures formed by linkage and propagation of earlier set 2 fractures. Set 4 is best developed within Domain II. To test the fracture timing relative to folding, bedding was rotated to horizontal (Figure 4. 3). This method allows us to restore the tilted strata from present-day orientation to their original horizontal position. When rotated, fractures of all sets show similar orientations regardless of their structural position. However, this method does not allow us to determine with certainty that all fractures predate folding, because folding-related bedding-perpendicular fractures are common, and these too would show overlapping orientations after restoration.

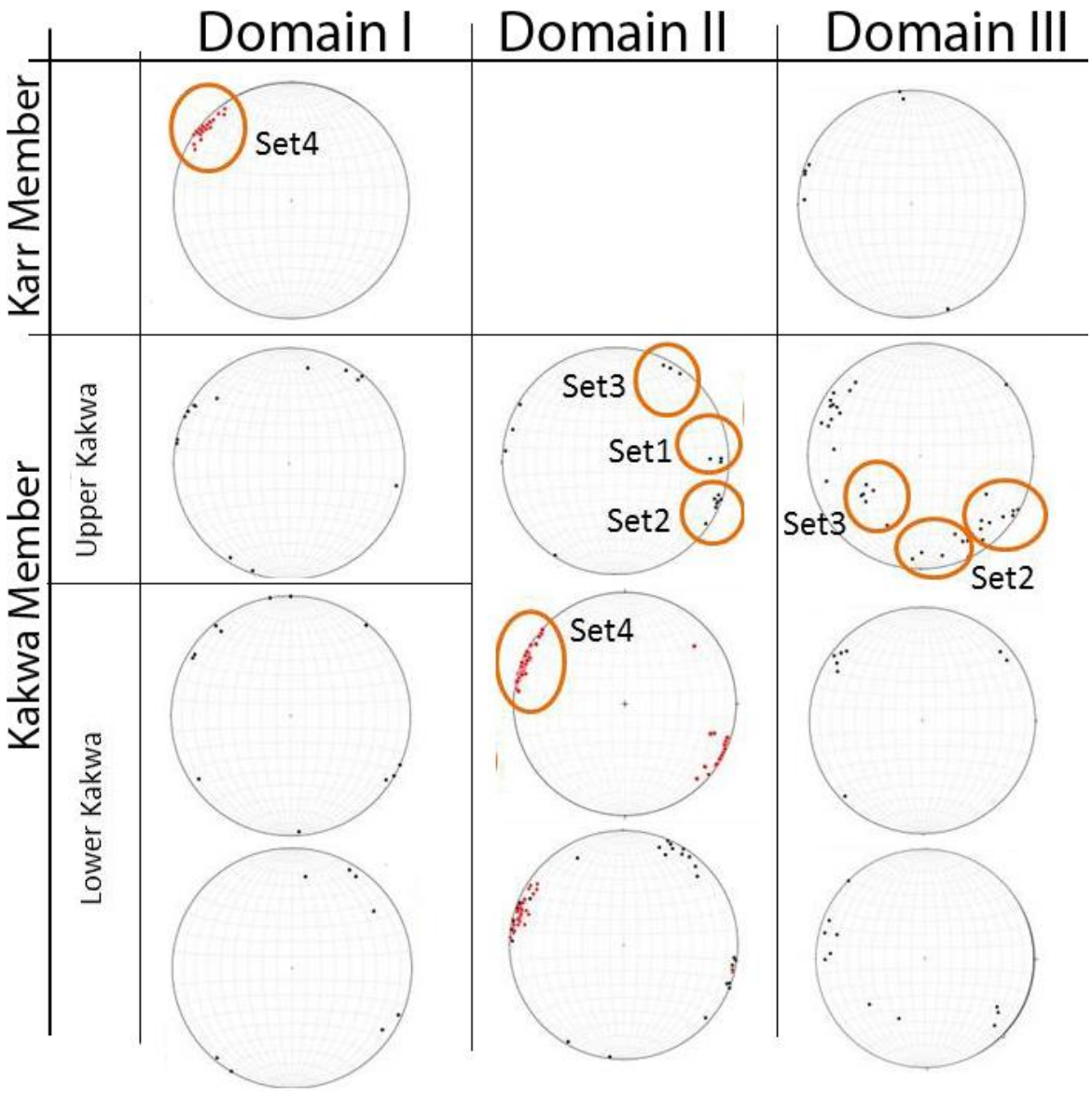

Figure 4. 3 Fracture orientations of Figure 4. 2, rotated with bedding restored to horizontal.

Figure 4. 4: Set 4 through-going fractures were measured in the Kakwa member in the Domain II. Dip azimuth and dip are labeled. The measuring stick is 1 meter long.

In addition to these bedding-perpendicular fractures, a set of bedding-parallel fractures is recognized (set 5).

FRACTURE CEMENTS

In the Red Deer River Area, all fractures sets are primarily filled with quartz cement. Some of the fractures also have minor calcite cement. Although most of the fractures are completely filled by quartz cement, some of the fractures still preserve some primary porosity (Figure 4. 5).

a) co-14-2a-d

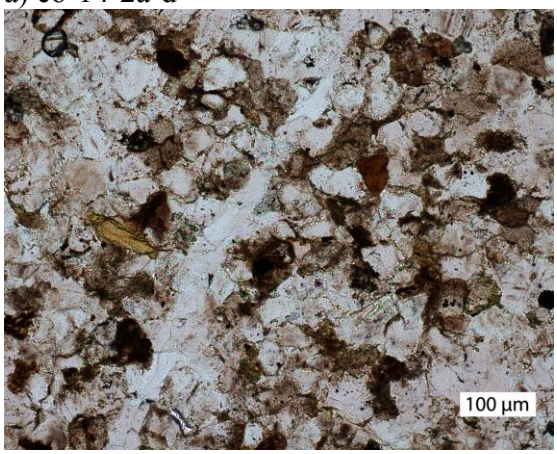

b) co-15-3a-b

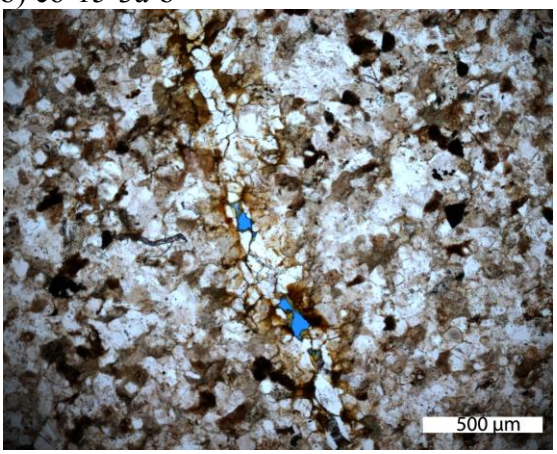

c) co-16-1b-b

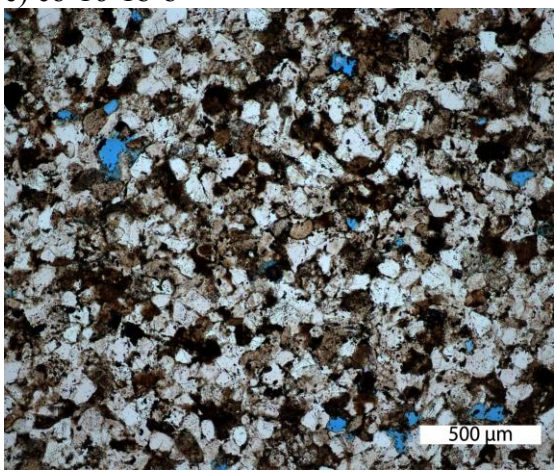

Figure 4. 5 Plane polarized light microscopy images. a) Completely quartz filled fracture b) Fracture porosity preserved in partially filled fracture c) Abundant primary porosity remains.

Most of the quartz cement in fractures consists of euhedral crystals (Figure 4. 6). Euhedral quartz cement is indicative of postkinematic growth of the cement relative to the opening of the fractures or synkinematic growth in fractures that opened later than quartz growth.

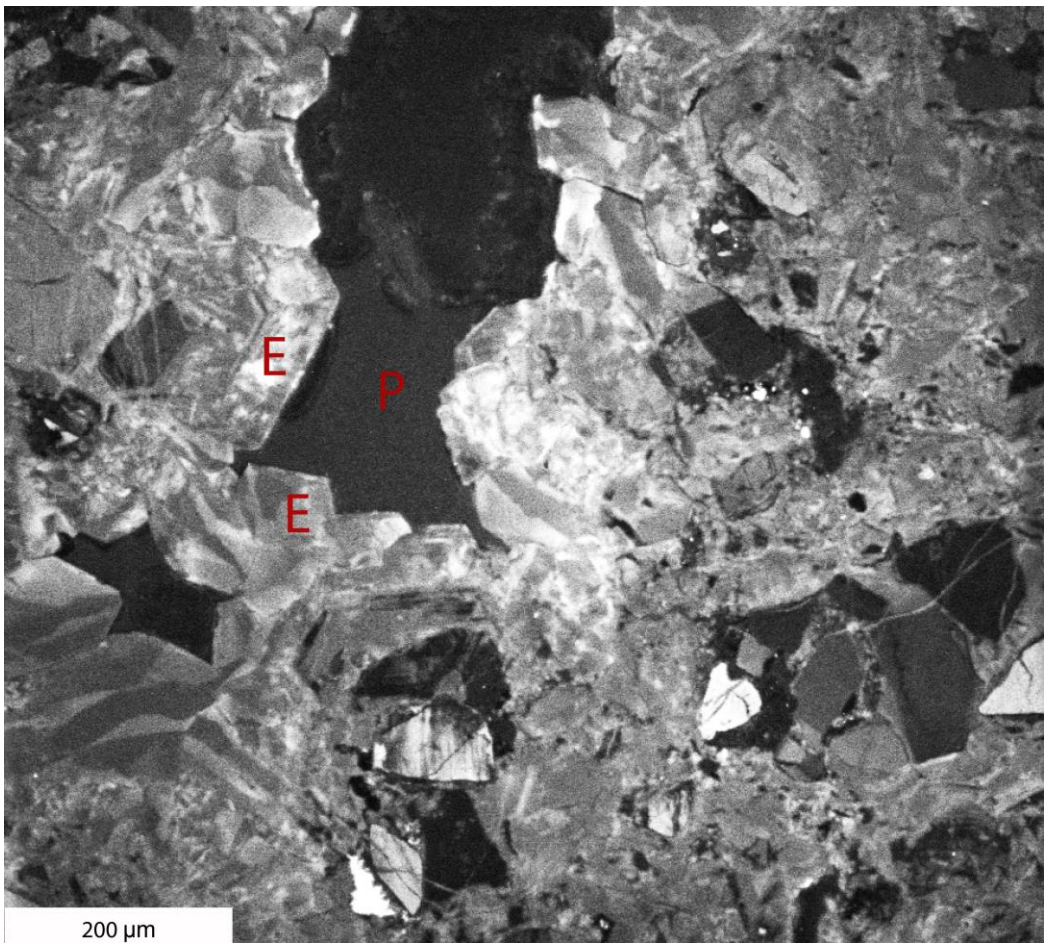

Figure 4. 6. SEM- CL image of the sample CO-14-2a-d. Fractures are filled by euhedral quartz cement. E indicates the euhedral quartz cement (E). P indicates fracture porosity.

Crack-seal texture in the Red Deer River samples is restricted to near fracture walls (Figure 4. 7). Crack-seal texture is indicative of synkinematic cementation where a fracture repeatedly opens with concurrent cementation (Ramsey, 1980; Laubach, 1988; Becker et al., 2010). Since rapid quartz cementation occurs at temperatures of at least 80°, the presence of quartz cement in these fractures indicates that fractures opened and cemented under deep-burial conditions (e.g. Walderhaug, 1994; Lander et al, 2008). For a paleogeothermal gradient of about 23°C/km in the area (Hitchon, 1984), and assuming a surface temperature of 25°C the fractures were cemented at depth of at least ~2.4 Km.

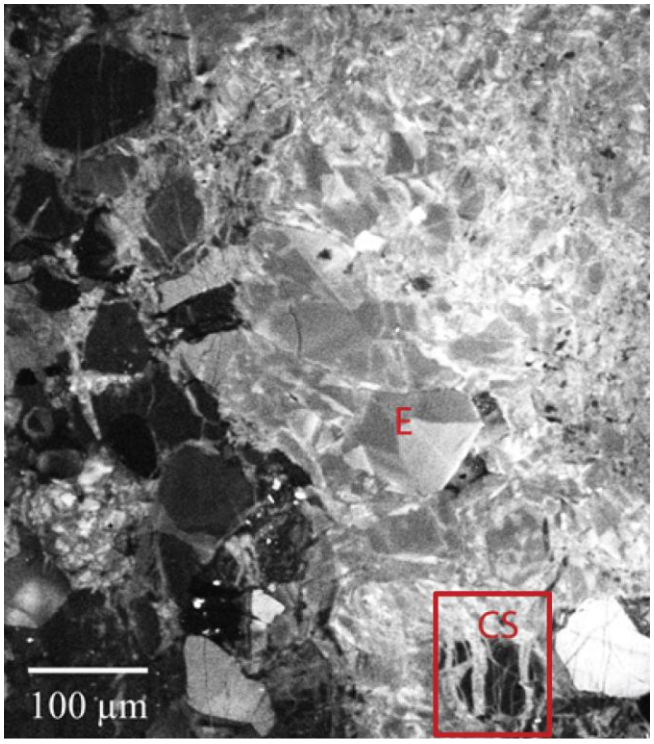

Figure 4. 7 SEM- CL image of the sample CO-14-2a-d. Crack-seal texture (CS) near the fracture wall is indicated by red square. E indicates euhedral quartz cement.

Faulting and reactivation in shear

Many set 4 fractures have striated surfaces and associated wing cracks at 30° indicating dip-slip sense of shear on set 4 fractures. Offset bedding planes indicate vertical displacements that range between 1 to 13 cm. A few set 4 fractures have subhorizontal striations indicating strike-slip sense of shear. Linkage patterns by oblique segments exposed on bedding surfaces (fracture pavements) within Domain III (Figure 4.8) are also compatible with strike-slip shear. Therefore, set 4 fractures seem to have formed by linkage and propagation of set 2 fractures, which were then reactivated in both strike-slip and apparent normal dip-slip motion. Although opening-mode fractures, which are oriented at high angles to bedding, are the most common fracture type in these outcrops, thrust faults orientated at a low angle to bedding and containing striated fault planes are also present in all three domains.

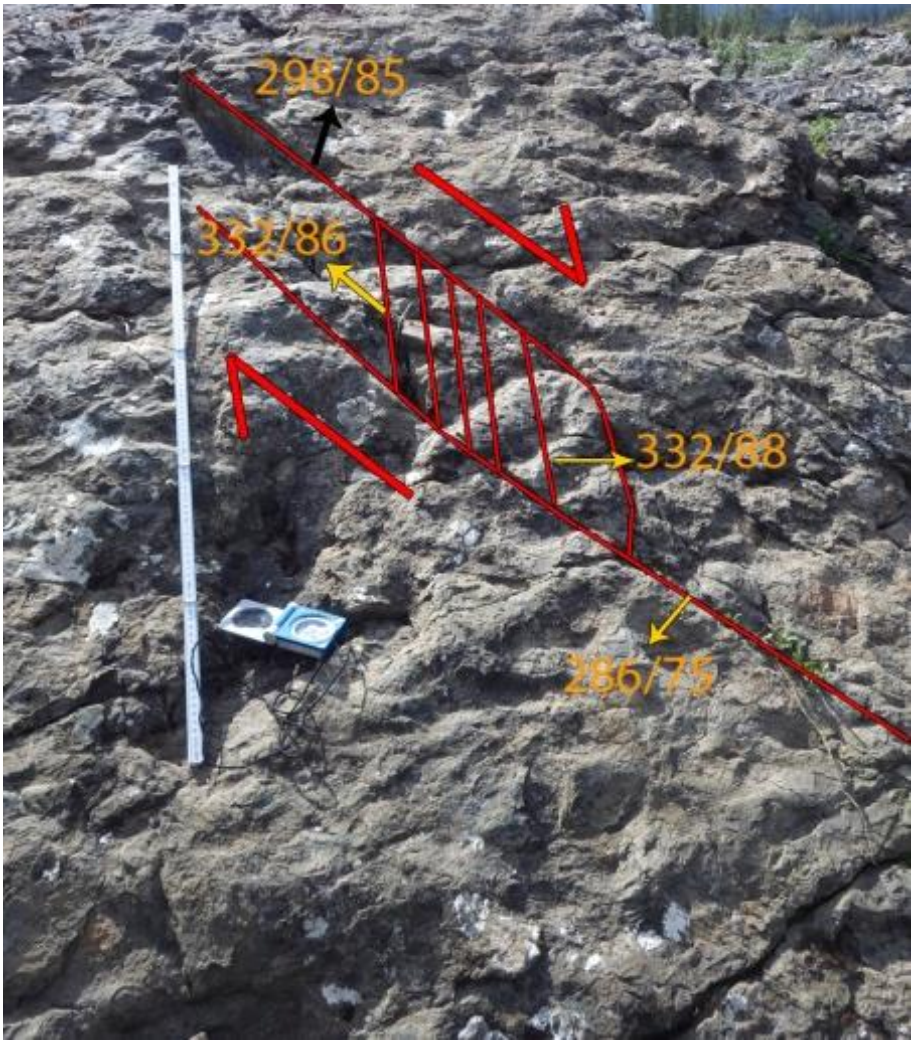

Figure 4. 8. Example of through-going fractures showing linkage of smaller fractures on bedding surface in Domain III. Outcrop on orographic right side of Red Deer River next to bridge. Structural measurements are dip azimuth/dip.

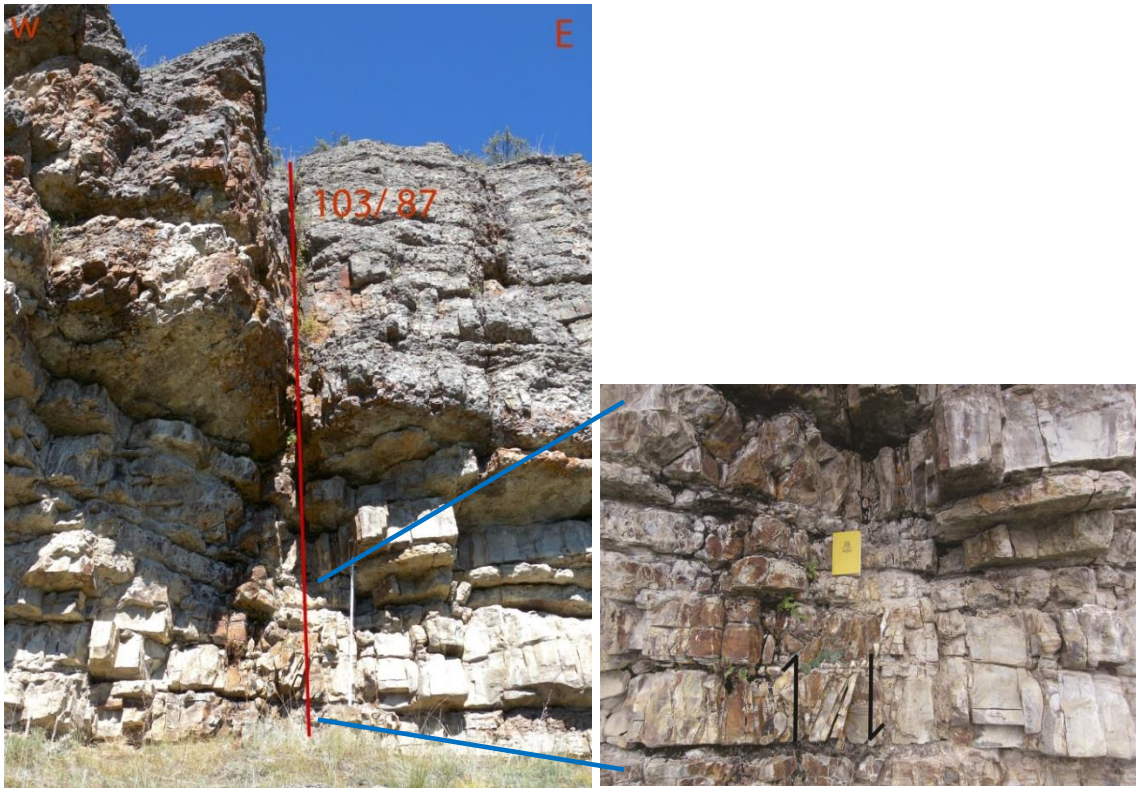

Figure 4. 9. Left: Through-going fractures were measured in the Kakwa member in Domain II. Right: Wind crack associated with through-going fractures in Domain II indicative of east side down relative to west side.

SYSTEMATIC CROSS-CUTTING RELATIONSHIPS

Cross-cutting relationships between different fracture sets indicate that set 1 fractures cut set 2, and set 3 cuts set 2 and set 1 (Figure 4. 10). Thus, set 2 fractures are the oldest and set 3 the youngest of these three fracture sets. Set 4 fractures are inferred to be younger than set 2 because they formed by linkage of set 2 fractures. In addition, set 4 fractures cut or abut against low-angle thrust faults, and low-angle faults do not displace the blocks cut by set 4 fractures, indicating that set 4 post-dates low angle thrust faults (Figure 4.11). Due to a lack of observed cross-cutting relations, the relative timing of set 5 remains unknown. Fault kinematics of low angle thrust faults and slip along set 4 fractures are kinematically compatible with folding of the Red Deer River anticline. Table 4.1 summarizes the general attributes of all opening-mode fracture set.

Attribute/ Set	Set 1	Set 2	Set 3	Set 4	Set 5
Strike	N-S	NE-SW	ENE-WSW	NE-SW	NE-SW
Strike (after unfolding)	N-S	NE-SW	NW-SE	NE-SW	NE- SW
Dip	Bedding-perpendicular	Bedding-perpendicular	Bedding-perpendicular	Bedding-perpendicular	Bedding parallel
Relative Age	Younger than set 2 and older than set 3	The oldest	Younger than set 1 and set 2 older than set 4	The youngest	Unknown
Quartz cement	Yes	Yes	Yes	Yes	Yes
Microfractures	Yes	Yes	Yes	No	No

Table 4.1 General attributes of all the fracture sets based on data collected Domain II

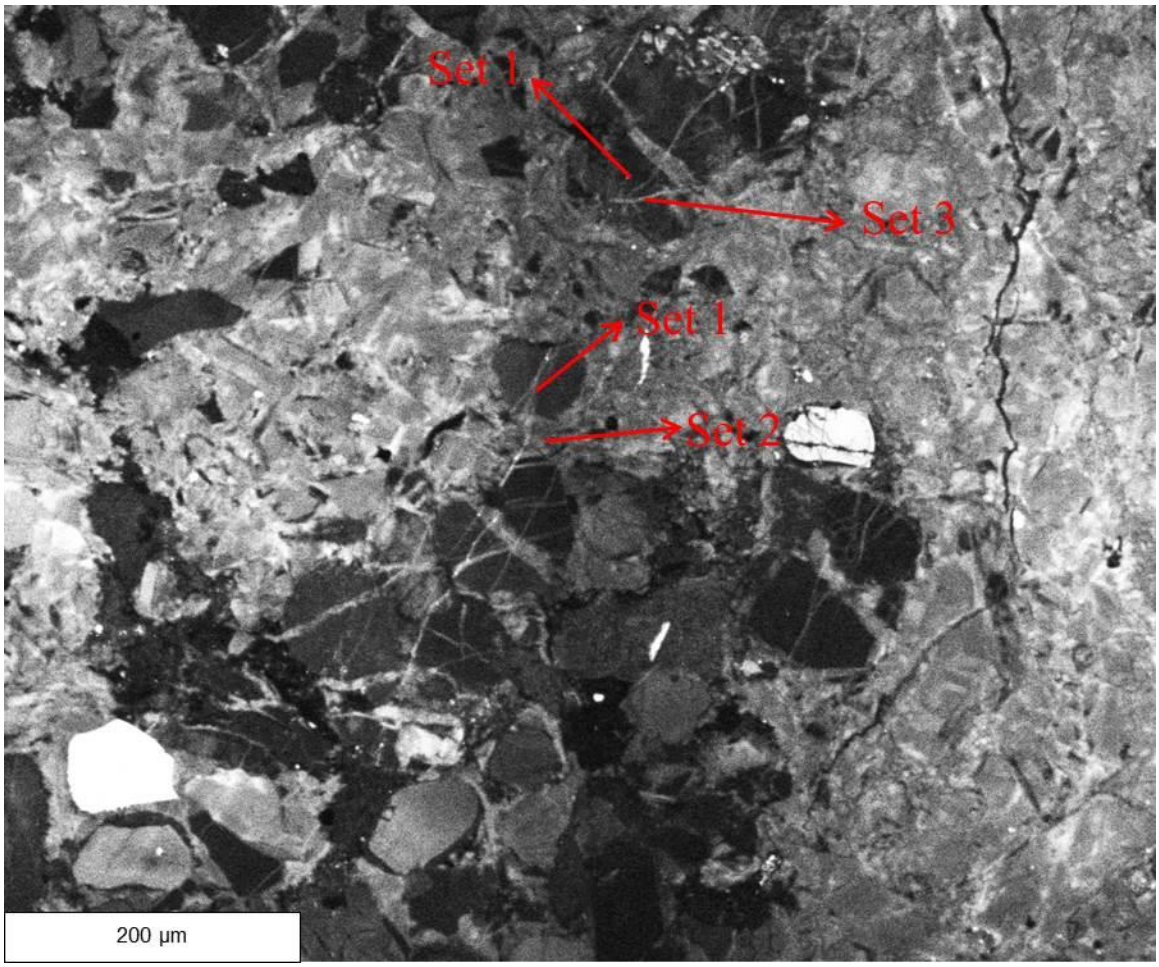

Figure 4. 10a Cross-cutting relationships between fracture sets based on SEM-CL images of Sample: CO-14-2a-d. Set 1 fractures cut Set 2 fractures and set 3 fractures cut set 1 fractures

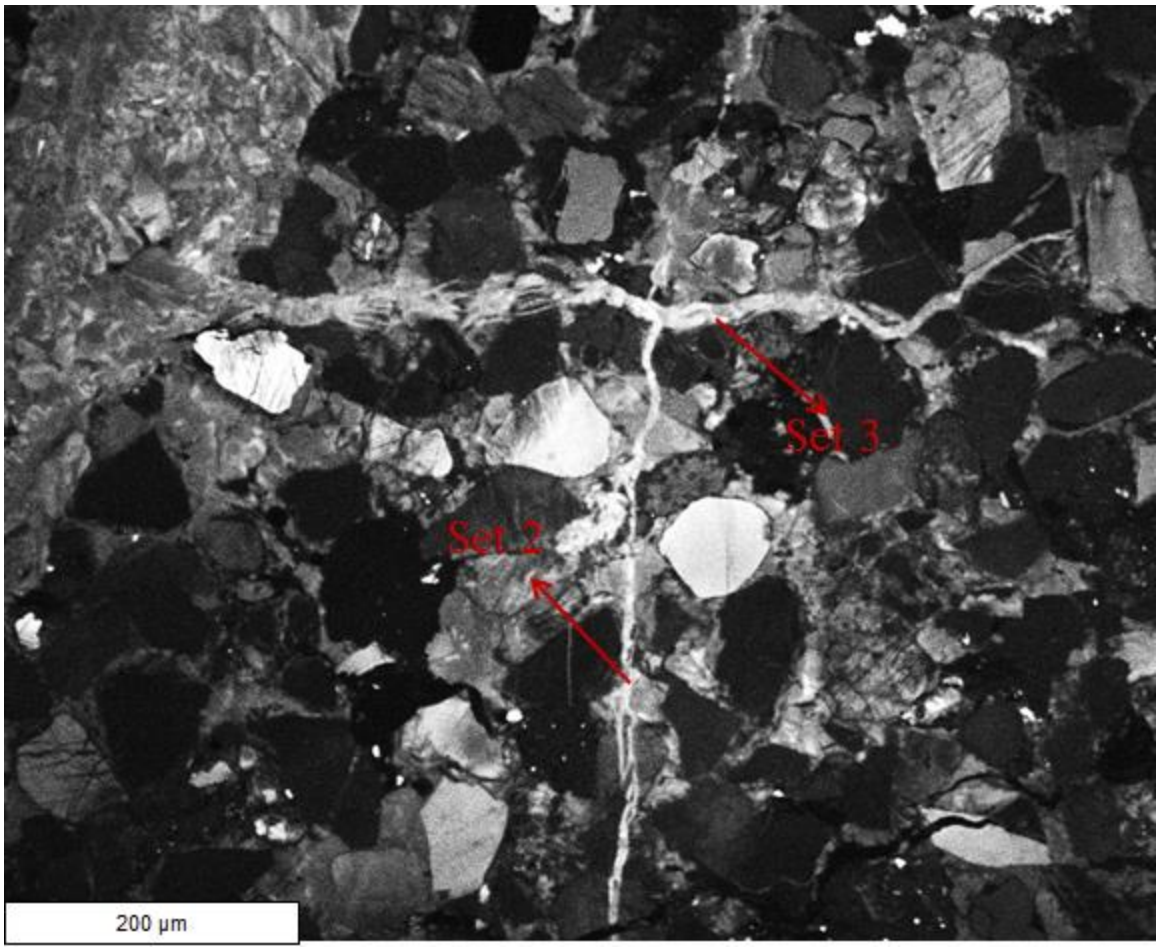

Figure 4. 10b Coss-cutting relationship between fracture sets based on SEM-CL images of Sample: CO-14-2a-d. Set 3 fractures cut Set 2

Figure 4. 11 Through-going fracture (white) cuts low-angle thrust faults (red). Green lines indicate slickenside striations. Numbers indicate dip azimuth/dip for planes, and plunge/trend for striations.

FRACTURE SCALING

Fracture size scaling analyses provide an opportunity to quantify fracture frequency (abundance) and predict macrofractures from microfracture populations by measuring fractures along a 1D line of observation (scanline) (Marrett et al., 1999; Ortega and Marrett, 2000; Hooker et al., 2012; see Appendix B Methods). Here, I use fracture-scaling analyses based on macro- and microfracture measurements to evaluate the

distribution and intensity of fractures with respect to their structural position across the Red Deer River anticline. Fracture scaling analyses of the Cardium Formation in the study area were done based on i) microfractures observed in SEM-cathodoluminescence images of seven samples collected from the field, and ii) macrofracture data collected by Ukar et al. (2013) along 2 scanlines, and microfracture data from 4 additional hand samples.

In order to address a possible relationship between fracture intensity and structural position within the anticline, Ukar et al. (2013) collected macrofracture and microfracture data from several locations across the Red Deer River anticline (Figure 4. 12). Ukar's dataset consists of two macroscanlines, one in Domain I and another in Domain II, and complementing microfracture data from three hand samples (one from Domain I and two from Domain II), as well as an additional hand sample from the Domain III exposure under the bridge across Red Deer River. To complement this dataset, I collected three hand samples from Domain I and four additional samples from Domain III. These samples were also used to address the effect of lithology on fracture abundance (Figure 4. 13).

Figure 4. 12. The location of the scanline measurement and collected hand samples by Ukar in 2013. The green squares show the location of the macroscanline measurements whereas the red circles show the location of the hand samples collected for microfracture analysis.

Figure 4. 13. The location of the collected hand samples that I collected in 2014 are shown by the blue circles. Hand samples were collected for microfracture analysis.

Cumulative frequency (equivalent to fracture intensity) is the ratio of the number of fractures to the length of observation; it has units of inverse length and its inverse indicates the average spacing of fractures (Ortega et al., 2006). Along a line of

observation (scanline), fracture intensity indicates the number of fractures per unit length of scanline, which is important because it indicates the fracture abundance potentially available for fluid flow (Ortega et al., 2006). To analyze the intensity of fractures, cumulative-frequency plots (Marrett, 1999; Ortega et al., 2006) were used (e.g., Figure 4. 14). In log-log plots of cumulative fracture frequency versus aperture, cumulative frequency indicates aperture-size rank (e.g., 1 is the widest fracture, 2 is the second widest, and so on) divided by scanline length. Kinematic aperture indicates the width of the fracture regardless of the presence of any fracture cement.

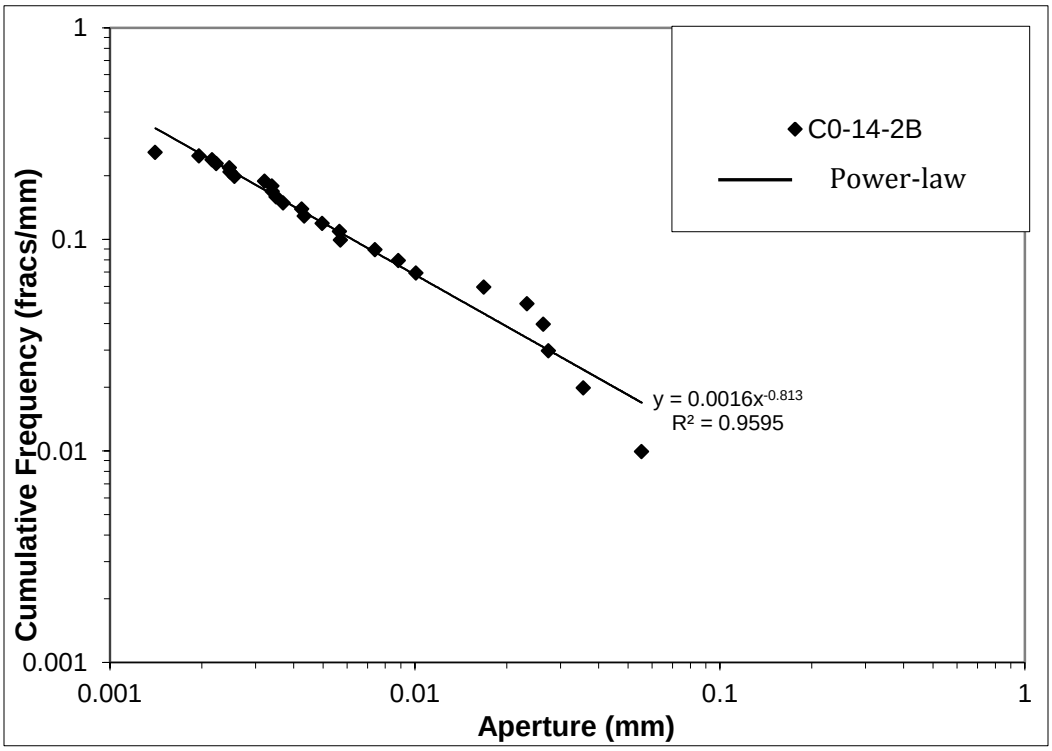

Figure 4. 14. Sample CO-14-1 collected from Domain III. Log-log plot exhibits a power-law distribution between kinematic aperture and cumulative frequency.

The Red Deer River datasets were plotted in cumulative frequency versus aperture plots (Figure 4. 16- 20). Figure 4. 16 shows log-log cumulative frequency versus aperture plots based on the data reported by Ukar et al. (2013). Opening-mode fractures commonly follow a power-law size distribution represented by a straight line on a log-log cumulative frequency versus aperture size plot (Marrett et al., 1999; Ortega et al., 2006). In other cases, opening-mode fracture populations follow scale-limited laws such as exponential or log-normal distributions (e.g. Gillespie et al. 2001; Bonnet et al., 2001; Hooker et al., 2012). Power-law distributions can be obscured due to common biases such as truncation and censoring (Pickering et al., 1995; Ortega et al. 2006; Hooker et al., 2009).

In general, microfracture data presented in Figure 4. 16 show power-law distributions with rollovers at the smallest apertures (truncation) and largest scales of observation (censoring). There is a scarcity of medium-sized microfractures (apertures between 0.01-0.1 mm) in these samples, perhaps reflecting an observation gap between data collected in outcrop (macrofractures) and through SEM imaging (microfractures). Because of this, in most cases the narrowest microfractures can be fitted by a power-law distribution that has a higher (steeper) slope than that of the medium-sized fractures (Figure 4.16). The slope of the narrowest microfractures ranges between -0.505 and -4.211 (most between -0.9 and -2.8) whereas that of the medium-sized fractures ranges between -0.813 and -0.204 (most between -0.3 and -0.8) (Table 4.2 and Figure 4.15). Intensities (intersection of the power-law with the y axis) of the narrowest microfractures show a range of up to 1 order of magnitude for the same fracture set within the same

domain. In contrast, the intensity of medium-sized fractures is similar and well constrained in each case. For example, the intensity of 0.1 mm aperture fractures is ~0.03-0.04 fractures/mm irrespective of the fracture set or structural position (Figure 4.18).

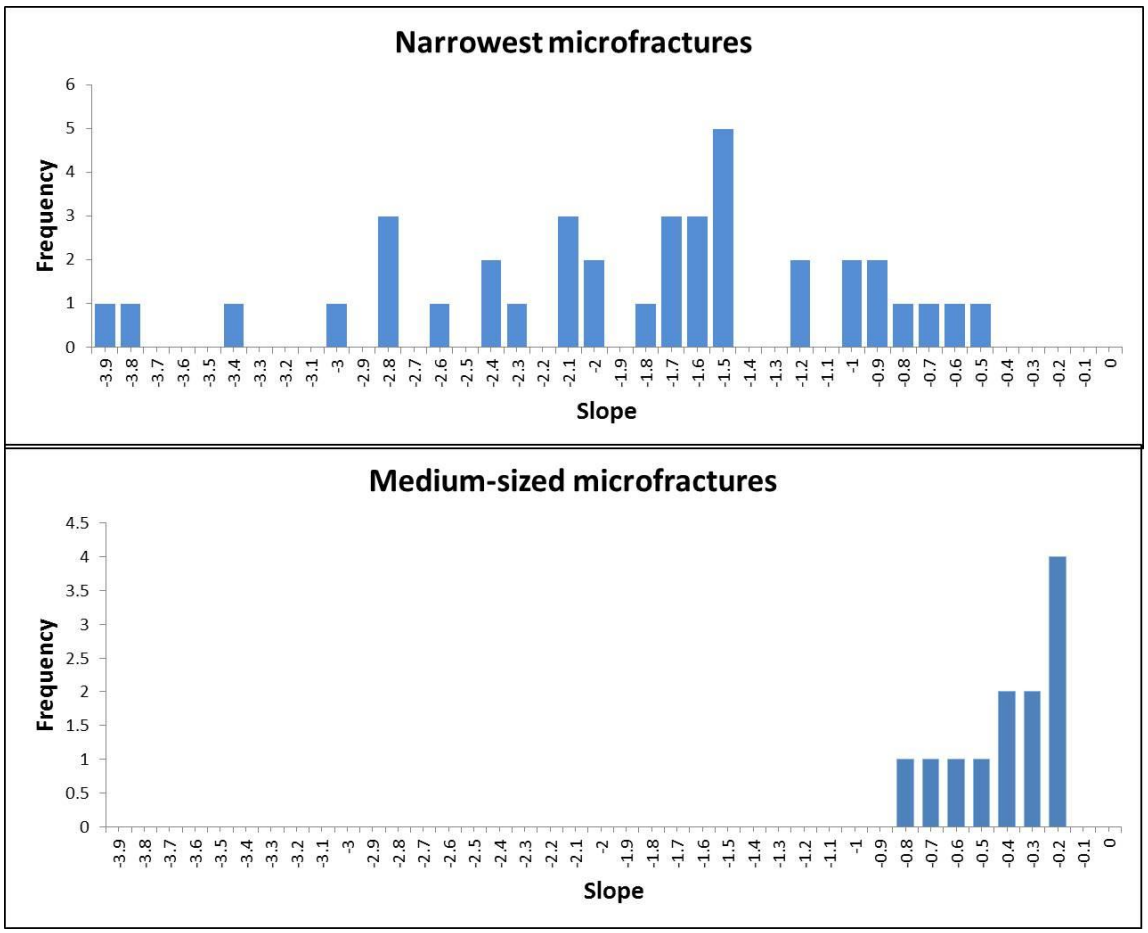

Figure 4. 15 Frequency of the slope of the narrowest and medium-sized microfractures.

Table 4.2 Best-fit equations and R^2 values of the narrowest and medium-sized microfractures

Sample #	Microfractures				Domain #
	narrowest microfractures		medium-sized microfractures		
co-15-1a-1	$y = 4E\text{-}07x^{-2.139}$	$R^2 = 0.9168$			I
co-15-2a-1	$y = 1E\text{-}05x^{-1.635}$	$R^2 = 0.9371$			I
co-15-2b-1	$y = 6E\text{-}05x^{-1.208}$	$R^2 = 0.969$			I
co-15-1a-2	$y = 2E\text{-}09x^{-3.099}$	$R^2 = 0.9843$			I
co-15-2a-2	$y = 3E\text{-}05x^{-1.534}$	$R^2 = 0.9638$			I
Rd-4b-all	$y = 5E\text{-}12x^{-4.211}$	$R^2 = 0.9852$			I
co-15-2b-2	$y = 0.0002x^{-1.093}$	$R^2 = 0.9656$			I
co-15-2a-3	$y = 0.0015x^{-0.724}$	$R^2 = 0.9853$			I
co-15-2b-3	$y = 1E\text{-}05x^{-1.737}$	$R^2 = 0.9672$	$y = 0.0105x^{-0.399}$	$R^2 = 0.9841$	I
Rd-4a-all	$y = 2E\text{-}05x^{-1.659}$	$R^2 = 0.9213$	$y = 0.0101x^{-0.435}$	$R^2 = 0.9936$	I
co-15-3b-1	$y = 1E\text{-}05x^{-1.533}$	$R^2 = 0.7489$			I
co-15-3a-1	$y = 4E\text{-}10x^{-3.454}$	$R^2 = 0.8848$			I
co-15-3a-2	$y = 1E\text{-}05x^{-1.779}$	$R^2 = 0.9656$	$y = 0.0153x^{-0.204}$	$R^2 = 1$	I
Rd-1b-all	$y = 1E\text{-}05x^{-1.687}$	$R^2 = 0.9876$	$y = 0.0061x^{-0.379}$	$R^2 = 1$	II
Rd-5b-all	$y = 9E\text{-}09x^{-2.817}$	$R^2 = 0.9865$			II
co-15-3a-3	$y = 3E\text{-}09x^{-3.113}$	$R^2 = 0.9553$			I
co-15-3b-3	$y = 0.0024x^{-0.698}$	$R^2 = 0.9511$			I

Table 4.2 continued

Rd-1a-all	$y = 1E\text{-}07x^{-2.493}$	$R^2 = 0.9721$	$y = 0.0023x^{-0.813}$	$R^2 = 0.9811$	II
Rd-5a-all	$y = 2E\text{-}06x^{-2.12}$	$R^2 = 0.8903$	$y = 0.0026x^{-0.729}$	$R^2 = 0.951$	II
co-14-1a-1	$y = 9E\text{-}07x^{-2.157}$	$R^2 = 0.9799$			III
co-14-2a-1	$y = 4E\text{-}05x^{-1.54}$	$R^2 = 0.9871$	$y = 0.0065x^{-0.425}$	$R^2 = 0.9978$	III
co-14-2b-1	$y = 3E\text{-}07x^{-2.045}$	$R^2 = 0.9661$			III
co-14-3a-1	$y = 7E\text{-}11x^{-3.816}$	$R^2 = 0.9832$			III
co-16-1a-1	$y = 0.0003x^{-1.016}$	$R^2 = 0.9835$			III
co-16-1b-1	$y = 0.0003x^{-0.944}$	$R^2 = 0.9381$			III
Rd-2b-1	$y = 5E\text{-}06x^{-1.856}$	$R^2 = 0.9639$	$y = 0.0201x^{-0.225}$	$R^2 = 0.9138$	III
co-14-1a-2	$y = 0.0011x^{-0.505}$	$R^2 = 0.9878$			III
co-14-2a-2	$y = 0.0005x^{-1.208}$	$R^2 = 0.9893$	$y = 0.0379x^{-0.207}$	$R^2 = 0.9693$	III
co-14-2b-2	$y = 8E\text{-}09x^{-2.686}$	$R^2 = 0.9525$			III
co-16-1a-2	$y = 5E\text{-}09x^{-2.826}$	$R^2 = 0.9089$			III
Rd-2b-3	$y = 2E\text{-}05x^{-1.567}$	$R^2 = 0.9739$	$y = 0.0019x^{-0.643}$	$R^2 = 0.9014$	III
co-14-1a-3	$y = 0.0003x^{-0.862}$	$R^2 = 0.9299$			III
co-14-2a-3	$y = 4E\text{-}05x^{-1.108}$	$R^2 = 0.9494$			III

Table 4.2 continued

co-14-2b-3	$y = 9E\text{-}08x^{-2.479}$	$R^2 = 0.9602$			III
co-16-1a-3	$y = 1E\text{-}08x^{-2.837}$	$R^2 = 0.8613$			III
co-16-1b-3	$y = 1E\text{-}05x^{-1.556}$	$R^2 = 0.9303$			III
Rd-2b-oblique to 2	$y = 4E\text{-}05x^{-1.511}$	$R^2 = 0.9517$	$y = 0.0067x^{-0.531}$	$R^2 = 0.9411$	III
Rd-2a-3	$y = 1E\text{-}05x^{-1.772}$	$R^2 = 0.974$	$y = 0.0121x^{-0.266}$	$R^2 = 0.9938$	III
Sample #	**Macrofractures**				**Domain #**
Eu-Rd-Sc-2	$y = 0.0006x^{-2.307}$	$R^2 = 0.9683$			I
Eu-Rd-Sc-1	$y = 0.0011x^{-2.027}$	$R^2 = 0.9526$			II

Because of the outcrop orientation, the two macroscanlines measured by Ukar et al. (2013) in domains I and II contained predominantly set 2 fractures. Figures 4.16 and 4.17 indicate that extrapolation of power-laws fitted through the narrowest set 2 microfracture data in these two domains is not a good predictor of the intensity of macrofractures, probably because the steep slopes of the narrowest microfractures are not maintained for fractures wider than about 0.01 mm.

Based on a large dataset, Hooker et al (2014) found that, in many cases, fitting a slope of -0.8 to measured microfracture data predicts the abundance of macrofractures to first approximation in many datasets. Figure 4.20 plots the -0.8 slope fitted to the frequency of microfractures in the Red Deer River area, predicting macrofractures frequency within half an order of magnitude.

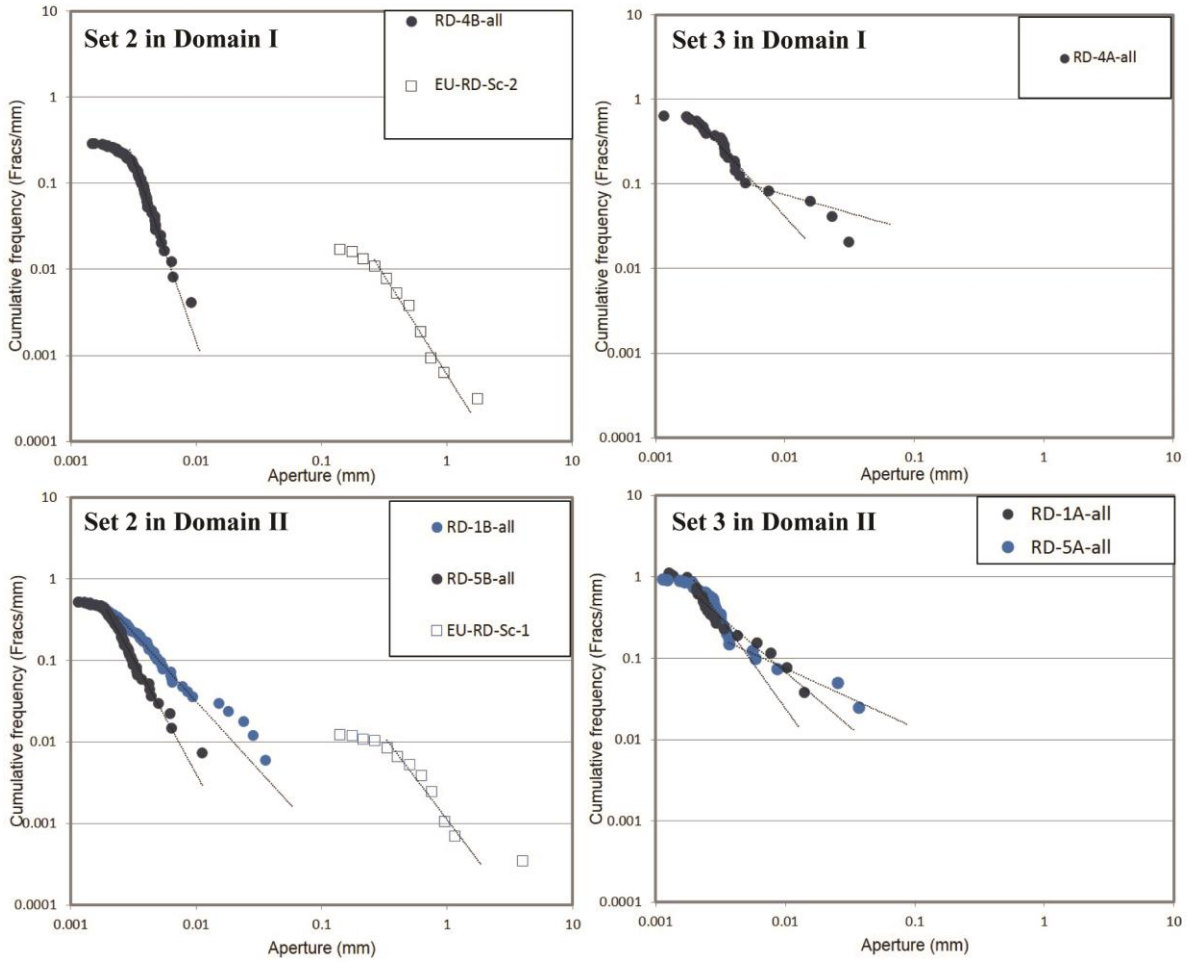

Figure 4. 16a The cumulative frequency versus aperture plots for data reported in Ukar et al. (2013).

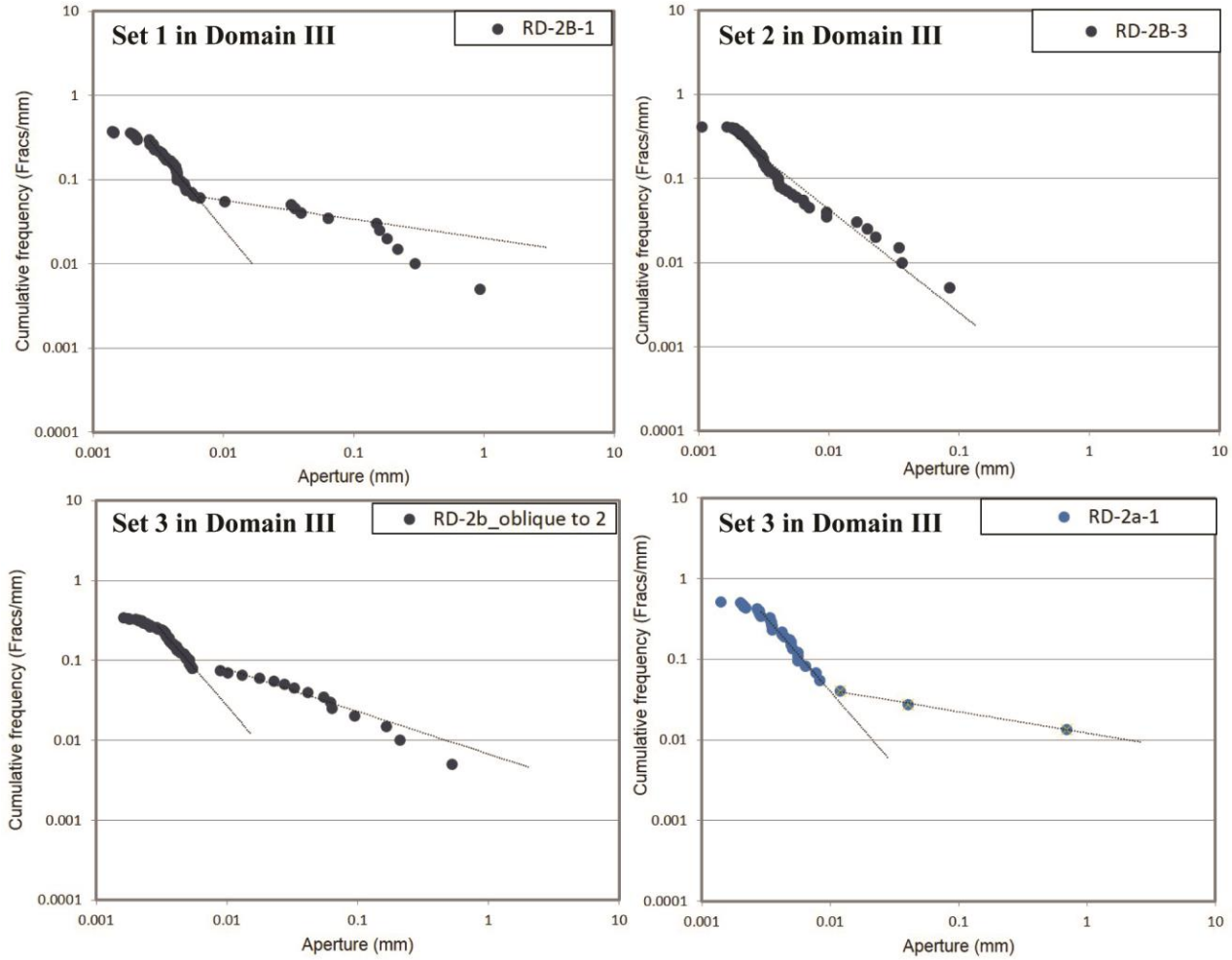

Figure 4. 16b The cumulative frequency versus aperture plots for data reported in Ukar et al. (2013).

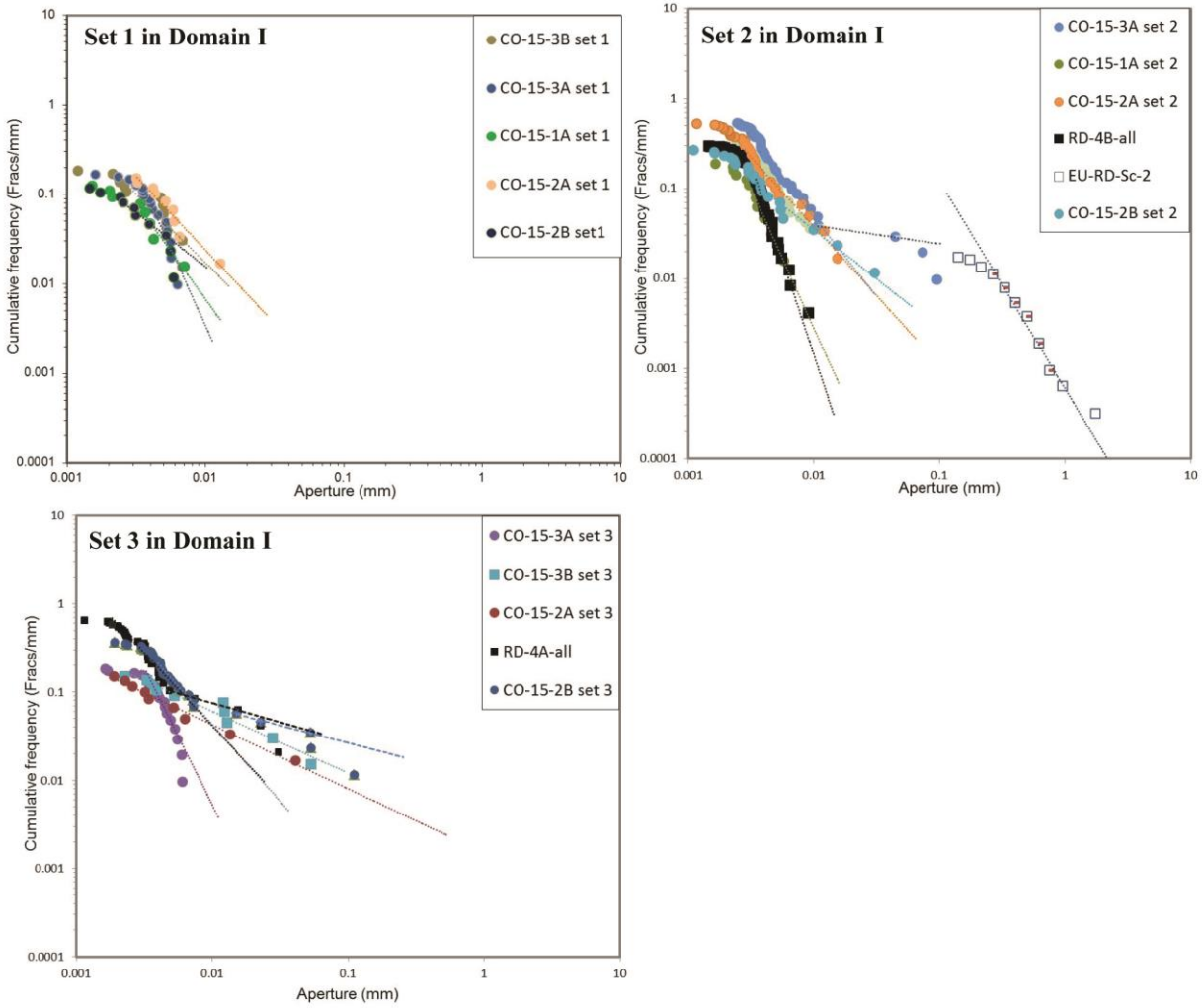

Figure 4. 17a Microfracture aperture-size distribution based on all micro and macroscanline data.

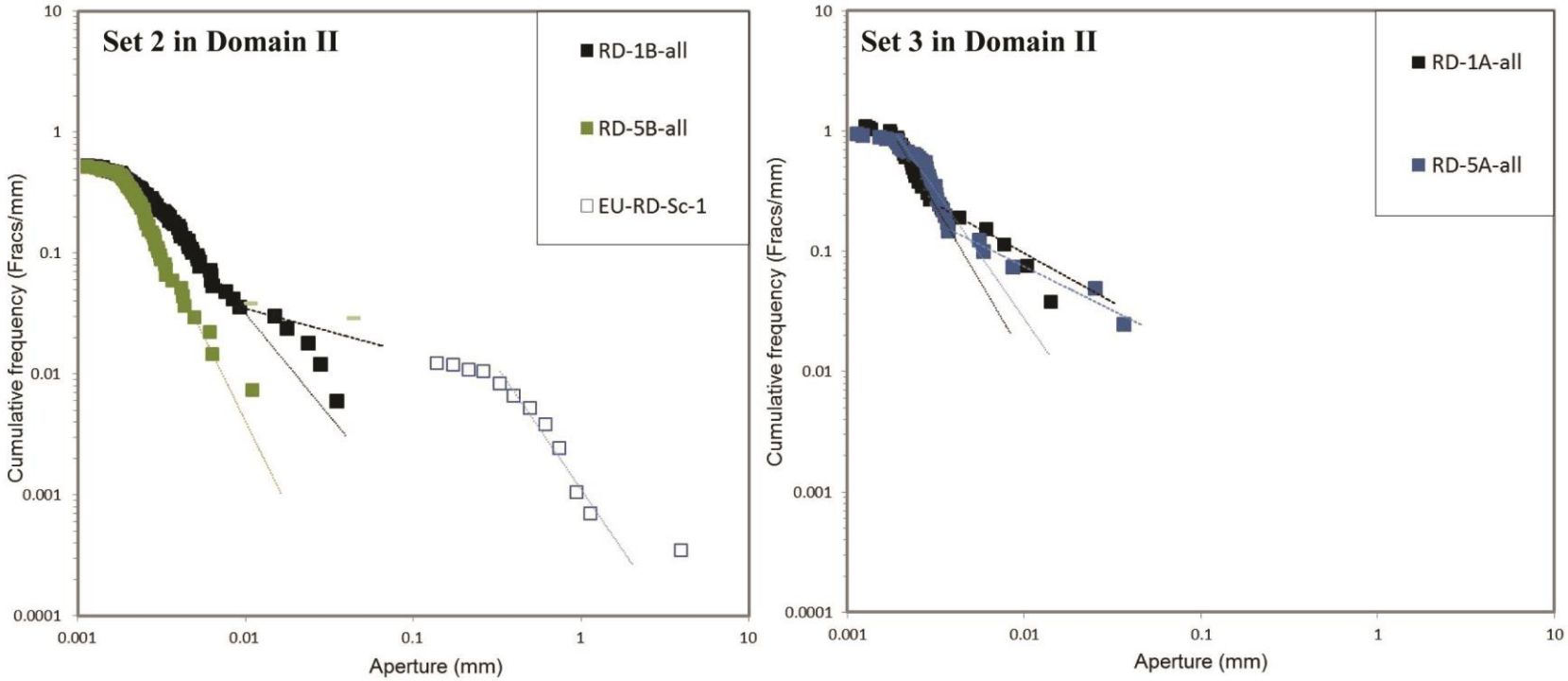

Figure 4. 17b Microfracture aperture-size distribution based on all micro and macroscanline data.

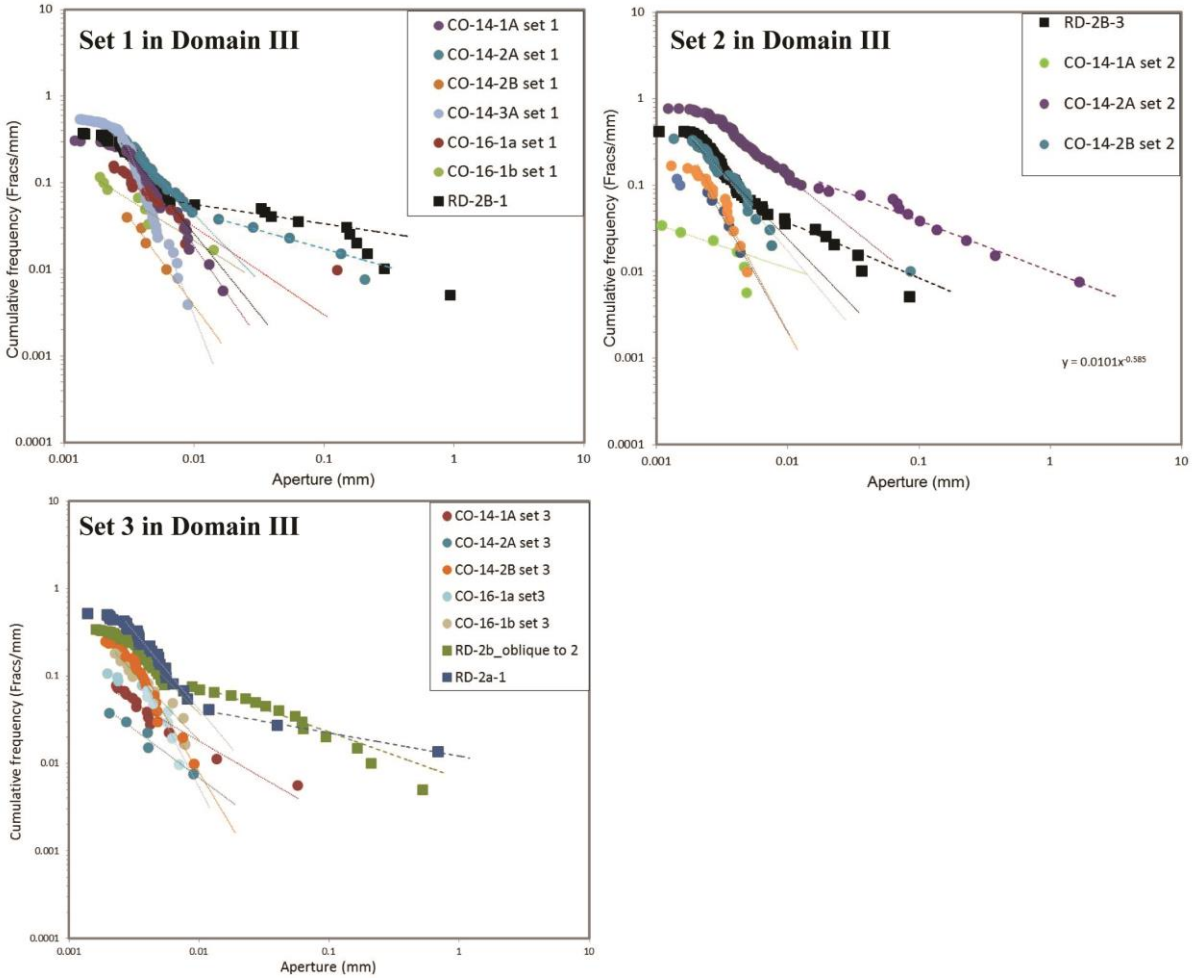

Figure 4. 17c Microfracture aperture-size distribution based on all micro and macroscanline data.

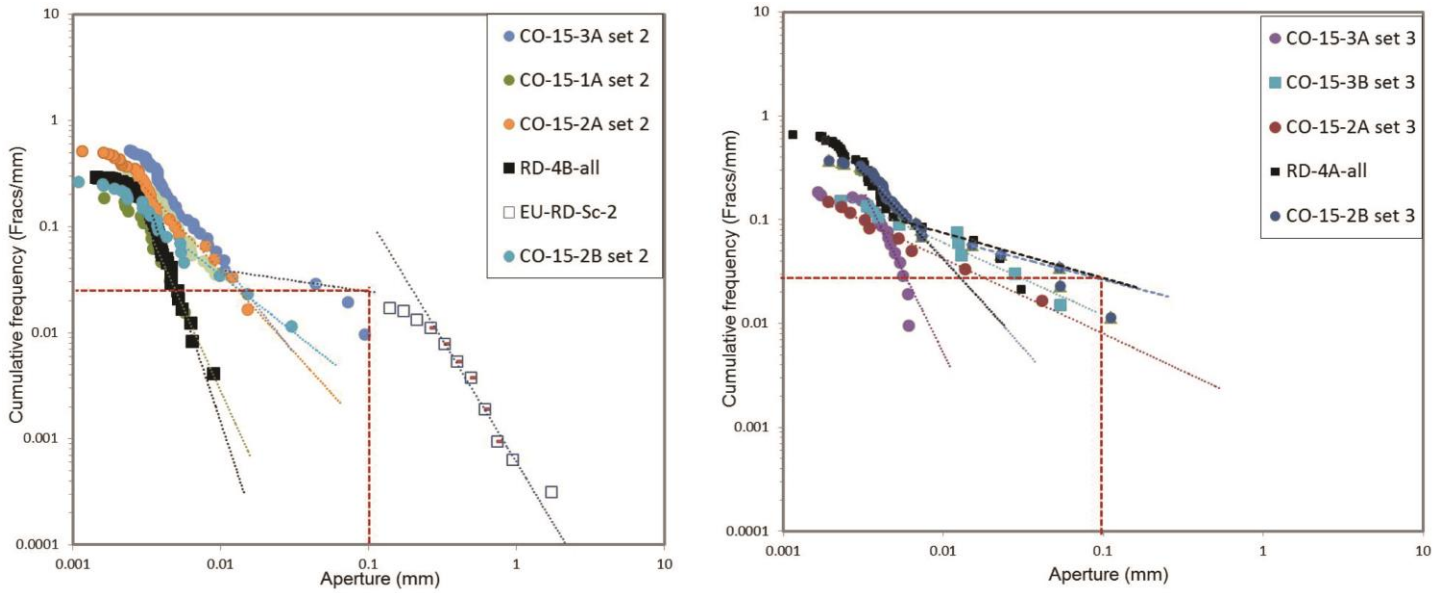

Figure 4. 18a Microfracture aperture-size distribution with intensity of medium-sized microfractures of aperture 0.1 mm highlighted by red lines.

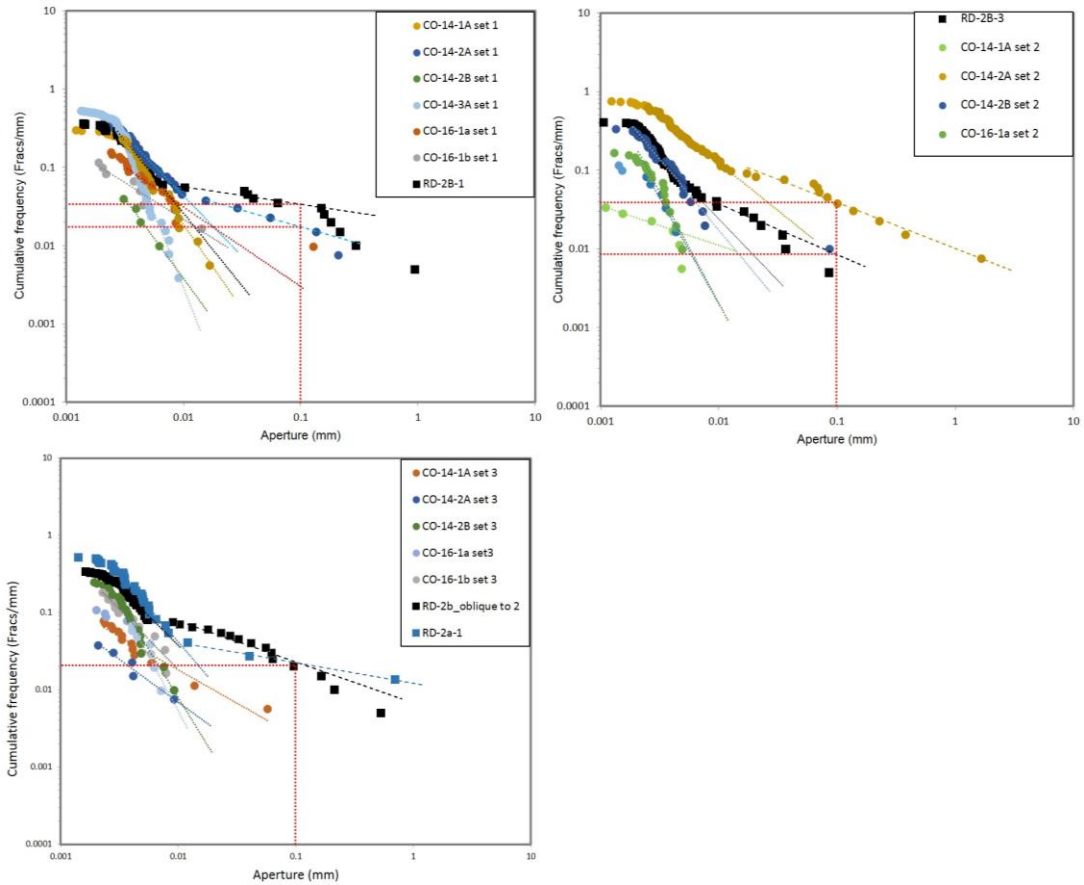

Figure 4. 18b Microfracture aperture-size distribution with intensity of medium-sized microfractures of aperture 0.1 mm highlighted by red lines.

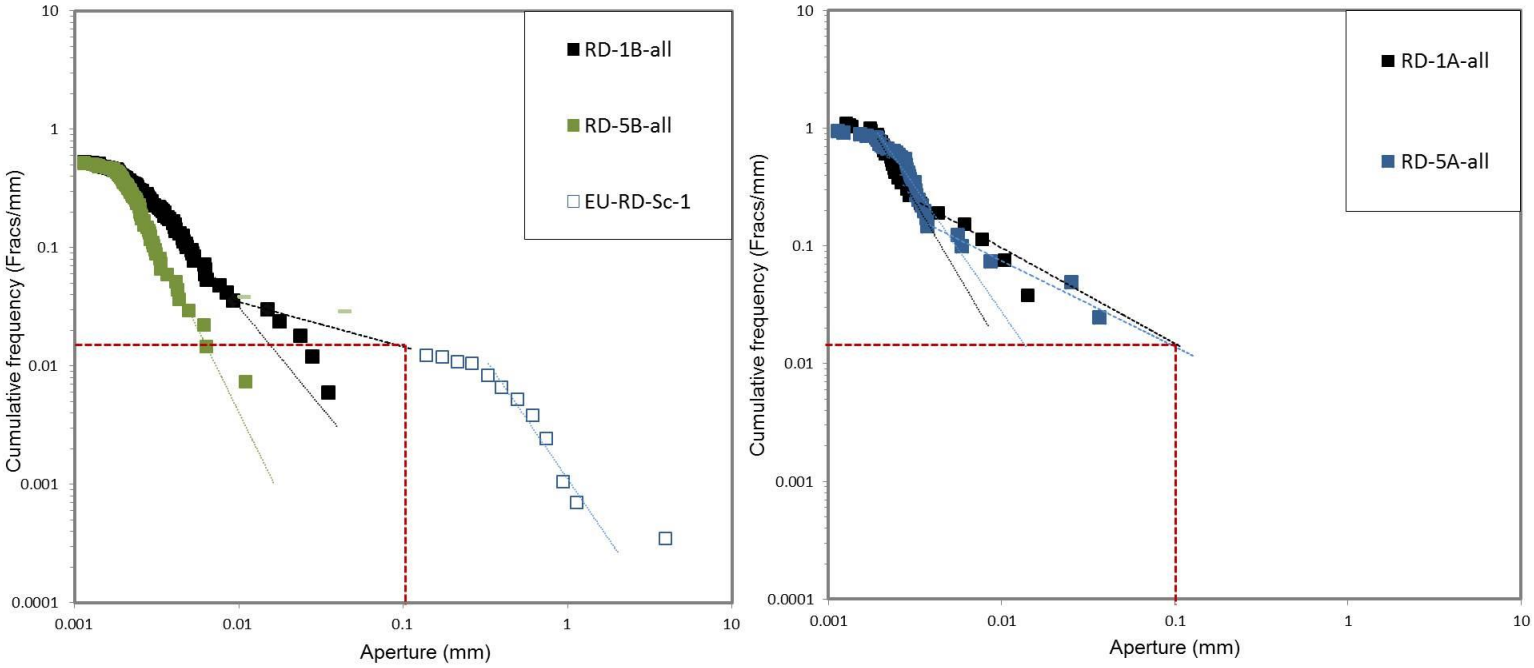

Figure 4. 18c Microfracture aperture-size distribution with intensity of medium-sized microfractures of aperture 0.1 mm highlighted by red lines.

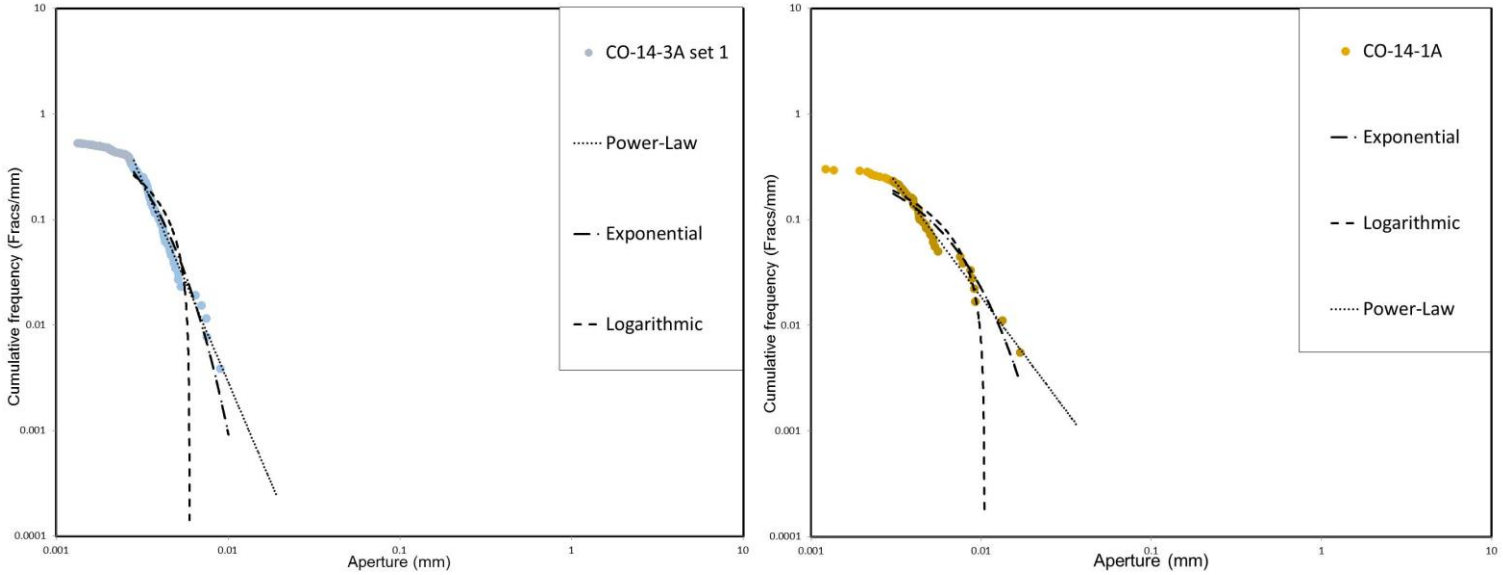

Figure 4. 19 Example of microfracture aperture-size distribution in which curves were fit with power law, exponential and logarithmic trendlines

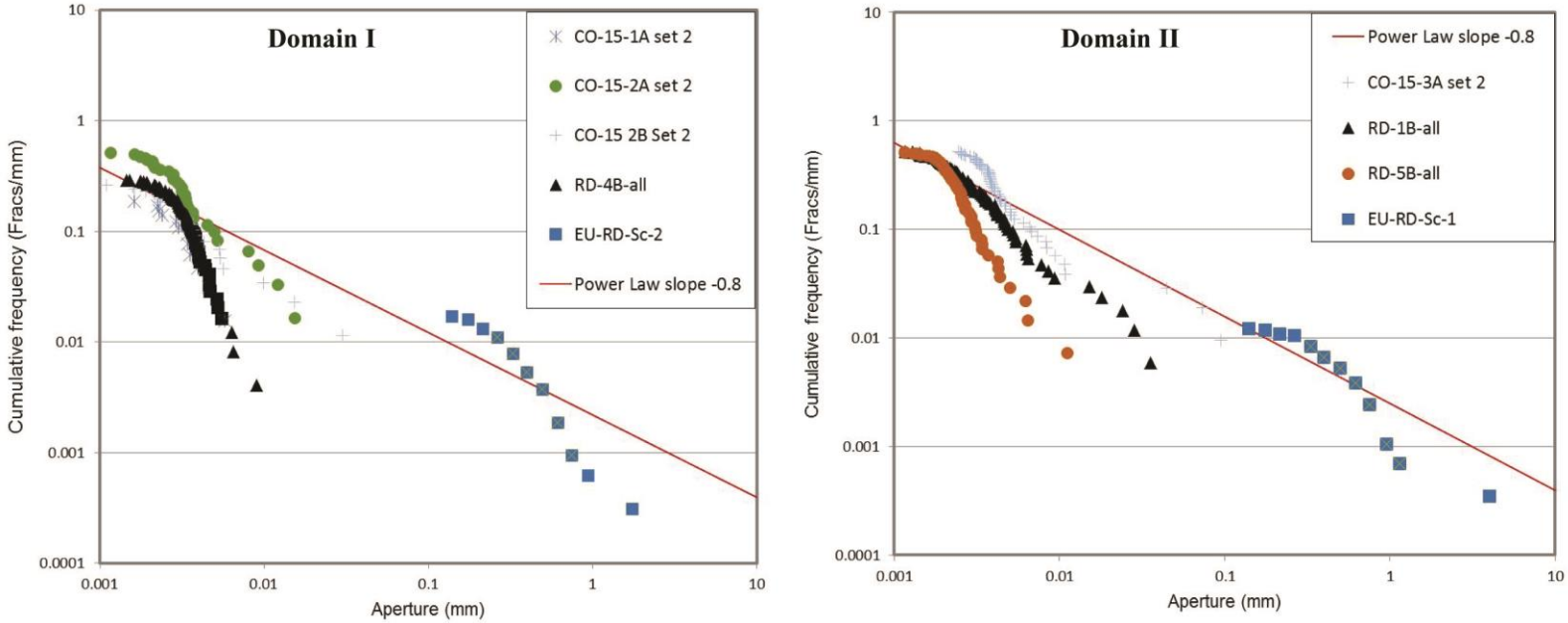

Figure 4. 20 Apertures of power law–distributed fracture data set from Domain I and II. Solid lines indicate empirical powerlaw extrapolation of –0.8 and tied to microfracture population following Hooker et al., 2014.

The effect of lithology in fracture intensity

In order to evaluate the effect of lithology on fracturing in the Cardium Formation, I examined fracture intensities in three adjacent samples from three different lithological units of Kakwa Member within Domain III (Figure 4.21): 1) sample co-14-3 of a bioturbated layer, 2) sample co-14-2 of a planar-laminated layer and 3) sample co-14-1 of a hummocky cross-stratified layer, and two samples co-15-1 and co-15-2 of the planar-laminated Upper and bioturbated Lower Kakwa Members within Domain I (Figure 3.10). These samples were cut in two orthogonal orientations in order to capture the main three fracture sets. Fracture intensities differ to within half an order of magnitude for the same fracture set in different lithologies. For example, the intensity of set 2 fractures in Domain III is significantly higher in the planar-laminated layer than in the bioturbated and hummocky-stratified layers (Figure 3.21). This same distribution is found in the Lower and Upper Kakwa Members within Domain I. It is noteworthy that there is no correlation between fracture abundance and layer thickness, as the thickest bioturbated beds of the Lower Kakwa Member are not the ones with the highest fracture intensity (Figures 4.21 and 4.22). Thus, it is inferred that bioturbation has a major effect – greater than layer thickness- in fracturing in the Cardium Formation. Whether bioturbation results in an increase or decrease of fracture intensity depends on the orientation of the fractures. Local lithological differences could be responsible for the observed variability in intensity of the narrowest microfractures among samples.

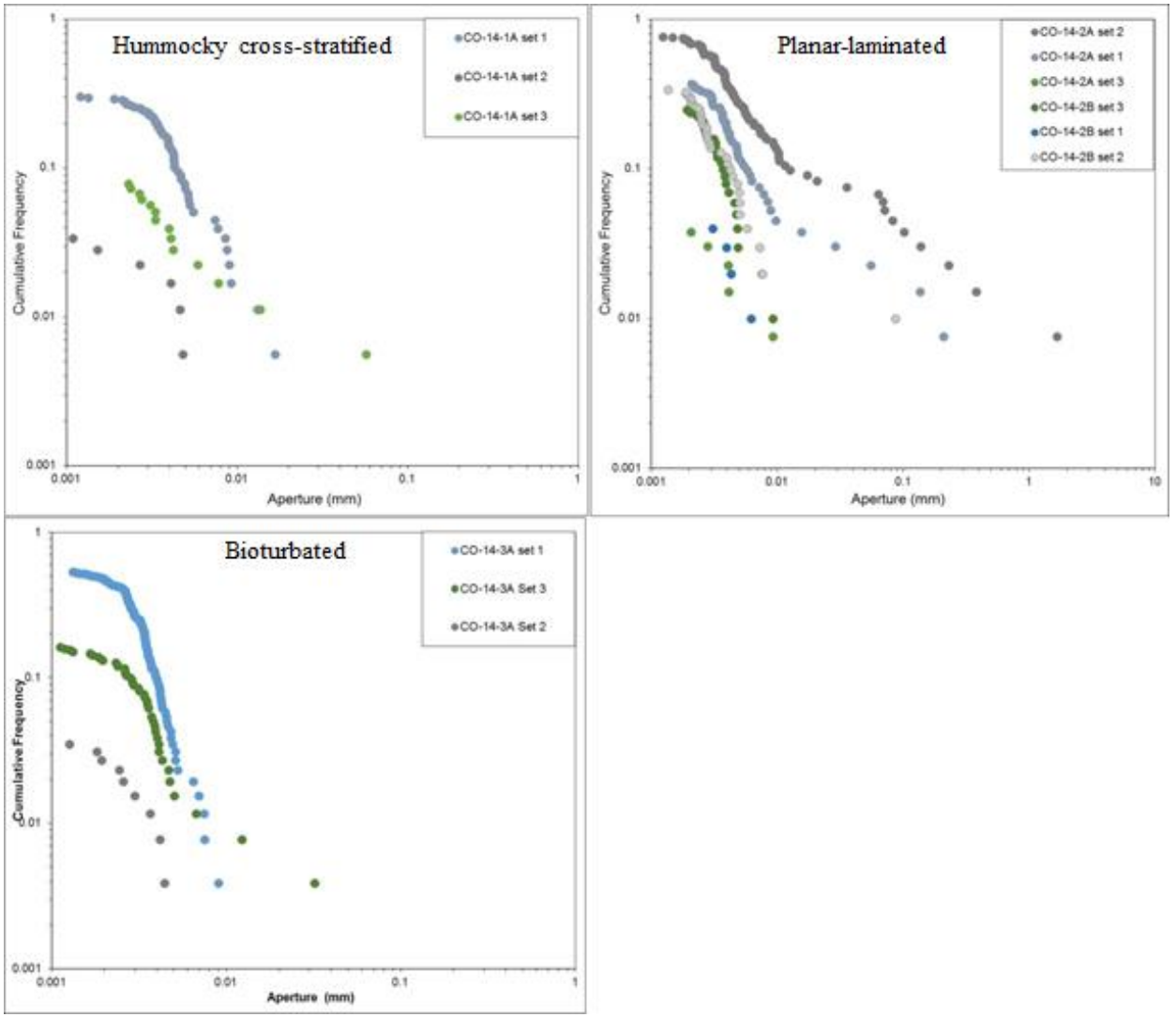

Figure 4. 21. Fracture intensity variation in different lithological units of Kakwa Member in Domain III. Sample CO-14-1 collected from hummocky cross-stratified part of the sandstone unit. Sample C0-14-2 collected from planar-laminated part of the sandstone unit. Sample C0-14-3 collected from bioturbated part of the sandstone unit.

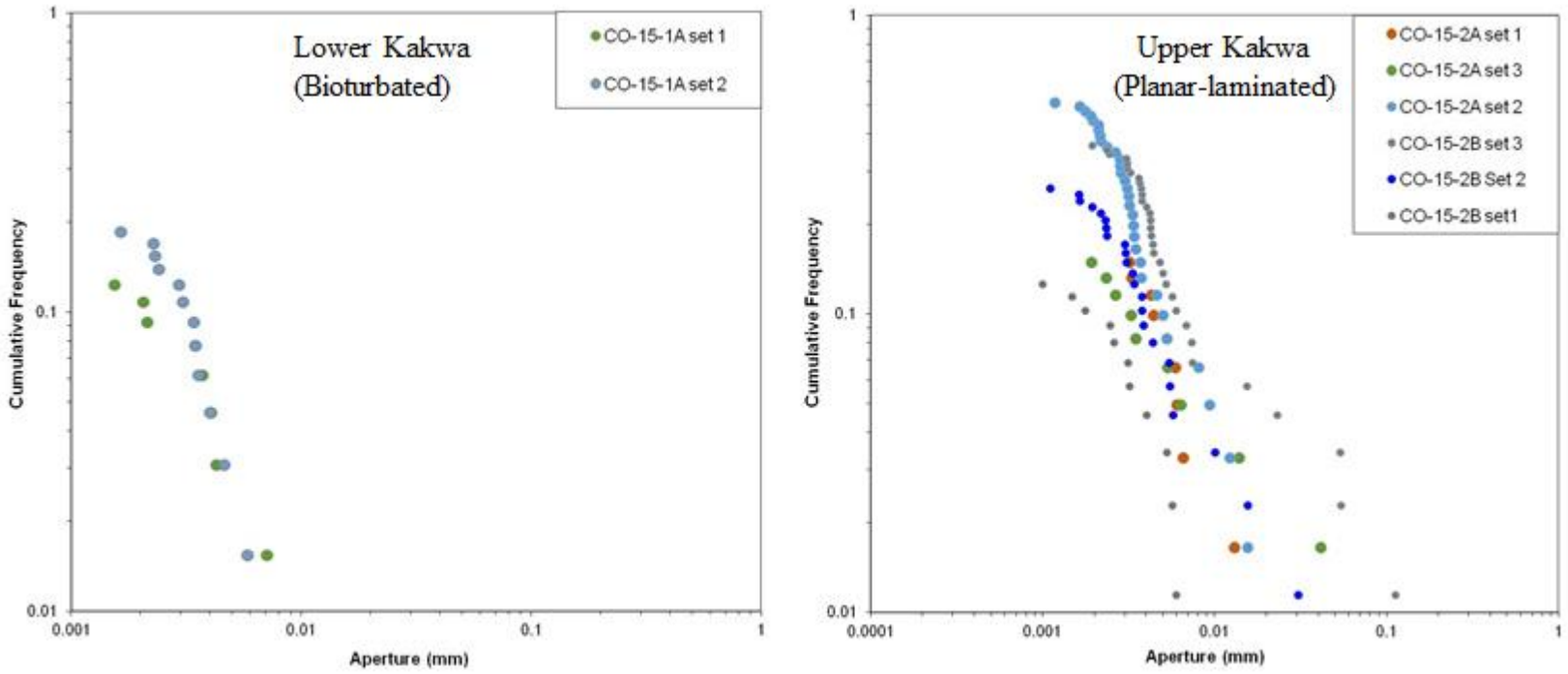

Figure 4. 22. Cummulative frequency and aperture graphs showing effect of lithology on fracture intensity in Domain I. Sample CO-15-1 collected from bioturbated part of the sandstone unit. Sample C0-15-2 collected from planar-laminated part of the sandstone unit.

Fracture Strain vs. Fold Geometry

Fracture strain can be readily measured from microfracture populations. Fracture strain ε is a measure of the extension along a 1D line of observation (the scanline):

$$\varepsilon = \frac{L - L_0}{L_0} = \frac{\Sigma\, Aperture}{\Sigma\, Spacing}$$

Where L is the final length and L_0 is the initial length. In this case, strain equals the sum of all apertures divided by the sum of all spacings.

Opening-mode fractures may release elastic strain during folding resulting in a correlation between folding strain and fracture strain (Beekman et al., 2000; Tavani et al., 2014). In this study, the relationship between fracture strain and structural position within the Red Deer River anticline was explored using fracture aperture and spacing measurements from the collected scanlines. Strain was calculated using fracture aperture and spacing measurements from the two macro scanlines of Ukar et al. (2013), and fifteen microfracture scanlines. For microfracture strain calculations, fractures with apertures >0.1 mm were excluded because they are part of the macrofracture measurements, whereas for macrofracture strain calculations, only fractures with apertures >0.1 mm were taken into account. Strain calculations are shown in Figures 4.23 and 4.24 and are listed in Table 4.3, 0.0012 and 0.0094. Strain calculated using microfractures <0.1 mm in aperture ranges between 9.39×10^{-3} and 1.17×10^{-3}, whereas

strain calculated using macrofractures >0.1 mm in aperture are $6.70x10^{-3}$ and $6.79x10^{-3}$ for both macroscanlines.

Table 4.3. Fracture strain values for fracture scanlines in the Red Deer River anticline

Sample #	Domain	Fracture strain (Microfractures)	Fracture strain (Macrofractures)
RD-1A-Sc-all	II	0.004364	
RD-1B-Sc-all	II	0.002624	
RD-2A-Sc-all	III	0.006959	
RD-2B-Sc-all	III	0.009395	
RD-4A-Sc-all	I	0.003465	
RD-4B-Sc-all	I	0.001173	
RD-5A-Sc-all	II	0.004896	
RD-5B-Sc-all	II	0.001683	
RD-Sc1-macro	II		0.006789
RD-Sc2-macro	I		0.006704
co-14-1A	III	0.002578	
co-14-2A	III	0.008610	

Table 4.3 continued

co-14-3A	III	0.002870	
co-15-1A	I	0.001767	
co-15-2a	I	0.006669	
co-15-3a	I	0.007636	
co-16-1a	III	0.002292	

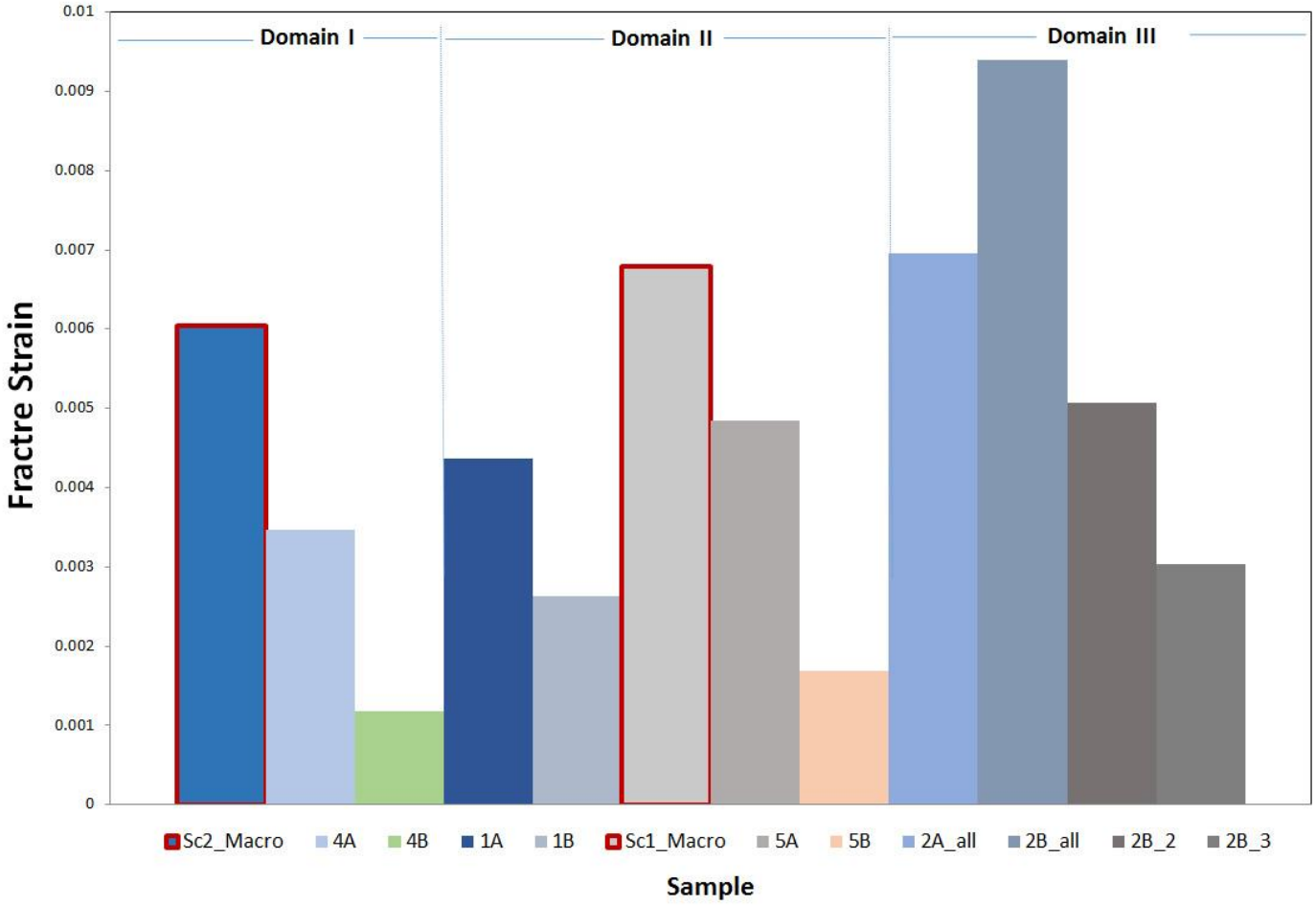

Figure 4. 23 Fracture strain values from macroscanline (outlined in red) and microscanline measurements based on Ukar et al. (2013) data.

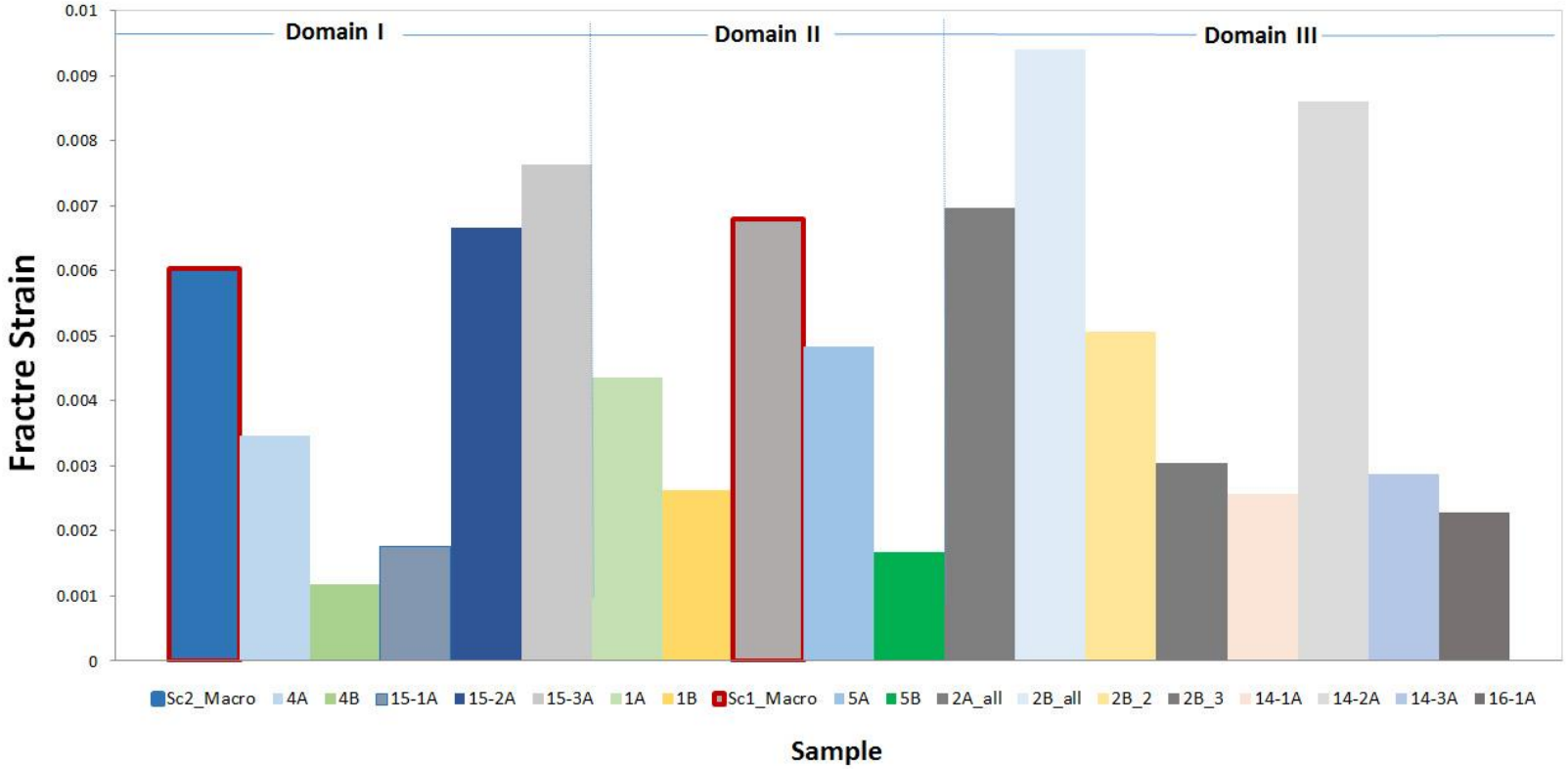

Figure 4. 24 Fracture strain values from macroscanline (outlined in red) and microscanline measurements based on all fracture scanline data collected in this study and by Ukar et al., 2013.

In order to facilitate visual comparison of fracture strain distribution with structural position for different fracture sets within the Red Deer River Anticline, strain measurements from the three structural domains are plotted in Figure 4.25. Strain calculations from the macro- and microfracture scanline data indicate similar fracture strain magnitudes across the fold regardless of structural position of all fracture sets. Although fracture strain in the planar-laminated Kakwa Member is higher in the steeper dipping domain III than in domain I, fracture strain for the Karr Member is higher in domain I compared to domain III. The large range in fractures strain within the Kakwa Member of domain II suggest that local variation in fracture strain are larger than variations among different domains of the fold. Variations between different lithologic units of the same member in the same domain are equally large. Fracture strain shows no consistent variation with structural position in the fold (Figure 4. 25).

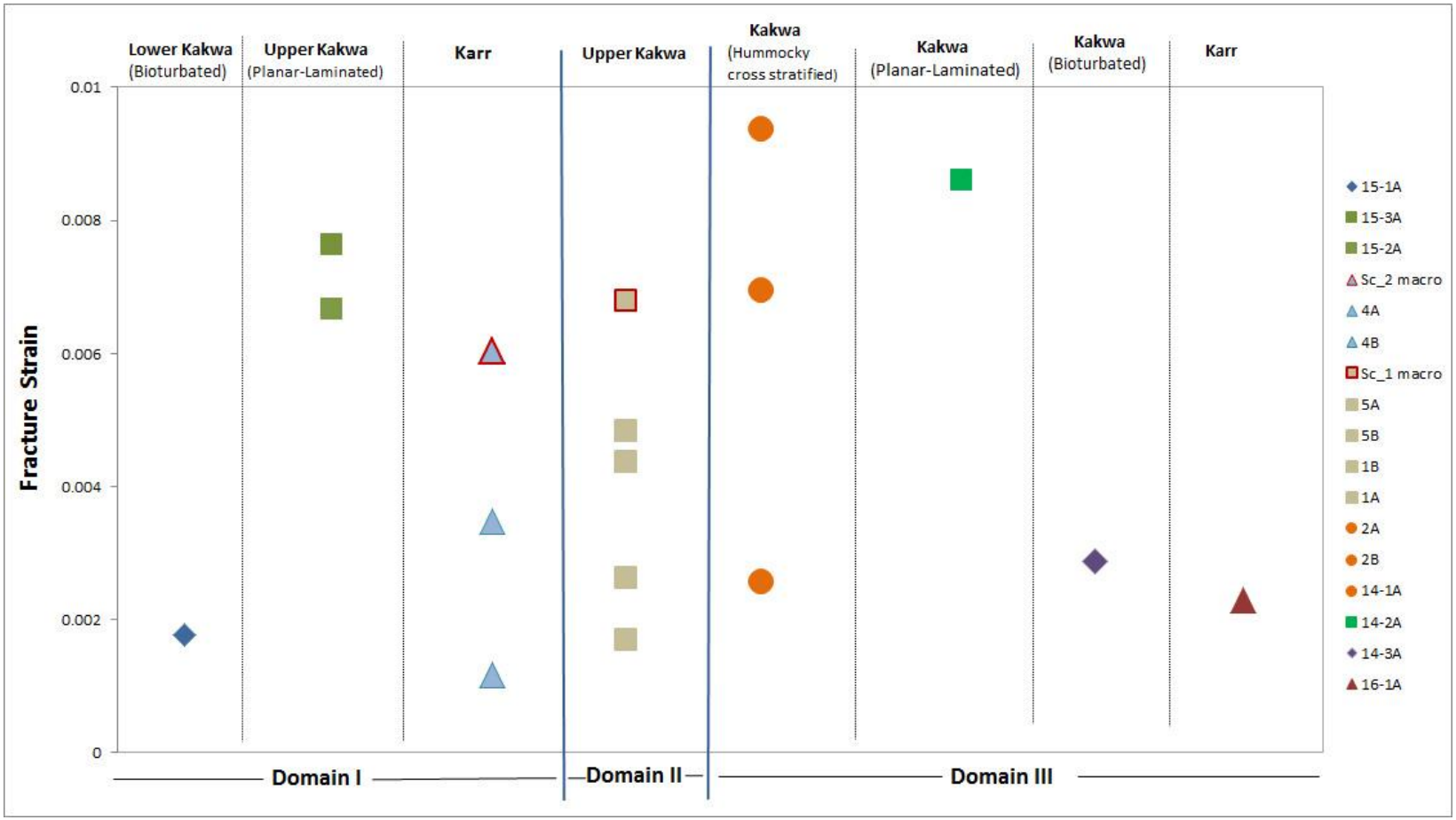

Figure 4. 25 Fracture strain for three positions (Domain I, II and III) on the Red Deer River anticline based on all microscanline and macroscanline (outlined in red) data combined.

Chapter 5: Kinematic Modeling

In the Red Deer River area, the spatial and temporal relationships of fractures to complex, seismic-scale structures (folds, faults) remain ambiguous. Geometrically valid framework models that adhere to geologic principles can be used to explain the relationship of deformational components, and their evolution throughout the deformation. In this study, Move Structural Modeling 2D and 3D software packages by Midland Valley were used to reconstruct balanced cross-sections and to construct forward kinematic models. Kinematic models were constructed in order to 1) validate the structural interpretation of regional structures, 2) explore possible deformation styles that could have produced present-day structures, and 3) constrain the timing of fracturing relative to the overall evolution of the folds and thrust faults. The constructed models were also used to calculate bed-parallel extension in the direction of tectonic transport during development of the fold and thrust belt. These strain calculations serve as a basis to predict fracture strain associated this deformation. Predicted fracture distribution and timing relative to fold and thrust development were tested by comparison to the distribution of fracture strain and timing obtained from field and petrographic observations.

(RE)CONSTRUCTION OF BALANCED CROSS SECTIONS

Data

For the reconstruction of balanced cross-sections and construction of kinematic forward models in the Red Deer River area, I used a cross section first published by Kubli and Langenberg (2002) and subsequently updated by Pana et al. (2013). The Red Deer River section by Kubli and Langenberg (2002) was constructed using a regional cross-section published by Rottenfusser et al (1991). Pana et al.'s (2013) updated cross section incorporates surface geologic, stratigraphic, seismic, and data from 16 wells. Pana et al.'s (2013) cross-section (Figure 5.1) offers an integrated stratigraphic and structural interpretation of the geology in the Alberta fold-and-thrust belt system and provides insight into the internal geometry of faulted and folded strata.

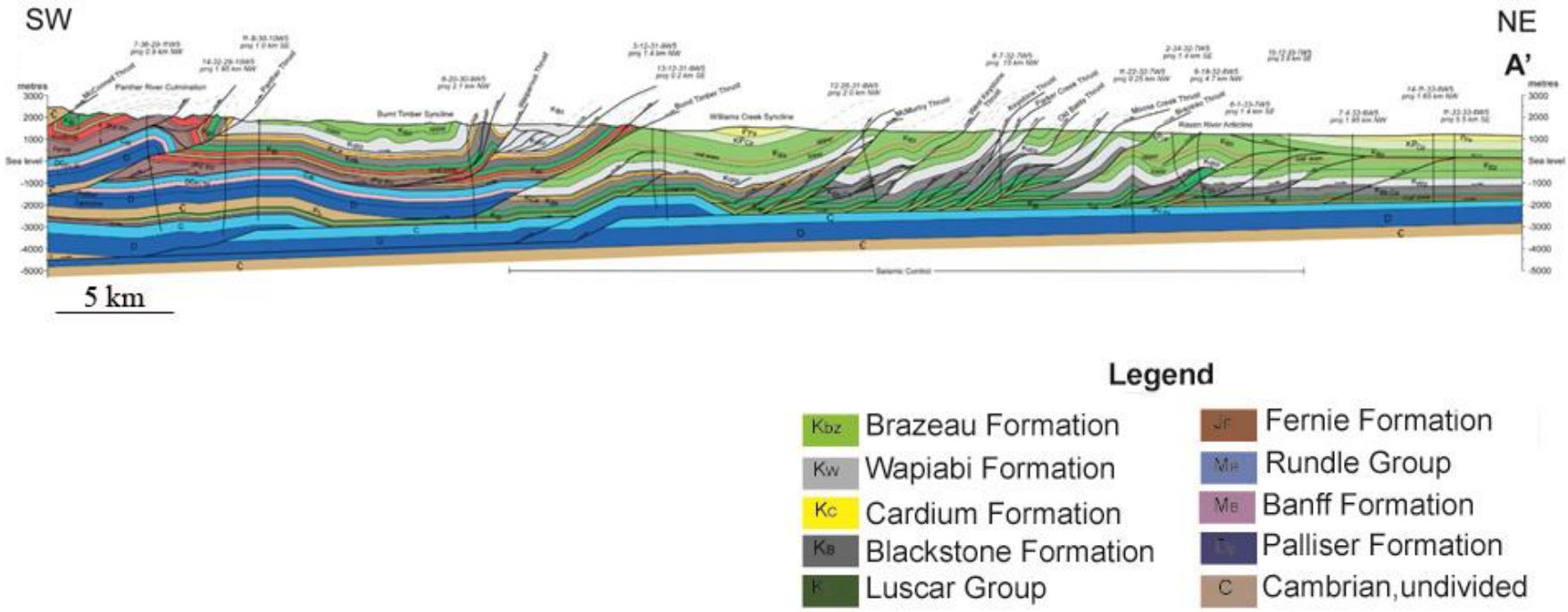

Figure 5.1.Cross-section of the Red Deer River area by Pana et al (2013). No vertical exaggeration.

For the construction of the cross-sections used in this study, I also used surface information obtained from Ollerenshaw's (1966) geologic map and the accompanying published cross section. Surface geological information was complemented with information acquired from seismic lines and 4 wells for the construction of this cross section (Figure 5.2). The location of these wells and their relationship to the regional structures is shown in Figure 5.2.

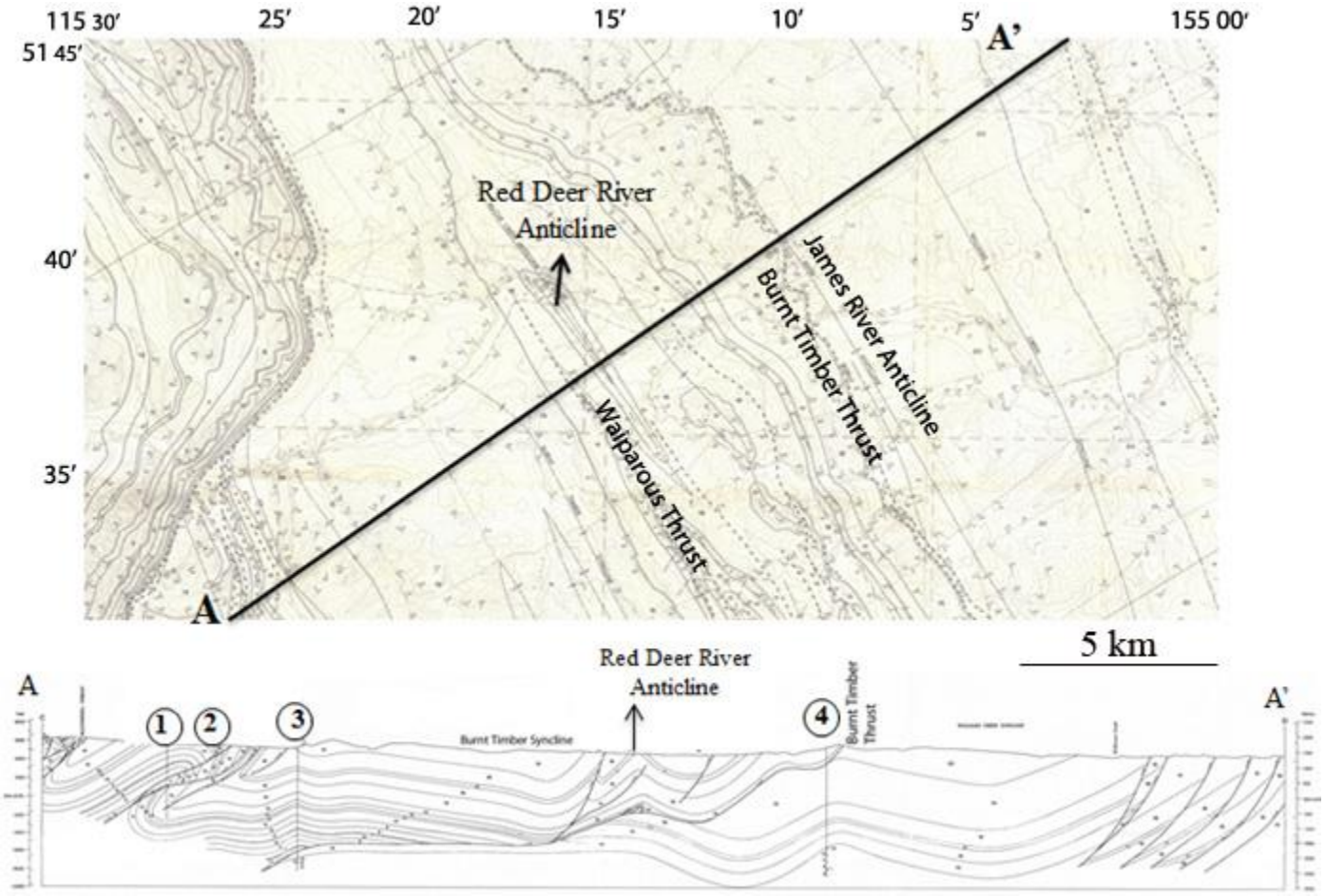

Figure 5.2 a. Structural map and b. cross-section of the Red Deer River anticline by Ollerenshaw (1966). Wells are numbered; Well 1:Union Can. Homestead (12-11-30-11 W5), Well 2: T.G.S Panther River (5-23-30-11 W5), Well 3: Shell Panther No.1 (5-19-30-10 W5) and Well 4: Shell Burnt Timber (6-22-31-9 W5). No vertical exaggeration.

Most surface geologic expressions in the section by Pana et al. (2013) correspond with Olleranshaw's (1966) geologic map with some exceptions: In Pana et al's cross section, an additional duplex structure was interpreted within the Wapiabi Formation in the hanging wall of the Burnt Timber Thrust and an additional fault between Waiparous and Burnt Timber trust faults. These structures are absent in Olleranshaw's (1996) cross-section.

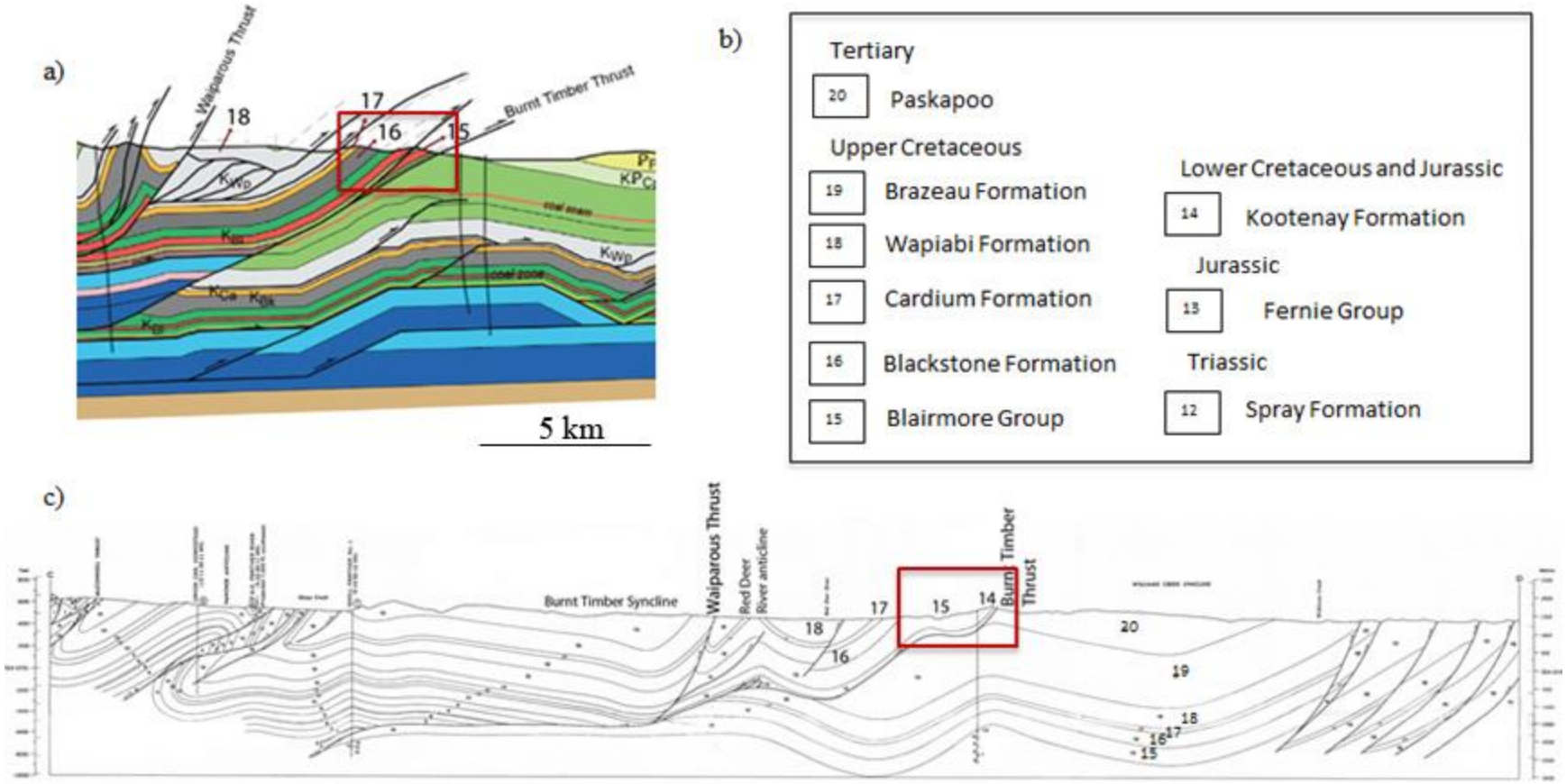

Figure 5.3 a: Part of the cross-section by Pana et al. (2013) covering the bedrock exposures between Waiparous Thrust and Burnt Timber Thrust. b: Legend showing the Cenozoic and Mesozoic age formations. c: Cross-section by Ollerenshaw (1996) showing dissimilarity of bedrock adjacent to Burnt Timber thrust and Waiparous fault. The rectangle highlights the inconsistency with the surface exposures. The location of the section is shown in Figure 5.2.

Besides surface geologic and stratigraphic data, Pana et al's (2013) cross section also includes findings from seismic and well data and can therefore be considered to be better constrained at depth. Thus, in this study I used Pana et al.'s (2013) cross-section to draw the geometry of deep structures. Olleranshaw's (1996) map was deemed more consistent with the mapped surface geology and more suitable for the reconstruction of shallow structures using Move. These limitations are discussed in the following section.

Construction of the balanced cross-sections

Published cross sections

Pana et al.'s (2013) cross-section includes some areas that do not provide the necessary information to establish the sequential order of thrusting or amount of displacement along some of the faults. For example, the amount of displacement along the imbricate structure located near the Red Deer River anticline (box in Figure 5.4) cannot be determined because there is inadequate information about the offset of individual faults in the duplex structure. Moreover, the strata carried over by the Burnt Timber thrust fault cannot be restored because the cross-section does not provide enough information to determine the location of footwall cutoffs of the strata in the southwest side of the section (Figure 5.5).

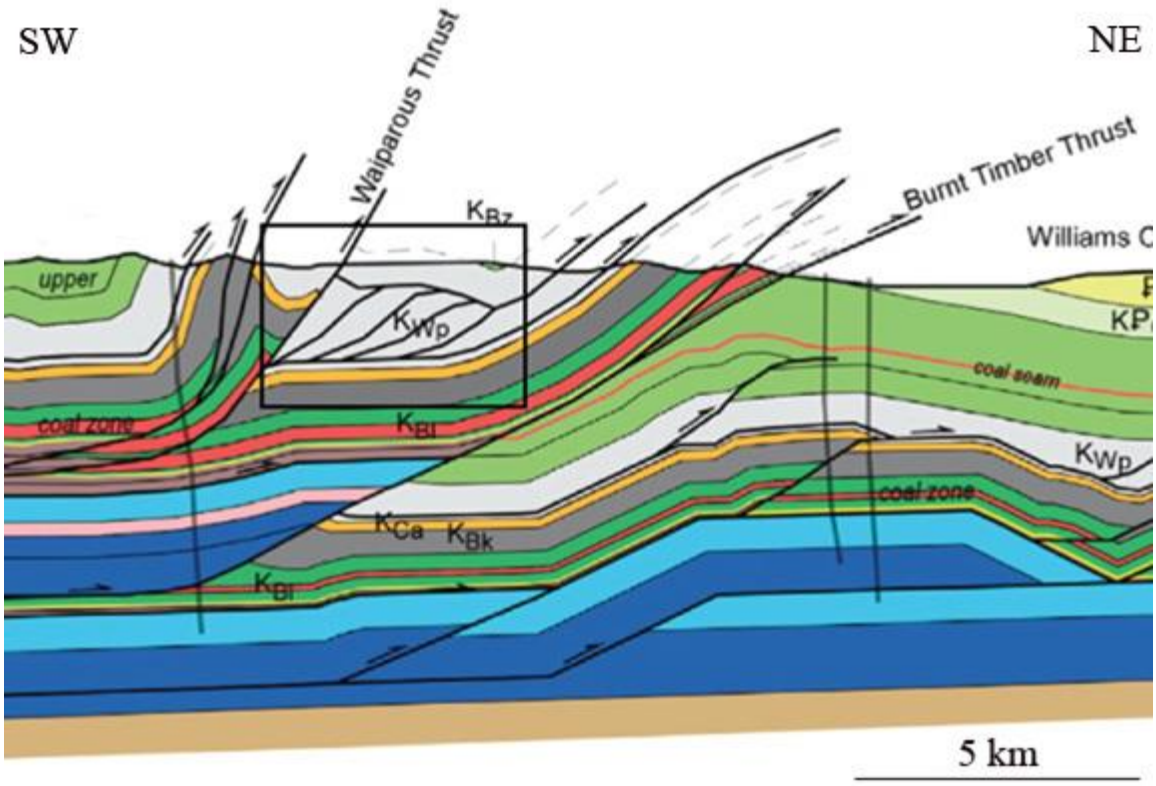

Figure 5.4. Imbricate structures and thickening in the shale unit (Kwp: Wapiabi Formation) enclosed by the rectangular creates obstacles to correct restorations.

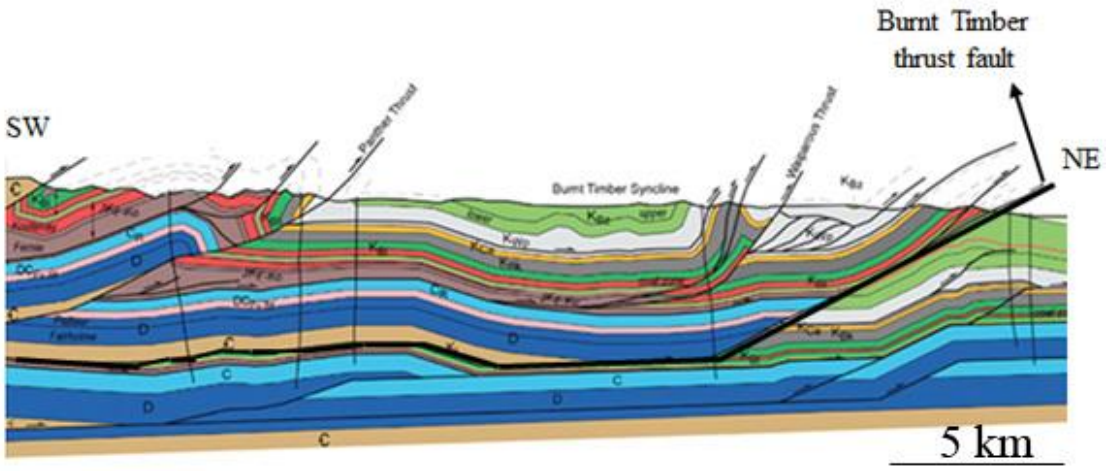

Figure 5.5. Lack of information about the footwall offset of strata located above the Burnt Timber thrust fault.

Besides incomplete information about the offset along faults, Pana et al.'s (2013) cross section has problematic areas that cannot be properly restored using the simple move-on-fault or simple shear deformation mechanisms of Move. For conventional area-based balancing techniques of cross-sections, the cross-sectional area of beds must be the same in both deformed and restored cross-sections (Dalhstrom, 1969). For 3D restoration in Move, line length of layers must be preserved during deformation. Pana et al.'s (2013) cross section includes areas that do not obey this area/line length balance constrictions. For example, the duplex in the Wapiabi Formation highlighted in Figure 5.4 is roof trust by slip along the Waiparous Thrust is missing south of the thrust. The shape of the duplex cannot be restored by retrodeforming the slip along the Waiparous Thrust. Also, the

footwall and hanging wall cutoffs in the duplex are cutting downsection relative to the tectonic transport direction as opposed to upsection.

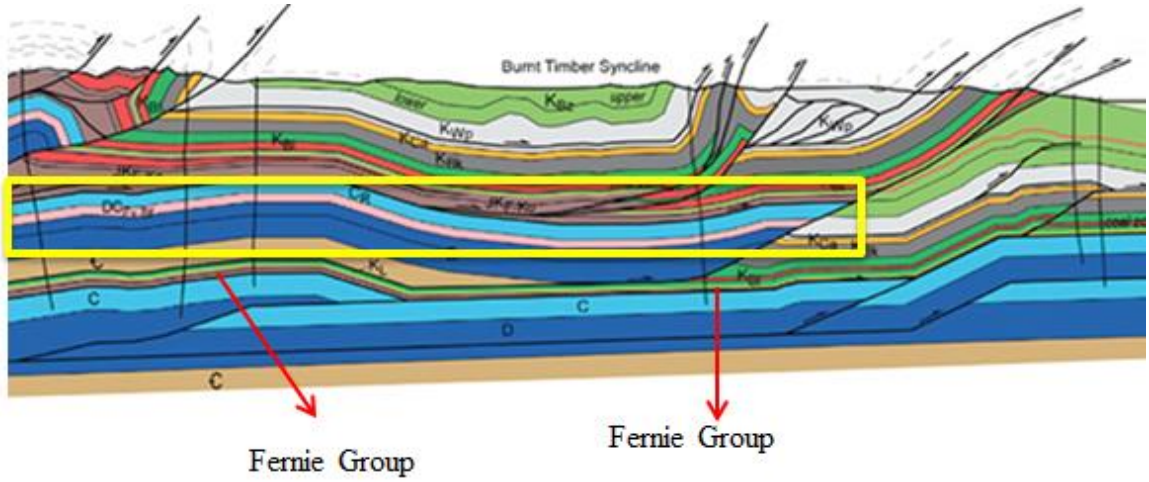

Figure 5.6 Simplifications made for cross-section restoration in the Pana et al. (2013) section: Arrows highlight thickness change in the Fernie Group (brown); yellow rectangle indicates Banff Formation which terminates against the Burnt Timber thrust fault. For restoration, both units are considered of uniform thickness along the section.

Additionally, the thickening of the Blackstone Formation (K_{bk}) in the core of the Red Deer River anticline (dark gray layer in Figure 5.6) cannot be modeled with the Move kinematic restoration tools without addition of internal small-scale structures such as small-scale thrust faults with an opposite transport direction or trishear (Figure 5.7). Although such complex faulting mechanisms can be modeled in 2D using Move, they cannot be replicated in 3D (see Appendix A Limitations). Therefore, alternative scenarios must be sought.

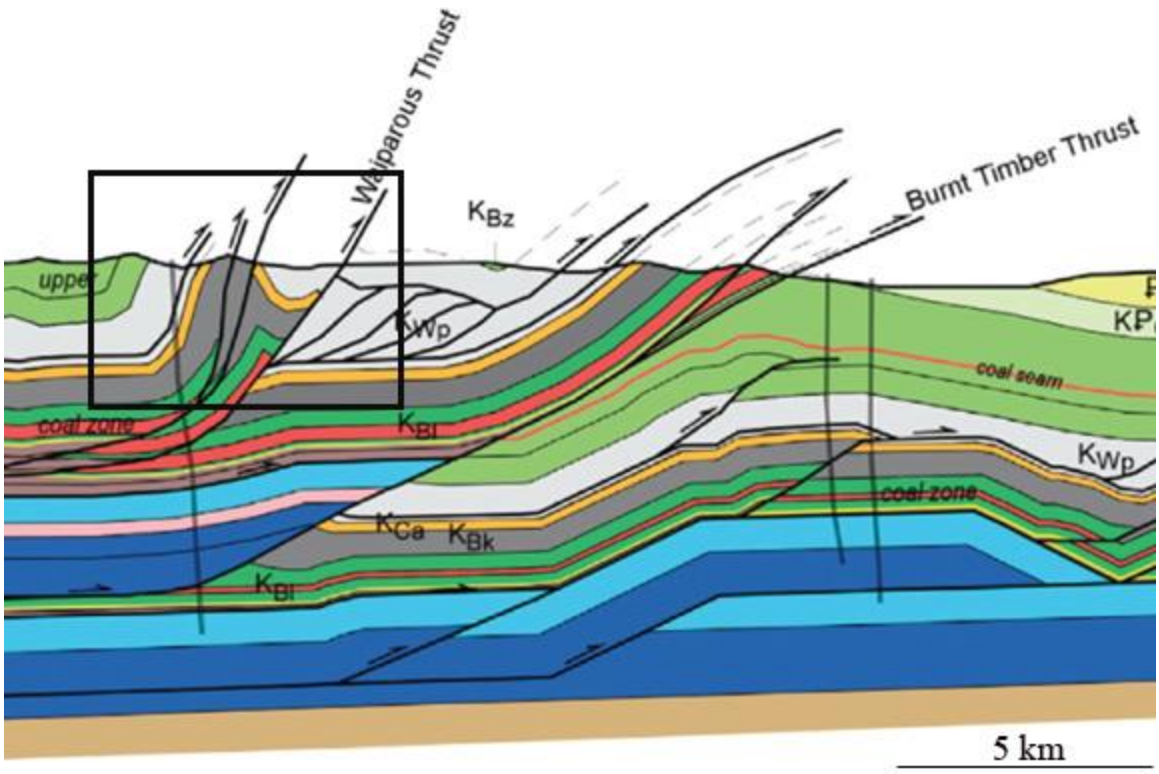

Figure 5.7 The geometry of the anticline enclosed by the black rectangle poses a problem for structural restoration.

Construction of a New, Simplified, and Balanced Cross-Section

Based on Ollerenshaw (1966)'s preliminary geologic map and accompanying cross-section, I constructed two new cross-sections, 3 km apart, through the anticlinal structure exposed in the Red Deer River area (Figure 5.8). These 2D cross-sections were used as the basis to create a 3D model of the Red Deer River anticline and surrounding structures.

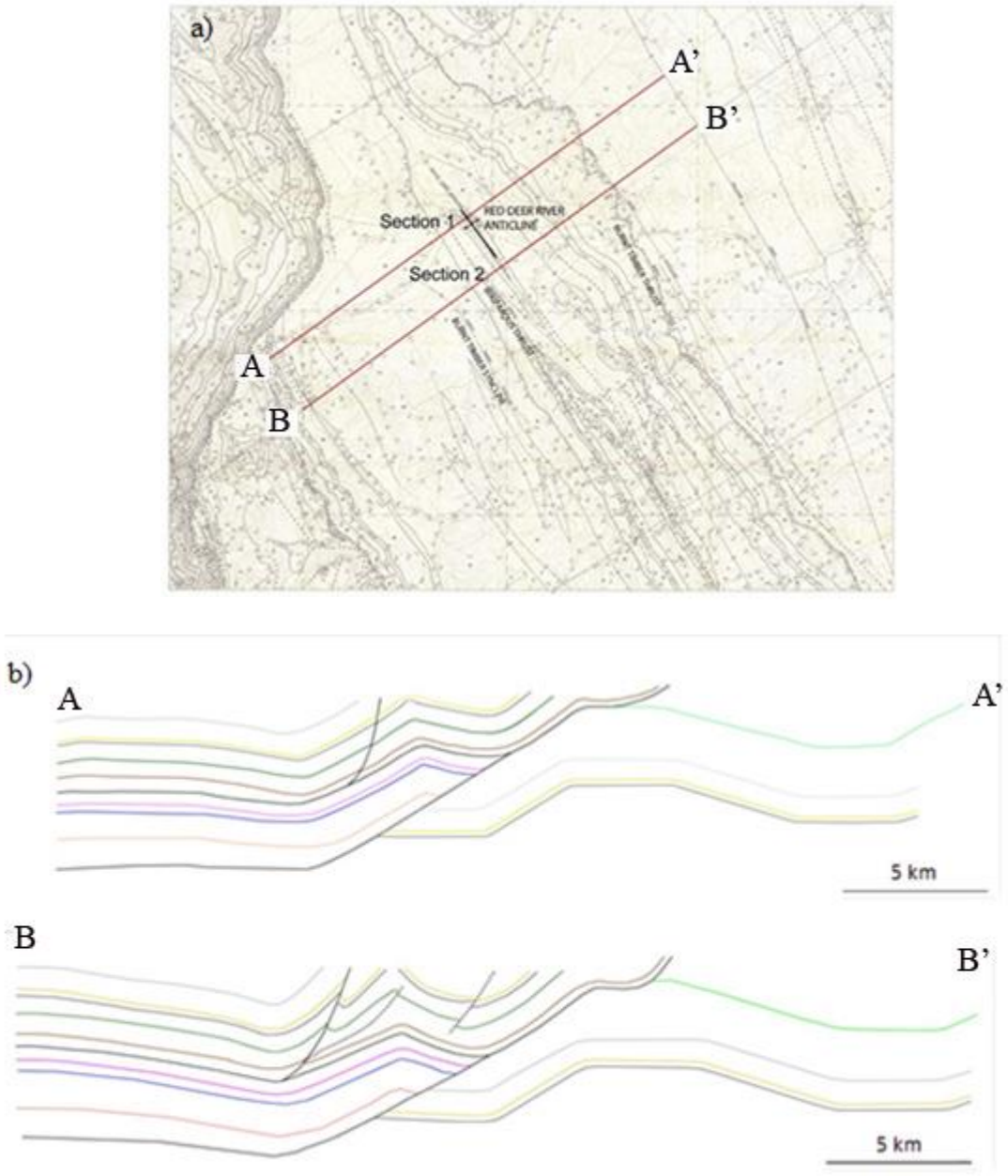

Figure 5.8. a: Geological map by Ollerenshaw (1966) showing the location of the cross-sections. b:Constructed new cross-sections for the near-surface structure. See Figure 5.1 for color key for layers. No vertical exaggeration.

Surface geologic and structural data as well as stratigraphic information from Ollerenshaw's (1996) map were used to construct the geometry of shallow structures to approximately 1500 m depth along the two cross-sections shown in Figure 5.8. The geometry of the structures at depths between approximately 1500 and 5000 m were constructed by extrapolating the seismically controlled structural interpretation from Pana et al.'s (2013) cross section. Figure 5.9 shows the constructed cross-sections combining information from Ollerenshaw (1966) and Pana et al. (2013).

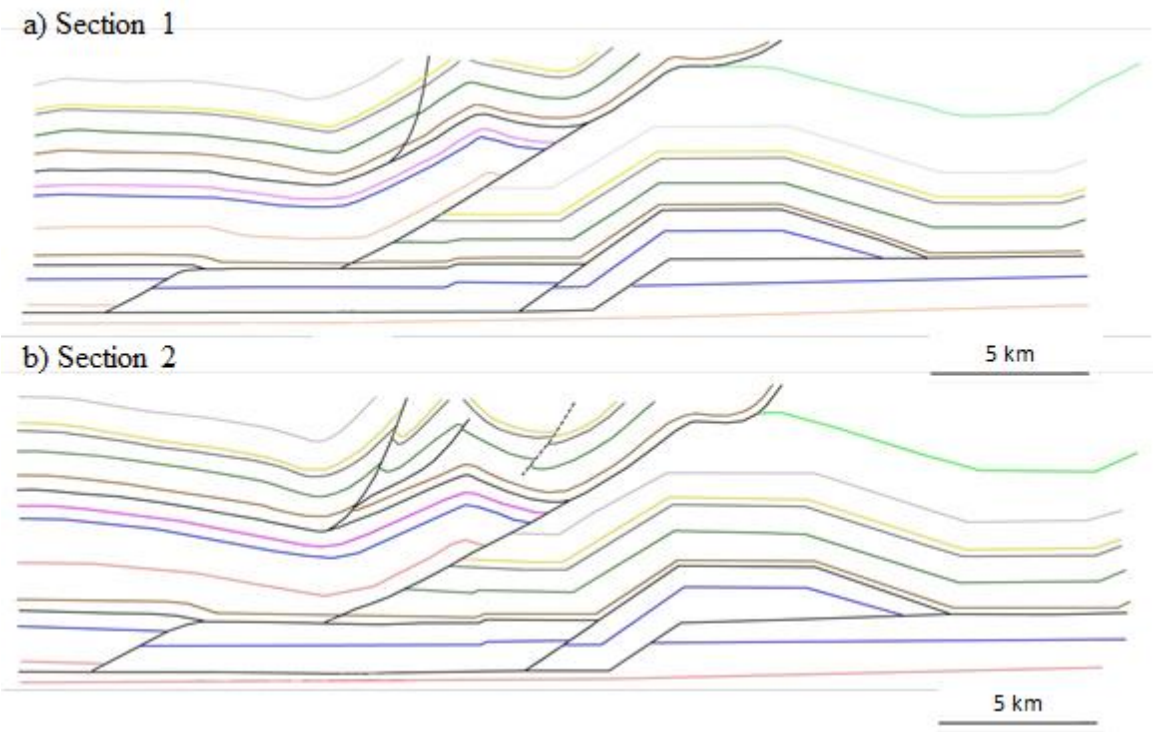

Figure 5.9. Cross-sections using map data from Ollerenshaw (1966) for the shallow structure and Pana et al., (2013) for the deeper structure. See Figure 5.8a for the location of the cross-sections. See Figure 5.1 for color key for layers.

Balanced cross-sections must obey fundamental geometric principles where either the surface area of beds or the line length of contacts is maintained (Dalhstrom, 1969). Because bed areas and layer thicknesses are not changed by deformation, line lengths of bed boundaries must be consistent in both deformed and restored sections and respective hanging wall and footwall cutoffs have to fit (Woodward et al., 1989). The final model geometry must be restored to its original horizontal bedding geometry. The cross-sections constructed in this study were verified to be balanced and geologically sound in an iterative effort through reconstruction and line adjustment. As with any extrapolation of surface structure to depth and with interpretation of seismic information, it is understood the cross-sections are interpretations that may not represent unique solutions. For example, the location of footwalls cutoffs beneath the layer-parallel detachment fault shown in Figure 5.10 can be interpreted in several ways.

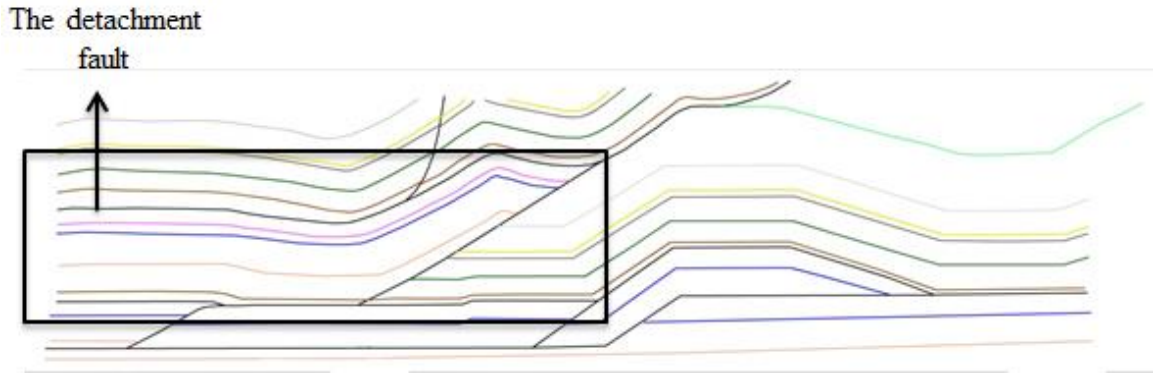

Figure 5.10. The hanging-wall strata beneath the layer-parallel detachment faults are highlighted by the box. Note that the section displays inadequate information about the location footwall cutoffs of the strata. See Figure 5.1 for color key for layers.

To interpret the deeper structure depicted in Figure 5.10, I applied Boyer and Elliott's (1982) geometric model for duplex structures beneath a layer-parallel detachment fault (Figure 5.11). This solution shows each individual imbricate horse with elongate folds, subsidiary faults that are parallel to bedding, and strata above the roof thrust displaying folded bedding (Boyer and Elliott, 1982). This configuration is consistent with the regional geology in the Red Deer River area.

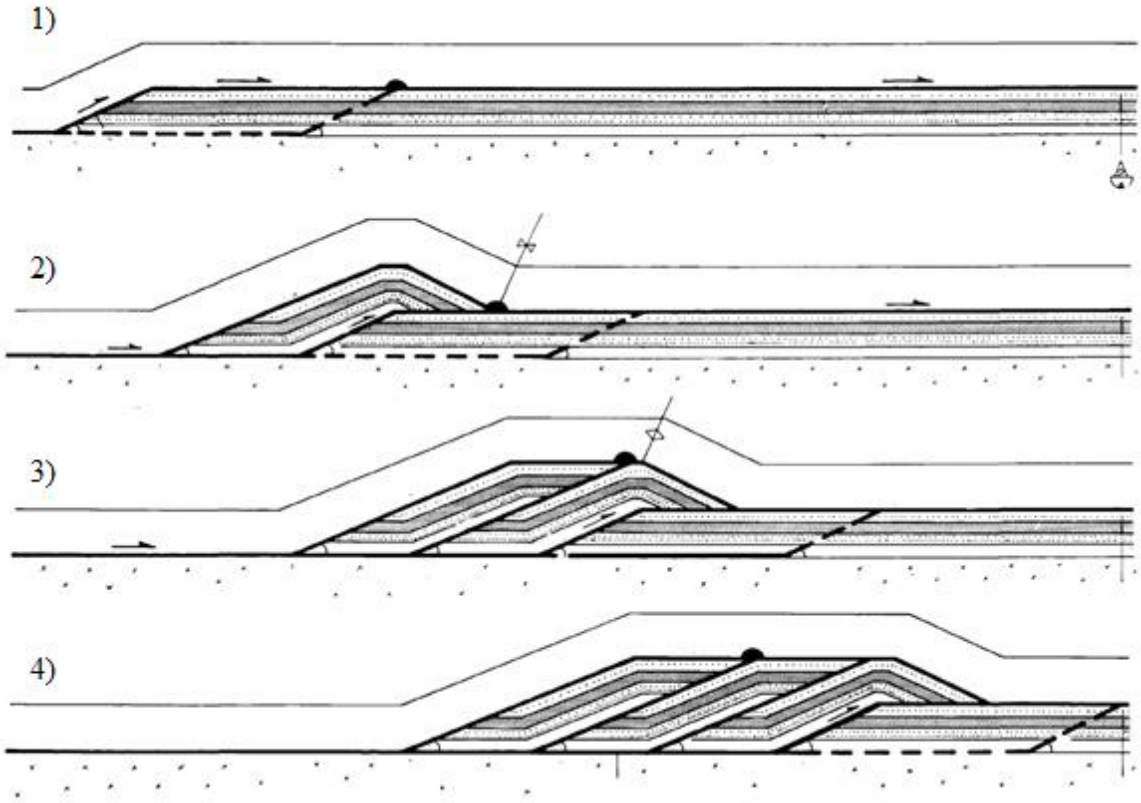

Figure 5.11. Geometric model for duplex structures showing the initial and deformed stages. (From Boyer and Elliot (1982).

Boyer and Elliot's (1982) duplex model was integrated into the previously constructed section shown in Figure 5.8 (Figure 5.12). This modification was first implemented by hand to check if the section obeys fundamental geologic principles such as constant bed thickness and boundary line length. While modifying the cross-section with this new model, duplexes and subsidiary faults, duplex structures' dimensions and angles were drawn based on stratigraphic thickness of the formations beneath the layer-parallel detachment fault. Then, duplexes with similar shape and size were constructed maintaining a uniform mean bed length in the horses (Figure 5.12).

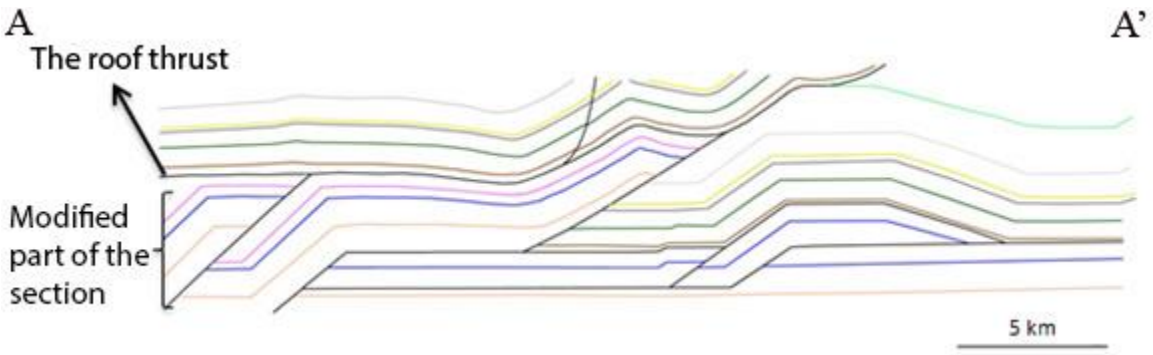

Figure 5.12 The modified and simplified cross-section following Boyer and Elliott's (1982) model.

The constructed sections were retrodeformed using Move 2D (see Appendix A) in order to prove that they are balanced. The resulting balanced sections were further simplified in preparation for 3D modeling and strain calculations. For example, multiple duplexes were simplified into a single duplex in sections 1 and 2 (Figure 5.13 and 4.14).

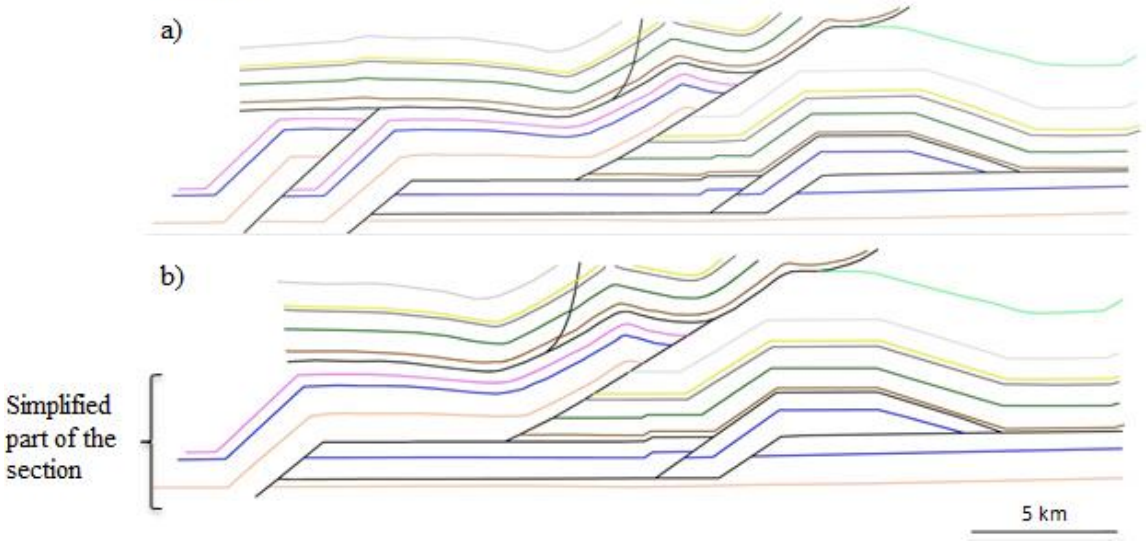

Figure 5.13 a; Complex duplex structures before simplification. b: final geometry of the modified and simplified sections. See Figure 5.1 for color key for layers.

The final sections show a noticeable difference in the geometry of deep structures compared to the initially constructed sections (Figure 5.14). Following Pana et al (2013), the thickness of the Banff Formation was maintained constant on the left hand side of both cross sections, but the Banff Formation is absent on the right as it terminates against the Burnt Timber thrust. The distance of continuation of the Banff Formation east of the Burnt Timber thrust is unknown. Termination against the Burnt Timber thrust is thus a simplification. The bed thickness between the top of the Rundle Group and the bottom of the Devonian Fairholme Group was maintained constant on both sides of the Burnt Timber thrust. The thickness of the Fernie Group decreases slightly towards the northeast.

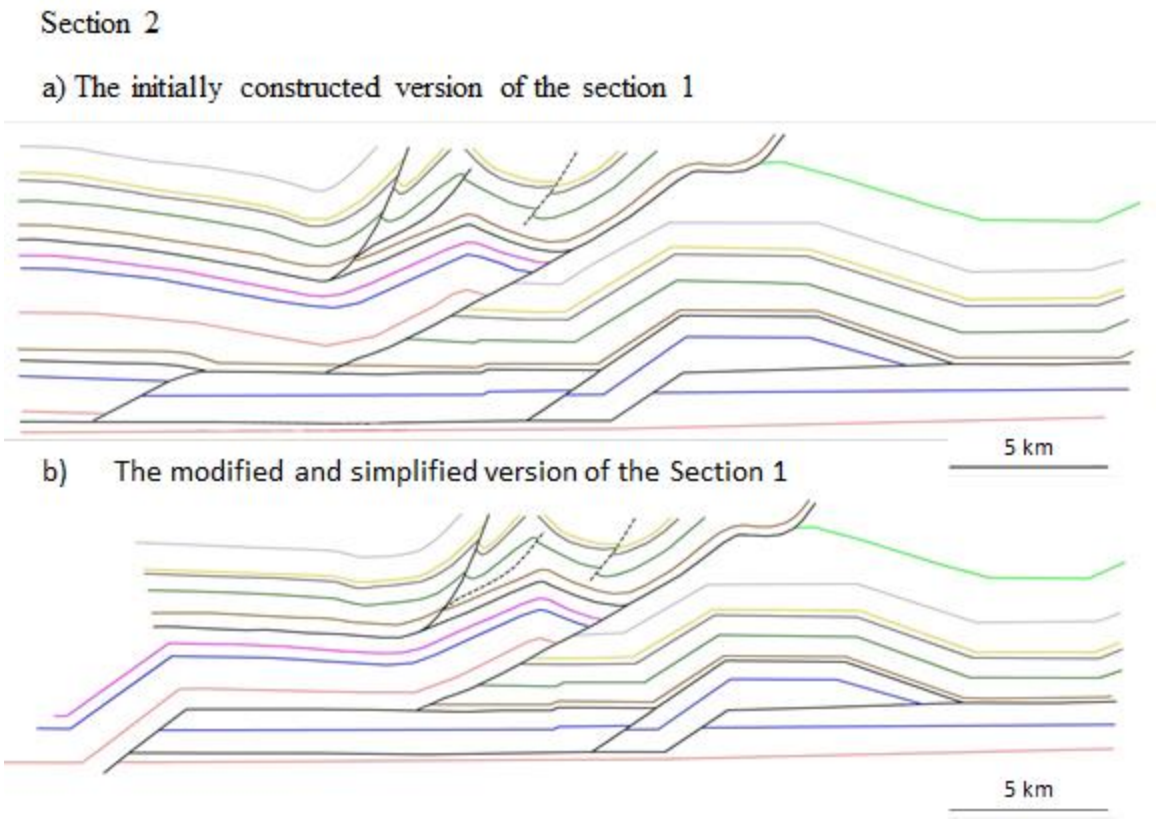

Figure 5.14. A comparasion between the final geometry of the section1. a: initially constructed section 1. b: Section 1 after modification and simplification. The modified and simplified section in b. was used in the subsequent structural restorations.

Figure 5.15 shows that the final balanced version of the reconstructed section has notable differences with the published cross-section.

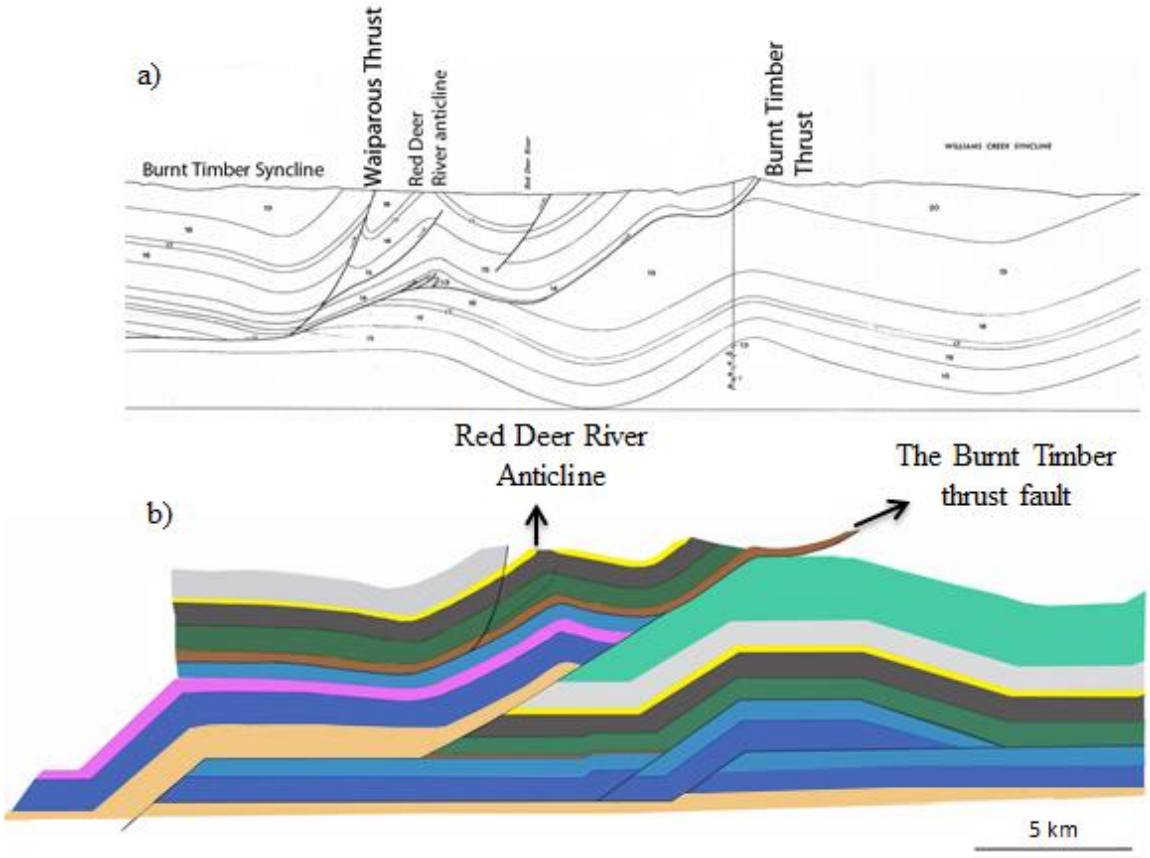

Figure 5.15 a: The initial section provided by Ollerenshaw (1966) b: the final version of the section used in restoration and forward modeling. See Figure 5.1 for color key for layers.

RESTORATION

The first step toward the structural restoration of a section is to establish the sequence of thrusting. Figure 5.16 shows a model by Mitra (1990) that indicates imbricate structures shortened and thickened in a sequence similar to structures in the study area. Based on the geometry of the structural framework, the hinterland-dipping imbricate thrust faults become younger toward the foreland.

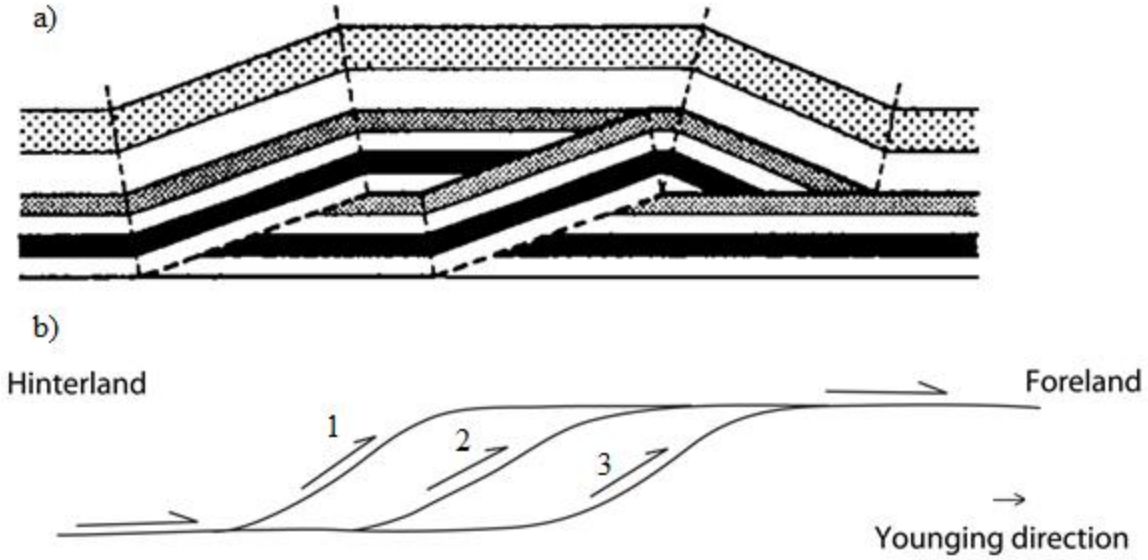

Figure 5.16 a. Duplex model by Mitra (1986) b: Simplified version of of the duplex of duplex in a. illustrating the hinterland dipping faults and the younging direction of thrusts toward foreland.

The structural interpretation of the constructed cross-sections is consistent with progressive translation of the deformation front toward the foreland. That is, thrust faults become progressively younger towards the foreland in the direction of tectonic transport from southwest to northeast (Figure 5.17). For the structural restoration of the new modified and simplified sections, all strata were restored to their initial geometry reversing this sequence of thrusting. The new cross-sections has five major faults, which are numbered in sequence of restoration, i.e. in descending (1 is the youngest) chronological order in Figure 5.17.

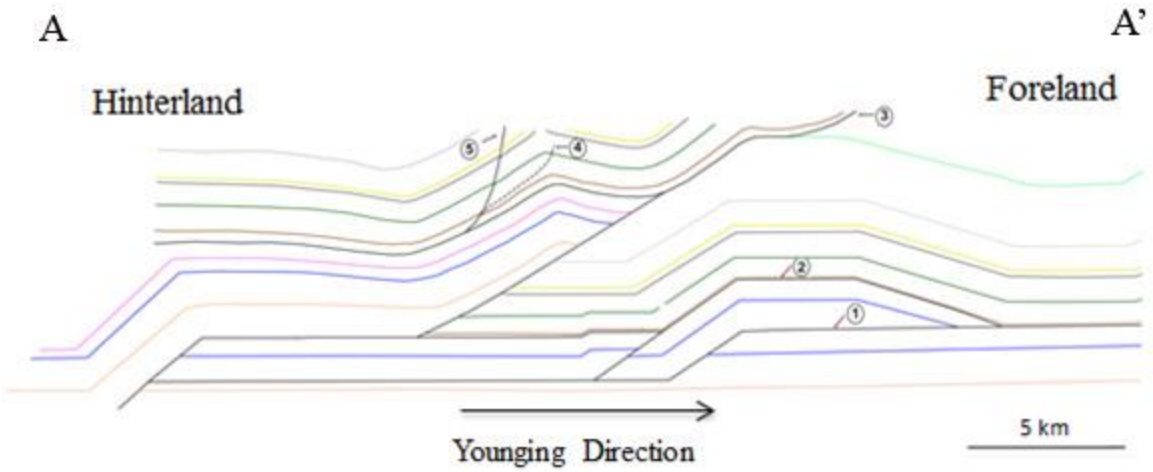

Figure 5.17 Chronological order of thrust faults. Faults are numbered in the sequence of restoration, i.e. in reverse sequence of formation.

The first stage of the restoration consists of removing the major displacement along the fault-bend-fold (fault 1) and matching the hanging wall cutoffs and footwall cutoffs (Figure 5. 18).

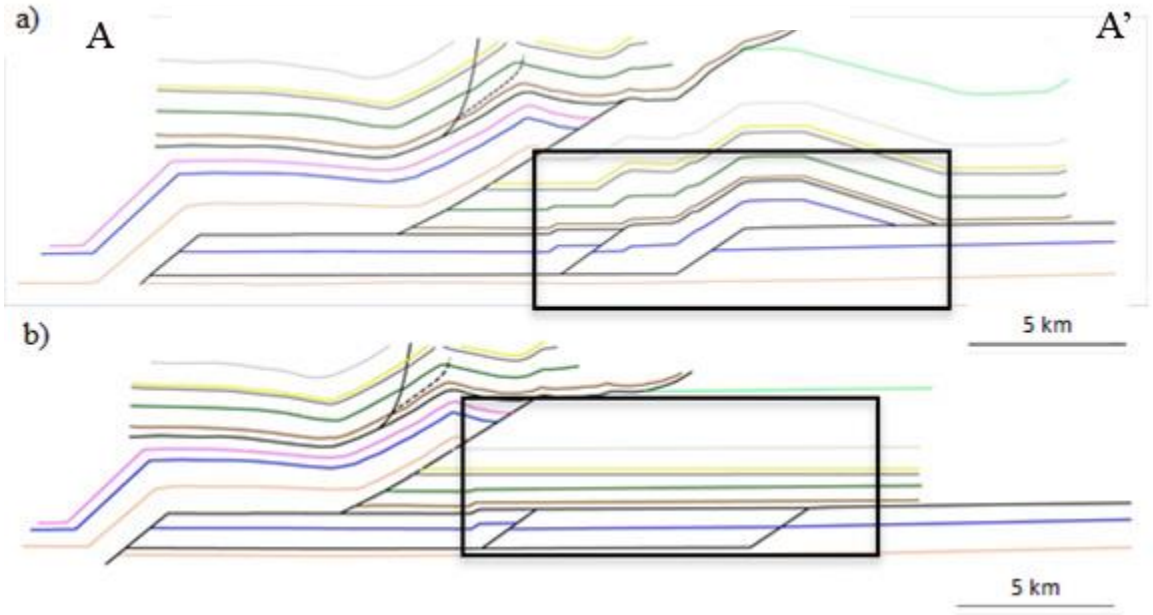

Figure 5.18 Restoration of the fault-bend-fold structure. The rectangle highlights the restored part of the section.

The second stage of the restoration involves a small amount of displacement along the second ramp that turns into a bedding-parallel basal detachment to the NE (fault 2) (Figure 5.19).

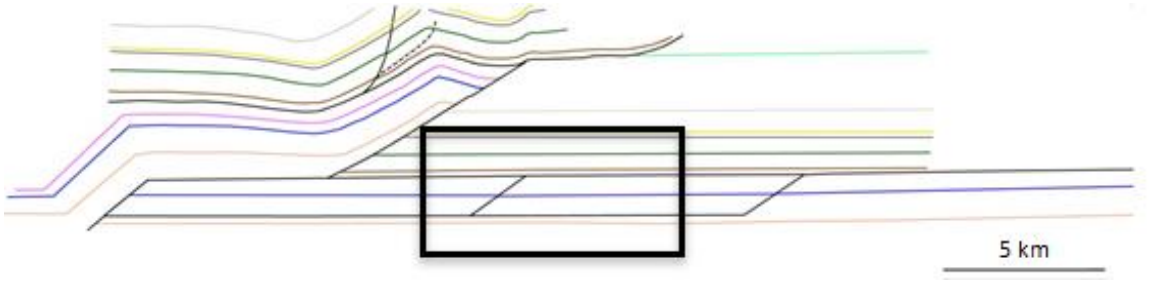

Figure 5.19. Restoration along the second ramp and basal detachment fault.

The third stage of the restoration consists of reversing slip along the Burnt Timber thrust fault (fault 3). This fault has a large amount of displacement and it has been subdivided into two individual increments for ease of visualization (Figure 5.20).

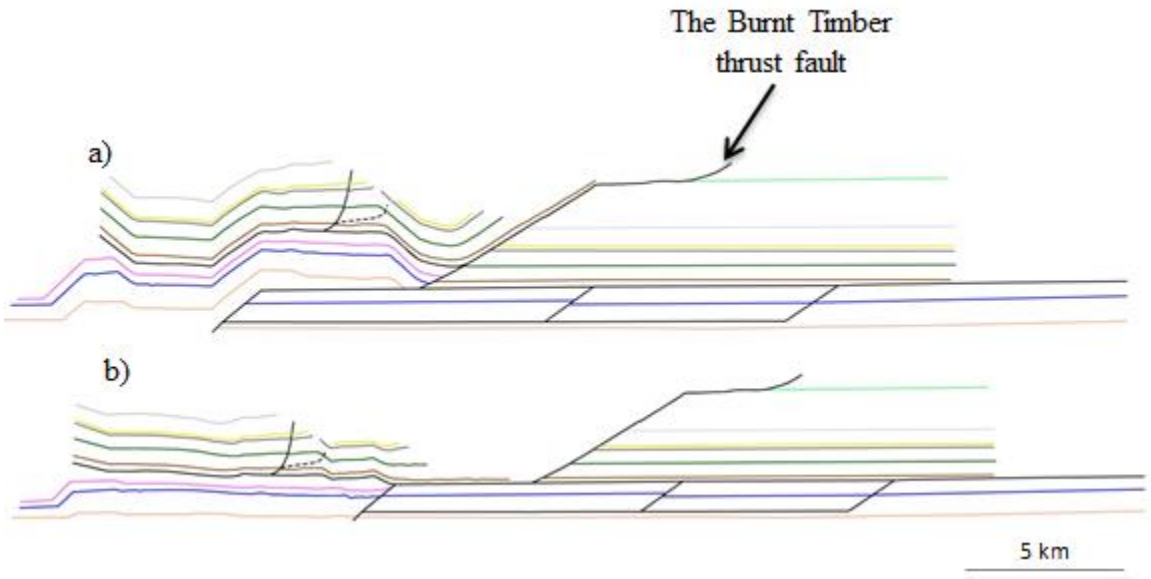

Figure 5. 20. Restoration of displacement along the Burnt Timber thrust fault.

Reverse slip along the Burnt Timber Creek fault in Move left strata with non-planar imperfections (wrinkles) (Figure 5.20b). Thus, after displacement was restored, the strata needed to be smoothed out using Move's unfold tool (see Appendix A Methods). The final two restoration steps involved reversing slip along two minor faults in the southwestern part of the cross section. Fault 4 is a blind fault that affects development of the Red Deer River anticline. This fault was restored by using the offsets of strata that were cut by the fault. When using the "move-on-fault" deformation mechanism in Move,

restoration of strata that are not cut by blind faults is done by passively restoring these strata following the displacement established by the cut strata. Next, the relatively small amount of displacement along fault 5 was restored as the last step of structural restoration. With the restoration completed, all strata have been brought to their initial undeformed positions. The eroded strata in the hinge of the Red Deer River anticline and above the Burnt Timber thrust have been reconstructed and are shown with dotted lines in Figure 5.21.

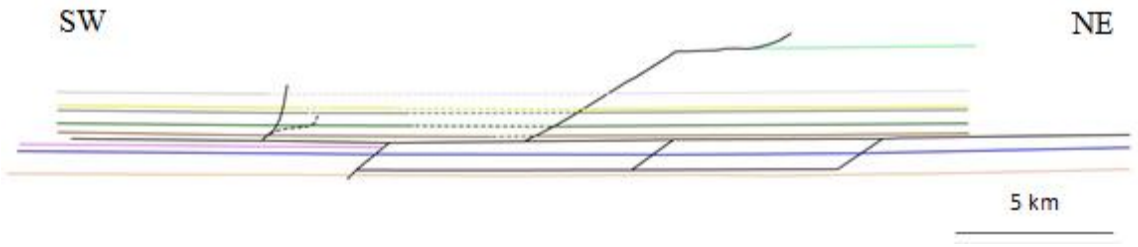

Figure 5.21 The last stage of restoration shows the initial geometry of strata. Dashed lines indicate reconstructed eroded strata.

Differences between sections 1 and 2 are minimal, with the addition in section 2 of an additional fault (Figure 5.22), therefore similar steps were followed for the restoration of both sections.

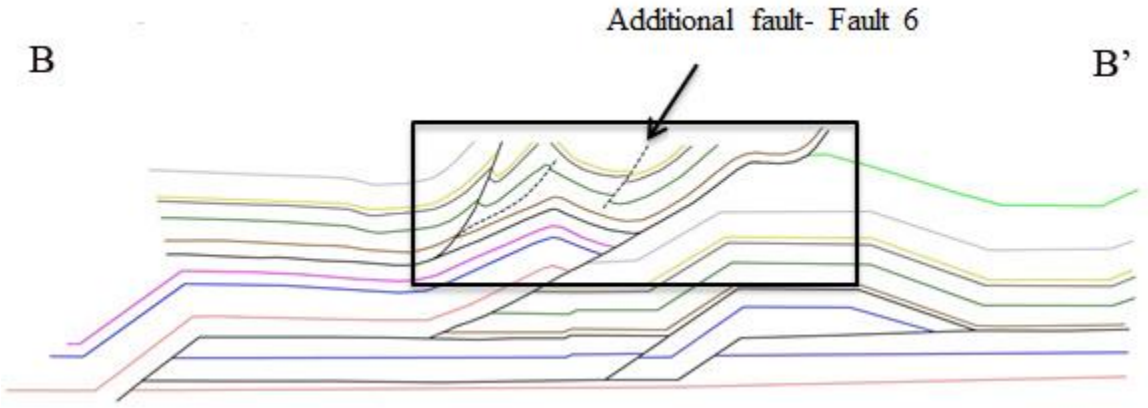

Figure 5.22 B-B' used in structural restoration. The rectangular highlights the slight difference in the shallow structures than section 1.

The displacement along the additional fault (fault 6) is relatively small and this fault only cuts through shallow layers (Figure 5.23 d). The complete restoration of B-B' is shown in Figure 5.23.

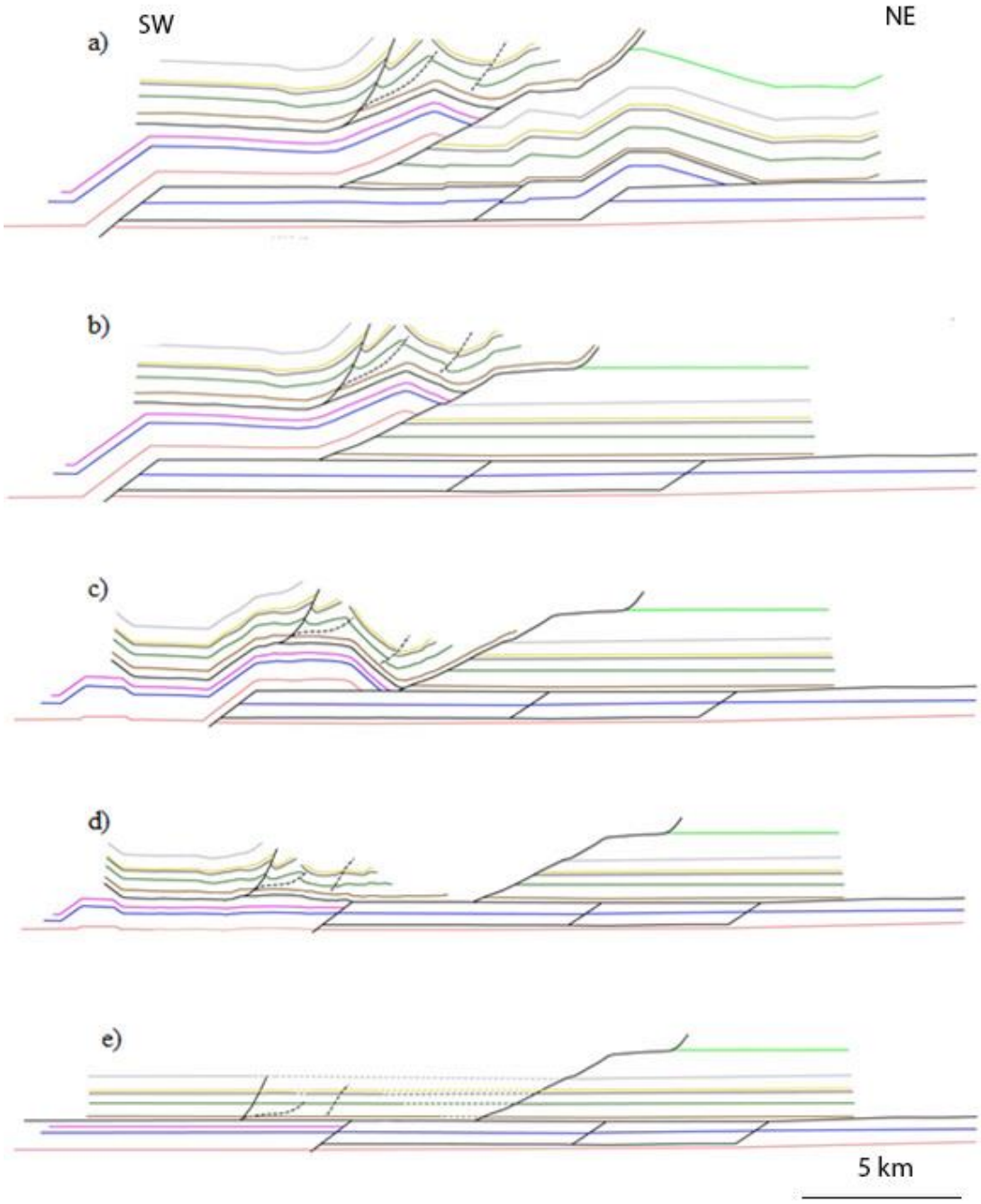

Figure 5.23 Structural restoration of the B-B'.

FORWARD MODELING VALIDATION

Forward models were constructed by reversing the restoration order of thrust faults in order to validate the kinematic viability of the constructed models. The simple shear algorithm of Move is best suited for extensional tectonic regimes, therefore I used the fault-parallel flow algorithm instead which is best for modeling the deformation style and hanging wall movement along faults in fold-and-thrust belt regimes (Move Tutorial 2013).

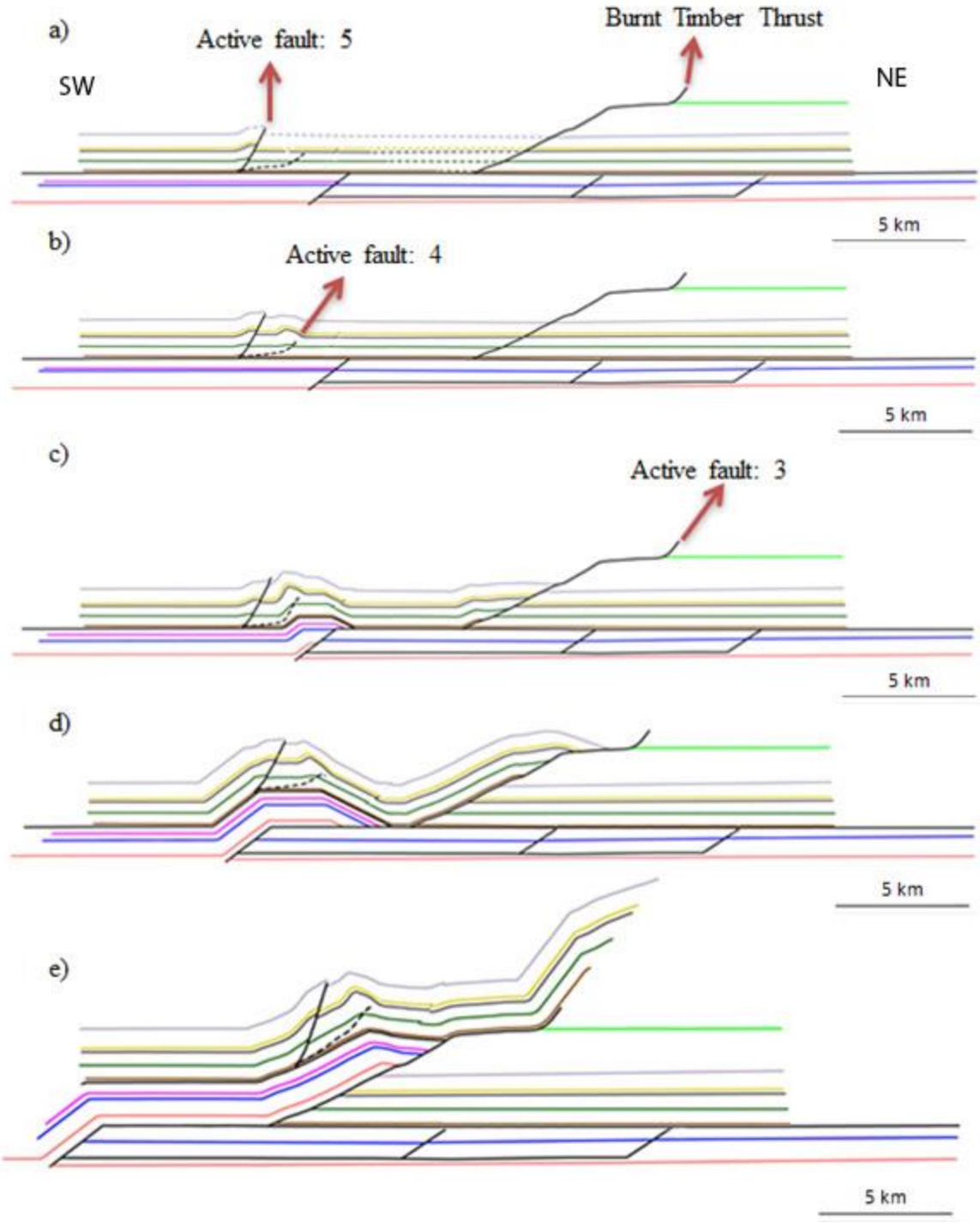

Figure 5.24. 2D forward modeling of the A-A'. Red circle indicate the eroded strata

Forward modeling illustrates that the slip along the Burnt Timber thrust accommodates a significant proportion of displacement through horizontal shortening (Figure 5.24c-e). Due to the ramp geometry of the Burnt Timber thrust fault –as modeled following Ollerenshaw's (1996) cross section- the strata highlighted by the red circle follow the fault geometry generating an apparent void underneath the fault (Figure 5.24 e-h). This fault most likely becomes parallel to the strata in the NE part of the section. However, because these strata are now eroded and do not affect development of the Red Deer River anticline, their progressive shape was not modeled.

CONSTRUCTION OF A 3D MODEL

As a prerequisite for calculating the strain distribution associated with the formation of the fault and fold structures in Move3D, I created a 3D model of the Red Deer River anticline area. The 3D model was constructed by placing the two 2D cross sections in their geologic context (Figure 5.25) and by creating surfaces between the same horizons and faults in these two parallel sections (see Appendix A for details) (Figure 5.26).

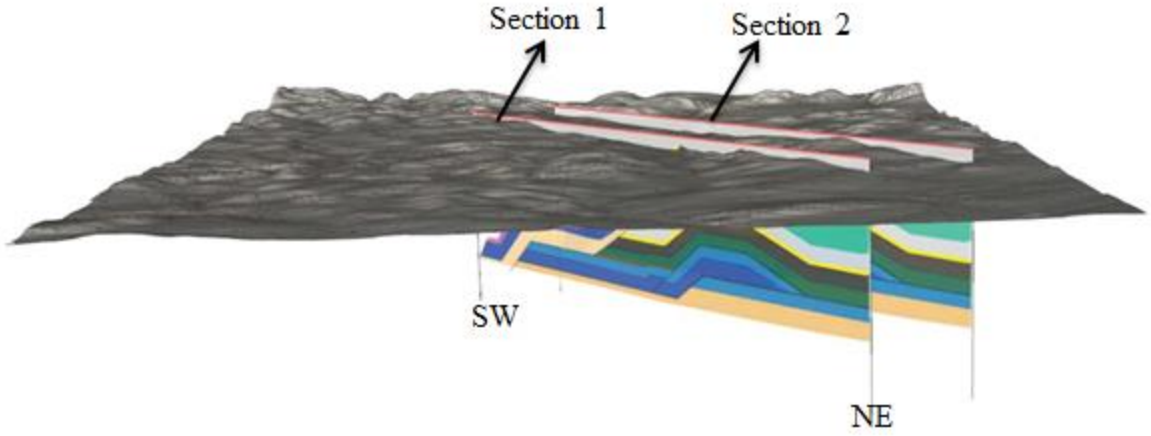

Figure 5.25 Generation of a 3D structural model by arranging the two 2D sections using a digital elevation model (DEM).

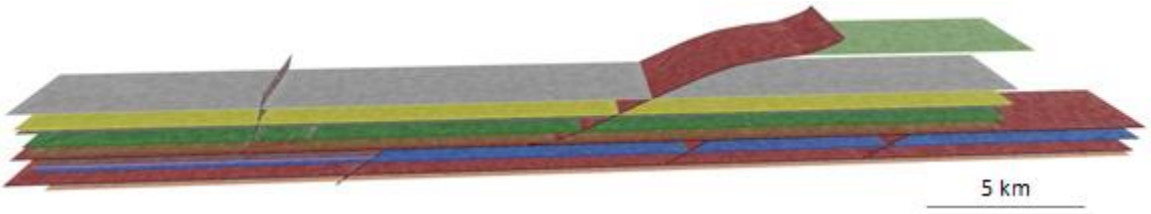

Figure 5.26 The 3D restored models, constructed between two 2D cross-sections serves as a basis for forward modeling. The top of the Cardium Formation is labeled by the yellow surface, and faults are labeled by the red surfaces.

3D FORWARD MODELING

The ultimate goal of constructing balanced forward structural models is to examine the evolution of strain and associated fracturing through time in the Red Deer River anticline from its original horizontal bedding to its present-day geometry. The evolution of the Red Deer River anticline was modeled using Move3D in progressive stages of faulting (Figure 5.27), as described in the forward modeling section of the 2D cross section, and

strain was recorded for each deformational step (see next section). Because fault 6 is absent in A-A', this fault cannot be digitized in 3D. Thus, Fault 6 is not a part of the 3D forward models.

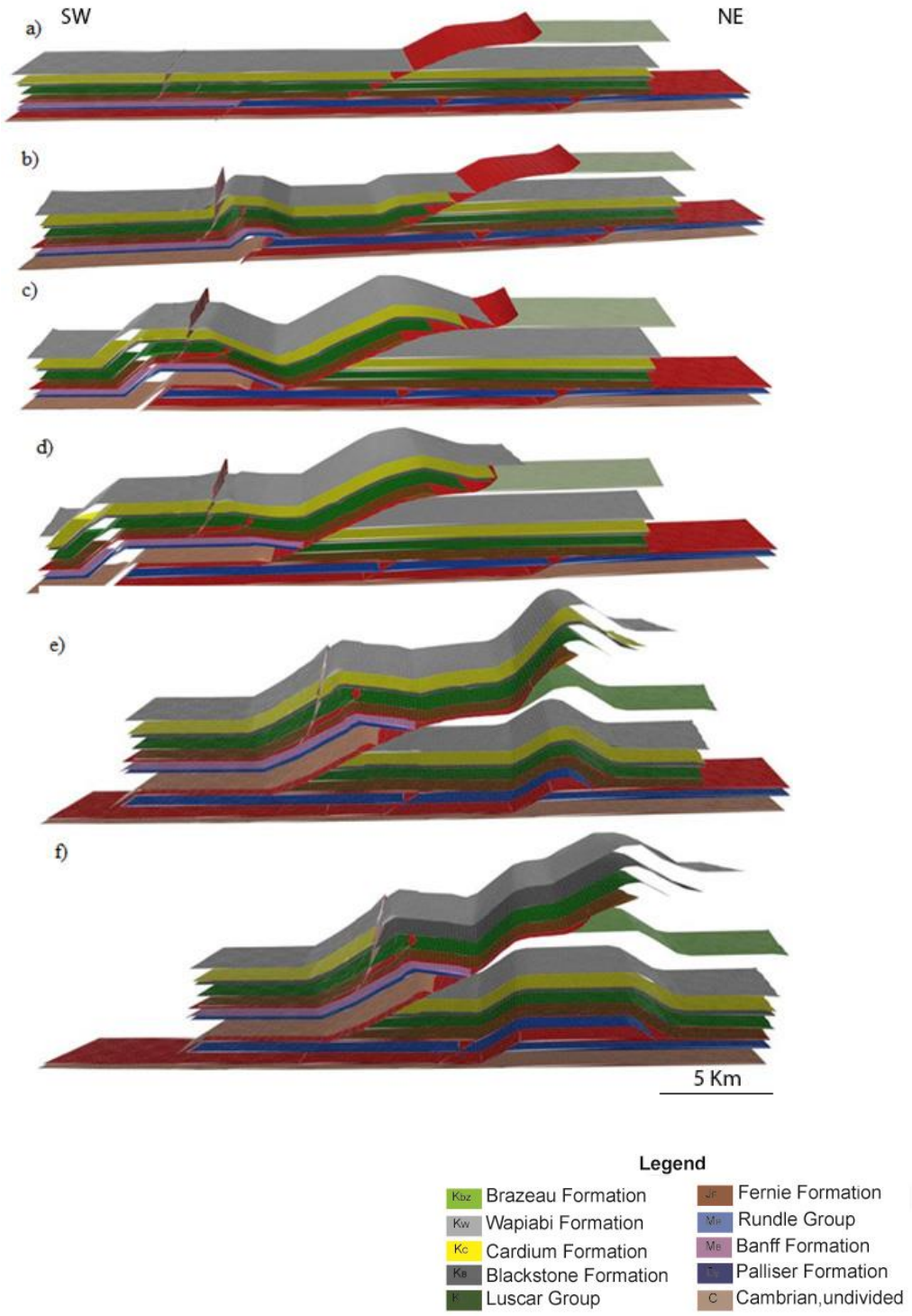

Figure 5.27 3D forward modeling of the Red Deer River section using Move3D.

STRAIN CALCULATIONS

To compare the strain accommodated by opening-mode fractures in the Red Deer River anticline with the kinematic models obtained in Move 3D, I calculated the magnitude of the maximum principal elongation e_1 and of the horizontal strain component e_{xx} for the top surface of the Cardium Formation during forward modeling of the Red Deer River area between movement on faults 5 and 3. The strain calculated in this tool results from displacements imposed on the layer of interest by the thrust and fold development in the underlying units. No strains are imposed on the lateral boundaries of the model. Move does currently not calculate the elongation parallel to bedding and thus orthogonal to fractures oriented perpendicular to bedding. Because bedding generally dips less than 45°, I will compare the measured fracture opening strain with the horizontal strain component e_{xx}. In the following section, magnitudes and directions of the incremental (non-cumulative) maximum principal elongation e_1 and of the horizontal strain in the transport direction e_{xx} are discussed first, followed by the cumulative (finite) strains e_1 and e_{xx}. All strains were calculated for the stages of forward models shown in the previous section. In the models shown below, blue indicates the areas of lower strain magnitude and red areas of higher strain magnitude. To increase visibility of small changes in strain, the color code for strain values changes throughout the figures, i.e., the same color does not necessarily correspond to the same strain value in all figures.

Distribution of Incremental Maximum Principal Strain e_1

Magnitudes of the maximum principal elongation e_1 were calculated for multiple stages of displacement along each fault relative to the previous stage of deformation, i.e. resetting the strain to zero after each deformation stage. Strain from earlier stages is thus not included in the strain of the following deformation stage.

During the first stage of forward displacement fault 5 is active. The Cardium Formation in the area of the Red Deer River anticline is unaffected (Figure 5. 28). During slip of fault 4, the highest strain is first concentrated in the eventual location of the Red Deer River anticline (Figure 5.29).

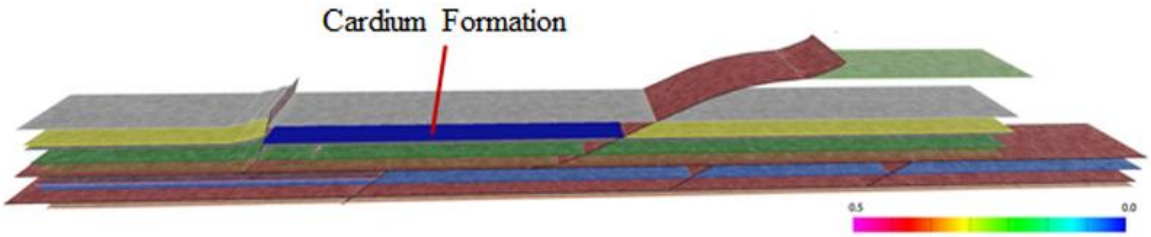

Figure 5.28 First step of deformation, with fault 5 as the active fault. The Cardium Formation between faults 5 and 3 experiences no strain during this stage of deformation.

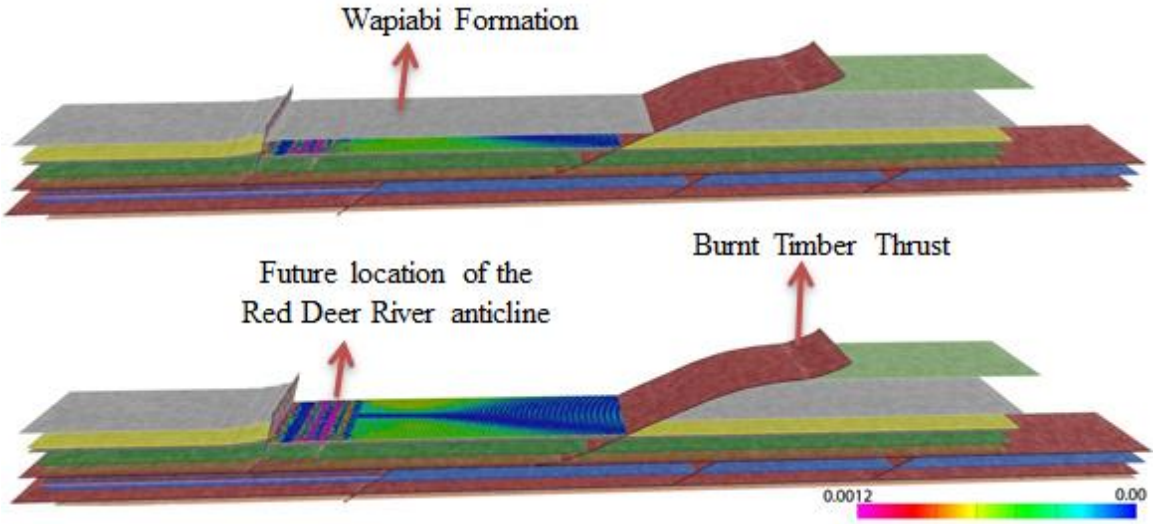

Figure 5.29 a: Strain in the top surface of the Cardium Formation during slip along fault 4. b: Same as a with the Wapiabi Formation toggled off to display the strain distribution in the Cardium Formation. The highest elongation strain is observed in the location of the future Red Deer River anticline. The along-strike irregularity in strain distribution is likely a numerical artifact.

Figure 5.30 shows strain calculations resulting from the progressive deformation associated with displacement along the Burnt Timber thrust (fault 3). Figure 5.30 shows that high elongation areas at this stage are located in the limbs of the evolving Red Deer River anticline.

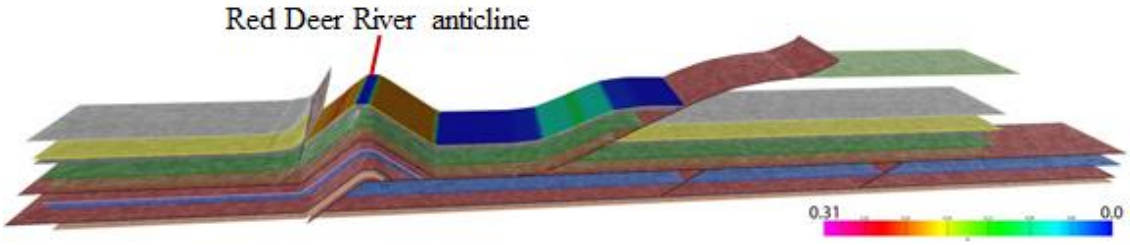

Figure 5.30 High and low strain areas as fold forming along the Burnt Timber thrust fault. The highest elongation strain is observed in the limbs of the Red Deer River anticline.

As displacement continues along the Burnt Timber thrust (Figure 5. 31), the location of high and low strain concentrations changes. During the early stage of deformation along the Burnt Timber thrust high elongation strain indicated by red subsequently decreases (blue colors) as the layer passes through the anticline and flattens in the forelimb.

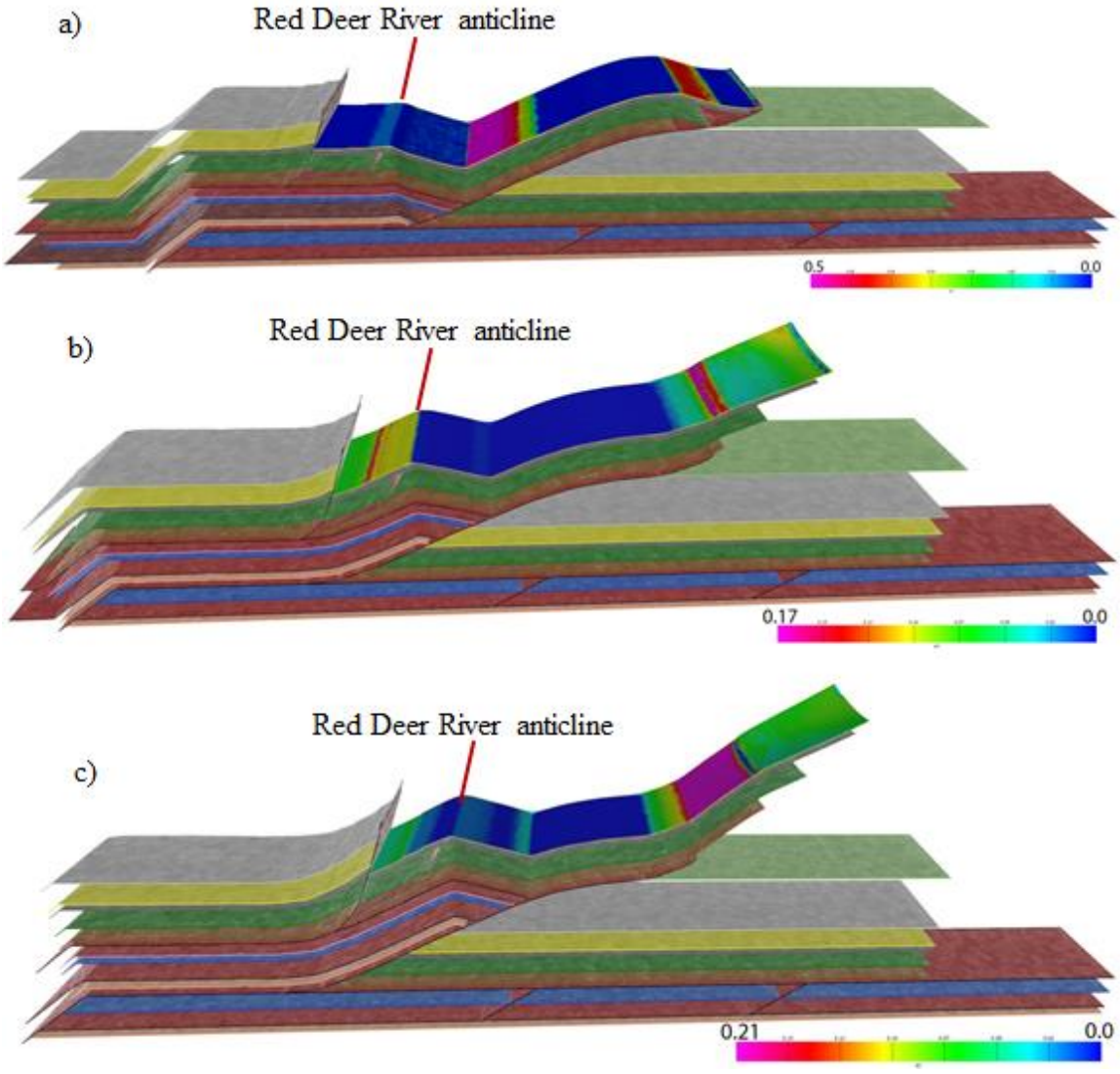

Figure 5.31. Evolution of the high elongation strain during deformation associated with continued displacement along the Burnt Timber thrust.

Displacement along fault 2 results in very low elongation in the area of the Red Deer River anticline (Figure 5.32).

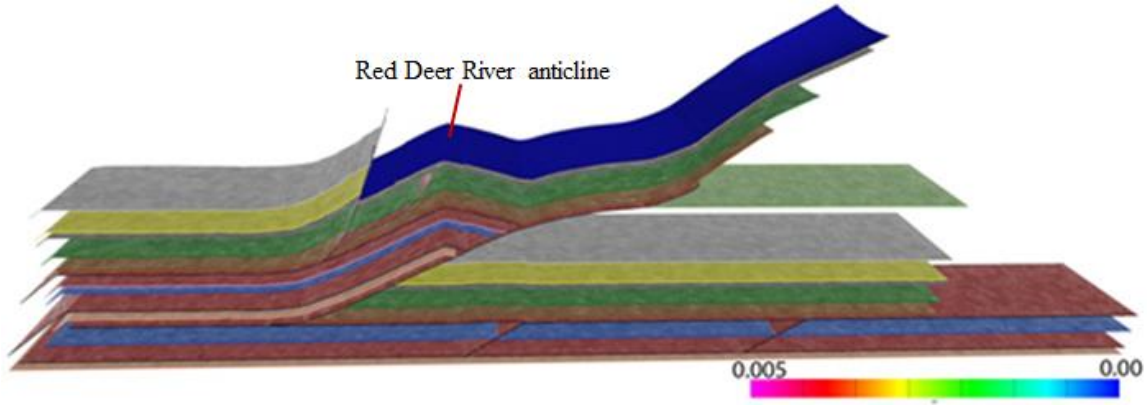

Figure 5.32. The evolution of the high elongation strain during deformation associated with displacement along the Burnt Timber thrust

Final displacement along fault 1 (Figure 5.33) affects the Cardium Formation to the east of the Red Deer River antlicline, in layers above the James River anticline, now largely eroded, while the Red Deer River anticline itself remains relatively undeformed. Figure 5.34 provides a summary of e1 for all forward modeling stages a through h.

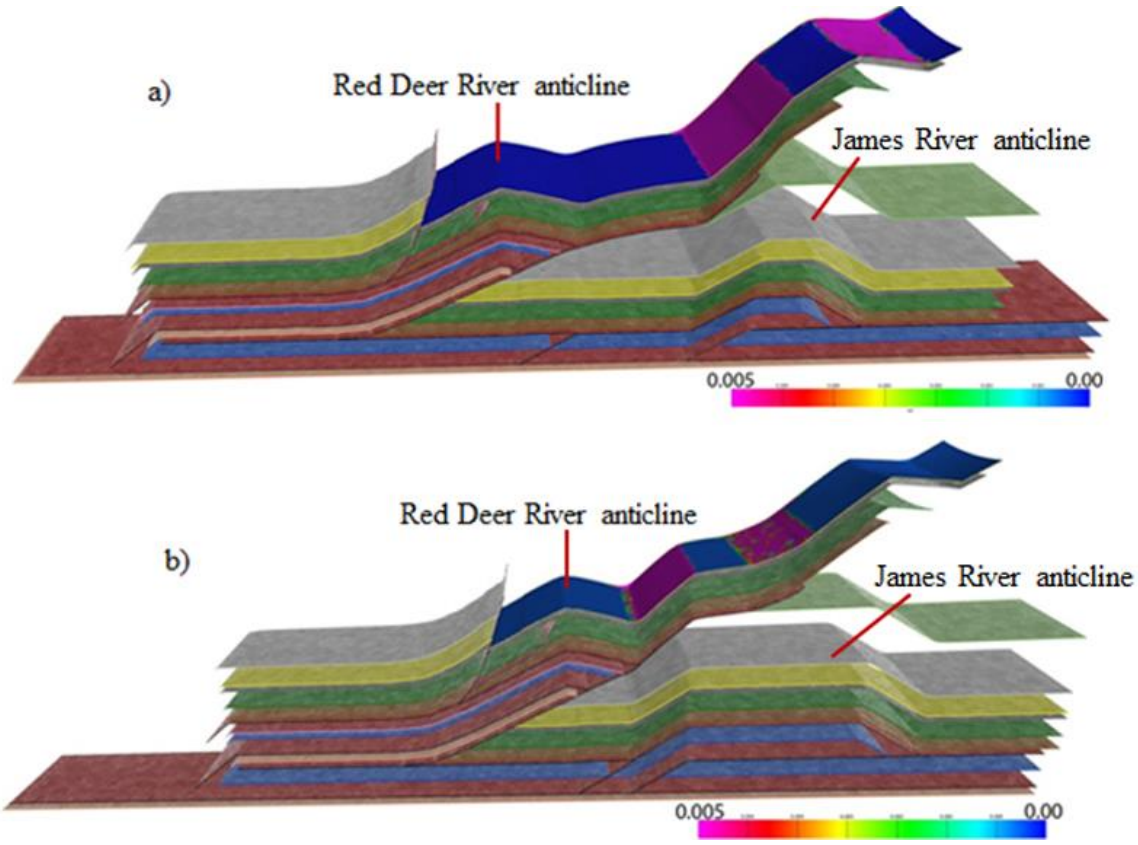

Figure 5.33 Strain distribution caused by deformation associated with the displacement along fault 1. The Cardium Formation in the Red Deer River anticline is largely unaffected.

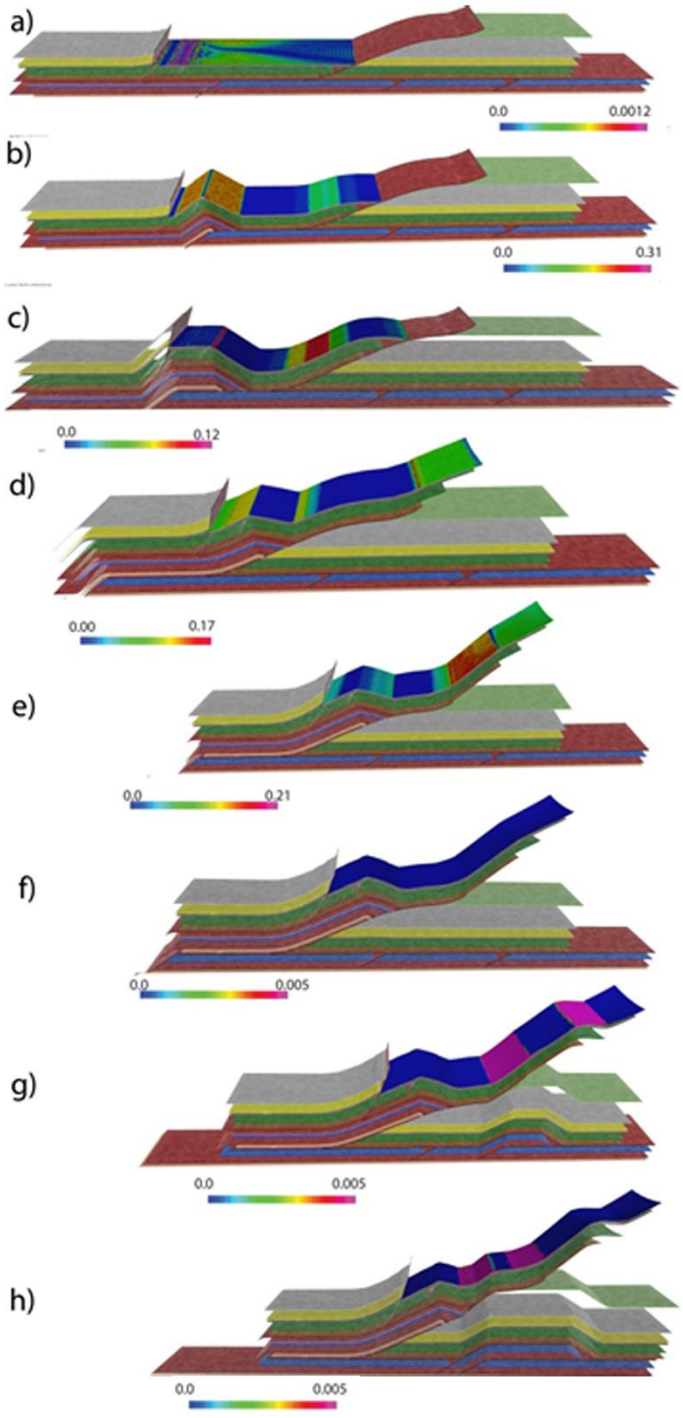

Figure 5.34. Evolution of the maximum principal elongation e_1 during forward modeling of the Red Deer River area.

The trajectories of the maximum principal elongation e_1 on the cross-section plane are plotted in Figure 5.35 for three selected stages of fold and thrust evolution (stages c, e, and h in Figure 3.54). The trajectories change in orientation systematically across the structure, displaying steeply plunging trajectories preferentially in the backlimbs, and near-bed-parallel orientations in the forelimbs.

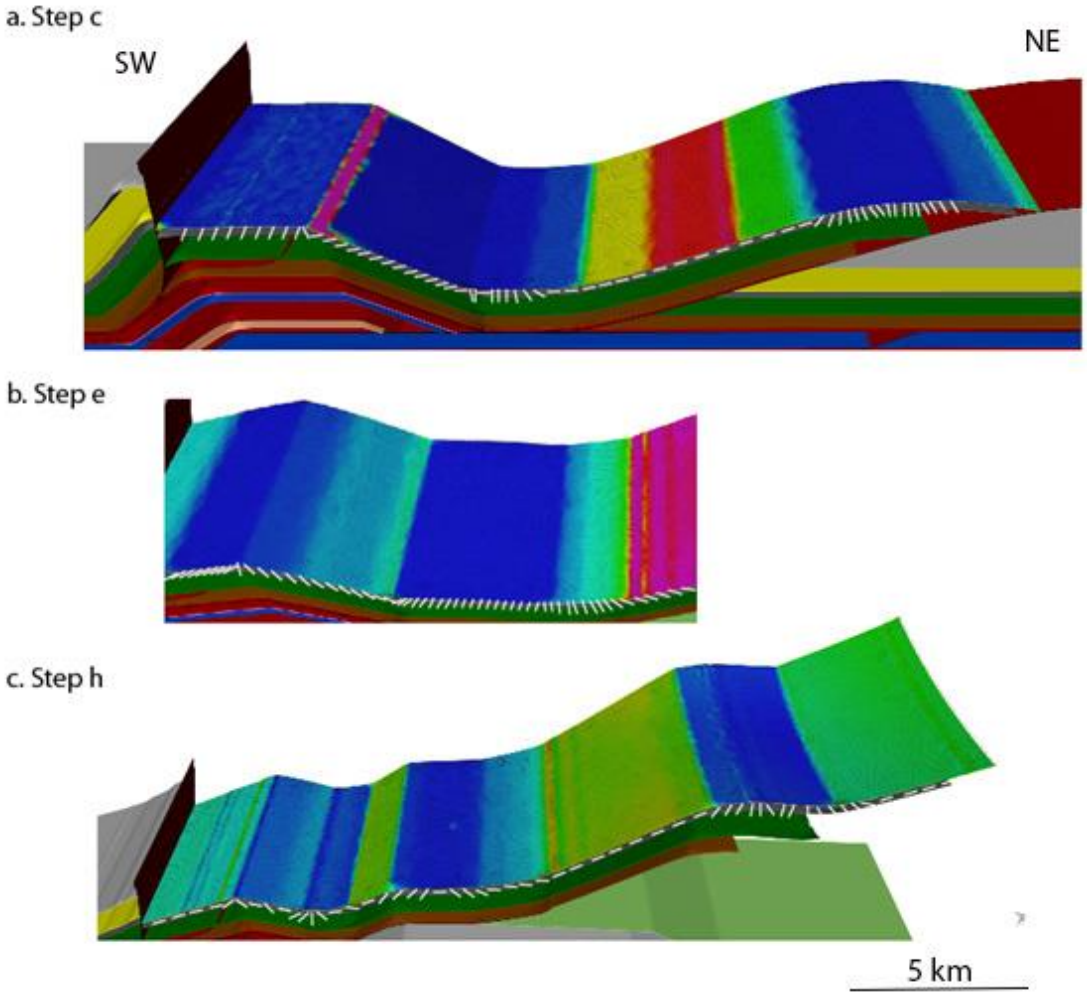

Figure 5.35. Close-up view of deformation stages c, e, and h in figure 5.34 showing the trajectories of the maximum extensional principal strain (e1) (white lines) in the cross section plane. This strain varies in orientation systematically across the folds. Colors indicate the magnitude of e_1 as in Figure 5.34.

Distribution of Incremental Maximum Horizontal Elongation e_{xx}

Figure 5.36 shows values of the incremental (non-cumulative) horizontal elongation e_{xx} during stages a through h in Figure 5.34. These models predict that most of the horizontal elongation experienced by the Cardium Formation in the Red Deer River anticline occured in the early stages of displacement along the Burnt Timber thrust (Fault 3) with a pronounced phase of extension in the backlimb of the Red Deer River anticline during stage d (Figure 5.34d).

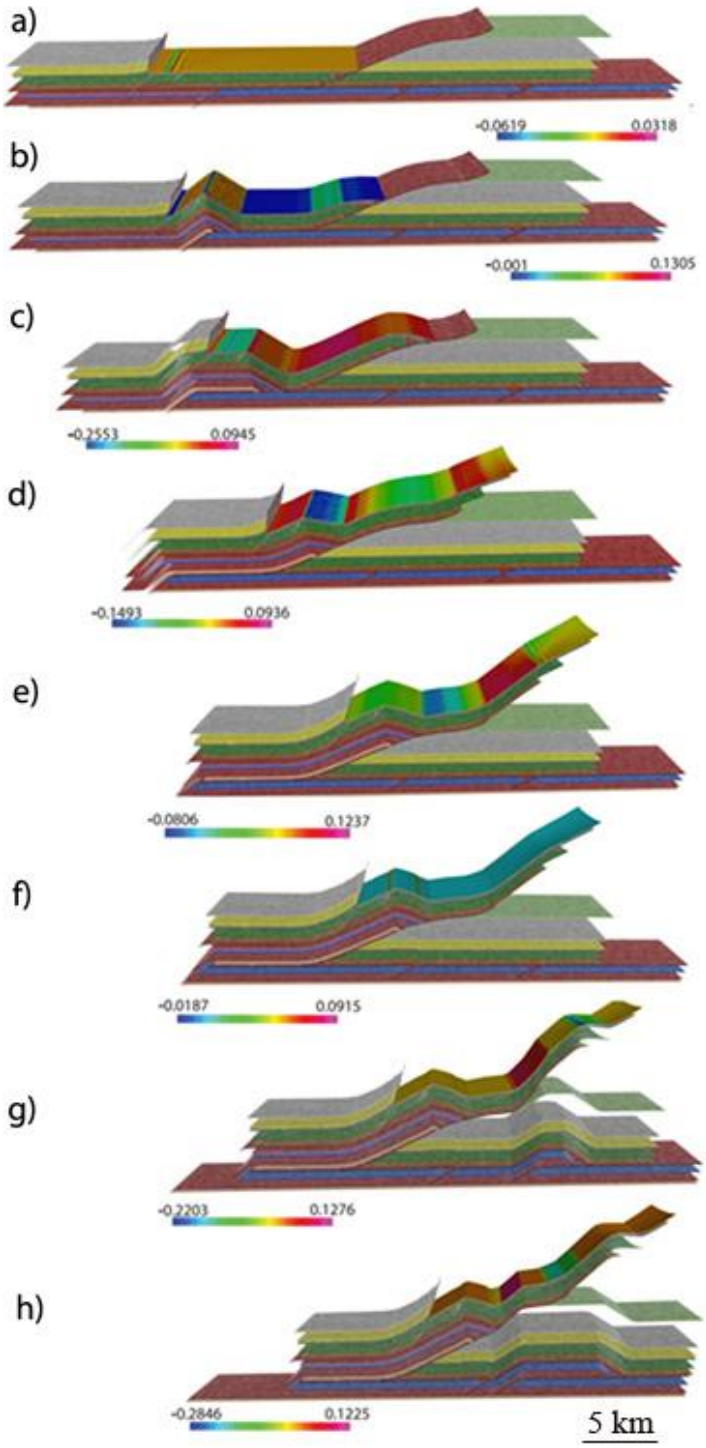

Figure 5.36. Evolution of the incremental horizontal elongation e_{xx} during stages a through h in Figure 5.34.

Distribution of the Cumulative Maximum Principal Elongation e_1

Cumulative or finite maximum elongation was calculated for stages a through h in Figure 5.34, adding all strain increments relative to the initial undeformed state. Each stage thus represents the finite strain the rock has experienced. Unlike the incremental strain calculations, the color scale in these figures is maintained equal, ranging between 0.0 and 0.5 in order to facilitate comparison between deformational stages.

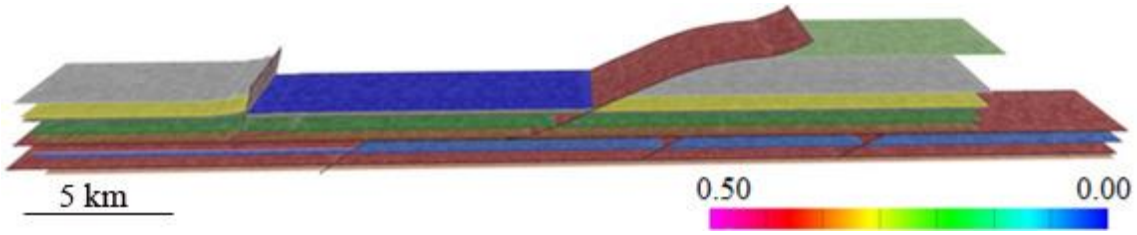

Figure 5.37 Displacement along fault 4 results in very low maximum principal elongation.

Similar to the incremental strain calculation, displacement along the Burnt Timber thrust initially results in the highest strain to be concentrated in both limbs of the Red Deer River anticline (Figure 5.38).

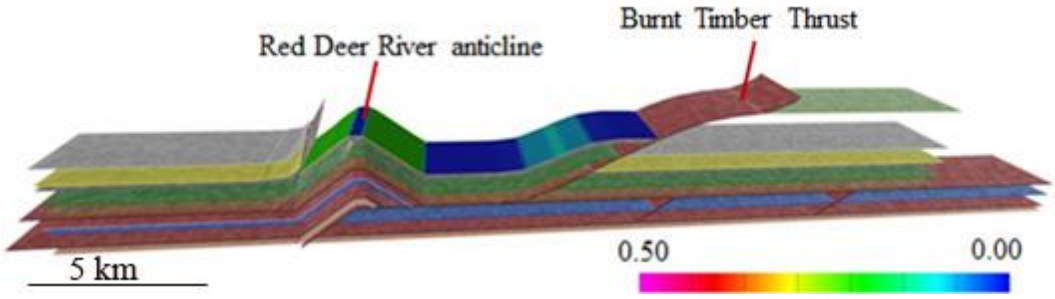

Figure 5.38 Fold formation during the displacement along Burnt Timber thrust yields high maximum principal elongation e_1 in the limbs of the Red Deer River anticline.

As displacement continues along the Burnt Timber thrust, areas of high strain in Figure 5.38 turn into lower-strain areas, indicating that strata that were first elongated undergo shortening as deformation progresses and folded layers flatten out as they migrate through the fold hinge (Figure 5.39). Further displacement along the Burnt Timber thrust results in elongation of the backlimb of the Red Deer River anticline. The areas of high elongation are also located in the strata above the James River anticline.

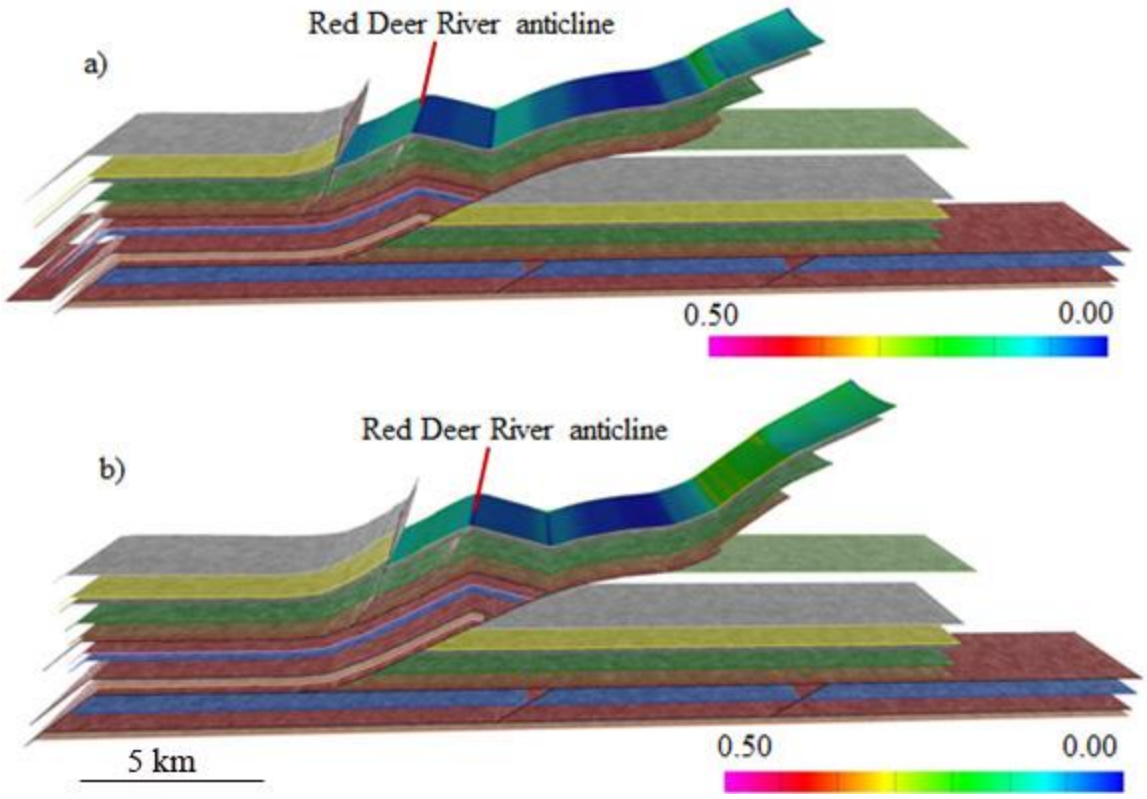

Figure 5.39 Evolution of the maximum principal elongation e_1 during slip along the Burnt Timber thrust.

The relatively small displacement along fault 2 does not have noticeable effects on the strain distribution within the Cardium strata (Figure 5.40).

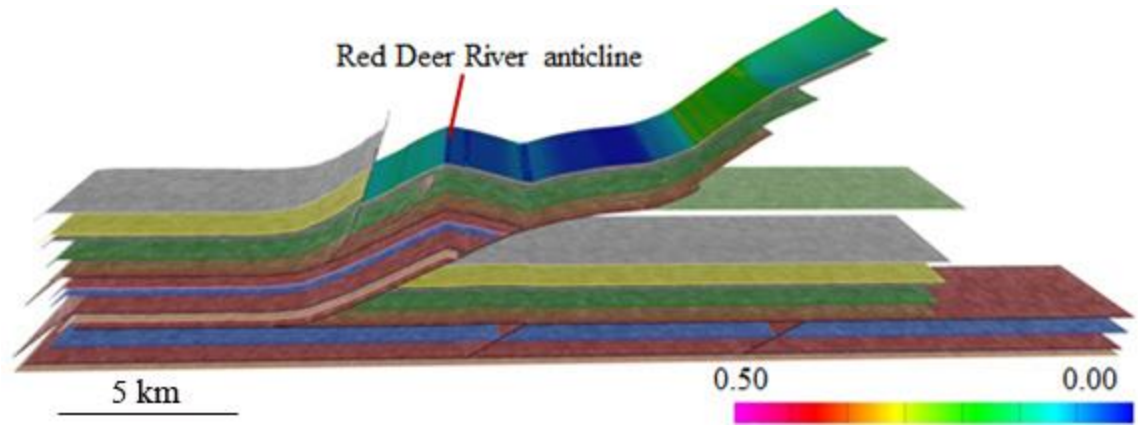

Figure 5.40 Distribution of the finite maximum principal elongation e_1 after slip along fault 2.

Slip of fault 1 causes elongation of the Cardium strata to the east of the Burnt Timber thrust, above the James River anticline, in association with fault 1. The final cumulative strain distribution shows larger elongation in the backlimb of the Red Deer River anticline than in the forelimb. The areas of highest elongation are located in the now eroded Cardium Formation east of the Red Deer River anticline (Figure 5.41).

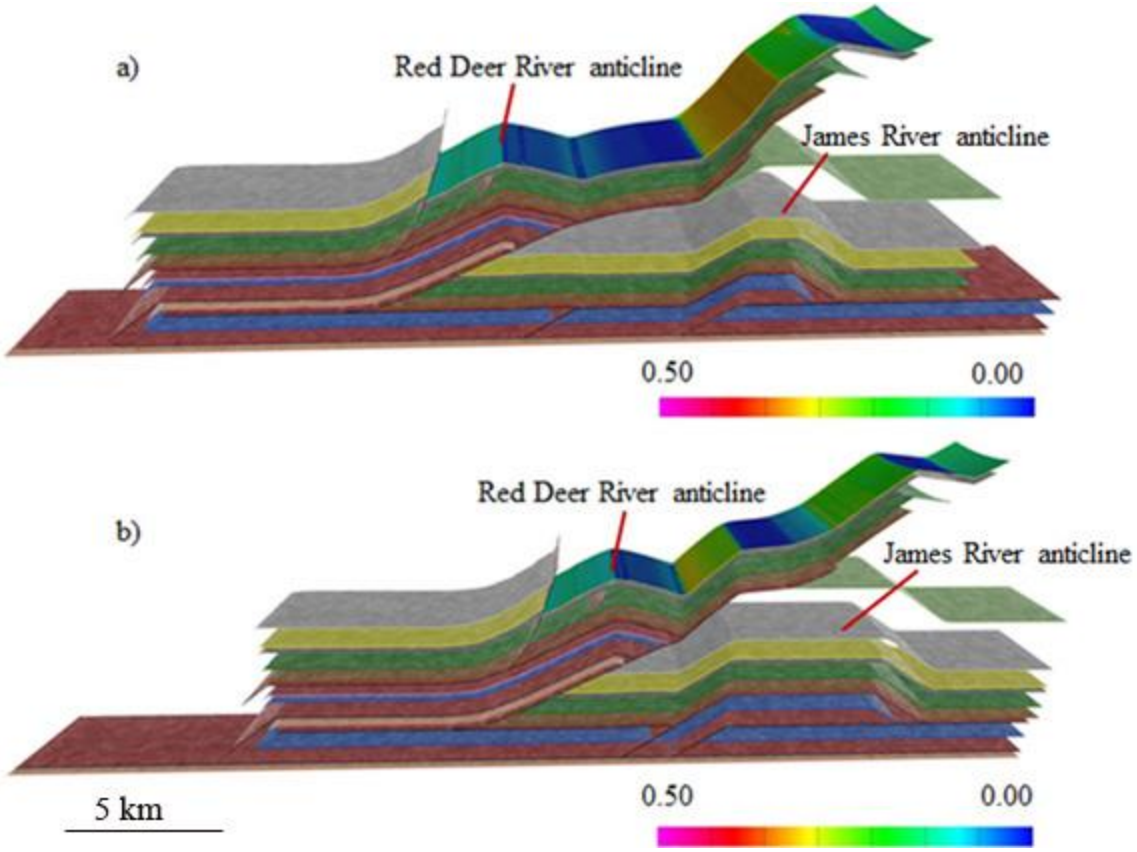

Figure 5.41 Finite maximum principal elongation e_1 in the Cardium Formation after slip of fault 1.

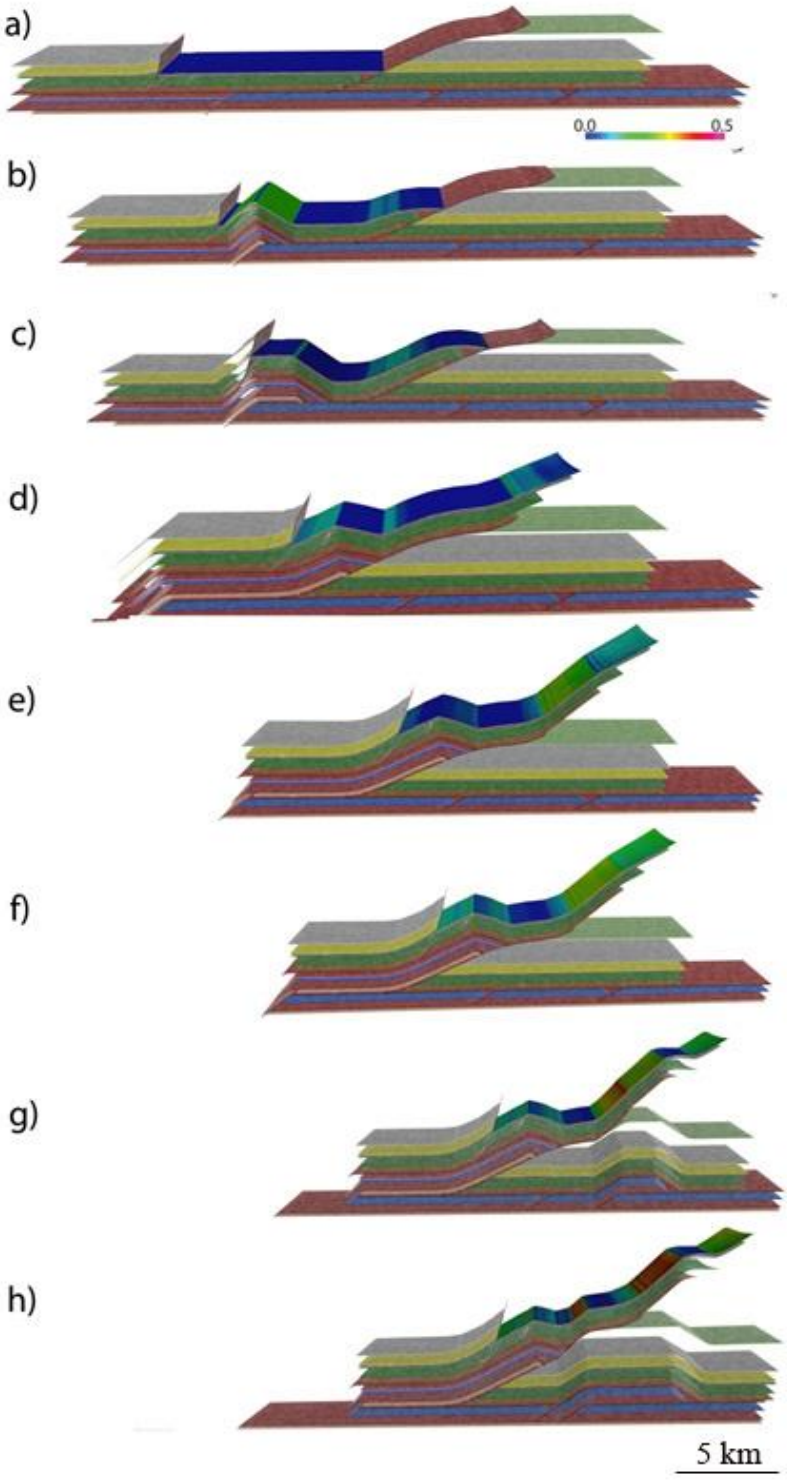

Figure 5.42. Evolution of the cumulative maximum principal elongation e_1.

Distribution of the Cumulative Horizontal Elongation e_{xx}

The evolution in cumulative (finite) horizontal elongation e_{xx} is shown in Figure 5.43. The forelimb of the Red Deer River anticline undergoes a distinct phase of finite extension during stage c. From stage d onward, somewhat higher elongation is observed in the backlimb (green colors) compared to the forelimb (blue colors) of the Red Deer River anticline. This difference is less than 0.1. Within the forelimb, somewhat lower strains are observed toward the crest, and higher strains toward the trough of the Red Deer River syncline which is located east of the anticline. A summary of cumulative elongation e_1 during stages a through h is shown in Figure 5.42.

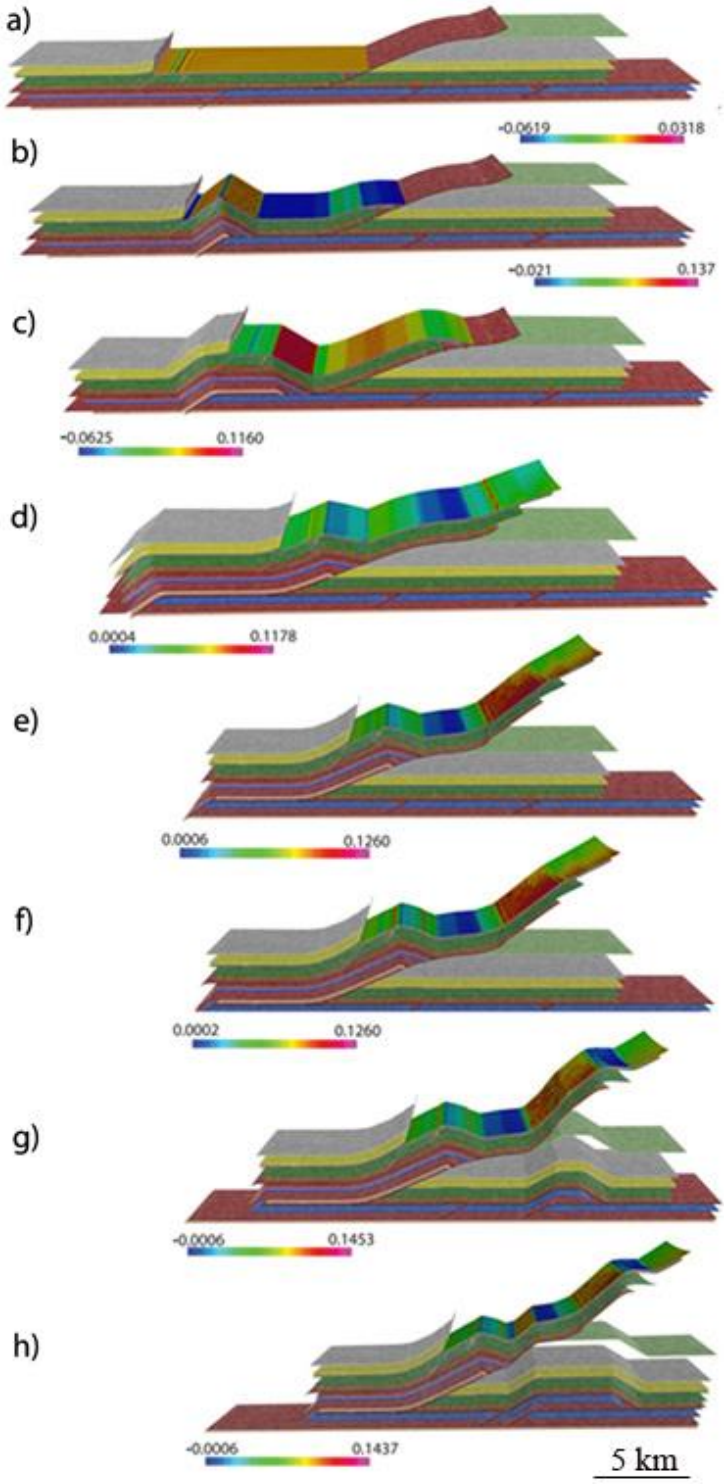

Figure 5.43. Evolution of the cumulative horizontal elongation e_{xx}.

FRACTURE MODELING

Based on the distributions of the maximum principal elongation e_1 calculated using the incremental and cumulative methods described above, fracture distribution models were generated using Move's "fracture modeling" tool (the horizontal elongation e_{xx} is currently not available for these simulations). These results provide a tool for a qualitative visualization of fracture density. However, because the maximum principal elongation e_1 is locally sub-parallel to the fractures, these results cannot be used for a quantitative comparison between mode predictions and the fracture strain obtained from field and lab measurements. This comparison will be based on the maximum horizontal elongation e_{xx} (see following chapter).

In order to generate fractures in Move, a 3D geocellular volume was created for the Cardium Formation. Strain attributes calculated in the previous step were saved onto this geocellular volume. For fracture modeling, the software requires certain parameters to be specified for the geocellular volume. These parameters include 1) the number of fracture sets that are expected, and 2) their orientation (azimuth). Based on my field observations (see Chapter 3), I generated three fracture sets in the 3D geocellular volume (Figure 5.44).

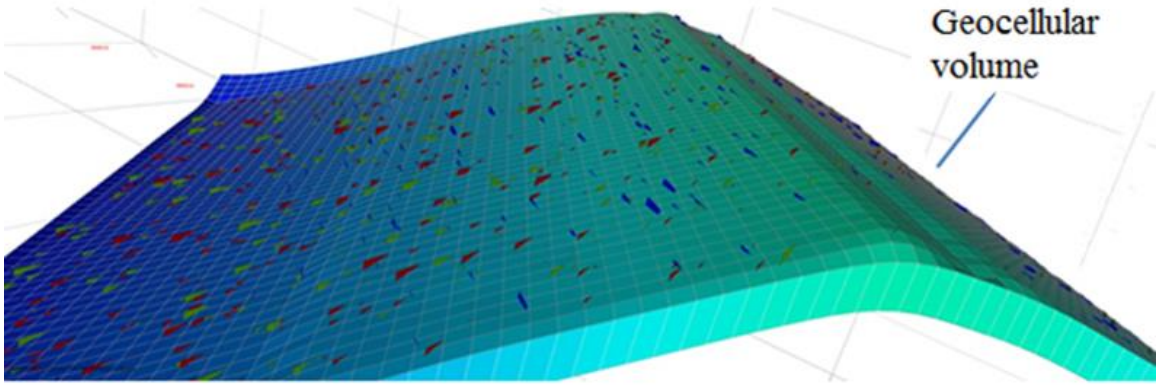

Figure 5.44 Example of generated fractures in the 3D geocellular volume. The three fracture sets (highlighted by green, blue and red) were generated statistically based on the dip and azimuth data measured in the field.

Fracture modeling based on incremental strain calculations

Displacement along fault 4 results in low e_1 strain values and therefore few associated fractures (Figure 5.45). As deformation progresses along the Burnt Timber thrust, strain is concentrated in both limbs of the evolving Red Deer River-anticline. Figure 5.46 shows high fracture intensities on both limbs at this stage, and fewer in the forefront of the faulted strata. Note that the hinge of the Red Deer River anticline remains relatively fracture-free.

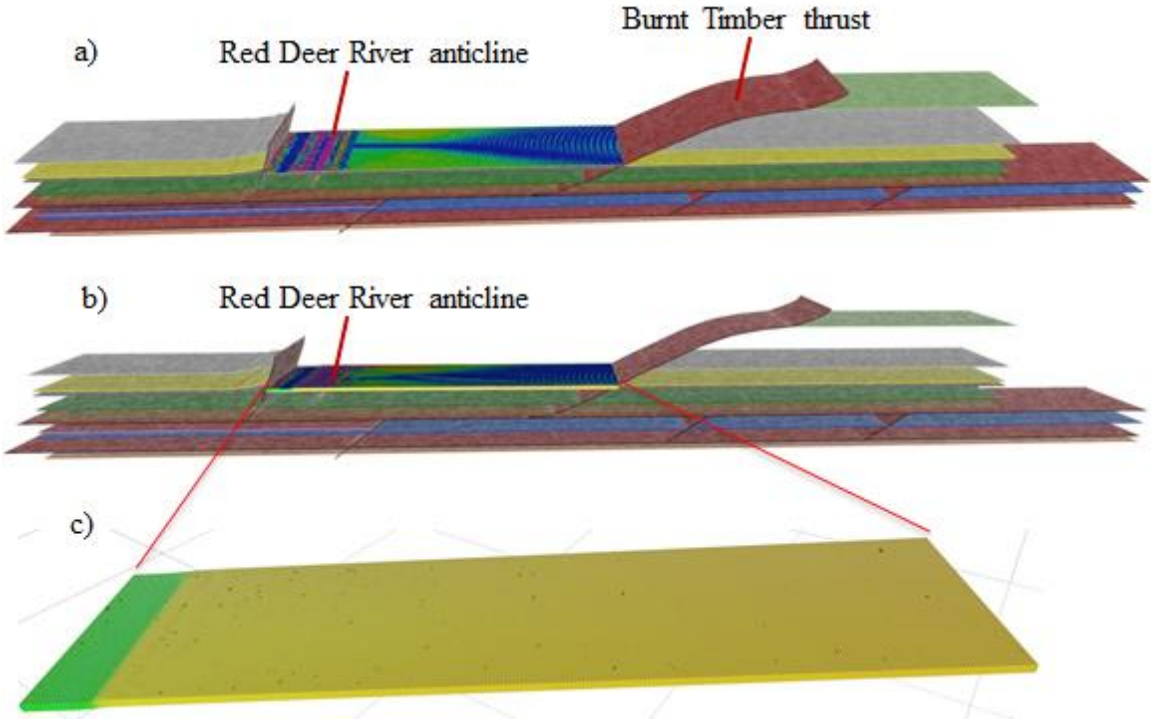

Figure 5. 45: a: Distribution of the maximum principal elongation e_1 associated with the first stage of deformation. b: The 3D geocellular volume generated for the Cardium Formation. c: The geocellular volume containing few fractures due to low elongation during this stage.

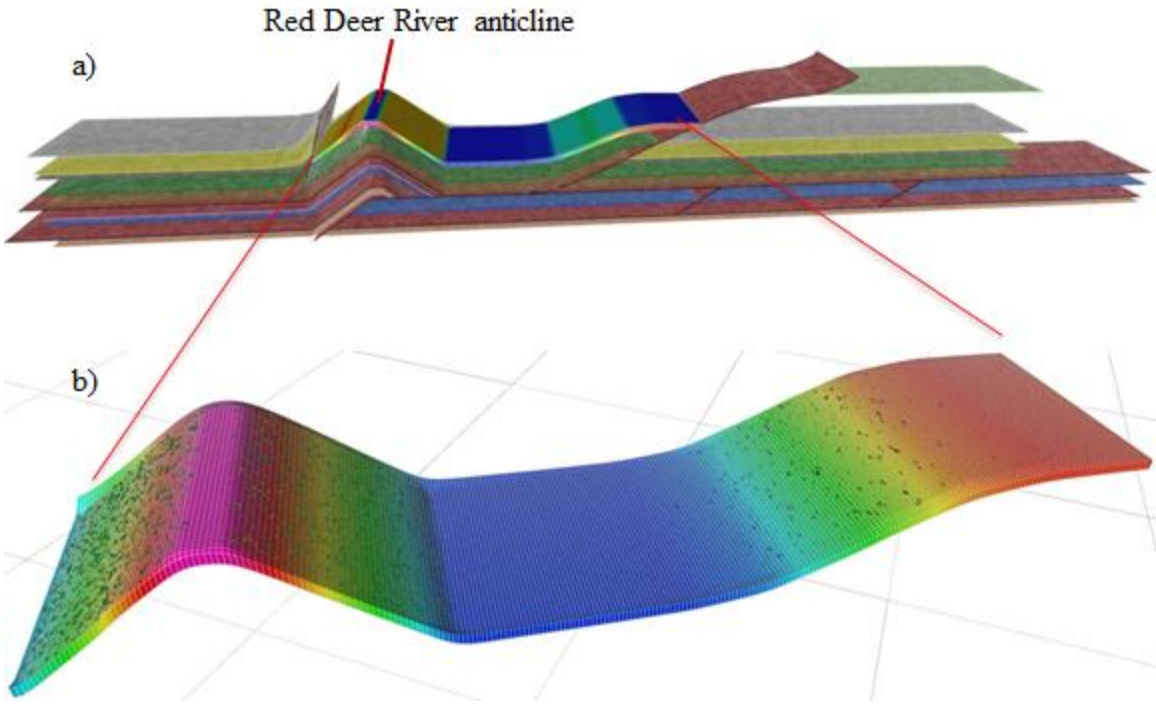

Figure 5.46 a: Incremental strain e_1 distribution for slip along the Burnt Timber thrust. b: Fractures develop primarily in the fold limbs of the Red Deer River anticline, with the hinge containing few fractures. Note that colors in geocellular volume indicate the elevation.

As displacement progresses along the Burnt Timber thrust, high fracture intensities are predicted in the forelimb of the Red Deer River anticline. Unlike in the previous stage, higher fracture intensities are generated in the crest of the Red Deer River anticline than on the limbs (Figure 5.47).

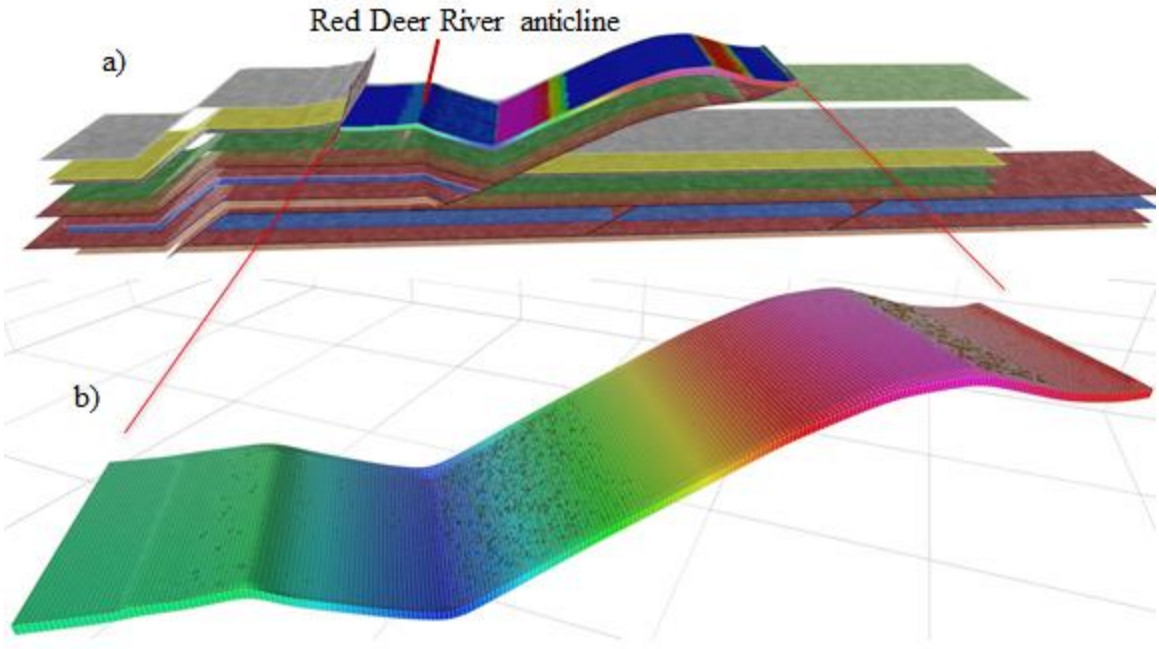

Figure 5.47 a: Incremental strain e_1 with continued slip along the Burnt Timber thrust. b: Fracture intensity is higher in the crest of the Red Deer River anticline and lesser in the fold hinges. Note that colors in geocellular volume indicate the elevation.

With increasing slip on the Burnt Timber thrust, fractures become more abundant in the backlimb of the Red Deer River anticline whereas the forelimb remains relatively fracture-free at this stage (Figure 5.48).

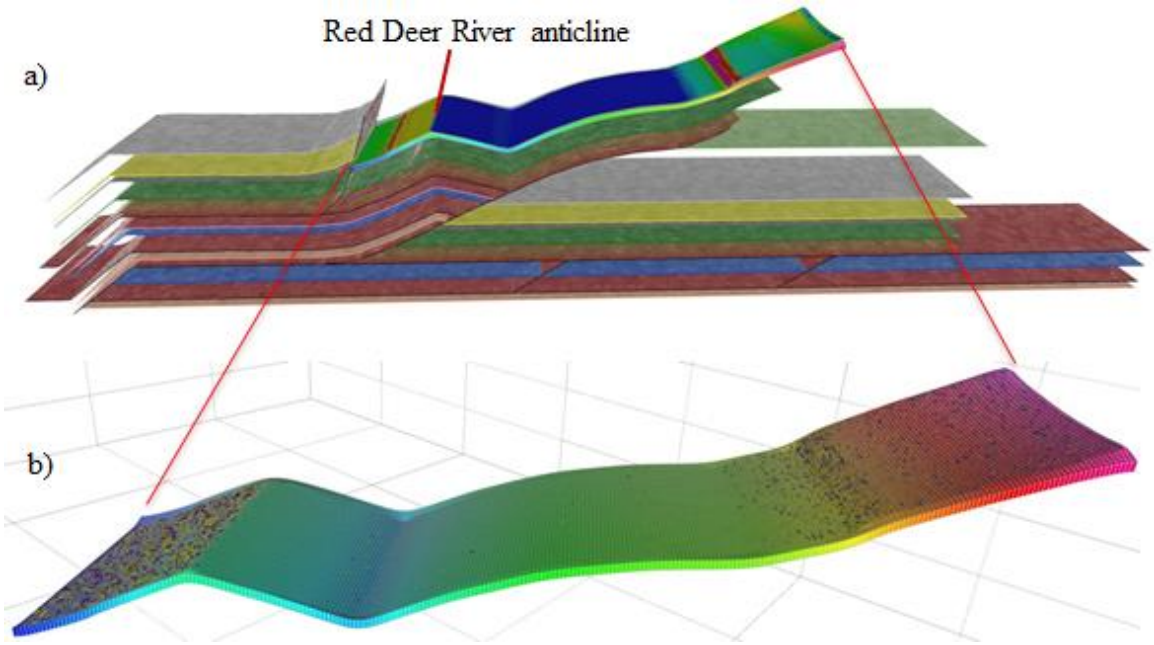

Figure 5.48 a: Incremental strain e_1 for continued slip on the Burnt Timber thrust. b: The geocellular volume showing the highest fracture intensity in the backlimb of the anticline. Note that colors in geocellular volume indicate the elevation.

The formation of the fault-bend fold associated with fault 1 results in high fracture intensity in the forefront of the Burnt Timber thrust fault (Figure 5.49), and later in both limbs of the James River anticline developed east of the Red Deer River anticline (Figure 5.50). Displacement along fault 1 does not result in further generation of fractures within the Red Deer River anticline.

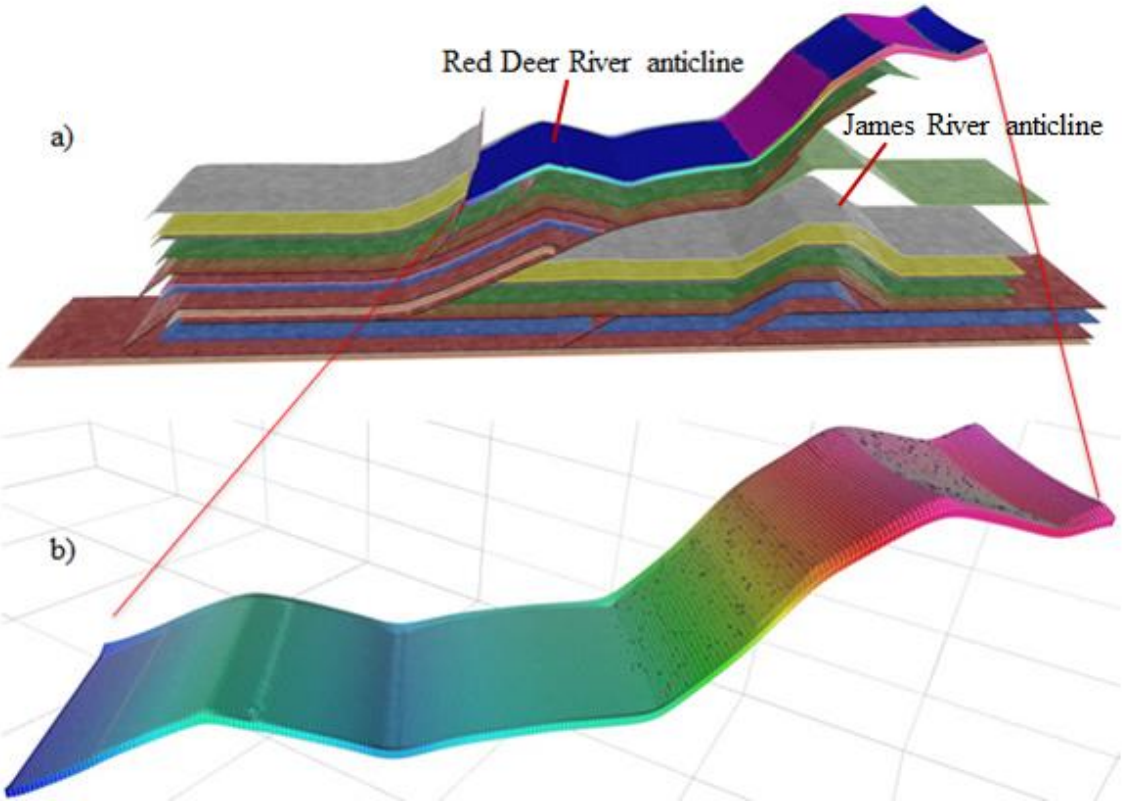

Figure 5.49 a: Incremental strain e_1 for slip on fault 1. b: Fracture intensity is higher in the strata above the James River anticline. Note that colors in geocellular volume indicate the elevation.

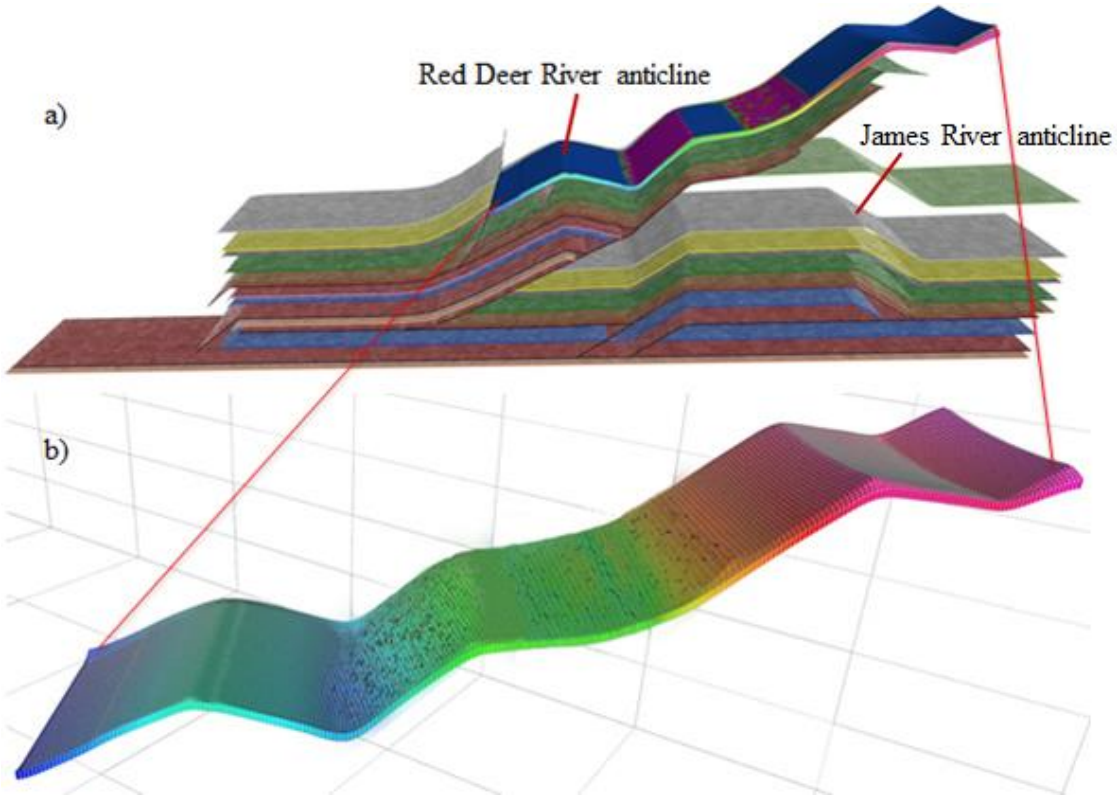

Figure 5.50 a: Incremental strain e_1 for continued slip on fault 1. b: High fracuture intensity is in both limbs of the anticline above James River anticline. Note that colors in geocellular volume indicate the elevation.

Fracture modeling based on cumulative strain calculations

Figure 5.51 shows the generated geocellular volume populated with scarce fractures for the same stage as in Figure 5.45. Similar to Figure 5.46, Figure 5.52 show that progressive deformation associated with displacement along the Burnt Timber thrust causes the highest fracture intensities to be localized on both limbs of the Red Deer River anticline.

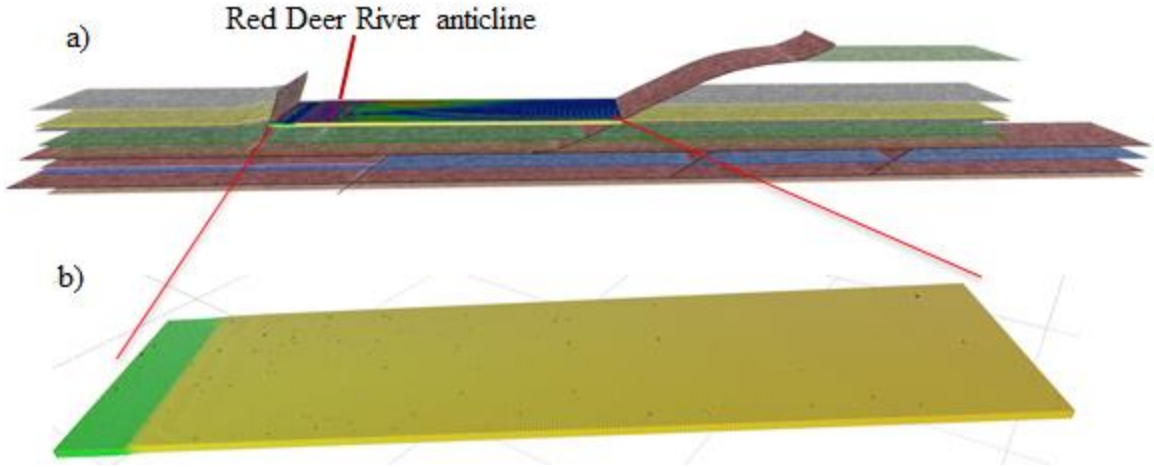

Figure 5.51. a: Strain distribution associated with the first stage of deformation. b: The 3D geocellular volume generated for the Cardium Formation contains few fractures due to low elongation during this stage.

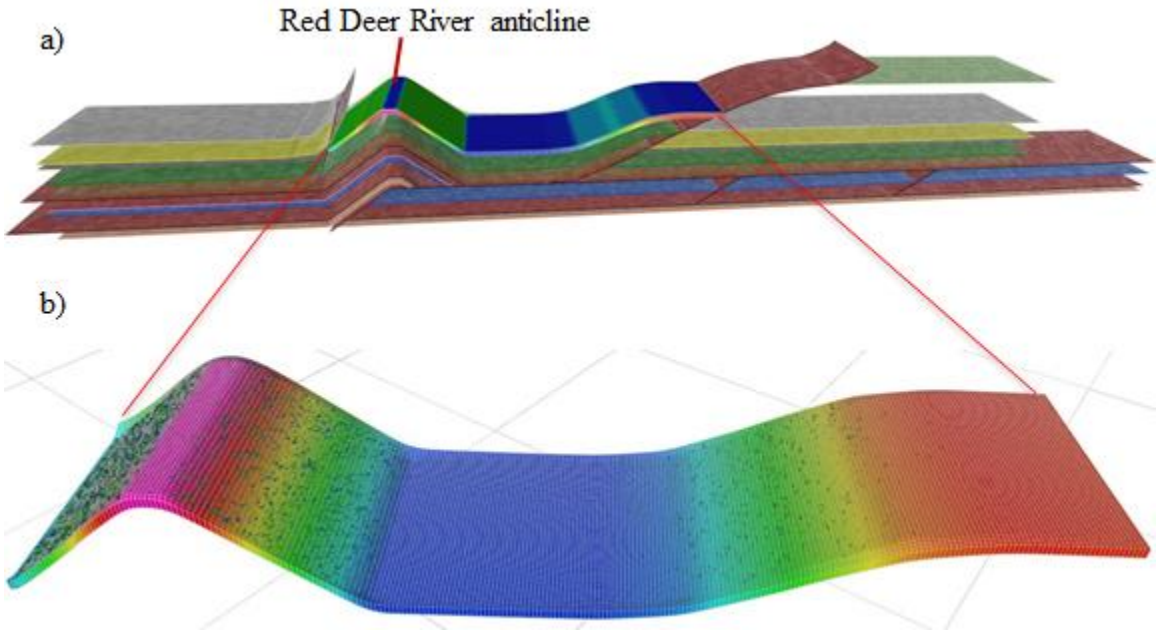

Figure 5.52 a: Cumulative strain e_1 distribution for slip along the Burnt Timber thrust. b: Fractures develop primarily in the fold hinges of the Red Deer River anticline, with the hinge containing few fractures.

In contrast with the low fracture intensity generated around the Red Deer River anticline at this stage in the incremental strain model (Figure 5.47), Figure 5.53 shows that progressive displacement along the Burnt Timber thrust causes high cumulative e_1 strain, and thus a higher fracture intensity, to develop in the forelimb and around the hinge of the Red Deer River anticline.

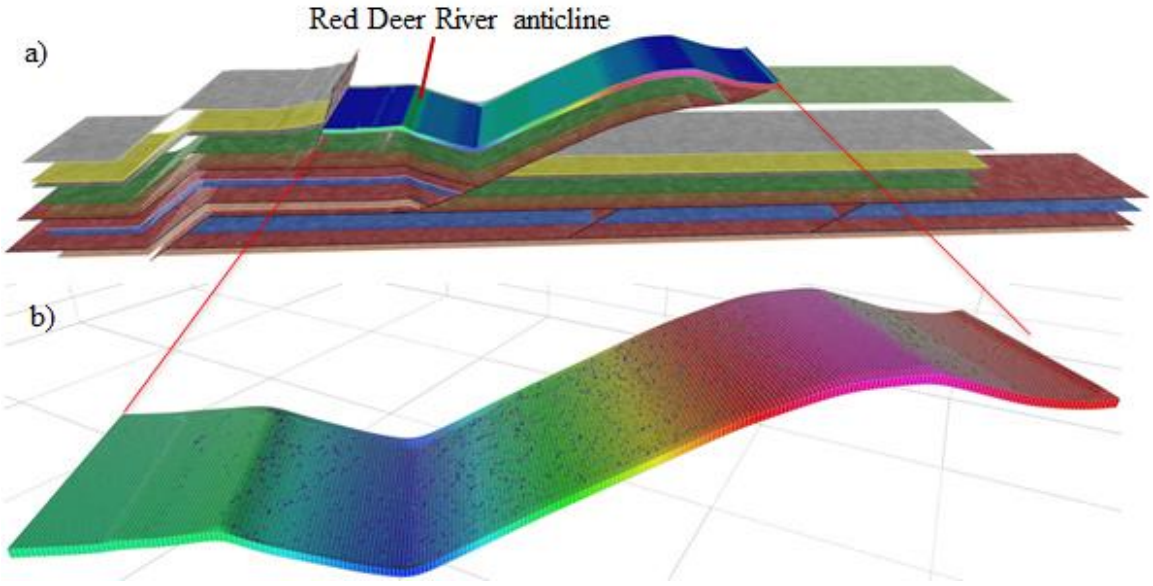

Figure 5.53 a: Cumulative strain e_1 distribution with continued slip along the Burnt Timber thrust b: Fracture intensity is higher in the crest of the Red Deer River anticline and lesser in the fold hinges.

As deformation progresses, fracture intensity increases in the backlimb of the Red Deer River anticline (Figure 5.54).

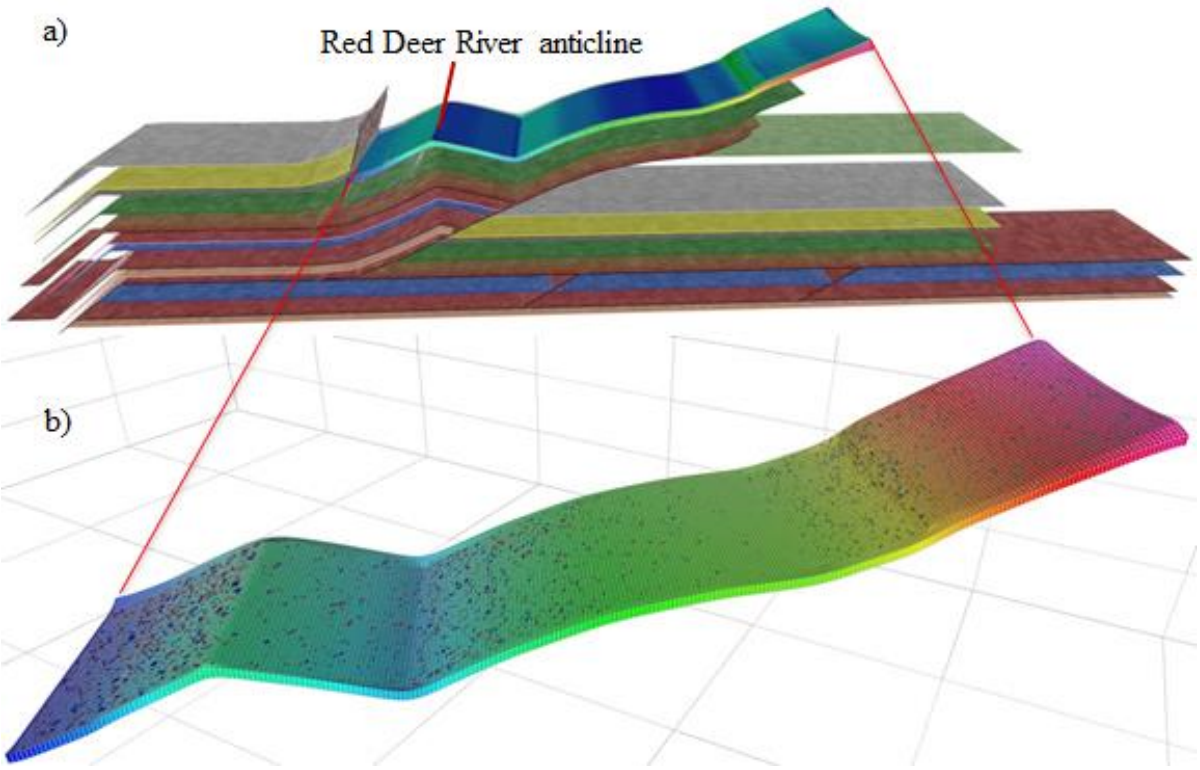

Figure 5.54 a: Cumulative strain e_1 for continued slip on the Burnt Timber thrust. b: The geocellular volume showing the higher fracture intensity in the backlimb of the anticline than forelimb.

Finally, deformation associated with displacement along fault 1 causes the highest fracture intensities to be concentrated at the forefront of the Burnt Timber thrust at first (Figure 5.55), as well as to the east of the Red Deer River anticline (Figure 5.56). Within the Red Deer River anticline, the highest fracture density is observed in the backlimb, followed by the forelimb, and the lowest fracture intensity in the fold hinge.

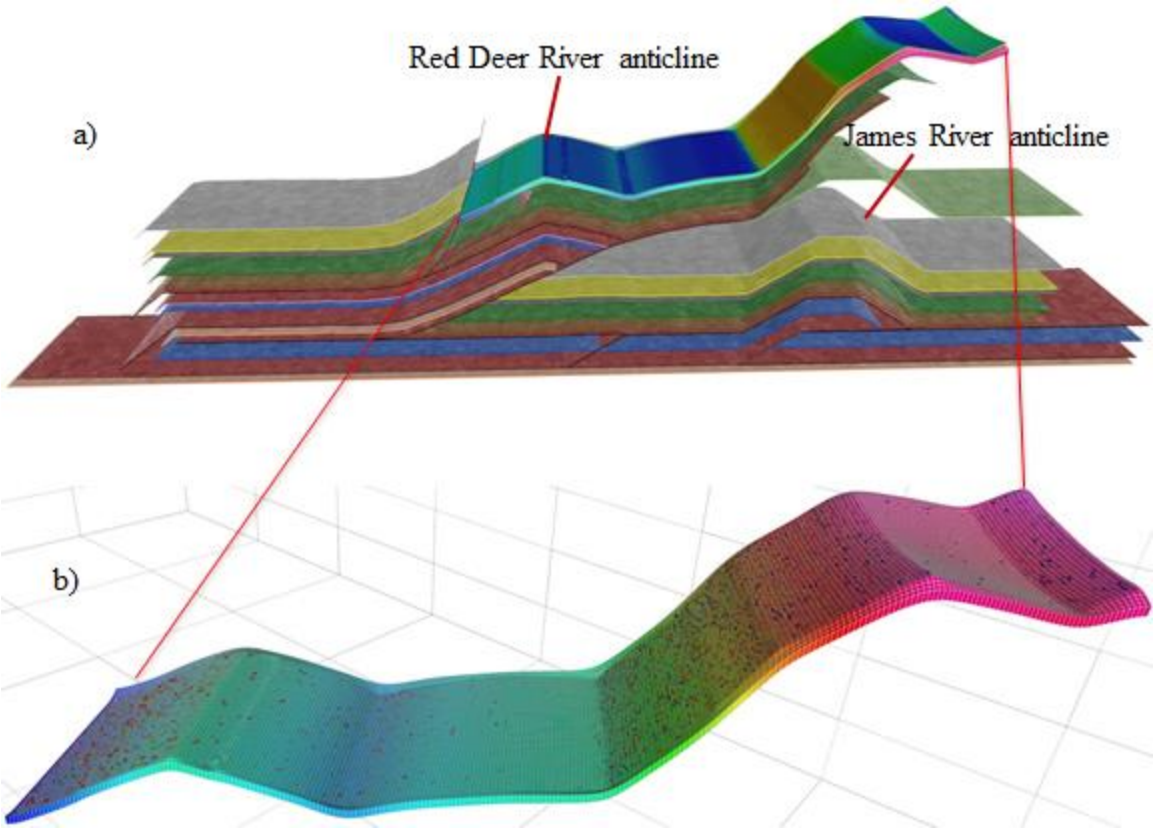

Figure 5.55 a: Cumulative strain e_1 for slip on Fault 1. b: Fracture intensity is higher in the backlimb of the Red Deer River anticline than in the forelimb. The areas of highest fracture intensity are located in strata above the James River anticline.

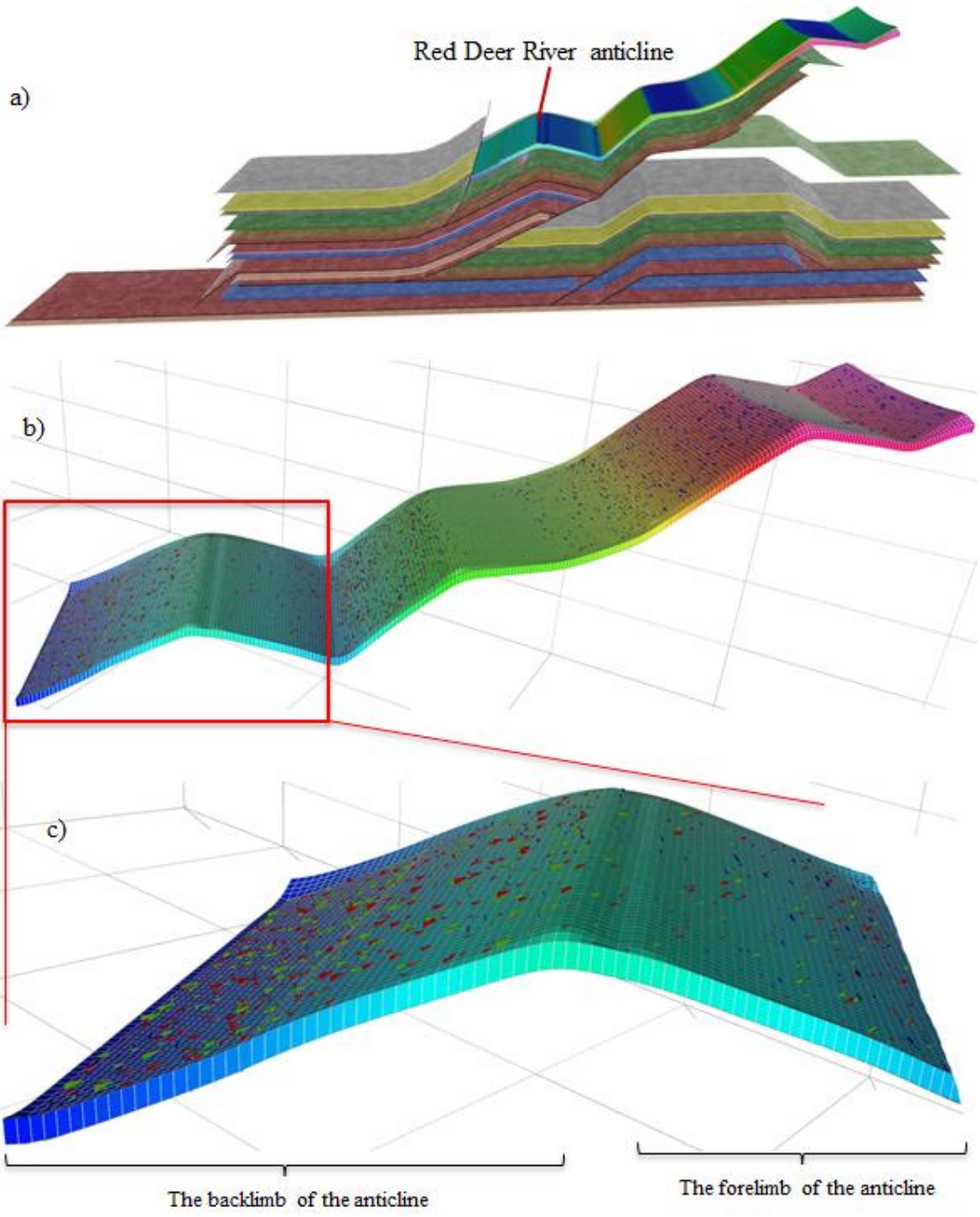

Figure 5.56 a: Strain e1 distribution model and geocellular volume. b: Fracture model based on the final stage of the cumulative strain calculations. c: close up image of Red Deer River anticline showing the highest fracture density in the backlimb, followed by the forelimb, and the lowest fracture intensity in the fold hinge.

Chapter 6: Discussion

Active-Hinge vs. Fixed-Hinge Folding Model for the Red Deer River Anticline

Two kinematic models have previously been proposed to predict the occurrence of opening-mode fractures in folds. The highest deformation intensity commonly occurs in the hinge of a fold where fold kinematics suggest fixed-hinge fold development (De Sitter, 1956; McConnell, 1994; Salvini and Storti, 2004). Bending of strata caused by layer-parallel shortening during deformation causes the maximum deformation in the hinge of folds (Murray, 1968). This assumption suggests that greater curvature equals greater layer-parallel strain experienced by the strata. This strain is contractional in the inner arc, and extensional in the outer arc of the folded layer. Therefore, the highest extensional strain is expected to be accommodated by opening-mode fractures in the hinge of a fold. For a fold where the hinge is stationary or fixed and where fractures form by bending of the layers, the highest fracture strain is expected in the outer arc of a fold hinge. In contrast to the fixed-hinge model, some folding mechanisms result in hinge migration where the distribution of high deformation intensity and associated high strain tracks the hinge migration path (Figure 6.1) (Suppe, 1983; Price and Cosgrove, 1990; Fischer et al., 1992; Salvini and Storti, 2004; Smart et al., 2012). Suppe (1985) described an active-hinge fold mechanism in which the anticline crest migrates throughout deformation resulting in changes in strain orientation and magnitude depending on the fold evolution path.

Strain calculations using Move for the Red Deer River anticline (see chapter 5) predict that fault-related fold development results in a complex strain path throughout deformation (Figures 5.34, 5.36, 5.42, and 5.43) with extensional strain localized primarily in the fold limbs. In these strain models, I consider the incremental (non-cumulative) strain calculation to provide information about the timing of fracture opening

relative to the thrust evolution. Using the incremental horizontal elongation in the thrust direction e_{xx} (Figure 5.36), we observe that the largest incremental extension is concentrated in the backlimb of the Red Deer River anticline early in the development of the Burnt Timber Thrust (stage d) when the forelimb undergoes a phase of shortening. Incremental horizontal strains are lesser during subsequent stages of the anticline development. Finite strains (Figure 5.43) in both limbs of the anticline are roughly similar from stage d onward, with somewhat higher extension in the backlimb, and lower extension in the forelimb close to the crest of the fold. This distribution of finite strain changes little during later stages of thrust fault activity, focusing deformation to the east of the Red Deer River anticline.

While incremental strain provides a proxy for fracture opening at specific stages of fold and thrust evolution, the cumulative (finite) strain can be considered an appropriate proxy for strain accommodated by fractures that are cemented by mineral cement concurrently or synkinematically with fracture opening. This cement would prevent closing of fractures with changing strain and stress boundary conditions thus preserving a record of cumulative strain. As shown in chapter 4, fractures in the Cardium Formation are generally cemented with synkinematic quartz cement (Figure 4.5) that would prevent closure of fractures when stress and strain conditions change in the fold during progressive evolution of the thrust sequence.

In comparison to the strain calculations obtained by Move, the fracture strain observed in the planar-laminated Upper Kakwa Member of the Cardium Formation shows little variation across the three domains (Figure 4.25), with Domain II, the upper section of the forelimb, showing somewhat lower strain than the lower forelimb (Domain III) and the backlimb (Domain I). Although the number of strain measurements in the Upper Kakwa Member is not evenly distributed across the three domains (with only one

measurement in Domain III), we find that the strain distribution is consistent with the finite strain calculations in Move (Figure 5.43) and thus with an active-hinge model of fracture formation. Consistency does not imply that the apparent fracture strain distribution necessarily indicates a syn-folding origin of the opening-mode fractures, because the rather uniform fracture strain across the fold could also suggest fracture formation prior or after to folding. I discuss possible evidence for fracture timing prior to folding in the next section.

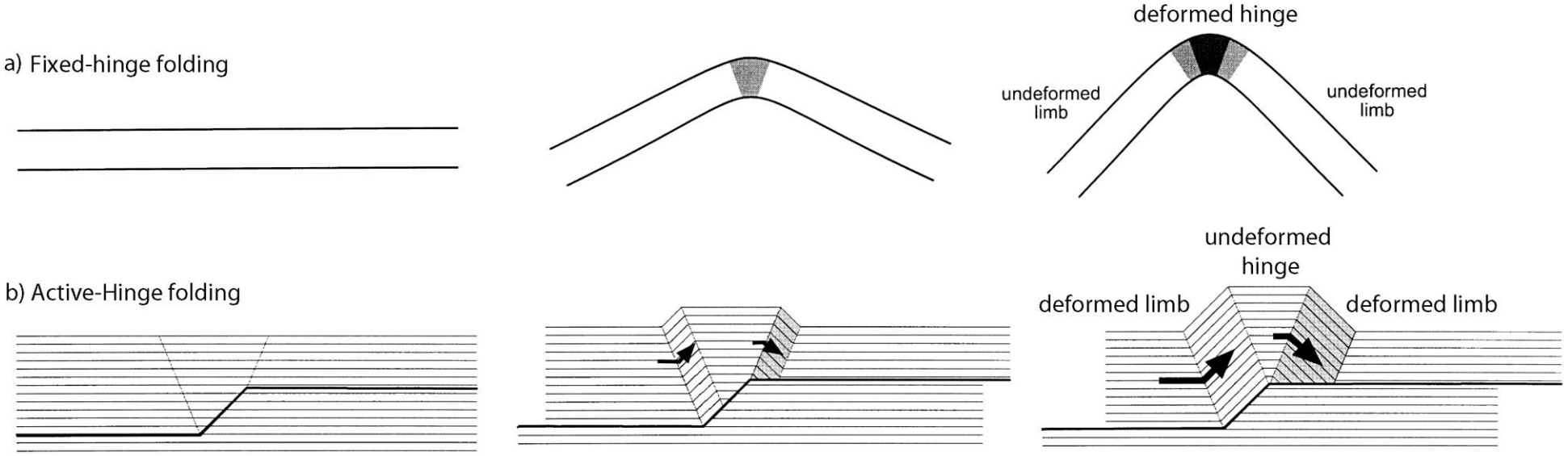

Figure 6.1. a: Fixed-hinge folding model indicating high deformation concentration in the hinge of the anticline corresponding to the maximum layer curvature (Salvini and Storti, 2000). b: Active-hinge folding model showing high deformation localization in the limb of anticline indicating migration of the hinge throughout deformation (from Salvini and Storti, 2000). High deformation density is indicated by shaded areas. Arrows indicate the migration path of the hinge.

Fracture Formation Relative to Folding

While the distribution of measured fracture strain can be considered consistent with the modeled distribution of horizontal extension obtained through Move simulations, I cannot rule out that the fractures formed prior to folding. Fractures that formed a regional set of uniform orientation are expected to show consistent angular relations relative to bedding after folding of the fractured layer. I tested for such consistent angular relations by unfolding the bedding to horizontal on a stereonet, and by rotating the fracture orientations by the same amount around the same rotation axis (fold test) (Figure 4.2). The rotated fracture orientations in Figure 4.2 cluster spatially more tightly than the unrotated (measured) fracture orientations suggesting that the fractures formed when bedding was flat prior to folding of the Red Deer River anticline. However, it is conceivable that fracture orientation can be influenced by the layer anisotropy, with fractures forming perpendicular to bedding regardless of bedding dip. The fold test may thus not provide a robust estimate of fracture timing relative to folding.

Cross-cutting relations among fracture sets observed in the Red Deer River anticline and evidence for slip on some of these fractures provide evidence for reactivation of fractures during folding. As described in chapter 4, slip on vertical through going set 4 fractures that reactivate shorter set 2 fractures of similar orientation, and slip on low-angle reverse faults that predate set 4 fractures are kinematically consistent with shortening accommodated by folding of the anticline. This suggests, but does not unambiguously prove, that the formation of the earliest fracture set 2 either predates folding, or that the fractures formed during an early phase of folding, with

reactivation during later stages of folding. An early synfolding origin would be consistent with the Move models as well.

Formation of through-going set 4 fractures by reactivation of set 2

Fractures observed in the field are considered to be important for reactivation and propagation because it is likely that their existence contribute to mechanical anisotropy that possibly has influence on subsequent fracturing during folding (Gross and Eyal, 2007; Pollard and Bergbauer, 2004). Through-going fractures commonly develop as a consequence of the linkage and reactivation of the preexisting fractures (Becker and Gross, 1996; Gross and Eyal, 2007). In the Red Deer River study area, fractures are prominent mesoscopic scale structures in the surface exposures of the Cardium Formation within the Red Deer River anticline. These fractures include two main types of opening-mode fractures based on their relative dimensions: (1) fractures that are confined to individual bedding planes (bedding-confined fractures), and (2) fractures that cut through multiple sandstone bedding planes (through-going fractures). The bedding-confined fractures that are perpendicular to bedding are nearly perpendicular to the fold axis and were designated as Set 2. As discussed in chapter 4, Set 2 fractures are interpreted to have formed early in the deformation history and prior to fold development. The orientations of the through-going fractures observed in the field correspond to orientation of the Set 2 preexisting fractures. According to Pollard and Bergbauer (2004) the orientation of preexisting fractures is considered to play a critical role in controlling the internal structures and the orientation of fractures that form during later in the deformation history. Also, Becker and Gross (1996) suggested that many through-going fractures observed in the field form in response to subsequent reactivation of preexisting fractures. The observed linkage geometry of these through going fractures suggests that

they formed by reactivation and linkage of earlier bedding-confined fractures. Several of these through-going fractures display dip-slip shear offset. Therefore, these through-going fractures are considered to be genetically related to preexisting fractures. In the study area, the existence of Set 2 fractures must have contributed to the mechanical weakness that possibly had an influence on subsequent fracturing during multiple phases of brittle deformation. Field observations indicate that these Set 2 fractures propagated and linked to each other to form through-going fractures. Therefore, the Set 2 fractures are interpreted to have been reactivated and formed the set 4 through-going fractures by folding that triggered propagation and linkage.

Chapter 7: Conclusions

The objective of this study was to analyze the temporal and spatial relationship between fracture formation and fault-related fold within the structural position of the Red Deer River anticline. In the study, I combined outcrop structural observations with results from kinematic numerical models and macro- and microscanline measurements analyses to assess possible kinematic controls of folding and thrust sheet emplacement on fracturing.

Opening-mode fractures are prominent in surface exposures of the Cardium Formation within the Red Deer River anticline. Systematic angular relations between three sets of opening-mode fractures oriented at high angle to bedding suggest that the fractures were progressively rotated when bedding planes were folded suggesting an early formation of fractures prior to formation of the anticline or during early onset of folding. Commonly observed through-going fractures formed by propagation and linkage are associated with wing cracks showing both strike-slip and dip-slip sense of shearing which are kinematically compatible with folding. This suggests that through- going fractures were reactivated in shear during later stages of fold development.

Based on fracture aperture and spacing data collected along macro- and micro scanlines for three structural domains within the Red Deer River anticline (backlimb, upper forelimb, and lower forelimb) I derived cumulative frequency versus kinematic aperture plots. Fracture strain calculations based on these results suggest that variations in fracture intensity are small among the three structural domains across the fold, with slightly lower intensity in the upper forelimb and higher but equal intensity in the backlimb and lower forelimb of the anticline.

Kinematic restoration of regional-scale cross-sections and forward modeling account for the large-scale fold geometry of the Red Deer River anticline. These kinematic models suggest that the Red Deer River anticline developed by active-hinge migration resulting from slip along the underlying Burnt Timber thrust. These kinematic models allow tracking the strain evolution within the anticline throughout its formation concurrent with slip along the underlying thrust, providing an estimate of incremental and cumulative strain resulting from this deformation. Based on these simulations, the structural development of the Red Deer River anticline appears to be the main control on the strain experienced by the Cardium Formation. As slip along the underlying thrust increases, the fore and backlimbs initially accommodate varying amount if incremental strain, ultimately reaching similar finite strains in both limbs, with somewhat lower extension in the transport direction in the upper forelimb. With continued slip along underlying thrust faults, the Red Deer River anticline becomes inactive and fold development shifts farther east.

A comparison of measured fracture strain with the kinematic model predictions, suggests that the observed fracture strain distribution across the three structural domains is consistent with fracture formation during early development of the Red Deer River anticline, concurrent with slip along the underlying Burnt Timber thrust. This is consistent with the field structural observations indicative of shear reactivation of these fractures during later stages of folding. However, a pre-folding origin of the fractures cannot be excluded because the differences in measured fracture strain across the three structural domains of the fold are small, and layer-to-layer variation in folding strain within each domain are large. The numerical simulations performed in this study demonstrate, however, that fold evolution in deforming fold and thrust belts can result in complex distribution in both space and time of bedding-parallel extension and thus in the

formation of opening-mode fractures, consistent with field observations of spatially variable fracture density in this structural setting.

Appendix A: Methods

DATA COLLECTION AND ANALYTICAL METHODS

Structural attributes of macrofractures (aperture >0.1 mm) were collected along 1D scanlines in outcrop of the Cardium Formation following the methods of Ortega et al. (2006). Fracture attributes included fracture spacing, kinematic aperture, infill type, and cross-cutting relationship. Scanline locations were chosen to include strata with continuuous exposure and containing a sufficient number of fractures of each set for scaling analysis (Figure 1). In addtion to macroscaline analyses, samples were collected from different lithological units in the same outcrop for microscanline analyses in the laboratory.

Figure A. 1. Macroscanline measurement of fracture attributes in Cardium Formation exposed in the Red Deer River anticline.

THIN SECTION PREPATATION AND SEM IMAGING

Hand samples collected from outcrops of the Red Deer River area were cut into thin-section-wide strips perpendicular to the main fracture set and parallel to bedding. Guidance lines were cut in the back of each rock strip, and the rock strips were then cracked by hand to make thin section arrays composed of multiple thin sections, prepared in such a way that no material was lost between sections (Gomez and Laubach, 2006) (Figure 2).

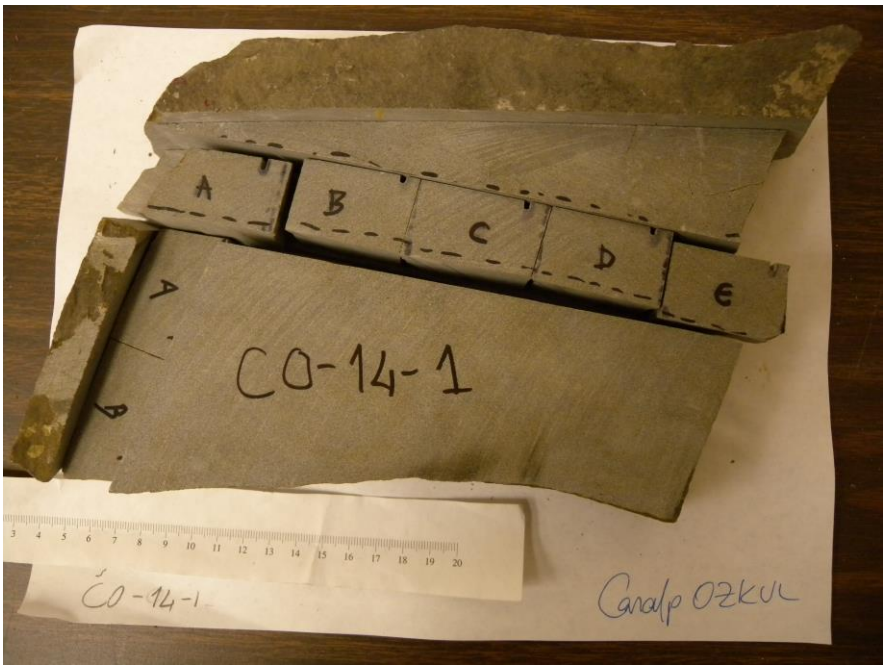

Figure A. 2. Collected hand sample co-14-1 was cut into rock strips to prepare thin sections.

Thin sections were imaged using a MonoCL2 cathodoluminescence (CL) system attached to a Philips XL30 SEM at 15 kV at the Bureau of Economic Geology at the University of

Texas at Austin was used to obtain CL images. CL imagers for microfracture scanline measurements were collected using a blue filter. Following Gomez (2000), images were assembled into mosaics with a continuous microfracture view (Figure 3). Fracture spacing was measured as the distance from one fracture wall to the wall of its closest neighbor.

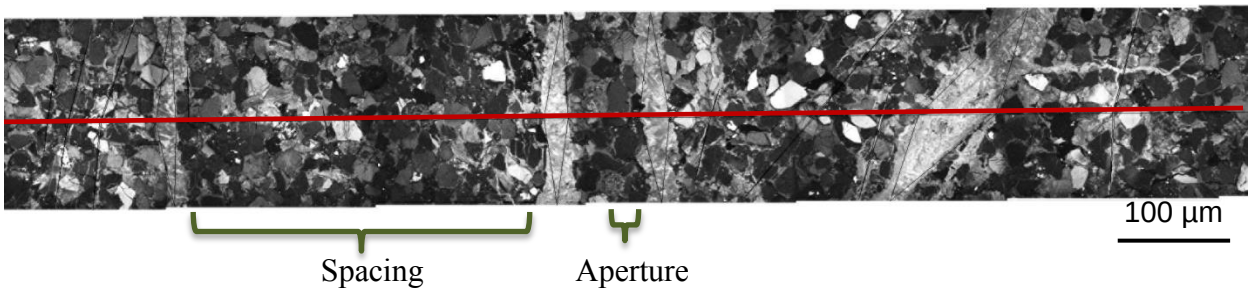

Figure A. 3 Sample co-14-3a-a. Fracture spacing and aperture data is measured for fracture scaling analysis. Red line indicates the scanline whereas black lines indicate fracture walls. Fracture cement is quartz.

The software Didger3 was used to digitize the position of transgranular microfractures along the microscanlines. Microfractures were separated into sets based on their orientation. The spatial coordinates of fracture aperture and spacing obtained using Didger 3 were imported to a spreadsheet that uses Excel macros (goMezure) for data reduction (Gomez and Laubach, 2006). Fracture aperture data were plotted in a log-log cumulative frequency versus kinematic aperture plots (Figure 4).

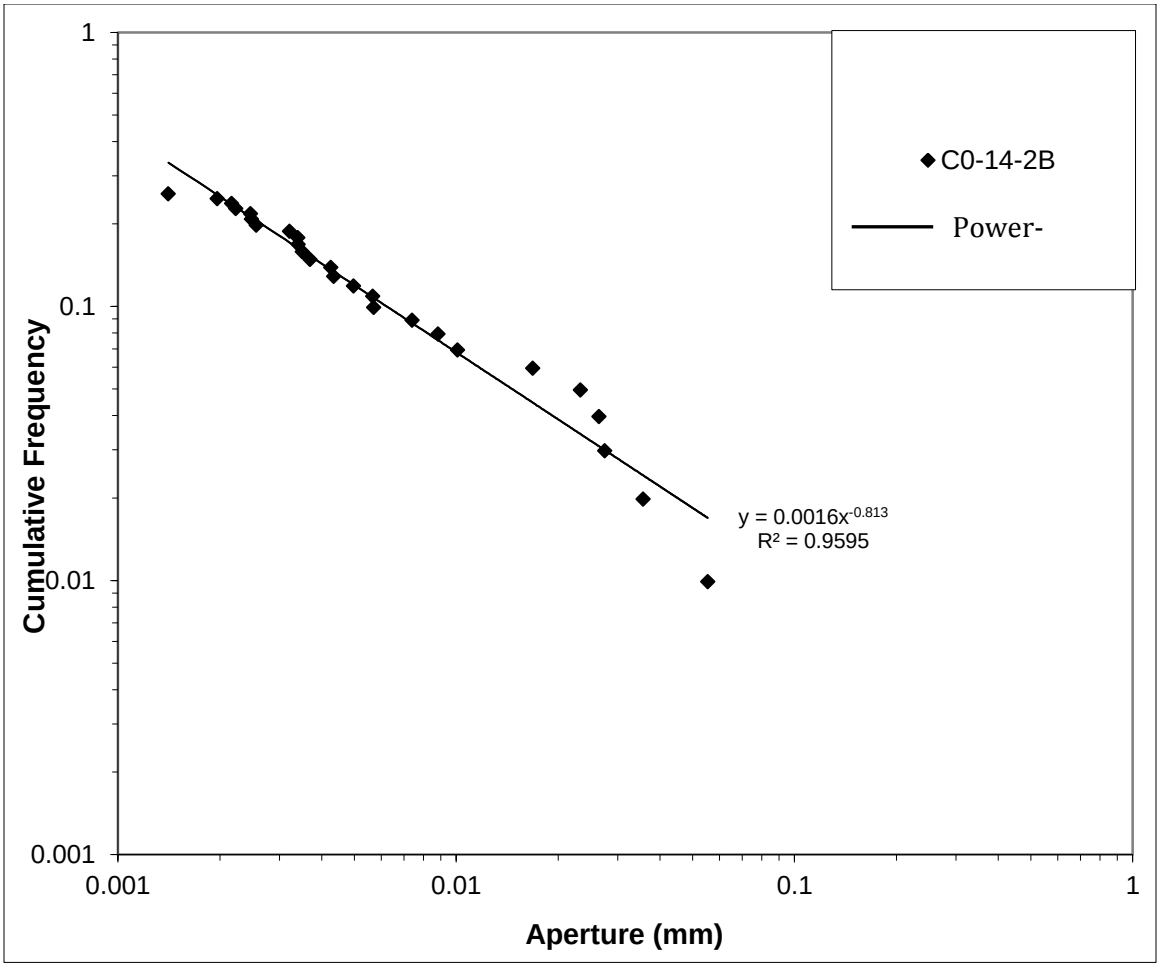

Figure A.4 Kinematic aperture versus cumulative frequency plots for sample CO-14-2B.

FRACTURE STRAIN CALCULATION

Fracture strain quantifies the extension accommodated by fracture opening along a line sample oriented perpendicular to the fractures. Fracture strain is equal to the sum of all apertures divided by the sum of all spacings which corresponds to the initial length of the scanline prior to fracture formation. The initial length of the scanline is represented by

the sum of kinematic aperture whereas the final length is represented by sum of the aperture plus spacing.

$$\boldsymbol{\varepsilon} = \frac{L - L_0}{L_0} = \frac{\Sigma\, Aperture}{\Sigma\, Spacing}$$

$$L = final\ length = \Sigma\, aperture + \Sigma\, spacing$$

$$L_0 = initial\ length = \Sigma\, spacing$$

In many cases, macrofractures reflect a higher strain than microfractures for power law exponents < 1 (Marrett 1996; Hooker et al 2011). A smaller number of fractures with larger aperture may yield greater strain and deformation magnitudes than larger fractures with smaller apertures. To avoid any biases due to high strain results from macrofracture strain calculations, where the scanline intersect fracture have more than 0.1 mm in aperture are left out of the aperture sum, and their aperture were subtracted from the total length of the microscanline. Note that lengthening is indicated by positive strain values whereas shortening is indicated by negative values. (Twiss and Moores, 2007).

KINEMATIC MODEL CONSTRUCTION

In this study, Midland Valley Move 2D and 3D structural geology software was used to construct balanced cross-sections and to restore the sections for forward modeling. The constructed models were also used to calculate strain associated with fold and thrust evolution. Construction of 3D models for restoration and forward modeling requires prior

construction of 2D models. Before restoring a cross-section in 2D, it is necessary to upload a digital elevation map (DEM) and georeferenced basemap to have a valid georeferenced model. The map image is first draped onto the DEM surface, and then the scanned cross-sections can be inserted at the location where they were drawn. The import menu asks, “how do you wish to import the data?” to ensure the data values represent elevation and to have the same units. In the next step, it is possible to change the import region and edit DEM data to ensure that the DEM data covers exactly the same region as the geologic map. In some cases, a DEM might represent a bigger or smaller region than the map. In order to avoid any misplacement of these DEM data and geologic map, the geologic map coordinates are used as input in this step to set up DEM data to cover the correct region. Depending on to the type of DEM data used, the option for projection parameters may also be selected (Figure 5). Once the DEM and geological map are loaded, the overlay menu that appears in the bottom left corner of the menu can be used to overlay the DEM onto the surface (Figure 6).

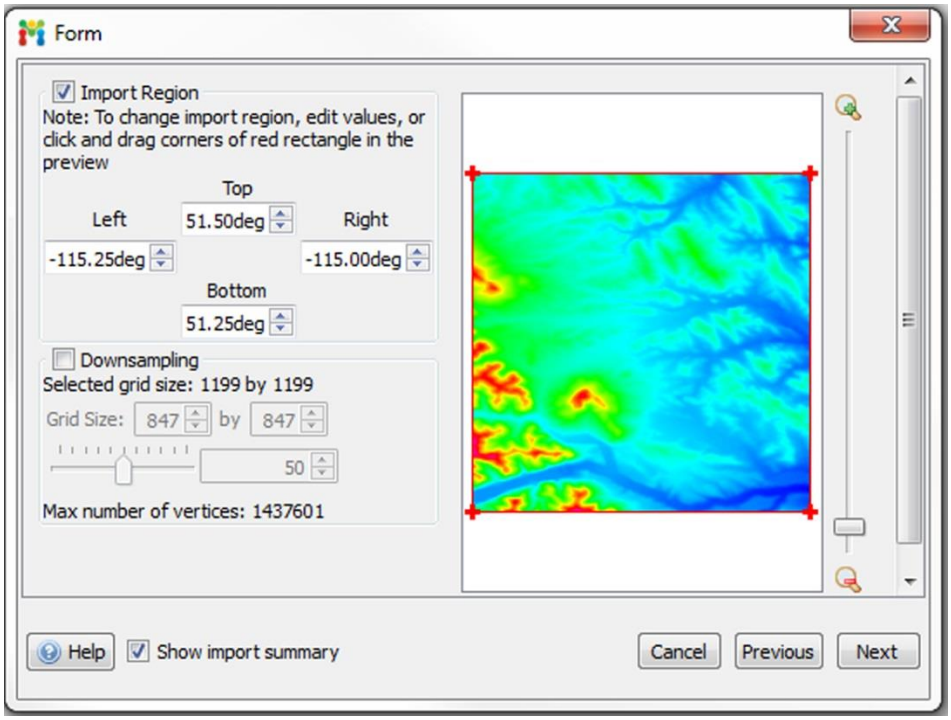

Figure A.5 Import Region selections from the menu.

a)

b)

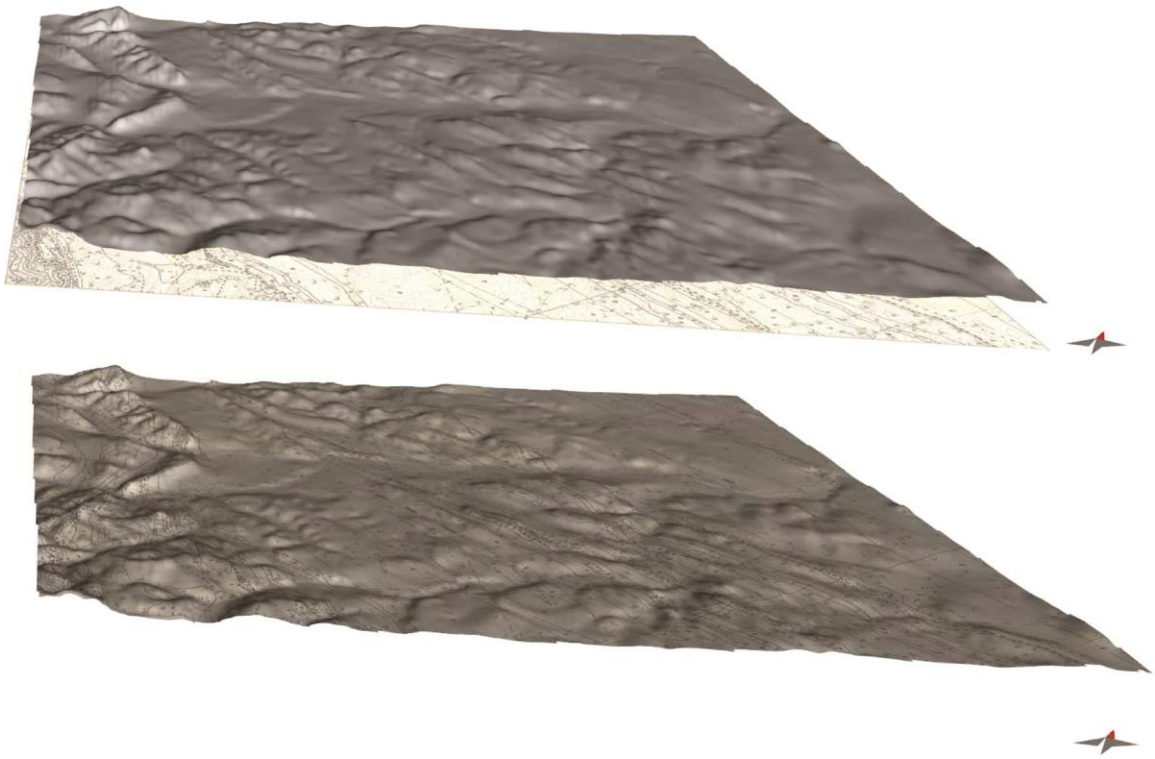

Figure A.6 .a: Inserted image and DEM into file. b:The DEM data draped onto the map.

The next step is to import the sections from the reference locations. First, the trace line showing the cross-section location is digitized. In the Model Building menu, the Trace option is used to draw a line referring to the trace for the cross-sections. Figure 7 shows the digitized section traces in the 2D map view.

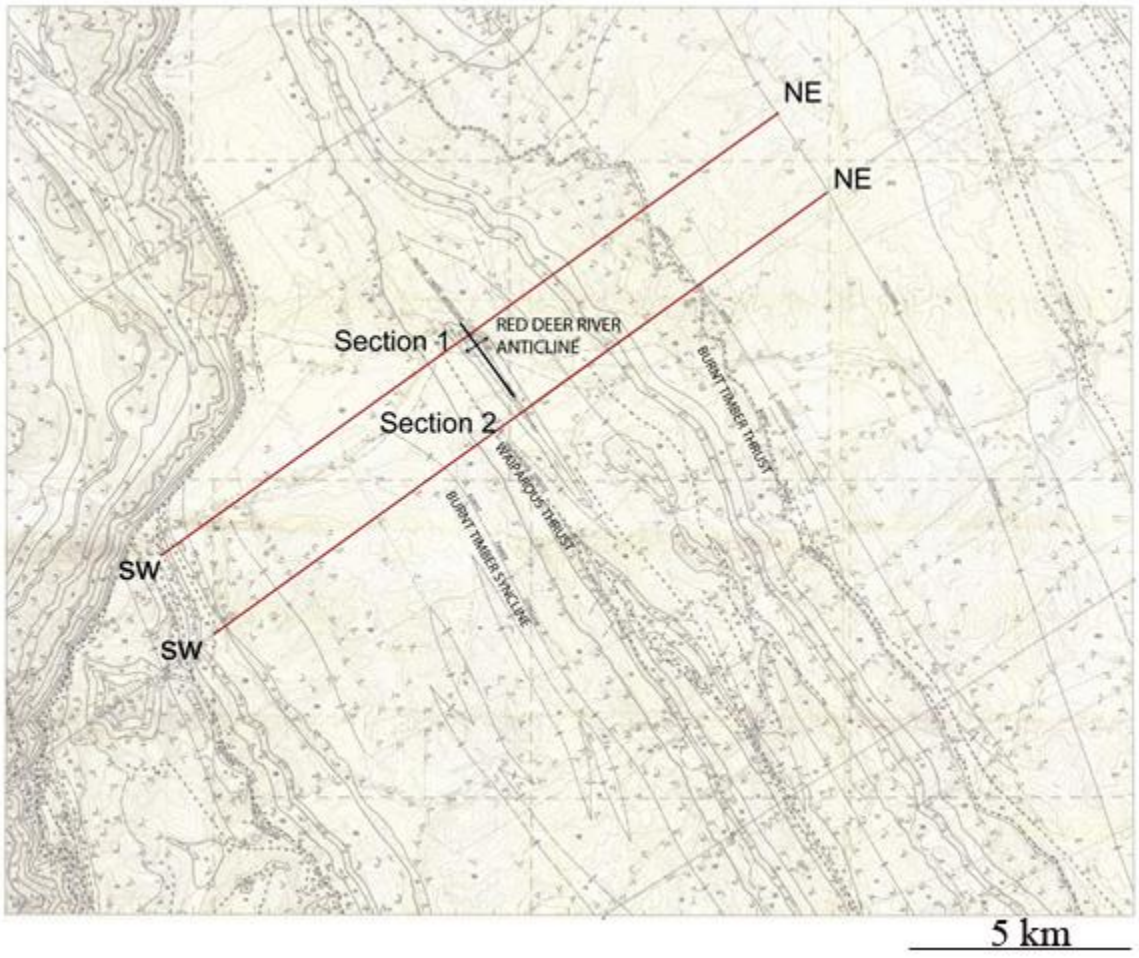

Figure A.7 Digitized section traces on the map.

The cross-section images are then imported using “insert a vertical image”. If the size of the image inserted does not match the digitized section, it is possible to change/resize the image. Figure 9 shows the inserted image from the digitized section. The same process can be repeated for multiple sections and images.

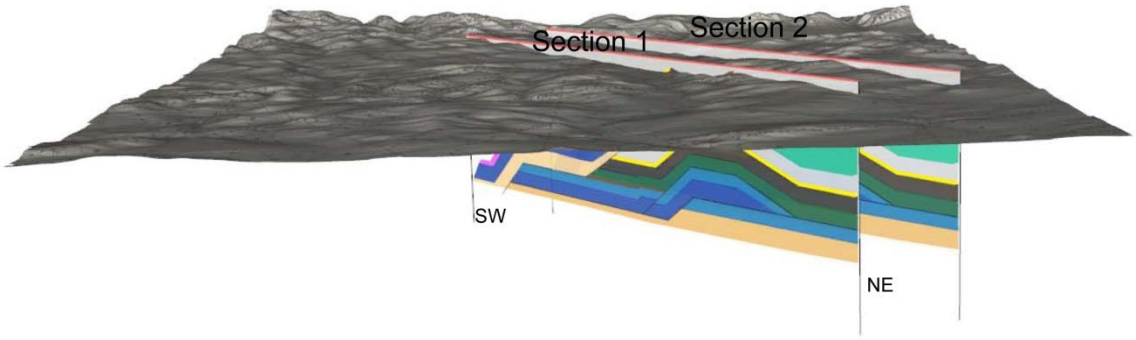

Figure A.8 The final step of data uploading showing the loaded cross-section, DEM data, and map.

Once the DEM data are draped over the map, all section traces are drawn, and images are loaded, then cross-sections can be digitized. To begin, Fault and/or Horizon options can be selected to digitize the scanned images that have been inserted into the section. As the strata and faults are digitized, they can be edited and/or retraced. Figure 9 shows the digitized stratigraphic layers and faults. After all horizons and faults are digitized, surfaces can be created between horizons in the parallel sections.

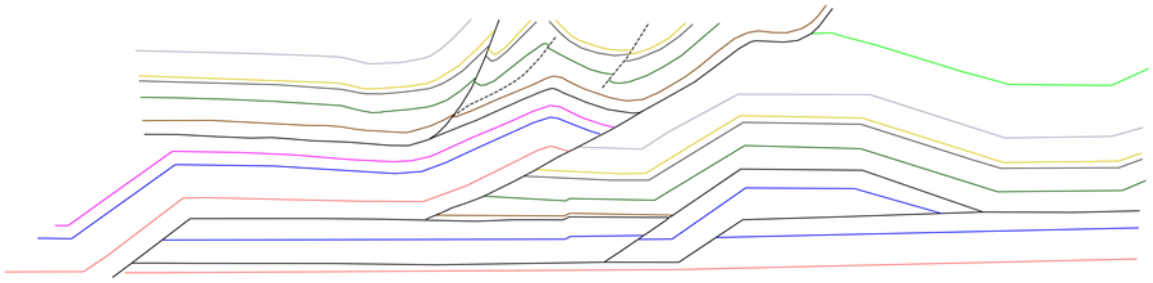

Figure A.9 Example of digitized fault and stratigraphic horizons.

In the Model Building menu, the “surface from lines” option can be selected to build a surface between the same horizon and fault in different sections. Figure 10 shows all surfaces created including faults and surfaces from the horizons.

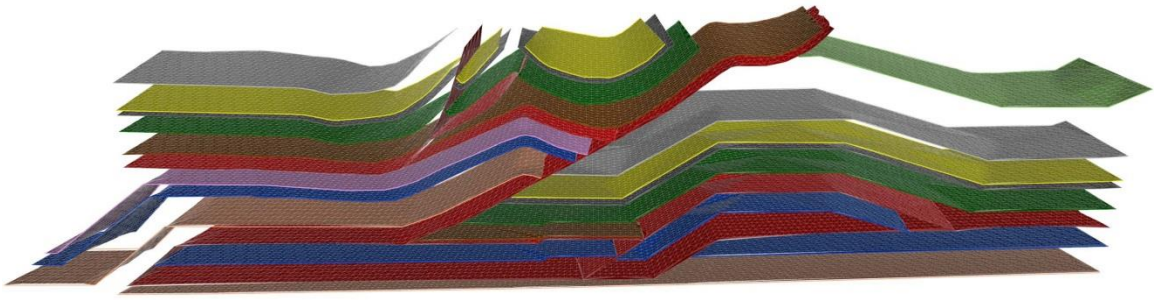

Figure A. 10 Example of all created surfaces. Red surface indicates faults

When the digitized sections including faults and horizons are ready, 2D restoration can be performed. To obtain restored and balanced 2D sections, the MOVE ON FAULT AND UNFOLDING algorithms are used. During the restoration workflow, fault offsets are restored using the MOVE ON FAULT algorithm and ductile deformations are restored using the UNFOLDING algorithm. While performing 2D KINEMATIC MODELING the sections are validated based on whether they are balanced or not (see Chapter 4 Kinematic Modeling for a detailed explanation). If they do not obey the area/line length balance constrictions, the problematic areas can be identified and corrected according to the possible deformation assumptions. To start the restoration workflow, the first step is to select the 2D MOVE ON FAULT option from the Module menu. Once the latest active fault is determined, it can be chosen as an active fault. The menu contains multiple options that can be selected according to the type of deformation, such as simple shear, and fault

parallel flow. The next step is to select the horizons affected by displacement along the fault. In the drop down menu, the horizons can be selected as OBJECTS TO BE MOVED. In the movement tab, there are multiple options that can be selected depending on the best way of restoring the displacement along the previously collected fault. The hanging wall and footwall offsets can be matched by using JOIN BEDS whereas the SLIP option can be used to provide a certain amount of displacement along the active fault. Once the restoration of displacement is done along each individual fault, it is important to save the section. This aids in finding individual restoration steps and understanding the tectonic history of the area after modeling is finished. While performing the 2D restoration workflow, the fault to be activated must be continuous along the hanging wall layers. For example, in some cases during restoration of the imbricated thrust fault attached to a single detachment fault, the individual fault should be split and joined where they intersect (Figure 11).

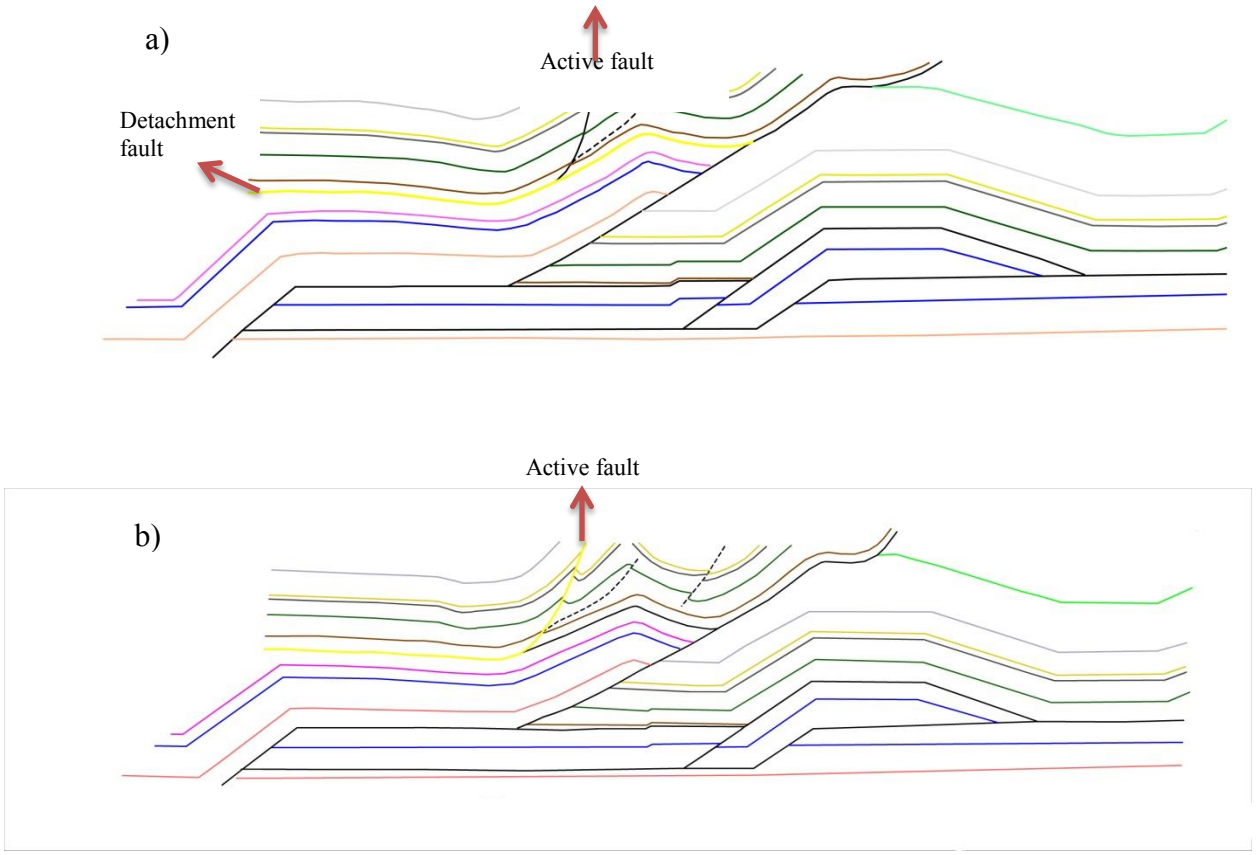

Figure A.11 Selecting the active detachment fault with active fault. a) The active fault is not split b) active fault is attached to the detachment fault

The end product of the restoration may show some degree of flexural bending that needs to be restored. In this case, the 2D Unfolding module is used to restore the model. For this purpose, a reference horizontal line is created in the same way that the horizons are created. With the 2D UNFOLDING algorithm selected, the new line is collected as a TARGET and the layers that will be restored are selected as OBJECTS TO UNFOLD input.

Once the unfolding is applied, the layer will show horizontal layering. The final restoration result shows the initial stage of the layers (Figure 12).

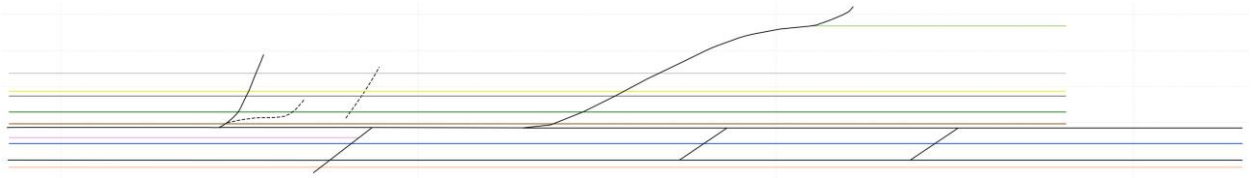

Figure A. 12 Example of completely restored and unfolded section.

The 2D and 3D forward models are based on the restored geological cross-sections obtained from their initial geometry to validate the structural interpretation and evolutionary development of geological structures. 3D models provide opportunities to visualize structures between the sections while performing progressive forward modeling. 3D Forward Modeling makes it possible to track strain accumulation and strain path simulations at the locations of higher and lower extensional strain during deformation. The final restoration stage can be used as the first step of forward modeling. When using the 2D or 3D Move on Fault selections under MODULES in the menu, the best option for the active fault depending on the deformation style can be selected. The 2D Forward Modeling algorithm contains the applications SIMPLE SHEAR, FAULT PARALLEL FOLDING, FAULT PROPAGATION FOLDING, FAULT BEND FOLDING, DETACHMENT FOLDING AND TRISHEAR whereas the 3D forward modeling offers only SIMPLE SHEAR, FAULT PARALLEL FLOW. After selecting the deformation style, the active fault, and the layer for the objects to move sections, the displacement can be performed.

During forward modeling in 3D, there are other important points that may affect the final result of the forward model workflow and the result of strain calculations. TRANSPORT DIRECTION must be correctly set up to produce a realistic and valid model. Transport Direction, which refers to the movement direction and inclination, is one of the most important controls for the movement of material over the fault in 3D modeling (Figure 13).

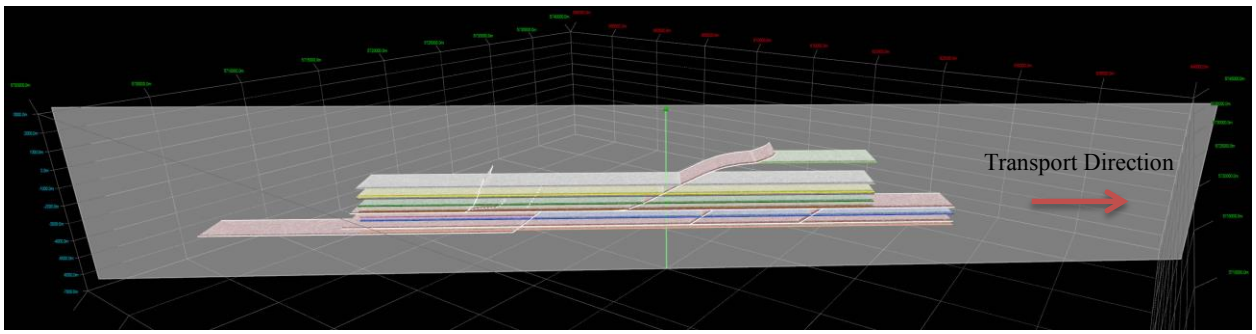

Figure A. 13 Transport direction indicated by the semi-transparent surface.

If Transport Plane is not set up correctly the beds move in the wrong direction. Transport plane is displayed as a semi-transparent plane in the 3D View. The long axis of the plane should be parallel to the transport direction. If incorrect values for the transport direction have been selected for forward modeling, the layer will move away from the section (Figure 14). Assuming thrust faults always follow bedding and cut upsection in the direction of transport, strata overlying the fault have to move along faults. As strata move

along a fault, they shift in relation to the fault location. This shifting issue can be resolved by inputting the correct transport direction.

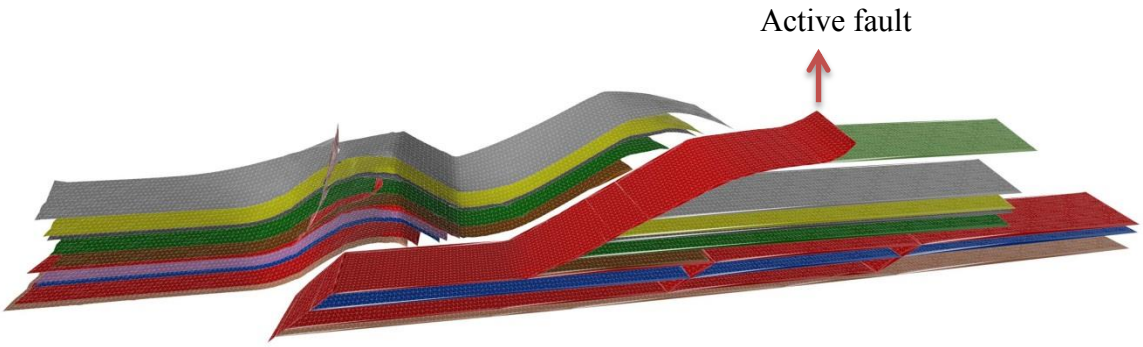

Figure A.14 Shifted strata translated along an incorrect transport direction.

One of the most important aspects of 3D modeling in Move is surface resampling. In 3D modeling, surfaces are created from points. The number of points directly affects how smoother surfaces can be used properly in 3D modeling. Using only a few points can lead to geologically unreasonable results. Therefore, the density of surface sampling is a crucial parameter. While performing MOVE ON A FAULT in 3D, using a low density of surface sampling on the active surfaces may cause the surfaces to pass through the fault instead of moving along the fault. Increasing the number of points on surfaces to have a higher sampling density can fix the problem of surfaces passing through the fault (Figure 15). As the surface is moved over the fault, the points are moved but as there are no central points on the surfaces, the parts without points are not affected by the fault. With

higher surface density, the active surfaces will not pass through the fault surface and the result will be geologically reasonable. Using reasonably resampled surfaces is also important for strain calculations. Because the movement of the points relative to each other is used to calculate strain, the density of surface sampling is critical for producing better strain results. A higher surface density produces a more detailed strain pattern whereas a low surface density produces less detailed results (Move Tutorial, 2013). As fracture modeling is performed, the sampling of your surface will have a big effect on the calculated strain, where the surface is highly sampled the strain will be calculated to a finer detail. Thus, surfaces were resampled by using "Adaptative Sampling" option in the menu to produce a surface mesh that is suitable for fracture modeling. In this study, surfaces were resampled with Adaptative Sampling. Maximum edge length and maxiumum distance were set up to 100 m and 1m, respectively (Figure 16).

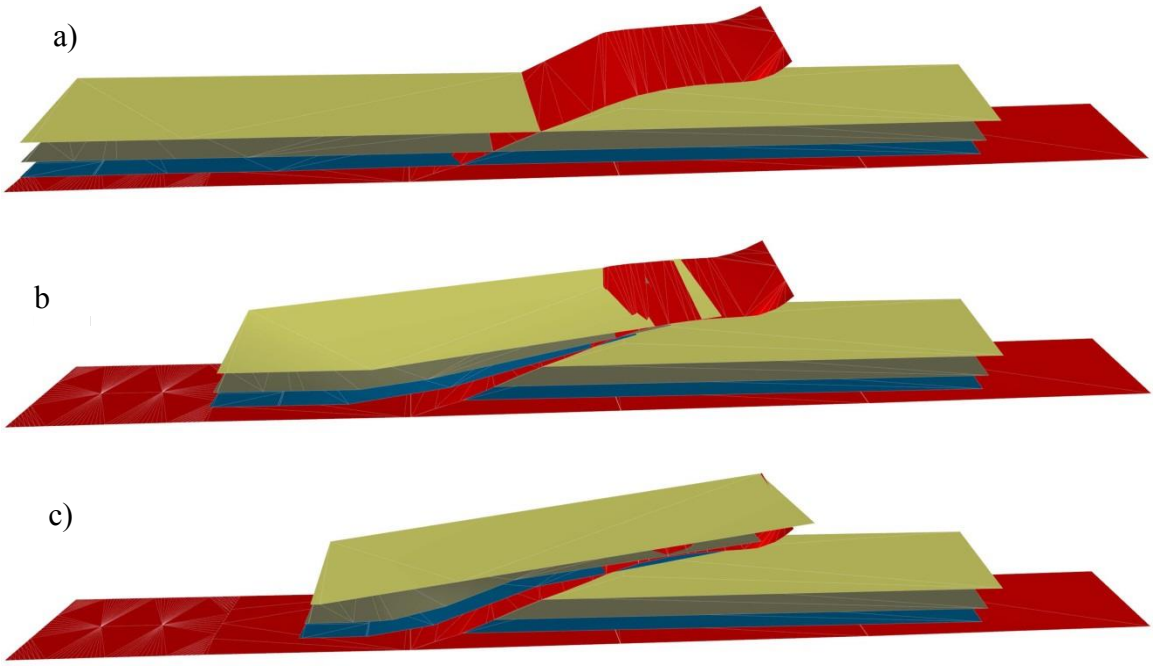

Figure A.15. Surface resampling in Move. a: there are only very few points on each of the surfaces moving over the fault. b: The surfaces without enough points passing through the fault . c: The surface with not enough sampling points do not move along the fault surface and deform by the fault.

a)

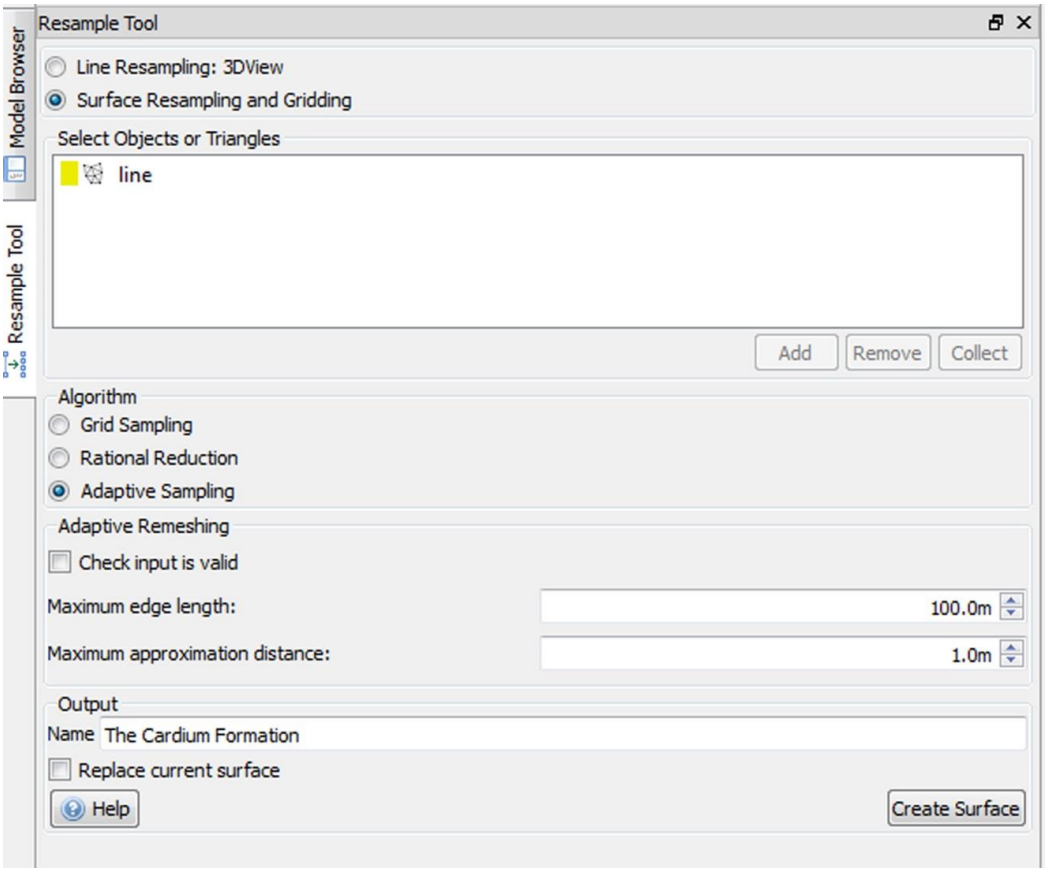

b)

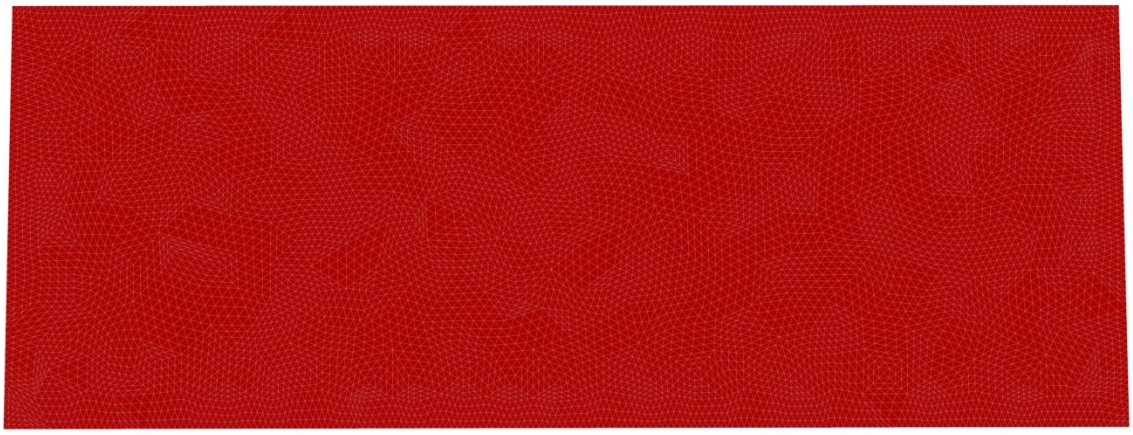

Figure A.16 Surface resampling using "Adaptative Resampling" a: The input used for the surfaces. b: The example of surfaces after resampling showing created small triangles in the surface.

As 3D modeling is performed, strain values were calculated. For all calculations e_1 and e_{xx} was selected by using the "strain" tool under Data & Analysis in Move and the orientation of maximum elongation was recorded. The generated structural models show the strain distribution associated with deformation on the top boundary of the Cardium Sandstone (Figure 17). Note that as strain is calculated the "Tensor" option under strain calculation menu should be toggled on to make sure the strain attributes can be saved onto Geocellular volume where resultant fractures could be generated later.

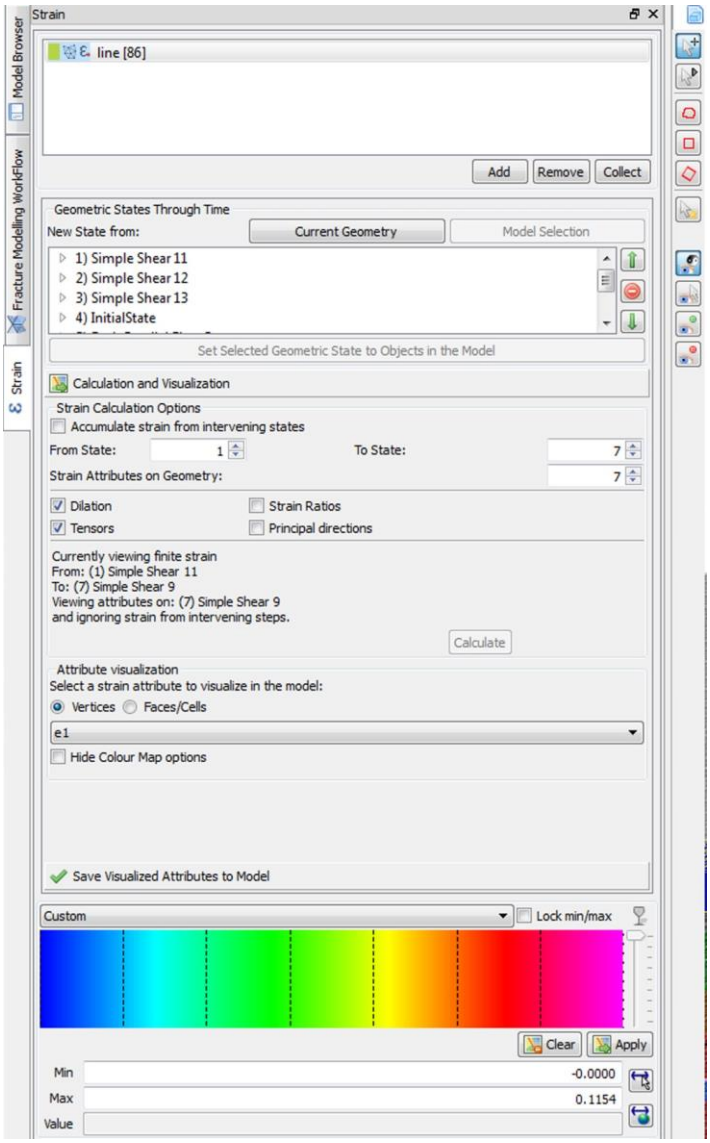

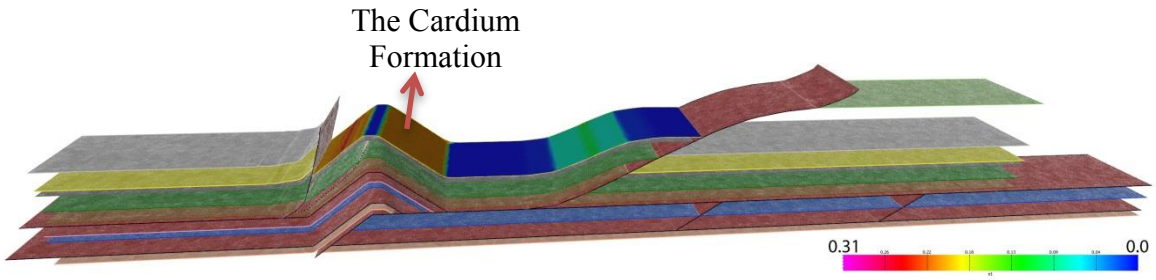

Figure A.17. a: e1 was selected for the strain calculation under strain tool. b:An example of strain calculation during forward modeling.

Using the strain distribution calculations derived from forward modeling, fracture distribution models were generated using Move's "fracture modeling" tool. To generate fractures, first of all, a 3D geocellular volume in which the fracture sets will be populated was created between the bottom of the Cardium Formation and the top of the Blackstone Formation. Strain attributes calculated in the previous step were saved onto the geocellular volume (Figure 18).

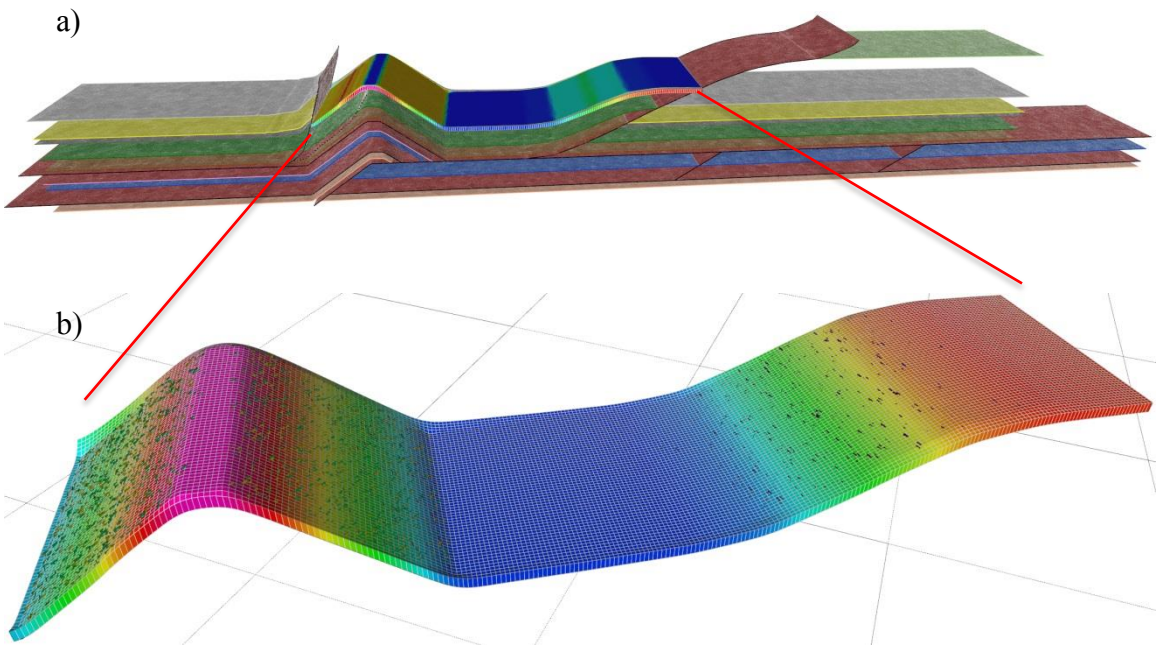

Figure A.18. a: Calculated strain distribution and the generated geocellular volume between the strata b: The geocellular volume including populated fractures showing fracture intensity difference based on the strain data.

As fracture modeling is performed, the software requires that certain information is fed in order to populate the geocellular volume with fractures: 1) the number of sets expected, and 2) the orientation (azimuth) of these fracture sets. Based on known fracture data measured in the field (see Chapter 3), three fracture sets were generated on the geocellular volume (Figure 19).

a)

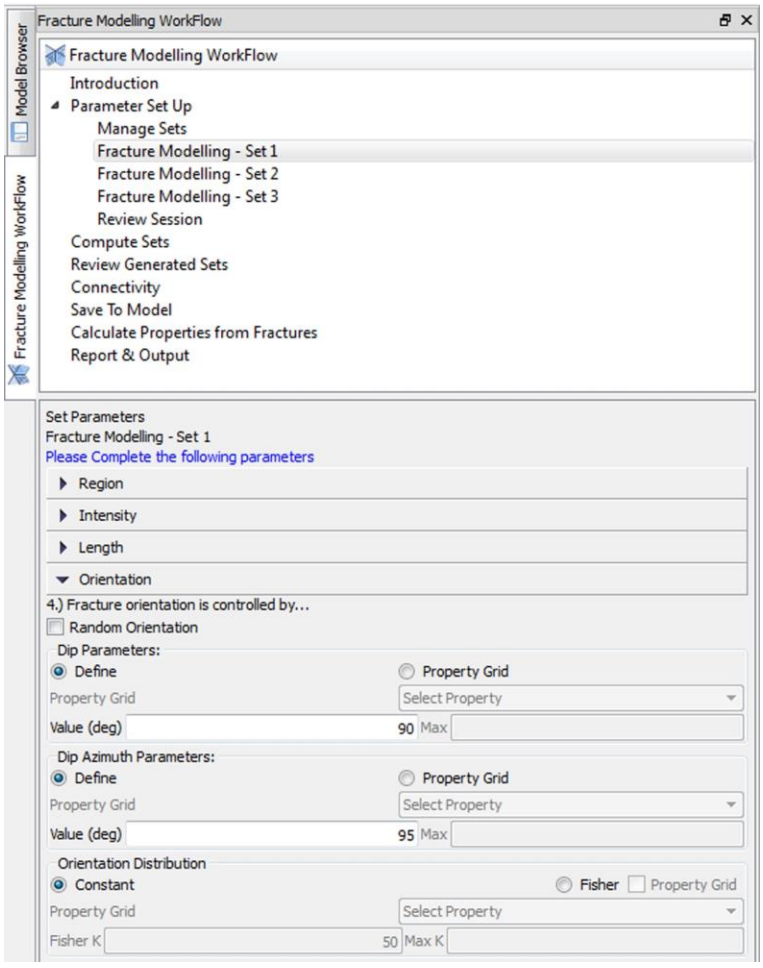

Figure A. 19 a Data input under fracture modeling tool b:An example of generated fractures in 3D geocellular volume. The three fracture sets (highlighted by green, blue and red) were generated based on the dip and azimuth data measured in the field.

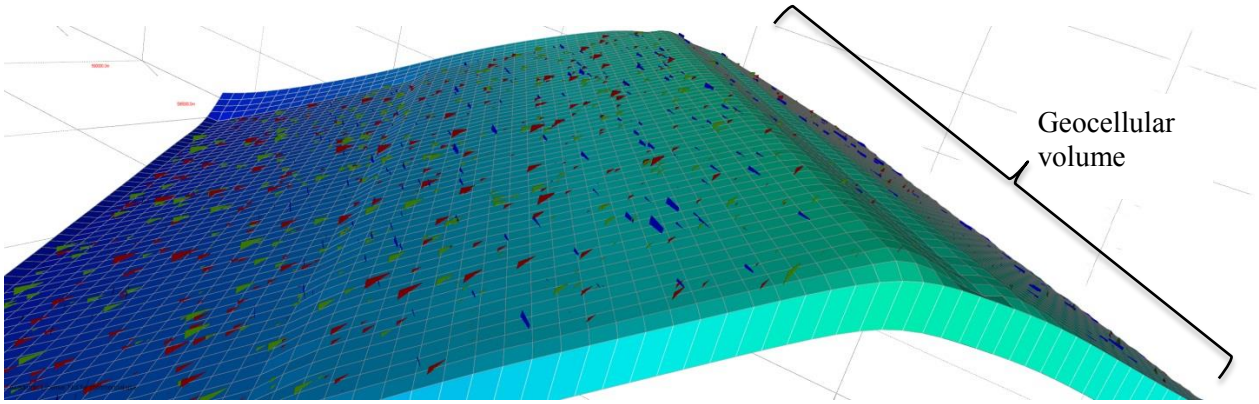

Figure A.19 b An example of generated fractures in 3D geocellular volume. The three fracture sets (highlighted by green, blue and red) were generated based on the dip and azimuth data measured in the field.

When you are carrying out the Fracture Modelling workflow, strain properties that were saved onto the GeoCellular Volume, such as e1, can be used as a proxy for fracture intensity. This can be set up under the "Intensity" tab for each fracture set (Figure 20).

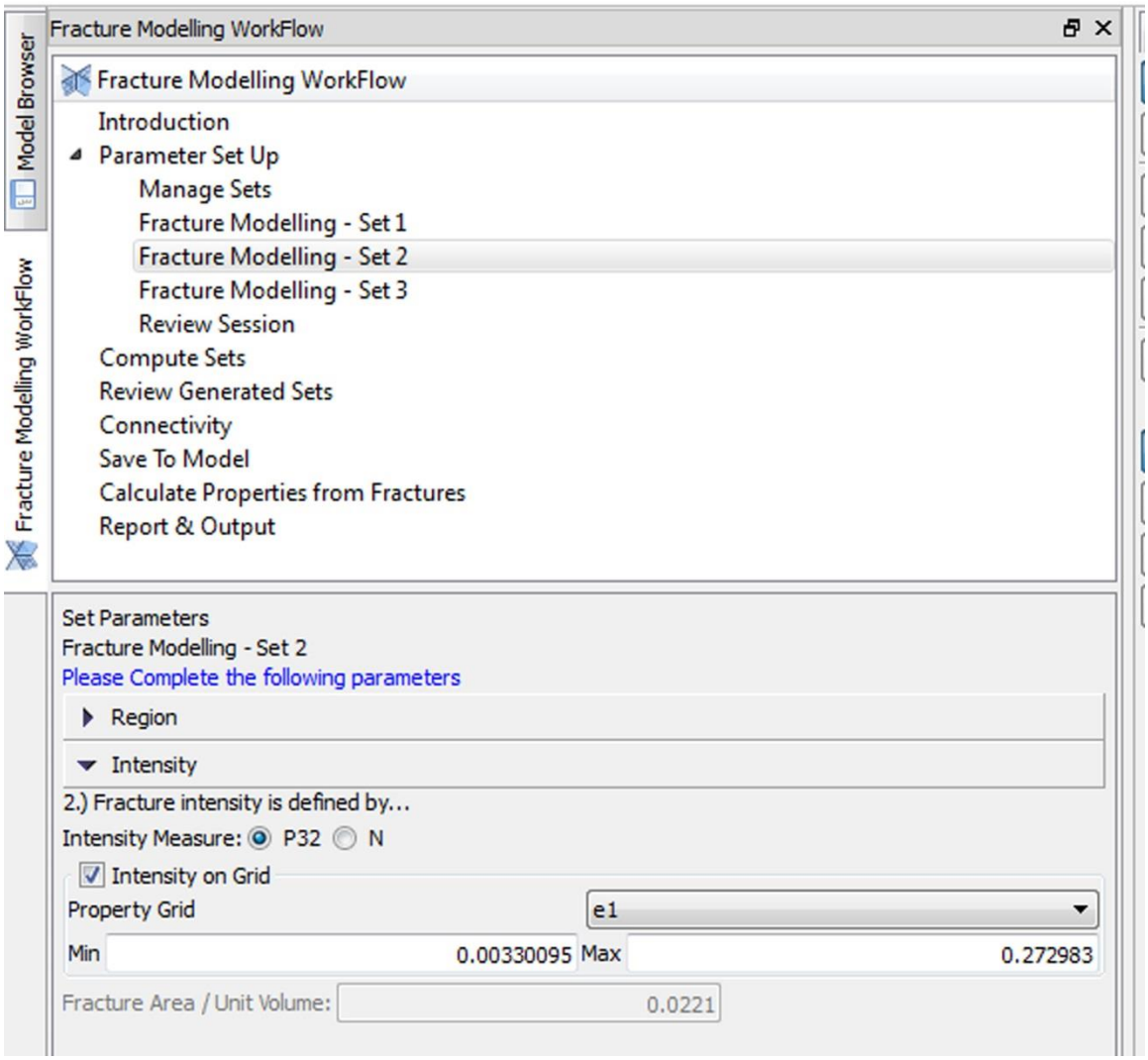

Figure A.20 Data input under fracture modeling tool showing e1 was selected as proxy for fracture intensity.

References

Bai, T., and D. D. Pollard, 2000, Fracture spacing in layered rocks: a new explanation based on the stress transition: Journal of Structural Geology, v. 22, p. 43-57.

Bally, A. W., P. Gordy, and G. A. Stewart, 1966, Structure, seismic data, and orogenic evolution of southern Canadian Rocky Mountains: Bulletin of Canadian Petroleum Geology, v. 14, p. 337-381.

Barton, C. C., 1983, Systematic jointing in the Cardium sandstone along the Bow River, Alberta, Canada: PhD thesis, Yale University, 301 p.

Beaumont, C., 1981, Foreland basins: Royal Astronomical Society Geophysical Journal International, v. 65, p. 291-329.

Becker, A., and M. R. Gross, 1996, Mechanism for joint saturation in mechanically layered rocks: an example from southern Israel: Tectonophysics, v. 257, p. 223-237.

Becker, S., P. Eichhubl, S. Laubach, R. Reed, R. Lander, and R. Bodnar, 2010, A 48 my history of fracture opening, temperature, and fluid pressure: Cretaceous Travis Peak Formation, East Texas basin: Geological Society of America Bulletin, v. 122, p. 1081-1093.

Beekman, F., M. Badsi, and J.-D. van Wees, 2000, Faulting, fracturing and in situ stress prediction in the Ahnet Basin, Algeria—A finite element approach: Tectonophysics, v. 320, p. 311-329.

Bellahsen, N., P. Fiore, and D. D. Pollard, 2006, The role of fractures in the structural interpretation of Sheep Mountain Anticline, Wyoming: Journal of Structural Geology, v. 28, p. 850-867.

Bergbauer, S., and D. D. Pollard, 2004, A new conceptual fold-fracture model including prefolding joints, based on the Emigrant Gap anticline, Wyoming: Geological Society of America Bulletin, v. 116, p. 294-307.

Boettcher, D., M. Thomas, M. Hrudey, D. Lewis, C. O'Brien, B. Oz, D. Repol, and R. Yuan, 2010, The Western Canada Foreland Basin: a basin-centred gas system: Petroleum Geology: From Mature Basins to New Frontiers – Proceedings of the 7th Petroleum Geology Conference., p. 1099-1123.

Bonnet, E., O. Bour, N. E. Odling, P. Davy, I. Main, P. Cowie, and B. Berkowitz, 2001, Scaling of fracture systems in geological media: Reviews of Geophysics, v. 39, p. 347-383.

Boyer, S. E., and D. Elliott, 1982, Thrust systems: AAPG Bulletin, v. 66, p. 1196-1230.

Casini, G., Gillespie, P.A. , 2011, Sub-seismic fractures in foreland fold and thrust belts: Insight from the Lurestan Province, Zagros Mountains, Iran: Petroleum Geoscience, v. 17, p. 263–282.

Cooper, M., 1992, The analysis of fracture systems in subsurface thrust structures from the foothills of the Canadian Rockies: Thrust tectonics, London, Chapman and Hall, p. 391-405.

Corbett, K., M. Friedman, and J. Spang, 1987, Fracture development and mechanical stratigraphy of Austin Chalk, Texas: AAPG Bulletin, v. 71, p. 17-28.

Couzens-Schultz, B. A., B. C. Vendeville, and D. V. Wiltschko, 2003, Duplex style and triangle zone formation: insights from physical modeling: Journal of Structural Geology, v. 25, p. 1623-1644.

Couzens, B. A., and D. V. Wiltschko, 1996, The control of mechanical stratigraphy on the formation of triangle zones: Bulletin of Canadian Petroleum Geology, v. 44, p. 165-179.

Creaney, S., and J. Allan, 1992, Petroleum Systems in the Foreland Basin of Western Canada: Chapter 10: AAPG Foreland Basins and Fold Belts, AAPG Memoir, v. 55, p. 279-308.

Dahlstrom, C., 1969, Balanced cross sections: Canadian Journal of Earth Sciences, v. 6, p. 743-757.

Dahlstrom, C. D., 1970, Structural geology in the eastern margin of the Canadian Rocky Mountains: Bulletin of Canadian Petroleum Geology, v. 18, p. 332-406.

Dahlstrom, C. D., 1990, Geometric constraints derived from the law of conservation of volume and applied to evolutionary models for detachment folding: AAPG Bulletin, v. 74, p. 336-344.

De Sitter, L. U., 1964, Structural geology, McGraw-Hill New York.

Dechesne, R. G. V., B., 2000, Fractured Cretaceous and Triassic strata of the Central Alberta Foothills, GeoCanada 2000, Field Trip Guide.

Deroo, G., T. Powell, B. Tissot, R. McCrossan, and P. Hacquebard, 1976, The origin and migration of petroleum in the Western Canadian sedimentary basin. Alberta—a geochemical and thermal maturation study, v. 262, Geological Survey of Canada Bulletin.

Dunne, W. M., 1986, Mesostructural development in detached folds: an example from West Virginia: The Journal of Geology, p. 473-488.

Eisbacher, G., M. A. Carrigy, and R. B. Campbell, 1974, Paleodrainage pattern and late-orogenic basins of the Canadian Cordillera: Tectonics and Sedimentation, The Society of Economic Paleontologists and Mineralogists (SEPM), v. 22, p. 143-166.

Fermor, P., 1999, Aspects of the three-dimensional structure of the Alberta Foothills and Front Ranges: Geological Society of America Bulletin, v. 111, p. 317-346.

Fischer, M., N. Woodward, and M. Mitchell, 1992, The kinematics of break-thrust folds: Journal of Structural Geology, v. 14, p. 451-460.

Fischer, M. P., and P. B. Jackson, 1999, Stratigraphic controls on eformation patterns in fault-related folds: a detachment fold example from the Sierra Madre Oriental, northeast Mexico: Journal of Structural Geology, v. 21, p. 613-633.

Fischer, M. P., Wilkerson, M.S, 2000, Predicting the orientation of joints from fold shape: results of pseudo-three-dimensional modeling and curvature analysis: Geology, v. 28, p. 15–18.

Fox, F. G., 1959, Structure and accumulation of hydrocarbons in southern Foothills, Alberta, Canada: AAPG Bulletin, v. 43, p. 992-1025.

Gale, J. F., S. E. Laubach, R. A. Marrett, J. E. Olson, J. Holder, and R. M. Reed, 2004, Predicting and characterizing fractures in dolostone reservoirs: using the link

between diagenesis and fracturing: The geometry and petrogenesis of dolomite hydrocarbon reservoirs: Geological Society (London) Special Publication, v. 235, p. 177-192.
Ghosh, G., and D. Saha, 2005, Kinematics of large scale asymmetric folds and associated smaller scale brittle—Ductile structures in the proterozoic somnur formation, pranhita—Godavari Valley, South India: Journal of Earth System Science, v. 114, p. 125-142.
Gillespie, P., J. Walsh, J. Watterson, C. Bonson, and T. Manzocchi, 2001, Scaling relationships of joint and vein arrays from The Burren, Co. Clare, Ireland: Journal of Structural Geology, v. 23, p. 183-201.
Gomez, L. A., and S. E. Laubach, 2006, Rapid digital quantification of microfracture populations: Journal of Structural Geology, v. 28, p. 408-420.
Gómez Torres, L. A., 2007, Characterization of the spatial arrangement of opening-mode fractures: PhD thesis, The University of Texas at Austin, Austin, Texas, 844 p.
Gordy, P. L., Frey, F.R., and Norris, D.K. , 1977, Geological guide for the CSPG and the 1977 waterton glacier park field conference, p. 93.
Gross, M. R., and Y. Eyal, 2007, Throughgoing fractures in layered carbonate rocks: Geological Society of America Bulletin, v. 119, p. 1387-1404.
Hamilton, W. N., Langenberg, C.W. and Price, M., 1999, Geological Map of Alberta (1:1 000 000): Alberta Energy and Utilities Board, Alberta Geological Survey.
Hancock, P., 1985, Brittle microtectonics: principles and practice: Journal of structural geology, v. 7, p. 437-457.
Hartel, T. H., 2013, Fractures in the Cardium and Normal Faults in Western Alberta.
Helgeson, D., and A. Aydin, 1991, Characteristics of joint propagation across layer interfaces in sedimentary rocks: Journal of Structural Geology, v. 13, p. 897-911.
Hitchon, B., 1985, Geothermal gradients, hydrodynamics, and hydrocarbon occurrences, Alberta, Canada: AAPG Bulletin, v. 68, p. 713-743.
Hobbs, B., E., Means, W. D. & Williams, P. F., 1976, An outline of structural geology, Wiley New York.
Hooker, J., J. Gale, L. Gomez, S. Laubach, R. Marrett, and R. Reed, 2009, Aperture-size scaling variations in a low-strain opening-mode fracture set, Cozzette Sandstone, Colorado: Journal of Structural Geology, v. 31, p. 707-718.
Hooker, J., L. Gomez, S. Laubach, J. Gale, and R. Marrett, 2012, Effects of diagenesis (cement precipitation) during fracture opening on fracture aperture-size scaling in carbonate rocks: Geological Society, London, Special Publications, v. 370, p. 187-206.
Hooker, J., S. Laubach, L. Gomez, R. Marrett, P. Eichhubl, K. Diaz-Tushman, and E. Pinzon, 2011, Fracture size, frequency, and strain in the Cambrian Eriboll Formation sandstones, NW Scotland: Scottish Journal of Geology, v. 47, p. 45-56.
Hooker, J. N., Laubach, S.E., and Marrett, R., 2014, A universal power-law scaling exponent for fracture apertures in sandstones.: Geological Society of America Bulletin, v. 126, p. 1340–1362.

Jaeger JC, C. N., Zimmerman RW 2007, Fundamentals of rock mechanics, John Wiley & Sons.
Jäger, P., S. Schmalholz, D. Schmid, and E. Kuhl, 2008, Brittle fracture during folding of rocks: A finite element study: Philosophical Magazine, v. 88, p. 3245-3263.
Jamison, W. R., 1992, Stress controls on fold thrust style, Thrust tectonics, Chapman and Hall: London, p. 155-164.
Jamison, W. R., 1997, Quantitative evaluation of fractures on Monkshood anticline, a detachment fold in the foothills of western Canada: AAPG Bulletin, v. 81, p. 1110-1132.
Kerr, W., 1980, A geological explanation for the variation in fluid properties across the Pembina Cardium Field: Journal of Canadian Petroleum Technology, v. 19, p. 76-84.
Krause, F., K., Deutsch, K.B., Joiner, S.D., Barclay, J.E., Hall, R.L. and Hills, L.V., 1994, Chapter 23, Cretaceous cardium formation of the Western Canada sedimentary basin In: Atlas of the Western Canada Sedimentary Basin. : Geological Atlas of the Western Canada Sedimentary Basin. GD Mossop and I. Shetson (eds.). Alberta Research Council and Canadian Society of Petroleum Geologists, p. 485-511.
Lander, R. H., R. E. Larese, and L. M. Bonnell, 2008, Toward more accurate quartz cement models: The importance of euhedral versus noneuhedral growth rates: AAPG Bulletin, v. 92, p. 1537-1563.
Langenberg, C., A. Beaton, and H. Berhane, 2006, Regional evaluation of the coalbed-methane potential of the Foothills/Mountains of Alberta, Canada: International journal of coal geology, v. 65, p. 114-128.
Langenberg, C. W., 1983, Polyphase deformation in the Canadian Shield of northeastern Alberta: Alberta Geological Survey Bulletin, v. 45, p. 1-33.
Langenberg, K. T. E. a. C. W., 2002, Structural cross sections, constructed to assess the coal-bed methane potential of the Foothills of Alberta: GeoConvention, Canadian Society of Petroleum Geologists.
Larson, K. P., R. A. Price, and D. A. Archibald, 2006, Tectonic implications of 40Ar/39Ar muscovite dates from the Mt. Haley stock and Lussier River stock, near Fort Steele, British Columbia: Canadian Journal of Earth Sciences, v. 43, p. 1673-1684.
Laubach, S. E., 1988, Subsurface fractures and their relationship to stress history in East Texas basin sandstone: Tectonophysics, v. 156, p. 37-49.
Laubach, S. E., 1997, A method to detect natural fracture strike in sandstones: AAPG Bulletin, v. 81, p. 604-623.
Laubach, S. E., J. E. Olson, P. Eichhubl, S. Fomel, and R. A. Marrett, 2010, Natural fractures from the perspective of diagenesis: Canadian Society of Exploration Geophysicists Recorder, v. 35, p. 27-31.
Leckie, D. A. a. S., D.G., 1992, Regional setting, evolution and depositional cycles of the Western Canadian foreland basin. In: Foreland Basins and Fold Belts: AAPG Memoir, v. 55, p. p. 9-46.

Lemiszki, P. J., J. D. Landes, and R. D. Hatcher, 1994, Controls on hinge-parallel extension fracturing in single-layer tangential-longitudinal strain folds: Journal of Geophysical Research: Solid Earth (1978–2012), v. 99, p. 22027-22041.

Lisle, R. J., 1994, Detection of zones of abnormal strains in structures using Gaussian curvature analysis: AAPG Bulletin, v. 78, p. 1811-1819.

MacKay, P. A., J. L. Varsek, T. E. Kubli, R. G. Dechesne, A. C. Newson, and J. P. Reid, 1996, Triangle zones and tectonic wedges: An introduction: Bulletin of Canadian Petroleum Geology, v. 44, p. I. 1-I. 5.

Marrett, Randall, and Laubach, S. E., 2001, Fracturing during burial diagenesis, in Marrett, R., ed., Genesis and controls of reservoir-scale carbonate deformation, Monterrey salient, Mexico: The University of Texas at Austin, Bureau of Economic Geology, Guidebook 28, p. 109-120.

Marrett, R., 1996, Aggregate properties of fracture populations: Journal of Structural Geology, v. 18 (2), p. 169-178.

Marrett, R., O. J. Ortega, and C. M. Kelsey, 1999, Extent of power-law scaling for natural fractures in rock: Geology, v. 27, p. 799-802.

McConaughy, D. T., and T. Engelder, 2001, Joint initiation in bedded clastic rocks: Journal of Structural Geology, v. 23, p. 203-221.

McConnell, D. A., 1994, Fixed-hinge, basement-involved fault-propagation folds, Wyoming: Geological Society of America Bulletin, v. 106, p. 1583-1593.

McMechan, M., 2012, Structural Style and Kinematic Evolution of the Central Rocky Mountain Foothills, British Columbia and Alberta: GeoConvention

Mercier, E., Rafi, S., Ahmadi, R., 2007, Folds kinematics in “Fold-and-Thrust Belts” the “Hinge Migration” question, a review, Thrust Belts and Foreland Basins, From Fold Kinematics to Hydrocarbon Systems, Chapter 7: Frontiers in Earth Sciences., Springer Berlin, Heidelberg,, p. 135-147.

Milliken, K. L., and S. E. Laubach, 2000, Brittle deformation in sandstone diagenesis as revealed by cathodoluminescence imaging with application to characterization of fractured reservoirs: Cathodoluminescence in geosciences, v. Heidelburg, Springer-Verlag, p. 225–244.

Mitra, S., 1990, Fault-Propagation Folds: Geometry, Kinematic Evolution, and Hydrocarbon Traps (1): AAPG Bulletin, v. 74, p. 921-945.

Monger, J. W. H., 1989, Overview of Cordilleran geology. In: Western Canada Sedimentary Basin, A Case History: Canadian Society of Petroleum Geologists, p. 9-23.

Muecke, G., and H. Charlesworth, 1966, Jointing in folded Cardium sandstones along the Bow River, Alberta: Canadian Journal of Earth Sciences, v. 3, p. 579-596.

Murray Jr, G. H., 1968, Quantitative Fracture Study--Sanish Pool, Mckenzie County, North Dakota: AAPG Bulletin, v. 52, p. 57-65.

Narr, W., and J. B. Currie, 1982, Origin of fracture porosity--example from Altamont field, Utah: AAPG Bulletin, v. 66, p. 1231-1247.

Narr, W., and J. Suppe, 1991, Joint spacing in sedimentary rocks: Journal of Structural Geology, v. 13, p. 1037-1048.

Nelson, R. A., 1985, Geologic analysis of naturally fractured reservoirs: Houston, Texas, Gulf Publishing, 320 p.
Neurath, C., and R. Smith, 1982, The effect of material properties on growth rates of folding and boudinage: experiments with wax models: Journal of Structural Geology, v. 4, p. 215-229.
Newson, A., 2003, The Foothills of Western Canada, a Fold and Thrust Belt Natural Gas Play: AAPG Annual Meeting 2003.
Newson, A. C., 2001, The future of natural gas exploration in the Foothills of the Western Canadian Rocky Mountains: The Leading Edge, v. 20, p. 74-79.
Ollerenshaw, N. C., 1966, Geology, Burnt Timber Creek, West of Fifth Meridian, Alberta, Geological Survey of Canada, Preliminary Map 11-1965 (1:63 360).
Olson, J. E., L. L. W., and L. S. E., 2003, Advanced Technology for Predicting the Fluid Flow Attributes of Naturally Fractured Reservoirs from Quantitative Geologic Data and Modeling, Austin, Texas, U.S. Department of Energy National Energy Technology Laboratory.
Ortega, O., and R. Marrett, 2000, Prediction of macrofracture properties using microfracture information, Mesaverde Group sandstones, San Juan basin, New Mexico: Journal of Structural Geology, v. 22, p. 571-588.
Ortega, O. J., R. A. Marrett, and S. E. Laubach, 2006, A scale-independent approach to fracture intensity and average spacing measurement: AAPG Bulletin, v. 90, p. 193-208.
Osborn, G., G. Stockmal, and R. Haspel, 2006, Emergence of the Canadian Rockies and adjacent plains: A comparison of physiography between end-of-Laramide time and the present day: Geomorphology, v. 75, p. 450-477.
Pana, D. I., and R. Elgr, 2013, Geology of the Alberta Rocky Mountains and Foothills; Energy Resources Conservation Board Map 560 (1:500000).
Pickering, G., J. Bull, and D. Sanderson, 1995, Sampling power-law distributions: Tectonophysics, v. 248, p. 1-20.
Plint, A. G., R. G. Walker, and W. L. Duke, 1988, An outcrop to subsurface correlation of the Cardium Formation in Alberta: Canadian Society of Petroleum Geologists, v. 15, p. 167- 184.
Pollard, D. D., and A. Aydin, 1988, Progress in understanding jointing over the past century: Geological Society of America Bulletin, v. 100, p. 1181-1204.
Price, N. J., 1966, Fault and joint development in brittle and semi-brittle rock, v. 1, Pergamon Press Oxford.
Price, N. J. a. C., J.W., 1990, Analysis of geological structures: Cambridge, Cambridge University Press.
Price, R.A., 1967, The tectonic significance of mesoscopic subfabrics in the Southern Rocky Mountains of Alberta and British Columbia: Canadian Journal of Earth Sciences, v. 4, p. 39-70.
Price, R., 1981, The Cordilleran foreland thrust and fold belt in the southern'Canadian Rocky Mountains: Thrust and Nappe Tectonics, ed. MP Coward, KR McClay. Geol Soc. Lond. Special Publication, v. 9, p. 427-28.

Price, R., 1994, Cordilleran tectonics and the evolution of the Western Canada Sedimentary Basin: Geological Atlas of the Western Canada Sedimentary Basin G.D. Mossop and I. Shetsen (compilers) Canadian Society of Petroleum Geologists and Alberta Research Council, v. 4, p. 13-24.

Price, R., and E. Mountjoy, 1970, Geologic structure of the Canadian Rocky Mountains between Bow and Athabasca Rivers—a progress report: Structure of the southern Canadian Cordillera: Geological Association of Canada Special Paper, v. 6, p. 7-25.

Price, R. A., 1986, The southeastern Canadian Cordillera: thrust faulting, tectonic wedging, and delamination of the lithosphere: Journal of Structural Geology, v. 8, p. 239-254.

Price, R. A. F., P. R., 1985, Structure section of the Cordilleran foreland thrust and fold belt west of Calgary, Alberta, p. 84-14.

Protzman, G. M., and G. Mitra, 1990, Strain fabric associated with the Meade thrust sheet: implications for cross-section balancing: Journal of Structural Geology, v. 12, p. 403-417.

Ramberg, H., 1964, Selective buckling of composite layers with contrasted rheological properties, a theory for simultaneous formation of several orders of folds: Tectonophysics, v. 1, p. 307-341.

Ramsay, J. G., 1967, Folding and fracturing of rock: New York, McGraw-Hill, 568 p.

Ramsay, J. G., 1974, Development of chevron folds: Geological Society of America Bulletin, v. 85, p. 1741-1754.

Ramsay, J. G., 1980, The crack-seal mechanism of rock deformation: Nature, v. 284, p. 135-139.

Reif, D., Decker, K., Grasemann, B. & Peresson, H. , 2012, Fracture patterns in the Zagros fold-and-thrust belt, Kurdistan Region of Iraq: Tectonophysics, v. 576–577, p. 46–62.

Ross, G. a. S., R.A. 1989, 1989, Crystalline basement: the foundations of Western Canada sedimentary Basin, Chapter 3. In: Western Canada Sedimentary Basin: Canadian Society of Petroleum Geologists Memoir, p. 33-45.

Rottenfusser, B., Langenberg, W., Mandryk, G., Richardson, R., Fildes, B., Olic, J., Stewart, S., Eccles, R., Evans, C., Spelrem, M., Sprecher, B., Brulotte, M., Gentzis, T., Wynne, D. and Yuan, L.P., 1991, Regional evaluation of the coal bed methane potential in the plains and foothills of Alberta,stratigraphy and rank study, Alberta Research Council, Special Report SPE-7,, p. 126 p.

Salvini, F., and F. Storti, 2001, The distribution of deformation in parallel fault-related folds with migrating axial surfaces: comparison between fault-propagation and fault-bend folding: Journal of Structural Geology, v. 23, p. 25-32.

Salvini, F., and F. Storti, 2004, Active-hinge-folding-related Deformation and its Role in Hydrocarbon Exploration and DevelopmentInsights from HCA Modeling: Thrust Tectonics and Petroleum Systems, AAPG Memoirs, v. 82, p. 453–472.

Sanderson, D. J., 1982, Models of strain variation in nappes and thrust sheets: a review: Tectonophysics, v. 88, p. 201-233.
Schultz-Ela, D. D., and Yeh, J. S., 1992, Predicting fracture permeability from bed curvature, Rock mechanics: Proceedings, 33rd U.S. symposium, Rotterdam, Balkema, p. 579–589.
Shank, J. A., and A. G. Plint, 2013, Allostratigraphy of the Upper Cretaceous Cardium Formation in subsurface and outcrop in southern Alberta, and correlation to equivalent strata in northwestern Montana: Bulletin of Canadian Petroleum Geology, v. 61, p. 1-40.
Smart, K. J., D. A. Ferrill, A. P. Morris, and R. N. McGinnis, 2012, Geomechanical modeling of stress and strain evolution during contractional fault-related folding: Tectonophysics, v. 576, p. 171-196.
Srivastava, D. C., and T. Engelder, 1990, Crack-propagation sequence and pore-fluid conditions during fault-bend folding in the Appalachian Valley and Ridge, central Pennsylvania: Geological Society of America Bulletin, v. 102, p. 116-128.
Stearns, D. W., 1968, Certain aspects of fracture in naturally deformed rocks: N.S.F. advanced science seminar in rock mechanics, p. 97-118.
Stockmal, G. S., D. Lebel, M. E. Mcmechan, and P. A. Mackay, 2001, Structural style and evolution of the triangle zone and external Foothills, southwestern Alberta: Implications for thin-skinned thrust-and-fold belt mechanics: Bulletin of Canadian Petroleum Geology, v. 49, p. 472-496.
Storti, F., and F. Salvini, 1996, Progressive rollover fault-propagation folding: a possible kinematic mechanism to generate regional-scale recumbent folds in shallow foreland belts: AAPG Bulletin, v. 80, p. 174-193.
Stott, D. F., 1963, The Cretaceous Alberta Group and equivalent rocks, Rocky Mountain Foothills, Alberta: Geological Survey of Canada, Memoir, v. 317, 306 p.
Stott, D. F., 1984, Cretaceous sequences of the foothills of the Canadian Rocky Mountains: Canadian Society of Petroleum Geologists Memoir, v. 9, p. 85-107.
Sukaramongkol, C., 1993, Seismic imaging of a non-emergent thrust front in the Fallen Timber Creek Area, southern Alberta Foothills, Unpublished M.Sc. thesis, The University of Calgary, p. 140.
Suppe, J., 1983, Geometry and kinematics of fault-bend folding: American Journal of Science, v. 283, p. 684-721.
Suppe, J., 1985, Principles of Structural Geology: Prentice-Hall Inc: Englewood Cliffs, New Jersey, 1-537 p.
Taerum, R. L., 2011, Effect of mechanical stratigraphy on structural style variations in the central Alberta fold and thrust belt: PhD thesis thesis, University of Calgary, 228 p.
Tavani, S., F. Storti, O. Fernández, J. Muñoz, and F. Salvini, 2006, 3-D deformation pattern analysis and evolution of the Añisclo anticline, southern Pyrenees: Journal of structural geology, v. 28, p. 695-712.

Tavani, S., F. Storti, O. Lacombe, A. Corradetti, J. Muñoz, and S. Mazzoli, 2014, Fracturing stages in foreland fold and thrust belts: European Geological Union General Assembly Conference Abstracts, p. 3030.

Tavani, S., F. Storti, F. Salvini, and C. Toscano, 2008, Stratigraphic versus structural control on the deformation pattern associated with the evolution of the Mt. Catria anticline, Italy: Journal of Structural Geology, v. 30, p. 664-681.

Tavani, S., Storti, F., Salvini, F., 2006, Double-edge fault-propagation folding: geometry and kinematics: Journal of structural geology, v. 27, p. 19-35.

Thompson, R. I., 1979, A structural interpretation across part of the northern Rocky Mountains, British Columbia, Canada: Canadian Journal of Earth Sciences, v. 16, p. 1228-1241.

Twiss, R. J. a. M., E.M., 1992, Structural Geology W.H. Freeman and Company, New York, 531 p.

Ukar, E., Fermor, P., and Eichhubl, P, 2013, Fractured Unconventional Reservoirs in the Alberta Foothills, Canada: Unpublished Guidebook for the FRAC IA Consortium Annual Meeting September 12-14, 2013 Field Trip, The University of Texas at Austin p. 59.

Walderhaug, O., 1994, Temperatures of quartz cementation in Jurassic sandstones from the Norwegian continental shelf--evidence from fluid inclusions: Journal of Sedimentary Research, v. 64.

Wall, J. H., 1967, Cretaceous foraminifera of the Rocky Mountain foothills, Alberta, v. 20, Research Council of Alberta Bulletin

Woodward, N. B., and E. Rutherford Jr, 1989, Structural lithic units in external orogenic zones: Tectonophysics, v. 158, p. 247-267.